LONDON'S GLOBAL UNIVERSITY

UCL

Filling Single-Walled Carbon Nanotubes with Highly Reactive Chemicals

Martin Hart

Thesis submitted in partial fulfilment of the requirements for the degree of Doctor of Philosophy

Department of Chemistry
University College London

December 2018

I, MARTIN HART, confirm that the work presented in this thesis is my own. Where information has been derived from other sources, I confirm that this has been acknowledged in the thesis.

Signature: ……..

Date: ……..

Abstract

Since the discovery of single-walled carbon nanotubes (SWCNTs) in 1993, there has been a deep fascination with the 1D (one dimensional) nanometre sized cavity that they possess. Having the ability to confine all manner of materials in such a small space had never been possible before, and the surge of new allotropes and chemicals that have either been grown or encapsulated in this nano-test tube has been staggering. Salts and elements have formed the bulk of the confined materials, but chemistry has also been achieved within the cavity, and the reduction of metal oxides has proven straightforward. Consistency in filling SWCNTs in high yields has been difficult to achieve and finding a routine technique that can ascertain a filling yield have been stumbling blocks for the research area. No standard definition of the filling yield has even been agreed upon. These issues have held the field back from becoming a more popular and viable method for enhancing the properties of SWCNTs. To combat some of these issues, this thesis uses consistent and simple practices to determine the filling yield and aims to make consistently high purity materials which can be used for novel purposes.

Elemental phosphorus, arsenic and antimony have all been confined within a range of SWCNTs and have been fully characterised to determine their properties. Tetrahedral phosphorus and arsenic molecules have been stabilised by this method in quantities higher than achieved using other techniques. These can be produced either from melt reactions or vapour phase fillings which confirms that these elements fill the voids of the SWCNT in the form of tetrahedral molecules.

The confined phosphorus and arsenic tetrahedra have been shown form two new allotropes namely the zigzag ladders and single zigzag chains. These are expected to form either from thermal excitation or when exposed to an electron beam during high-resolution transmission electron microscopy (HRTEM). The structure produced is dependent on the diameter of nanotube and has shown consistent results with what is predicted by DFT calculations. There seems to be some dynamic behaviour at play between the conversion of the allotropes due to the small activation energy calculated for transitioning between the structures.

SWCNTs have also been filled with aluminium iodide, a strong Lewis acid, in order to induce charge transfer effects. A reliable method of producing high purity samples was developed and Raman spectroscopy has shown that these materials show charge

transfer in the correct direction. Unfortunately, despite the enhanced properties of the SWCNTs, the samples were found to be no more effectively functionalised than their empty counterparts.

Impact Statement

The research described in this thesis shows the potential single-walled carbon nanotubes have in confining and protecting highly air-sensitive materials. The materials confined within the cavity of the nanotubes have never been encapsulated in such ways before and have shown a remarkable stability that would be unachievable in their bulk configurations. Two new phosphorus allotropes have been discovered as well as isostructural arsenic analogues. Stabilised molecular phosphorus and arsenic have also been imaged. These materials have been fully characterised in a convenient and bulk manner in order to fully understand the properties of the material. A significant hurdle within the research community regards determining the success of a filling experiment. The use of corroborating data from multiple sources within this thesis has shown that a reliable quantity of filling material can be determined and can be used as a standard for this type of research.

The one-dimensional pnictogen allotropes are predicted to help understand the mechanisms the bulk materials may take in order to convert between the various allotropes. This is vital information that has perplexed scientists for centuries and will help materials scientists achieve full control over the growth of these materials. This is essential in order to keep up with the ever-growing demand for new and bespoke electronic devices. The stability of the confined materials and the thermodynamic properties of the composites will also provide fundamental insights into the reactivities of these main group elements. The confined polymers have also been predicted to show differing band gaps and electronic properties which may help with controlling any doping occurring between the filling material and nanotube.

The filling of single-walled carbon nanotubes is still a young field, and while the full potential of these composites yet to be reached, some great results have already been achieved. Filled nanotubes have already been used to create gas sensors and nano-thermometers amongst other applications. The materials created in this thesis can be seen as potential energy storage devices and as material transport applications of highly reactive chemicals. This work has made significant steps forward and it is hoped that these findings may be of use for theoreticians, materials scientists and industrial researchers.

Acknowledgements

This project would not have been achievable without the invaluable help and support of Prof. Christoph G. Salzmann, Prof. Milo S. P. Shaffer and Prof. Andrea Sella. I have worked with Christoph since my Third-year dissertation and I thank him for providing an excellent research environment. I would like to thank Milo for coming on board with this project and his vast knowledge and experience has proved vital for creating high quality output. Lastly, I would like to thank Andrea for reminding me that science can be fun even when your experiment is on fire.

I would also like to acknowledge all the people which have helped along the way such as Dr. Steve Firth, Dr. Catriona McGilvery, Dr. Edward White, Dr. Robert Palgrave, Dr Adam Clancy and not forgetting John Cowley who is probably sick of the sight of me asking for more quartz ampoules! Also, a special mention goes to Ji Chen for carrying out all the DFT work that has been fundamental to the success of this project. I would also like to highlight the Chemistry World article and "Phosphorus, Smoke and Lightning" BBC Radio 4 episode for creating some excellent exposure for the work we have published during this project.

To all the various members of the Salzmann group who have come and gone over the years, thanks for putting up with all my rants and ravings. In particular, Jacob, Alex, Zainab and Martin have provided great support and memories over the years. Rachael, Siriney and Sukhi, well, you're all bonkers. The Nanohac group has been an incredible source of expertise and I thank all the members that have listened to my presentations and gave excellent feedback and advice.

To the ACM-CDT, firstly thanks for funding my research and providing the access to facilities that otherwise would not have made my project possible. The course, schools and events that have been run have all provided good experiences and memories which made my PhD more than just research. To Cohort One, each and every one of you have made my PhD experience a pleasure! It was such a pleasure to meet and know you, you're all amazing people and I look forward to the next drinks.

Oli and Dougal, where would I be without you? Better off probably, but that's the price you pay I guess. Bruce and Kieran have also been great at keeping me honest, even at the expense of the odd nickname or two. Luke, Gibraltar (the Notorious G.I.B.) and Jamie,

excellent friends who have formed many of my good memories over the years. Mad and Kev, well the less said about them the better, but I know you meant well…

To Emma, how would I have done this without you? You're a fantastic person and one that has enriched my life. I am so grateful to have found you, you have inspired and encouraged me every step of the way.

And finally, Mum and Dad who have supported me every step of the way. For the work ethics you instilled in me, for not being afraid to get my hands dirty, for common sense and a sense of humour. I could not have asked for better parents and this work is a testament to you as much as anyone.

Table of Contents

List of Symbols

$Å$	angstrom	Å
c	speed of light	m s^{-1}
e	elementary charge	C
E_B	binding energy	eV
E_k	kinetic energy	eV
h	Planck constant	J s
I	intensity of transmitted light	n/a
η	coordination number	n/a
K	kelvin	K
°	degrees	°
Θ	angle	°
$°C$	degrees Celsius	°C
π	pi	n/a
ρ	*density*	*g* cm^{-3}

List of Abbreviations

0D	0 dimensional
1D	1 dimensional
2D	2 dimensional
3D	3 dimensional
AlI_3@Tuball	Tuball single-walled carbon nanotubes filled with aluminium iodide
v-As@CoMoCat	CoMoCat single-walled carbon nanotubes filled with arsenic by a vapour process
v-As@HiPCO	HiPCO single-walled carbon nanotubes filled with arsenic by a vapour process
at%	atomic percentage
ATR	attenuated total reflectance
B.E.	binding energy
CNTs	carbon nanotubes
CoMoCat	single-walled carbon nanotubes produced by the cobalt/molybdenum method
CVD	chemical vapour deposition
DWCNTs	double-walled carbon nanotubes
EDX	energy-dispersive X-ray spectroscopy
EELS	electron energy loss spectroscopy
FT-IR	Fourier-transform infrared spectroscopy
HiPCO	single-walled carbon nanotubes produced by the high-pressure carbon dioxide method

HOMO	highest occupied molecular orbital
HRTEM	high-resolution transmission electron microscopy
IR	infrared
I	path length
LUMO	lowest unoccupied molecular orbital
MOFs	molecular organic frameworks
MS	mass spectroscopy
MWCNTs	multiwalled carbon nanotubes
nm	nanometres
PXRD	powder X-ray diffraction
RBM	radial breathing modes
m-P@CoMoCat	CoMoCat single-walled carbon nanotubes filled with white phosphorus by a melt (*m*-) process
m-P@HiPCO	HiPCO single-walled carbon nanotubes filled with white phosphorus by a melt (*m*-) process
m-P@Tuball	Tuball single-walled carbon nanotubes filled with white phosphorus by a melt (*m*-) process
v-P@CoMoCat	CoMoCat single-walled carbon nanotubes filled with red phosphorus by a vapour (*v*-) process
v-P@HiPCO	HiPCO single-walled carbon nanotubes filled with red phosphorus by a vapour (*v*-) process
m-Sb@HiPCO	HiPCO single-walled carbon nanotubes filled with antimony by a melt (*m*-) process
m-Sb@Tuball	Tuball single-walled carbon nanotubes filled with antimony by a melt (*m*-) process
v-Sb@HiPCO	HiPCO single-walled carbon nanotubes filled with antimony by a vapour (*v*-) process

v-Sb@Tuball	Tuball single-walled carbon nanotubes filled with antimony by a vapour (*v*-) process
SEM	scanning electron microscopy
SWCNTs	single-walled carbon nanotubes
TEM	transmission electron microscopy
TGA	thermogravimetric analysis
TGA/DSC	thermogravimetric analysis coupled with differential scanning calorimetry
XPS	X-ray photoelectron spectroscopy

List of Figures

List of Tables

List of Appendix Figures

List of Publications

I would like to declare that part of this thesis has been adapted from the first two publications listed below.

1. Hart, M.; White, E. R.; Chen, J.; McGilvery, C. M.; Pickard, C. J.; Michaelides, A.; Sella, A.; Shaffer, M. S. P.; Salzmann, C. G., Encapsulation and Polymerization of White Phosphorus Inside Single-Wall Carbon Nanotubes. *Angewandte Chemie-International Edition* **2017,** *56* (28), 8144-8148.

2. Hart, M.; Chen, J.; Michaelides, A.; Sella, A.; Shaffer, M. S. P.; Salzmann, C. G., One-Dimensional Arsenic Allotropes: Polymerization of Yellow Arsenic Inside Single-Wall Carbon Nanotubes. *Angewandte Chemie-International Edition* **2018,** *57* (36), 11649-11653.

3. Rosillo-Lopez, M.; Lee, T. J.; Bella, M.; Hart, M.; Salzmann, C. G., Formation and chemistry of carboxylic anhydrides at the graphene edge. *Rsc Advances* **2015,** *5* (126), 104198-104202.

4. Shephard, J. J.; Slater, B.; Harvey, P.; Hart, M.; Bull, C. L.; Bramwell, S. T.; Salzmann, C. G., Doping-induced disappearance of ice II from water's phase diagram. *Nature Physics* **2018,** *14* (6), 569-572.

5. "First sighting of 'pink phosphorus' caged in carbon nanotubes" By James Urquhart – Chemistry World, 2017.

6. "Phosphorus, Smoke and Lightning" – In Their Element, Series 2, Episode 2, BBC Radio 4, 2018.

1 Introduction

1.1 The Discovery of Carbon Nanotubes

The discovery of single-walled carbon nanotubes (SWCNTs) paved the way for a new era of nanotechnology[1], which can be seen by the tens of thousands of papers which have been published using the material. The creation of fullerenes and then multi-walled carbon nanotubes (MWCNTs) showed the complexity carbon can display as a nanostructure, however, the real breakthrough came with Iijima's paper entitled: "Single-shell Carbon Nanotubes of 1 nm Diameter", which made use of metal nanoparticles to catalyse the growth of the SWCNTs.[1] Their highly defined nature makes them much easier to define and characterise compared to their multi-walled analogues. Although the focus of the research will only concern SWCNTs, there are some key papers concerning the filling of carbon nanotubes which use multi-walled carbon nanotubes as the confining medium.

1.2 Properties of Single-Walled Carbon Nanotubes

This section will describe how many of the properties that SWCNTs are known for can be attributed to the structure of a carbon nanotube. The matter of chirality will be described from which the fundamental electronic properties of SWCNTs are derived and thus makes SWCNTs one of the most unique materials in the world.

1.2.1 Geometry of SWCNTs

SWCNTs are, simply put, tubes of graphitic carbon with diameters in the nanometre range. We can unravel this tube to make a flat sheet of graphene. Graphene, a single sheet of carbon atoms, was first isolated and characterised in 2004 by Novoselov in Manchester.[2] The carbon atoms are arranged in a hexagonal lattice and it is the sp^2 hybridisation which allows the carbon atoms to form a flat sheet with bond angles of 120° between atoms. The sheet can be rolled in many different paths which will vary the orientation of the carbon hexagons with respect to the tube axis. This is the roll-up vector and can be observed in the figure below.

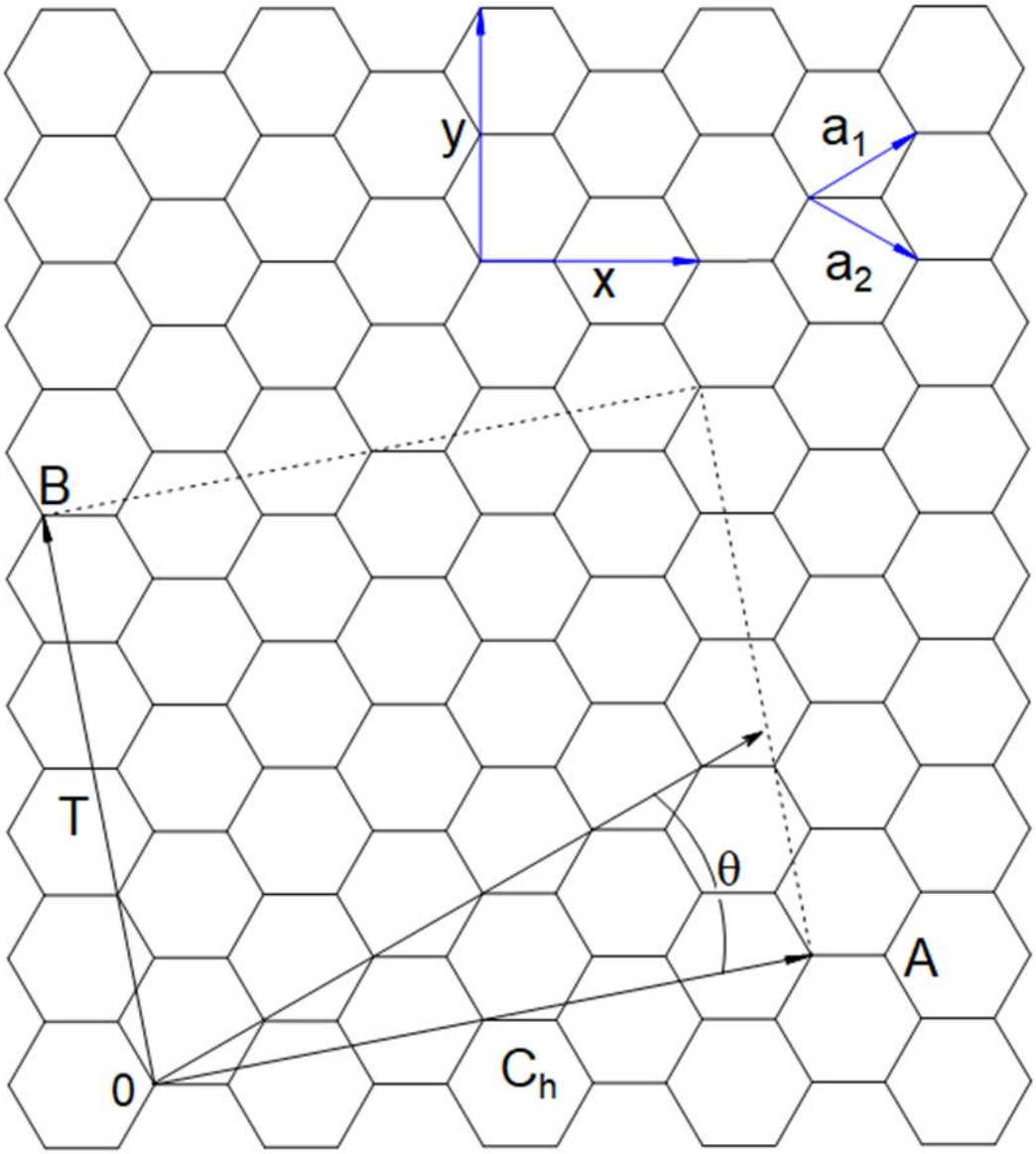

Figure 1.1 Illustration showing the geometric rules that show how every SWCNT can be defined from a single sheet of graphene that is rolled into a cylinder.

Table 1.1 Classification of the different SWCNT types.

Type	Superimposable	Chiral Angle	Chiral Vector
Chiral	No	$0 \leq \lvert\theta_c\rvert \leq 30°$	$(n,m \neq 0,n)$
Zigzag	Yes	0°	$(n,0)$
Armchair	Yes	30°	(n,n)

Figure 1.1 shows the hexagonal lattice of a sheet of graphene. Marked on the sheet is a unit cell for a SWCNT with the vector **T** marking the longitudinal axis of the nanotube, or

c-axis. The vector $\mathbf{C_h}$ is the chiral vector in the radial direction. By connecting **O** to **A**, we produce a SWCNT.

We can use the chiral vector as a means of identifying and defining a SWCNT by describing it in real space using the unit vectors $\mathbf{a_1}$ and $\mathbf{a_2}$:

$$\mathbf{C}_h = n\mathbf{a_1} + m\mathbf{a_2} \equiv (n,m) \qquad (n,m \text{ are integers, } 0 \leq |m| \leq n) \qquad [1.1]$$

For example, the SWCNT drawn in Figure 1.1 has the chirality (4,2). The chiral angle defines the orientation of the hexagons with respect to the longitudinal axis of the SWCNT. The symmetry of the hexagonal axis confines this to $0 \leq |\theta_c| \leq 30°$. This angle restriction allows SWCNTs to be grouped into either chiral or achiral types. Chiral SWCNTs can have any chiral angle between the limits and have a mirror image that cannot be superimposed onto the original image. Achiral SWCNTs do have superimposable mirror images but can also be split into two further groups depending on their chiral angle. A zigzag SWCNT can have the chiral indices (*n,m*) of (*n,*0) and a chiral angle of $\theta_c = 0°$. An armchair SWCNT can have the indices (*n,n*) and a chiral angle $\theta_c = 30°$.

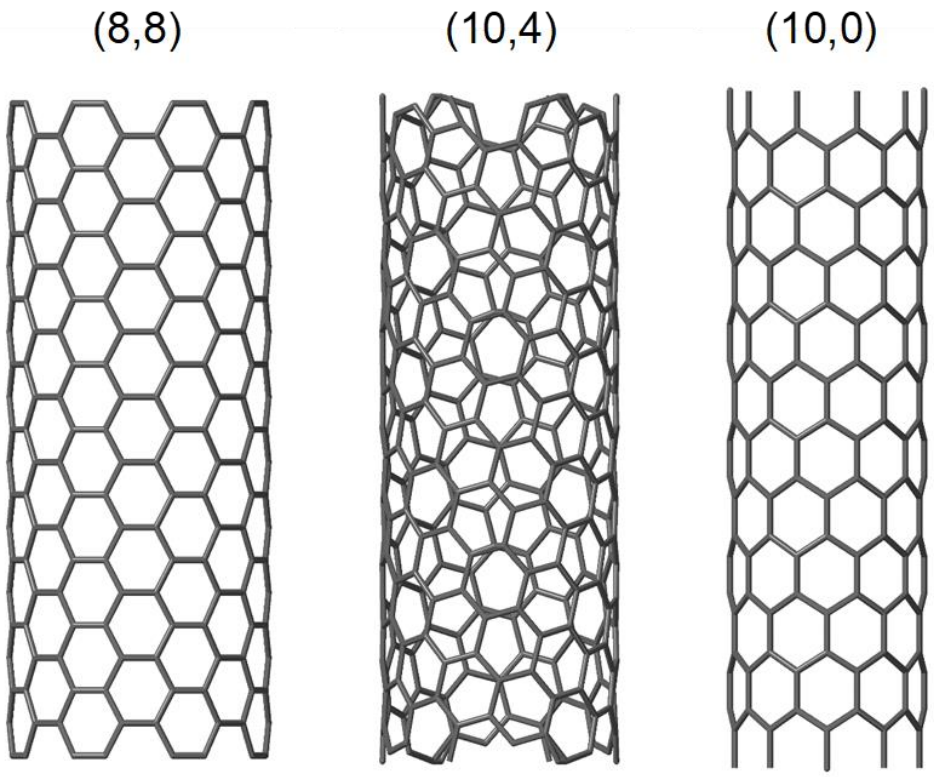

Figure 1.2 Examples of SWCNTs for each of the three chirality types. On the left there is an armchair SWCNT, centre is a chiral SWCNT and lastly a zigzag SWCNT.

The chiral vector, $\mathbf{C_h}$, can also be used to determine the diameter of the SWCNT by this simple relationship:

$$d_t = \frac{\|\mathbf{C_h}\|}{\pi} \qquad [1.2]$$

This relationship now allows the diameter to be calculated if only the (*n,m*) indices are known:

$$\begin{aligned} \|\mathbf{C_h}\|^2 &= \mathbf{C_h}\cdot\mathbf{C_h} \\ &= (n\mathbf{a_1} + m\mathbf{a_2}) \cdot (n\mathbf{a_1} + m\mathbf{a_2}) \\ &= n^2\mathbf{a_1}\cdot\mathbf{a_1} + m^2\mathbf{a_2}\cdot\mathbf{a_2} + 2nm\mathbf{a_1}\cdot\mathbf{a_2} \\ &= n^2\left(\sqrt{3}a_{c-c}\right)^2 + m^2\left(\sqrt{3}a_{c-c}\right)^2 + 2nm\left(\frac{3}{2}a_{c-c}^2\right) \\ &= \left(\sqrt{3}a_{c-c}\right)^2(n^2 + m^2 + nm) \end{aligned} \qquad [1.3]$$

where $a_{c\text{-}c}$ is the carbon nearest neighbour distance, 1.421 Å,[3] and is related to $\mathbf{a_1}$ and $\mathbf{a_2}$ by:

$$\mathbf{a_1} = \left(\frac{3}{2}a_{c-c}, \frac{\sqrt{3}}{2}a_{c-c}\right) = \left(\frac{\sqrt{3}}{2}, \frac{1}{2}\right)a \qquad [1.4]$$

$$\mathbf{a_2} = \left(\frac{3}{2}a_{c-c}, -\frac{\sqrt{3}}{2}a_{c-c}\right) = \left(\frac{\sqrt{3}}{2}, -\frac{1}{2}\right)a \qquad [1.5]$$

and $a = \|\mathbf{a_1}\| = \|\mathbf{a_2}\| = \sqrt{3}a_{c-c}$.

1.2.2 Optoelectronic Properties of SWCNTs

The basic structure of a SWCNT and how they can be defined by their geometry has been explained above. These terms can now be used to help define the optoelectronic properties of SWCNTs. From these properties, it is possible to determine the chirality and thus diameter from spectroscopic results.

SWCNTs can be split into two groups which define their electronic properties: metallic and semi-conducting. The key to understanding their differences is how the carbon atoms bond to each other. SWCNTs are one of a number of sp^2 carbon materials. The atomic orbitals of the valence carbon electrons, $2s^2 2p^2$, combine to give the molecular orbitals 2s, $2p_x$, $2p_y$, $2p_z$. The 2s, $2p_x$ and $2p_y$ molecular orbital hybridise to form the in-plane σ-bonds that holds the material together. It is for this reason that makes SWCNTs so notably strong.[4] This leaves the out of plane $2p_z$ orbital which overlap along the nanotube to form π-bonding above and below the nanotube sidewall. It is this bonding which defines the electronic properties of the nanotube.

If the bonding π (valence) orbitals and the anti-bonding π* (conduction) orbitals show degeneracy, the nanotube will be metallic at room temperature. There will be no band gap at the Fermi level and instead displays a continuous electronic density of states across the Fermi level, Figure 1.3. A separation of the density of states will lead to a band gap at the Fermi level and thus will be classified as semi-conducting.[5] Energy transitions across the Fermi level occur between distinct levels known as van Hove singularities.[6]

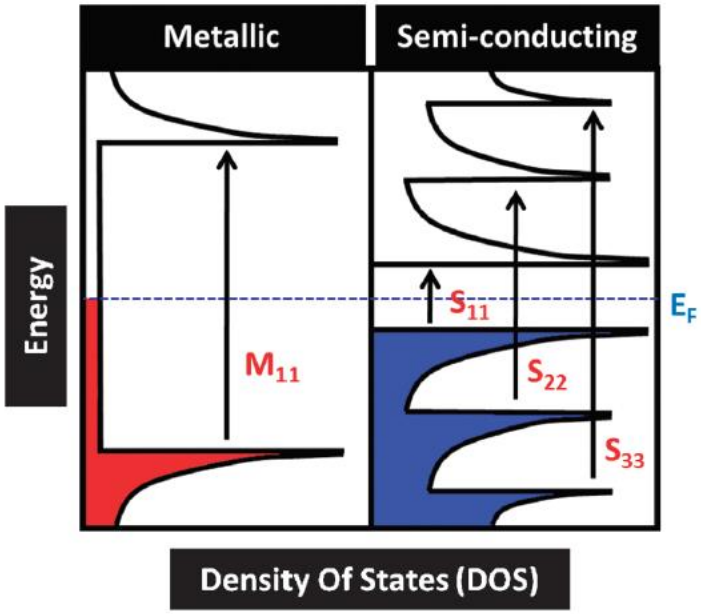

Figure 1.3 The electronic density of states of metallic and semi-conducting SWCNTs. The electronic transitions that are allowed occur between van Hove singularities, represented by the black arrows. M_{11} and S_{11} show the lowest energy transition for metallic and semi-conducting SWCNTs respectively. Figure reproduced with permission from reference [6].

The chirality of the nanotube can be linked to its electronic properties by these rules:

$$\text{Semi-conducting: } (n\text{-}m) \neq 3q \qquad [1.6]$$

$$\text{Metallic: } (n\text{-}m) = 3q \qquad [1.7]$$

where q is an integer. In an ideal sample of nanotubes, with every possible (*n*,*m*) chirality present, 1/3 will be metallic and therefore 2/3 will be semi-conducting.[5]

1.3 Production Methods of Single-Walled Carbon Nanotubes

This section will primarily focus on the synthesis techniques used to produce the SWCNTs used in this thesis. As they are all based around the same technique, chemical

vapour deposition (CVD), I will briefly outline the other two main methods currently used for the mass production of SWCNTs.

1.3.1 The Arc Discharge Method

The arc-discharge method consists of a hollowed graphite anode filled with an yttrium-nickel alloy powder. A graphite cathode is placed a few millimetres away and a current is passed through them.[7] The nanotubes grow on the walls of the reaction chamber, which is kept under an inert atmosphere of helium. The nanotubes are in the form of a soot which needs to be purified in order to extract the SWCNTs and leave behind any other carbonaceous materials.[8]

1.3.2 The Laser Ablation Method

Laser ablation involves firing a laser at a carbon target which is laced with a catalyst (cobalt-nickel for example) within an oven. The carbon is vaporised and then condensed into CNTs on a water-cooled surface.[9] Both laser ablation and arc-discharge methods create high quality CNTs, however, they are both energy consuming and require solid carbon feedstocks which limit their potential for mass production.[10]

1.3.3 CoMoCat

CoMoCat SWCNTS are produced using a CVD technique[11]. It gets its name from the fact it uses both cobalt (Co-) and molybdenum (-Mo-) to catalyse (-Cat) the growth of the SWCNTs. It uses carbon monoxide as the carbon source which thermally decomposes and then grows on the catalyst nanoparticles. It was discovered that the catalysts have a synergistic relationship, meaning that if either of the metals are absent, the technique will either not work (cobalt absent) or is unselective (molybdenum absent)[12]. The general mechanism for SWCNT growth is then as follows; the CO decomposes on the cobalt nanoparticles. The cobalt exists as cobalt oxide, which reduces in the presence of CO. This forms the active carbon species needed to grow the SWCNTs. The active carbon either reacts with any molybdenum oxide present in the molybdenum nanoparticles to form molybdenum carbide or catalyses on the reduced cobalt nanoparticles to form SWCNTs.

The Boudouard reaction is key to how carbon monoxide can be used to grow carbon nanotubes. The CO can disproportionate on the catalyst nanoparticles and grow SWCNTs:

$$CO + CO \rightarrow CO_2 + C(SWCNTs) \qquad [1.8]$$

There are two key reasons as to why this mechanism helps produce SWCNTs. Firstly, the molybdenum carbides act as an active carbon sink for the excess active carbon produced from the decomposition of CO by the cobalt nanoparticles. If there is too many active carbon species present, MWCNTs will form. Secondly, the molybdenum can stabilise the cobalt oxide nanoparticles which will then prevent them from agglomerating when they are reduced by the CO. The diameters of the cobalt nanoparticles determine the eventual diameter of the SWCNTs grown so by keeping the nanoparticles small in this way helps grow small diameter SWCNTs.

One of the key advantages of the CoMoCAT method is the extremely high selectivity for specific chiralities it achieves, with a very narrow diameter distribution range[13]. A few main chiralities dominate, the (6,5), (7,5) and the (7,6) SWCNTs.

1.3.4 HiPCO

Similarly, to CoMoCAT SWCNTs, HiPCO tubes are also produced using a CVD technique that uses carbon monoxide as the carbon source.[14] High (Hi-) pressure (-P-) carbon monoxide (-CO) is used to decompose iron pentacarbonyl, $Fe(CO)_5$, into smaller iron carbonyl clusters on which the SWCNTs growth is catalysed via the Boudouard reaction.

These tubes have a larger diameter range than CoMoCAT which makes them incredibly useful for containment purposes. Their calculated range is from 7 Å to 13 Å from Resonance Raman Spectroscopy studies with a preference for semi-conducting tubes.[15], [16]

1.3.5 Tuball

The Tuball SWCNTs which have been used in this project are made using a modification of the arc discharge method whereby the anode is made of the catalyst itself. Tiny particles evaporate from the surface whilst the current is passed through them. The SWCNTs can then grow on these nanoparticles from a gaseous feedstock.[17]

The tubes produced by this method are much wider than the two types described above with diameters ranging from 1.1 nm to 2.2 nm.[18]

1.4 Filling SWCNTs

1.4.1 In the Beginning there was nothing…

SWCNTs were not the first hollow material to be filled. Fullerenes had been filled as far back as 1985, using fairly similar techniques as to how carbon nanotubes would eventually be grown. By having some lanthanide salt present in the graphite during laser

vaporisation, the C_{60} fullerenes produced would contain lanthanum atoms.[19] Multi-walled carbon nanotubes had also been filled previously with various materials, and could even be filled during the synthesis process. The catalyst used during their synthesis would often be found within the MWCNT cavity[20] or by having the filling material present during the MWCNT synthesis.[21]

However, it was when SWCNTs were first successfully filled with ruthenium chloride by Sloan *et al.* in Oxford that the potential of filled carbon nanotubes really took off.[22] The most common filling material of these early attempts were metal halides and oxides which have relatively low melting points that allow for simple encapsulation methods. Things swiftly moved onto a wider variety of chemicals such as iodine,[23] fullerenes[24] and endofullerenes[25] and also *o*-carborane [26] molecules in a bid to determine the potential that filling SWCNTs has to offer.

1.4.2 Nanostructural Determination of Confined Metal Halides

The principal question that dominates any filled SWCNT regards how the encapsulated material's structure changes. Confining materials to one dimension offered new potential to the types of structures that materials could take. MWCNTs had shown previously that the cavity was wide enough to encapsulate enough material for it to retain its bulk structure[20] but with the synthesis of much narrower SWCNTs, we can finally explore structure on a truly one dimensional basis.

Metal halides were chosen as the main types of materials for this initial work. They present a series of useful characteristics such as easily attainable melting points, simple structures and as they tend to contain heavy elements, should provide good contrast to carbon when imaged under a TEM. Potassium iodide has been an extensively characterised filling material for these very reasons, as can be seen by the micrographs in Figure 1.4.[27]

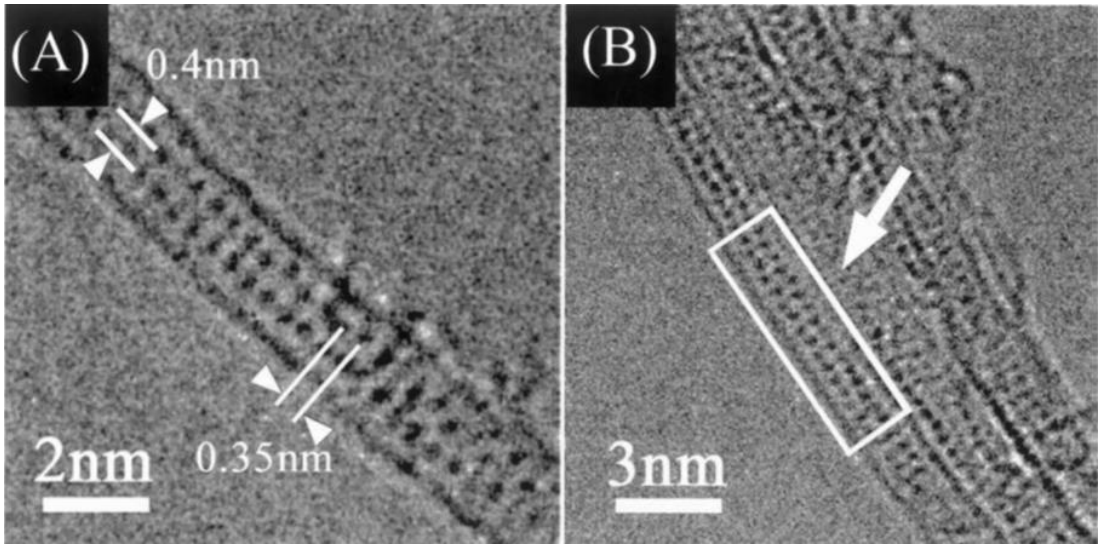

Figure 1.4 Example micrograph of potassium iodide filled SWCNTs. Reproduced from reference [27].

Rows of black dots within the tube are formed by alternating K-I and I-K columns. This bilayer crystal shows some tetragonal lattice distortion perpendicular to the direction of the tube. The KI rocksalt structure has a {200} d-spacing of 0.353 nm which, although observed in the nanocrystal along the tube direction, is smaller than the observed measurement in the SCWNT. Instead, an increase by ~14% to ~0.4 nm is seen which shows that some tetragonal distortion has occurred.[27] This can be attributed to two factors. Firstly, the diameter of the SWCNT is ~1.4 nm which gives an internal diameter of ~1 nm once the van der Waals radius of carbon is considered. This allows the atoms some freedom of movement within the tube and thus causes the expansion of the crystal. Secondly, there is a reduction from a 6-fold coordination environment in the bulk to a 4-fold coordination environment within the SWCNT. The atoms are effectively all surface atoms, so some rearrangement of the bond distances could be expected. KI crystals contained within a ~1.6 nm SWCNT form 3x3 structures which also show signs of tetragonal distortion due to the relative bond distances in the bulk compared to the volume available within the cavity.

Potassium iodide has the simple rocksalt structure, which is one of the reasons why it is still so extensively studied,[28] and it is not difficult to see how the bulk structure can be adapted to form a one-dimensional chain. Lead iodide poses a trickier problem due to its more complicated hexagonal close packed structure containing alternating layers of lead and iodide ions.[27] Figure 1.5 shows how a segment of the crystal can be used to fit within the tube and produce a very similar image to the one imaged. Some iodide ions had to be

removed to maintain its neutrality which gives rise to both octahedral and square pyramidal lead.

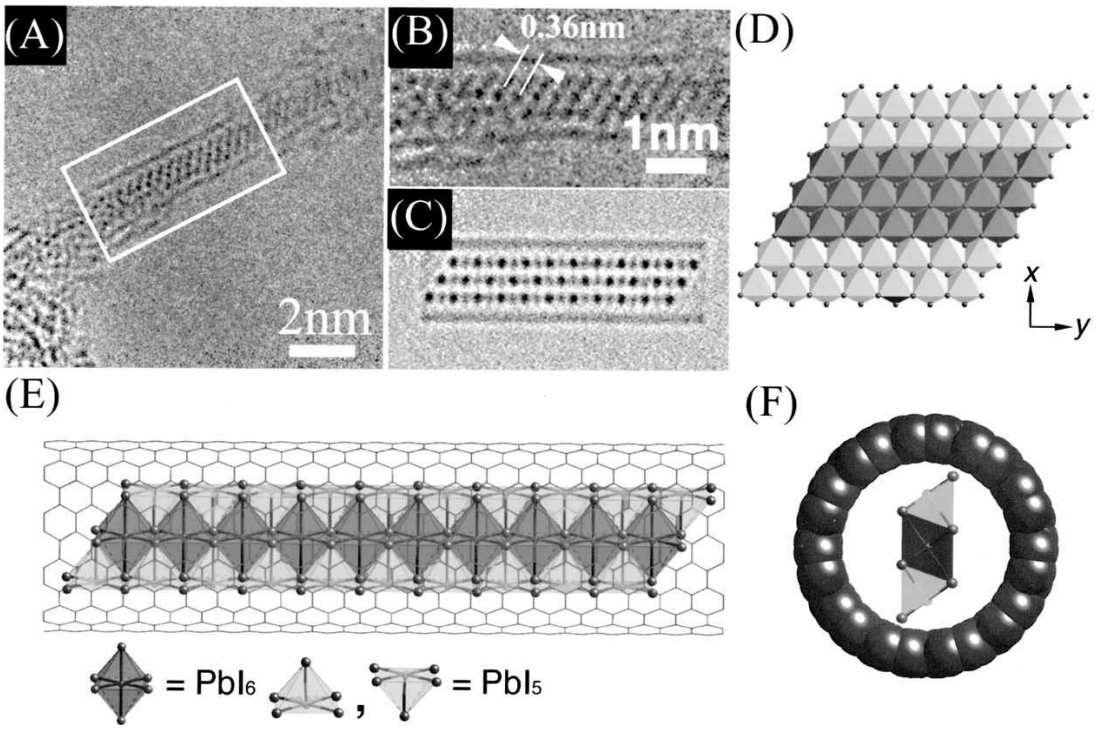

Figure 1.5 Example of lead iodide filled SWCNTs. Reproduced from [27].

These kinds of findings were very frequent in the metal halide filled SWCNTs. Sections of the bulk crystal structure could be found to match the structure seen within the cavity with some small distortion. A whole series of lanthanide halides have also shown similar results and shows the importance of obtaining good microscopy results in order to help understand the material's structure.

1.4.3 More Complicated Structures

The types of filling materials have become more complicated, and with that so has the structure which the material has taken. One of the most ground breaking discoveries was the formation of crystalline ice tubes within SWCNTs.[29] It had been predicted that water may exhibit vastly different properties to bulk water when confined within such narrow spaces. The spontaneous freezing of water into ice nanostructures was predicted by molecular dynamics simulations and showed that these structures take on far more complex structures than other contained material had previously shown.[30] The confined ice takes the form of ice nanotubes which are constructed from stacked layers of 3-8 sided shapes depending on the diameter of the SWCNT.[30] This remarkable discovery showed the potential of confinement as a way to mould materials into new structures.

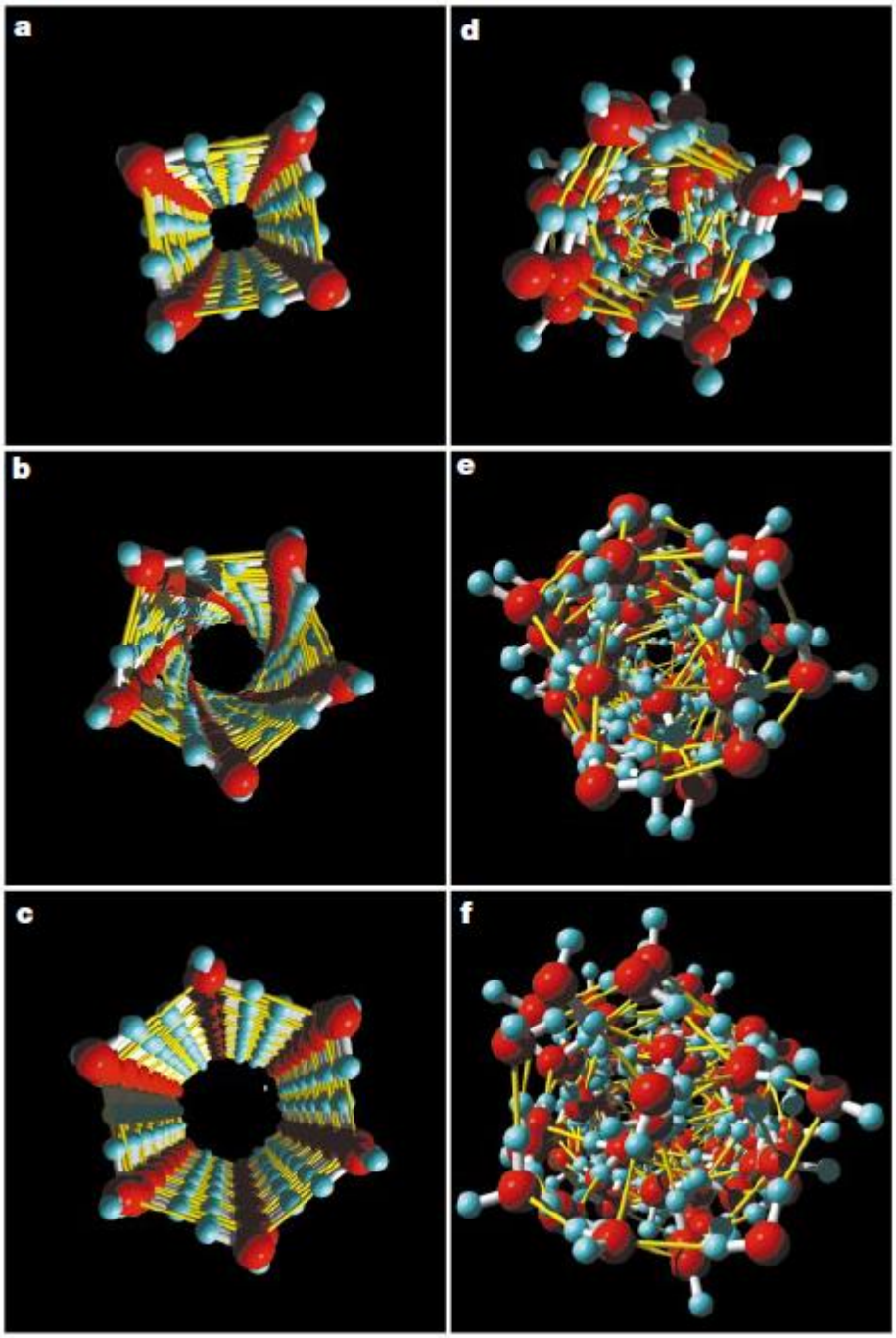

Figure 1.6 MD simulations of ice nanotubes confined within SWCNTs. Reproduced from reference [29].

An interesting feature of water filled nanotubes is the extreme difference in melting points between the confined water and for bulk ice.[31] A distinct dependence of the melting point observed to the nanotube diameter was seen with the melting point reaching 424 K for 1.05 nm wide nanotubes but dropping to 238 K for 1.15 nm wide nanotubes, with a range of other temperatures seen in between for other nanotubes. The thermal conductivity of the nanotubes would change as the phase changed within the cavity allowing for potentially interesting applications.

Iodine was another material which showed unique structures when confined. One dimensional chains of iodine could be seen to wrap around one another in stark contrast to the structure of bulk iodine, although its ease of forming polyiodides may have been a hint at its ability to form these types of chains.[32] There was a similar dependence to nanotube diameter on the type of structure seen. In wider SWCNTs, up to three iodine chains could be seen which helps support the growing potential of using SWCNTs as moulds for different types of structures. Sulphur has also exhibited similar behaviour with the formation of linear chains in contrast to the eight membered rings that make up bulk sulphur.[33] They also showed remarkable thermal stability, evidence of sulfur's presence could still be seen up to 800 K. The polymerisation of the sulphur atoms may help immobilise the structures from leaking during heating and make them suitable for high temperature electronic devices.

There has been a whole host of materials now which show these types of linear structures when confined. Selenium,[34] tellurium,[35] and carbon[36] have all shown similar structures of single or double chains depending on the nanotube diameter.

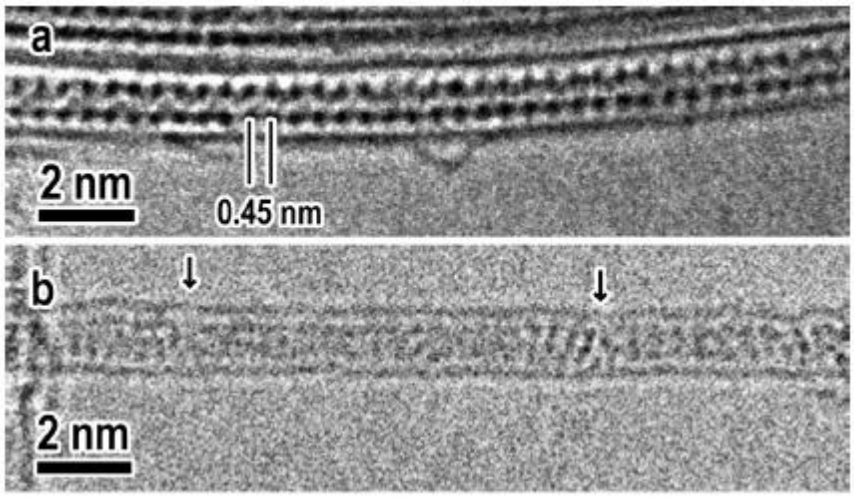

Figure 1.7 Linear chains of tellurium within SWCNTs. Reproduced from reference [34].

1.4.4 Reactions within SWCNTs

One of the interesting ideas of confinement was to use the SWCNT as a nanoscale test tube. Not only could you force materials into one dimension, but potentially create reaction products with highly defined dimensions. Metal nanowires have been routinely created by filling a SWCNT with a metal halide and then reducing the salt to the metal using a flow of hydrogen. This was attempted in the first filing paper which reduced ruthenium chloride to ruthenium.[22] The formation of nanowires in this way has allowed the creation of numerous metal nanowires that would be unachievable without the

SWCNT to mould and protect the wire from oxidation which would ruin any electronic properties the wire would possess.

Silver,[37] iron,[38] gold, platinum, palladium,[39] manganese, titanium, cobalt and nickel[40] nanowires have all been successfully created within SWCNTs by first filling with a salt and then reducing or decomposing the composite. This fairly reliable method means that devices and properties can be investigated more thoroughly. More complex reactions have also begun to push the boundaries of nanoscale reactions. Cadmium sulphide has been formed within a SWCNT from cadmium iodide and sulphur.[41] The high melting point of CdS would prevent it to fill a SWCNT by normal means so by exposing CdI@SWCNT to molten sulphur, CdS@SWCNT can be formed.

1.4.5 Methods of Filling SWCNTs

As the field has developed, many different methods for filling SWCNTs have been described. These procedures can be grouped into either *in situ* or *ex situ*, with the vast majority of these being *ex situ,* where the nanotubes are filled after they have been grown. These types of methods have dominated as they allow for a greater range of materials to be incorporated into the nanotube. *In situ* methods predominantly only allow for carbon molecules to be incorporated into the tube during the growing process, such as C_{60}, C_{70} and C_{80},[42, 43] except for bismuth which has also been successfully encapsulated in this way.[44] There is a much wider variety of filled MWCNTs created by this method, though.[21, 45] MWCNTs can be grown without the need for a metal nanoparticle catalyst, so the wanted filling material can replace the metal during the synthesis and grow inside the nanotube.

Both vapour and melt-phase filling *ex situ* procedures have shown excellent results and they generally use a similar method. The materials are combined by grinding to form a homogenous mixture and then sealed in an ampoule under vacuum. The ampoule is heated in a furnace for a given time and then the material is washed to remove any excess material.[46]. The key property required for melt filling procedures is that the material has a low enough melting point and low enough surface tension. If the material has a very high melting point, the SWCNTs will anneal before they are filled and if the surface tension is too high, it will not wet the SWCNT and so will not fill.[46, 47] As mentioned earlier, a lot of metal salts were chosen as filling materials due to their low melting points, making them easier to encapsulate.[37, 48, 49] Oxides are therefore less commonly filled in this way, due to generally higher temperatures, but it has still been achieved.[50, 51] If the filling material sublimes or has a high enough vapour pressure, a vapour phase

procedure will be used. Sulfur and selenium have been filled in this way.[33, 34] The sulfur filling procedure used a forked ampoule with the empty SWCNTs in one end and sulfur in the other. This allows for the sulfur to be easily sublimed across and onto the SWCNTs. This method is so versatile that even gases have been inserted into SWCNTs using similar methods.[52]

If the melting point is too high, liquid-phase or solution filled SWCNTs can also be achieved.[53] Soaking the SWCNTs in a solution of CrO_3 in HCl allowed filled SWCNTs without the need for any ampoules or furnaces, making for a very convenient procedure. Many other salts have been filled in similar methods, by using a suitable solvent for the salt used for example H_2O for $RuCl_3$,[22] HNO_3 for $Bi(NO_3)_3$ and $CHCl_3$ for $FeCl_3$.[44, 54] The pre-requisite for this method is that the critical diameter of the dissolved material and solvent shell is small enough for the filling material to diffuse through the cavity.[55]

These above descriptions form the main methods for filling SWCNTs. Other unique procedures exist though, such as a plasma ion irradiation method used to fill SWCNTs with caesium and using supercritical CO_2 as a solvent which has allowed various fullerene materials to be encapsulated at room temperature.[55-58]

A key discussion within the field has been the need for the SWCNTs to have open ends before the filling procedure can occur. A large number of methods have been developed to cause the opening of the tips, usually a mild oxidative process is used such as heat treatment in air or washing in an oxidative acid.[59] A procedure such as this is usually always performed before the filling procedure,[60] but there is some research where this procedure is omitted.[37, 61-64] It is theorised that the molten salt will react with the nanotube at these elevated temperatures to form CI_4. Despite current thermodynamic data showing that these reactions should not be feasible, it is maintained that as the thermodynamic data neither takes into account the strain at the tips of the nanotube nor the presence 5-membered rings at the tips, both which make the carbon more reactive and allow these reactions to occur.[61] The key step which allows these reactions to occur is the formation of I_2 gas from the molten salts caused by dimerization of the salt. I_2 has previously been shown to fill SWCNTs in similar circumstances,[65] so perhaps this explanation might be plausible.

The last main issue regards the purification of filled SWCNTs. Often there is a lot of external material which needs to be removed after the filling procedure. Usually a solvent is used to wash away any excess material,[55] but there is a risk that it will also wash away the internal material too.[66] In order to remove this risk, various methods

have been used to try and reduce this risk. Capping the already filled nanotubes using fullerenes or annealing them at high temperatures have been both been attempted in the literature.[66-70] Corking the ends of SWCNTs usually uses C_{60} fullerenes which are sonicated with the filled SWCNTs in a solvent that does not interfere with the filling material. Ethanol is commonly used as it has had good success at creating C_{60} peapods.[55] The strong interaction of C_{60} with the nanotube as opposed to ethanol encourages the C_{60} to enter the nanotube and remain there after filling. This has led to good results with regards to preventing the filling material to leak during the purification step.[69] A recent investigation into the purification of $LuCl_3$@SWCNT showed that a Soxhlet apparatus combined with dialysis allowed a high level of purification whilst reducing the quantity of water used for the process by up to 95%.[71] The method of filling made use of annealing the nanotubes first at 973-1173 K which allowed the internal material to remain risk-free of being washed away due to the SWCNT tips reforming and protecting the filling material.

1.5 Scope of Thesis

The main objective for this work is to expand on the field of filled SWCNTs and to also explore the current interest in the formation of new allotropes of main group elements, such as phosphorene.[72] The majority of this work will focus on encapsulating pnictogens. These elements show similar structural motifs such as a molecular form that phosphorus, arsenic and antimony can all adopt. These tetrahedral molecules are air and light-sensitive, so their confinement and stabilisation will push the boundaries of what SWCNTs are capable of. Phosphorus, arsenic and antimony tetrahedral molecules have never been encapsulated in this manner before, so they will provide a good comparison to other methods of stabilisation. Lastly, the encapsulation of aluminium iodide will dope the SWCNT and allow for easier and controllable functionalisation of the nanotube.

The structure of the thesis can be summarised as follows: Chapter 2 will outline the various procedures and characterisation techniques used to make and characterise these materials. Chapters 3 to 6 describe the findings of this thesis with each chapter being proceeded by a literature review to set the work in context. Chapter 3 shows how phosphorus molecules can be encapsulated and stabilised effectively within SWCNTs using either melt or vapour-phase techniques. Chapter 4 describes the encapsulation of arsenic within SWCNTs. Chapter 5 will compare and contrast the findings of the confined pnictogens and will incorporate new work showing the encapsulation of antimony to round out the encapsulation of pnictogens within SWCNTs. Lastly, Chapter 6 describes

how Lewis acid confinement can be used to manipulate the properties of SWCNT for the improvement in functionality. Chapter 8 will review the results of the previous chapters and looks to the future of nanoscale confinement.

1.6 References

1. Iijima, S.; Ichihashi, T., Single-shell carbon nanotubes of 1-nm diameter. *Nature* **1993,** *363* (6430), 603-605.
2. Novoselov, K. S.; Geim, A. K.; Morozov, S. V.; Jiang, D.; Zhang, Y.; Dubonos, S. V.; Grigorieva, I. V.; Firsov, A. A., Electric field effect in atomically thin carbon films. *Science* **2004,** *306* (5696), 666-669.
3. Budyka, M. F.; Zyubina, T. S.; Ryabenko, A. G.; Lin, S. H.; Mebel, A. M., Bond lengths and diameters of armchair single wall carbon nanotubes. *Chem. Phys. Let.* **2005,** *407* (4), 266-271.
4. Robertson, D. H.; Brenner, D. W.; Mintmire, J. W., Energetics of nanoscale graphitic tubules. *Phys. Rev. B* **1992,** *45* (21), 12592-12595.
5. Dai, L., *Carbon Nanotechnology: Recent Developments in Chemistry, Physics, Materials Science and Device Applications*. Elsevier Science: 2006.
6. Hodge, S. A.; Bayazit, M. K.; Coleman, K. S.; Shaffer, M. S. P., Unweaving the rainbow: a review of the relationship between single-walled carbon nanotube molecular structures and their chemical reactivity. *Chem. Soc. Rev.* **2012,** *41* (12), 4409-4429.
7. Shi, Z. J.; Lian, Y. F.; Zhou, X. H.; Gu, Z. N.; Zhang, Y. G.; Iijima, S.; Zhou, L. X.; Yue, K. T.; Zhang, S. L., Mass-production of single-wall carbon nanotubes by arc discharge method. *Carbon* **1999,** *37* (9), 1449-1453.
8. Moon, J. M.; An, K. H.; Lee, Y. H.; Park, Y. S.; Bae, D. J.; Park, G. S., High-yield purification process of singlewalled carbon nanotubes. *J. Phys. Chem. B* **2001,** *105* (24), 5677-5681.
9. Guo, T.; Nikolaev, P.; Thess, A.; Colbert, D. T.; Smalley, R. E., Catalytic growth of single-walled nanotubes by laser vaporization. *Chem. Phys. Let.* **1995,** *243* (1-2), 49-54.
10. Rafique, M. M. A.; Iqbal, J., Production of Carbon Nanotubes by Different Routes - A Review. *J. Encap. Ads. Sci.* **2011,** *1*, 5.
11. Kitiyanan, B.; Alvarez, W. E.; Harwell, J. H.; Resasco, D. E., Controlled production of single-wall carbon nanotubes by catalytic decomposition of CO on bimetallic Co-Mo catalysts. *Chem. Phys. Let.* **2000,** *317* (3-5), 497-503.
12. Alvarez, W. E.; Kitiyanan, B.; Borgna, A.; Resasco, D. E., Synergism of Co and Mo in the catalytic production of single-wall carbon nanotubes by decomposition of CO. *Carbon* **2001,** *39* (4), 547-558.
13. Bachilo, S. M.; Balzano, L.; Herrera, J. E.; Pompeo, F.; Resasco, D. E.; Weisman, R. B., Narrow (n,m)-distribution of single-walled carbon nanotubes grown using a solid supported catalyst. *J. Amer. Chem. Soc.* **2003,** *125* (37), 11186-11187.
14. Nikolaev, P.; Bronikowski, M. J.; Bradley, R. K.; Rohmund, F.; Colbert, D. T.; Smith, K. A.; Smalley, R. E., Gas-phase catalytic growth of single-walled carbon nanotubes from carbon monoxide. *Chem. Phys. Let.* **1999,** *313* (1-2), 91-97.
15. Jorio, A.; Fantini, C.; Pimenta, M. A.; Capaz, R. B.; Samsonidze, G. G.; Dresselhaus, G.; Dresselhaus, M. S.; Jiang, J.; Kobayashi, N.; Gruneis, A.; Saito, R., Resonance Raman spectroscopy (n,m)-dependent effects in small-diameter single-wall carbon nanotubes. *Phys. Rev. B* **2005,** *71* (7).
16. Kuwahara, S.; Kuwahara, Y.; Shinohara, H., Quantitative Analysis of Isolated Single-Wall Carbon Nanotubes with Their Molar Absorbance Coefficients. *J. Nanomat.* **2014**.

17. Predtechensky, M. R. Plasma-Chemical Reactor. 6,846,467 B1, 2005.
18. Clancy, A. J.; White, E. R.; Tay, H. H.; Yau, H. C.; Shaffer, M. S. P., Systematic comparison of conventional and reductive single-walled carbon nanotube purifications. *Carbon* **2016,** *108*, 423-432.
19. Heath, J. R.; O'Brien, S. C.; Zhang, Q.; Liu, Y.; Curl, R. F.; Tittel, F. K.; Smalley, R. E., Lanthanum complexes of spheroidal carbon shells. *J. Amer. Chem. Soc.* **1985,** *107* (25), 7779-7780.
20. Lei, Y. J.; Zhao, R.; Xu, M. Z.; Zhao, X.; Yang, X. L.; Guo, H.; Zhong, J. C.; Liu, X. B., Production of empty and iron-filled multiwalled carbon nanotubes from iron-phthalocyanine polymer and their electromagnetic properties. *J. Mater. Sci.-Mater. Electron.* **2012,** *23* (4), 921-927.
21. Loiseau, A.; Pascard, H., Synthesis of long carbon nanotubes filled with Se, S, Sb and Ge by the arc method. *Chem. Phys. Let.* **1996,** *256* (3), 246-252.
22. Sloan, J.; Hammer, J.; Zwiefka-Sibley, M.; Green, M. L. H., The opening and filling of single walled carbon nanotubes (SWTs). *Chem. Comm.* **1998,** (3), 347-348.
23. Guan, L. H.; Suenaga, K.; Shi, Z. J.; Gu, Z. N.; Iijima, S., Polymorphic structures of iodine and their phase transition in confined nanospace. *Nano Let.* **2007,** *7* (6), 1532-1535.
24. Smith, B. W.; Monthioux, M.; Luzzi, D. E., Encapsulated C-60 in carbon nanotubes. *Nature* **1998,** *396* (6709), 323-324.
25. Smith, B. W.; Luzzi, D. E.; Achiba, Y., Tumbling atoms and evidence for charge transfer in La-2@C-80@SWNT. *Chem. Phys. Let.* **2000,** *331* (2-4), 137-142.
26. Morgan, D. A.; Sloan, J.; Green, M. L. H., Direct imaging of o-carborane molecules within single walled carbon nanotubes. *Chem. Comm.* **2002,** (20), 2442-2443.
27. Sloan, J.; Friedrichs, S.; Meyer, R. R.; Kirkland, A. I.; Hutchison, J. L.; Green, M. L. H., Structural changes induced in nanocrystals of binary compounds confined within single walled carbon nanotubes: a brief review. *Inorganica Chim. Acta* **2002,** *330*, 1-12.
28. Ivanov, V. G.; Kalashnyk, N.; Sloan, J.; Faulques, E., Vibrational dynamics of extreme 2 x 2 and 3 x 3 potassium iodide nanowires encapsulated in single-walled carbon nanotubes. *Phys. Rev. B* **2018,** *98* (12).
29. Kolesnikov, A. I.; Zanotti, J.-M.; Loong, C.-K.; Thiyagarajan, P.; Moravsky, A. P.; Loutfy, R. O.; Burnham, C. J., Anomalously Soft Dynamics of Water in a Nanotube: A Revelation of Nanoscale Confinement. *Phys. Rev. Let.* **2004,** *93* (3), 035503.
30. Koga, K.; Gao, G. T.; Tanaka, H.; Zeng, X. C., Formation of ordered ice nanotubes inside carbon nanotubes. *Nature* **2001,** *412* (6849), 802-805.
31. Agrawal, K. V.; Shimizu, S.; Drahushuk, L. W.; Kilcoyne, D.; Strano, M. S., Observation of extreme phase transition temperatures of water confined inside isolated carbon nanotubes. *Nat. Nano.* **2017,** *12* (3), 267-+.
32. Svensson, P. H.; Kloo, L., Synthesis, Structure, and Bonding in Polyiodide and Metal Iodide−Iodine Systems. *Chemical Reviews* **2003,** *103* (5), 1649-1684.
33. Fujimori, T.; Morelos-Gomez, A.; Zhu, Z.; Muramatsu, H.; Futamura, R.; Urita, K.; Terrones, M.; Hayashi, T.; Endo, M.; Hong, S. Y.; Choi, Y. C.; Tomanek, D.; Kaneko, K., Conducting linear chains of sulphur inside carbon nanotubes. *Nat. Comm.* **2013,** *4*.
34. Fujimori, T.; dos Santos, R. B.; Hayashi, T.; Endo, M.; Kaneko, K.; Tomanek, D., Formation and Properties of Selenium Double-Helices inside Double-Wall Carbon Nanotubes: Experiment and Theory. *Acs Nano* **2013,** *7* (6), 5607-5613.
35. Kobayashi, K.; Yasuda, H., Structural transition of tellurium encapsulated in confined one-dimensional nanospaces depending on the diameter. *Chem. Phys. Let.* **2015,** *634*, 60-65.
36. Shi, L.; Rohringer, P.; Suenaga, K.; Niimi, Y.; Kotakoski, J.; Meyer, J. C.; Peterlik, H.; Wanko, M.; Cahangirov, S.; Rubio, A.; Lapin, Z. J.; Novotny, L.; Ayala, P.; Pichler, T.,

Confined linear carbon chains as a route to bulk carbyne. *Nat. Mat.* **2016,** *15* (6), 634-+.
37. Sloan, J.; Wright, D. M.; Woo, H. G.; Bailey, S.; Brown, G.; York, A. P. E.; Coleman, K. S.; Hutchison, J. L.; Green, M. L. H., Capillarity and silver nanowire formation observed in single walled carbon nanotubes. *Chem. Comm.* **1999,** (8), 699-700.
38. Borowiak-Palen, E.; Mendoza, E.; Bachmatiuk, A.; Rummeli, M. H.; Gemming, T.; Nogues, J.; Skumryev, V.; Kalenczuk, R. J.; Pichler, T.; Silva, S. R. P., Iron filled single-wall carbon nanotubes - A novel ferromagnetic medium. *Chem. Phys. Let.* **2006,** *421* (1-3), 129-133.
39. Govindaraj, A.; Satishkumar, B. C.; Nath, M.; Rao, C. N. R., Metal nanowires and intercalated metal layers in single-walled carbon nanotube bundles. *Chem. Mat.* **2000,** *12* (1), 202-205.
40. Sean, B.; Steve, C.; Robert, G.; Alex, M.; Leonid, G., Carbon nanotube-based ethanol sensors. *Nanotechnology* **2009,** *20* (23), 235502.
41. Eliseev, A. A.; Chernysheva, M. V.; Verbitskii, N. I.; Kiseleva, E. A.; Lukashin, A. V.; Tretyakov, Y. D.; Kiselev, N. A.; Zhigalina, O. M.; Zakalyukin, R. M.; Vasiliev, A. L.; Krestinin, A. V.; Hutchison, J. L.; Freitag, B., Chemical Reactions within Single-Walled Carbon Nanotube Channels. *Chem. Mat.* **2009,** *21* (21), 5001-5003.
42. Sloan, J.; Dunin-Borkowski, R. E.; Hutchison, J. L.; Coleman, K. S.; Williams, V. C.; Claridge, J. B.; York, A. P. E.; Xu, C. G.; Bailey, S. R.; Brown, G.; Friedrichs, S.; Green, M. L. H., The size distribution, imaging and obstructing properties of C-60 and higher fullerenes formed within arc-grown single walled carbon nanotubes. *Chem. Phys. Let.* **2000,** *316* (3-4), 191-198.
43. Zhang, Y.; Iijima, S.; Shi, Z.; Gu, Z., Defects in arc-discharge-produced single-walled carbon nanotubes. *Philos. Mag. Let.* **1999,** *79* (7), 473-479.
44. Kiang, C. H.; Choi, J. S.; Tran, T. T.; Bacher, A. D., Molecular nanowires of 1 nm diameter from capillary filling of single-walled carbon nanotubes. *J. Phys. Chem. B* **1999,** *103* (35), 7449-7451.
45. Muller, C.; Leonhardt, A.; Kutz, M. C.; Buchner, B.; Reuther, H., Growth Aspects of Iron-Filled Carbon Nanotubes Obtained by Catalytic Chemical Vapor Deposition of Ferrocene. *J. Phys. Chem. C* **2009,** *113* (7), 2736-2740.
46. Monthioux, M., Filling single-wall carbon nanotubes. *Carbon* **2002,** *40* (10), 1809-1823.
47. Dujardin, E.; Ebbesen, T. W.; Hiura, H.; Tanigaki, K., Capillarity and wetting of carbon nanotubes. *Science* **1994,** *265* (5180), 1850-1852.
48. Sloan, J.; Terrones, M.; Nufer, S.; Friedrichs, S.; Bailey, S. R.; Woo, H. G.; Ruhle, M.; Hutchison, J. L.; Green, M. L. H., Metastable one-dimensional AgCl1-xIx solid-solution wurzite "tunnel" crystals formed within single-walled carbon nanotubes. *J. Amer. Chem. Soc.* **2002,** *124* (10), 2116-2117.
49. Satishkumar, B. C.; Taubert, A.; Luzzi, D. E., Filling single-wall carbon nanotubes with d- and f-metal chloride and metal nanowires. *J. Nanosci. Nanotech.* **2003,** *3* (1-2), 159-163.
50. Friedrichs, S.; Meyer, R. R.; Sloan, J.; Kirkland, A. I.; Hutchison, J. L.; Green, M. L. H., Complete characterisation of a Sb2O3/(21,-8)SWNT inclusion composite. *Chem. Comm.* **2001,** (10), 929-930.
51. Hulman, M.; Kuzmany, H.; Costa, P.; Friedrichs, S.; Green, M. L. H., Light-induced instability of PbO-filled single-wall carbon nanotubes. *App. Phys. Let.* **2004,** *85* (11), 2068-2070.
52. Serpell, C. J.; Rutte, R. N.; Geraki, K.; Pach, E.; Martincic, M.; Kierkowicz, M.; De Munari, S.; Wals, K.; Raj, R.; Ballesteros, B.; Tobias, G.; Anthony, D. C.; Davis, B. G., Carbon nanotubes allow capture of krypton, barium and lead for multichannel biological X-ray fluorescence imaging. *Nat. Comm.* **2016,** *7*.

53. Mittal, J.; Monthioux, M.; Allouche, H.; Stephan, O., Room temperature filling of single-wall carbon nanotubes with chromium oxide in open air. *Chem. Phys. Let.* **2001,** *339* (5-6), 311-318.
54. Mittal, J.; Monthioux, M.; Allouche, H., *Extented Abstracts of the 25th Biennial Conference on Carbon, Lexington, Kentucky* **2001**.
55. Khlobystov, A. N.; Britz, D. A.; Wang, J. W.; O'Neil, S. A.; Poliakoff, M.; Briggs, G. A. D., Low temperature assembly of fullerene arrays in single-walled carbon nanotubes using supercritical fluids. *J. Mat. Chem.* **2004,** *14* (19), 2852-2857.
56. Hatakeyama, R.; Li, Y. F., Synthesis and electronic-property control of Cs-encapsulated single- and double-walled carbon nanotubes by plasma ion irradiation. *J. App. Phys.* **2007,** *102* (3).
57. Britz, D. A.; Khlobystov, A. N.; Wang, J. W.; O'Neil, A. S.; Poliakoff, M.; Ardavan, A.; Briggs, G. A. D., Selective host-guest interaction of single-walled carbon nanotubes with functionalised fullerenes. *Chem. Comm.* **2004,** (2), 176-177.
58. Pagona, G.; Rotas, G.; Khlobystov, A. N.; Chamberlain, T. W.; Porfyrakis, K.; Tagmatarchis, N., Azafullerenes encapsulated within single-walled carbon nanotubes. *J. Amer. Chem. Soc.* **2008,** *130* (19), 6062-+.
59. Hirahara, K.; Suenaga, K.; Bandow, S.; Kato, H.; Okazaki, T.; Shinohara, H.; Iijima, S., One-dimensional metallofullerene crystal generated inside single-walled carbon nanotubes. *Phys. Rev. Let.* **2000,** *85* (25), 5384-5387.
60. Kharlamova, M. V., Advances in tailoring the electronic properties of single-walled carbon nanotubes. *Progress in Materials Science* **2016,** *77*, 125-211.
61. Nie, C. Y.; Galibert, A. M.; Soula, B.; Flahaut, E.; Sloan, J.; Monthioux, M., A new insight on the mechanisms of filling closed carbon nanotubes with molten metal iodides. *Carbon* **2016,** *110*, 48-50.
62. Sloan, J.; Novotny, M. C.; Bailey, S. R.; Brown, G.; Xu, C.; Williams, V. C.; Friedrichs, S.; Flahaut, E.; Callender, R. L.; York, A. P. E.; Coleman, K. S.; Green, M. L. H.; Dunin-Borkowski, R. E.; Hutchison, J. L., Two layer 4 : 4 co-ordinated KI crystals grown within single walled carbon nanotubes. *Chem. Phys. Let.* **2000,** *329* (1-2), 61-65.
63. Xu, C. G.; Sloan, J.; Brown, G.; Bailey, S.; Williams, V. C.; Friedrichs, S.; Coleman, K. S.; Flahaut, E.; Hutchison, J. L.; Dunin-Borkowski, R. E.; Green, M. L. H., 1D lanthanide halide crystals inserted into single-walled carbon nanotubes. *Chem. Comm.* **2000,** (24), 2427-2428.
64. Sloan, J.; Friedrichs, S.; Flahaut, E.; Brown, G.; Bailey, S. R.; Coleman, K. S.; Xu, C.; Green, M. L. H.; Hutchison, J. L.; Kirkland, A. I.; Meyer, R. R., The characterisation of sub-nanometer scale structures within single walled carbon nanotubes. *Elec. Prop. Molec. Nano.*, Kuzmany, H.; Fink, J.; Mehring, M.; Roth, S., Eds. 2001; Vol. 591, pp 277-282.
65. Fan, X.; Dickey, E. C.; Eklund, P. C.; Williams, K. A.; Grigorian, L.; Buczko, R.; Pantelides, S. T.; Pennycook, S. J., Atomic arrangement of iodine atoms inside single-walled carbon nanotubes. *Phys. Rev. Let.* **2000,** *84* (20), 4621-4624.
66. Shao, L.; Tobias, G.; Huh, Y.; Green, M. L. H., Reversible filling of single walled carbon nanotubes opened by alkali hydroxides. *Carbon* **2006,** *44* (13), 2855-2858.
67. Shao, L.; Lin, T.-W.; Tobias, G.; Green, M. L. H., A simple method for the containment and purification of filled open-ended single wall carbon nanotubes using C-60 molecules. *Chem. Comm.* **2008,** (18), 2164-2166.
68. Ren, Y.; Pastorin, G., Incorporation of hexamethylmelamine inside capped carbon nanotubes. *Adv. Mat.* **2008,** *20* (11), 2031-+.
69. Luksirikul, P.; Ballesteros, B.; Tobias, G.; Moloney, M. G.; Green, M. L. H., pH-triggered release of materials from single-walled carbon nanotubes using dimethylamino-functionalized fullerenes as removable "corks". *Carbon* **2010,** *48* (7), 1912-1917.

70. Spinato, C.; de Garibay, A. P. R.; Kierkowicz, M.; Pach, E.; Martincic, M.; Klippstein, R.; Bourgognon, M.; Wang, J. T. W.; Menard-Moyon, C.; Al-Jamal, K. T.; Ballesteros, B.; Tobias, G.; Bianco, A., Design of antibody-functionalized carbon nanotubes filled with radioactivable metals towards a targeted anticancer therapy. *Nanoscale* **2016,** *8* (25), 12626-12638.
71. Kierkowicz, M.; Gonzalez-Dominguez, J. M.; Pach, E.; Sandoval, S.; Ballesteros, B.; Da Ros, T.; Tobias, G., Filling Single-Walled Carbon Nanotubes with Lutetium Chloride: A Sustainable Production of Nanocapsules Free of Nonencapsulated Material. *ACS Sustain. Chem. Eng.* **2017,** *5* (3), 2501-2508.
72. Khandelwal, A.; Mani, K.; Karigerasi, M. H.; Lahiri, I., Phosphorene – The two-dimensional black phosphorous: Properties, synthesis and applications. *Mat. Sci. Engin.: B* **2017,** *221*, 17-34.

2 Experimental Procedures and Characterisation Techniques

2.1 Introduction

This chapter will set out the basic principles and experimental techniques used to complete the research described in this thesis. It will start by setting out how SWCNTs are opened and purified, and will then describe the various procedures to fill the SWCNTs with each material. The rest of this chapter will briefly discuss the techniques used to characterise these samples in order to establish both the filling yield and structure of the confined material.

2.2 Purification and Opening of SWCNTs

2.2.1 Steam Purification of Tuball SWCNTs

Raw SWCNTs purchased from OCSiAl were purified using a steam treatment procedure developed by Tobias *et al.* and followed by an acid wash in HCl.[1] Nitrogen gas is passed through a Dreschel flask containing distilled water which is kept at 343 K to produce steam. This is then passed over the SWCNTs, using the nitrogen as a carrier gas, at 100 mL min^{-1}. The SWCNTs are heated to 1173 K in a tube furnace and held for 5 h and then allowed to cool back to room temperature whilst the nitrogen/steam mixture is still passed over them.

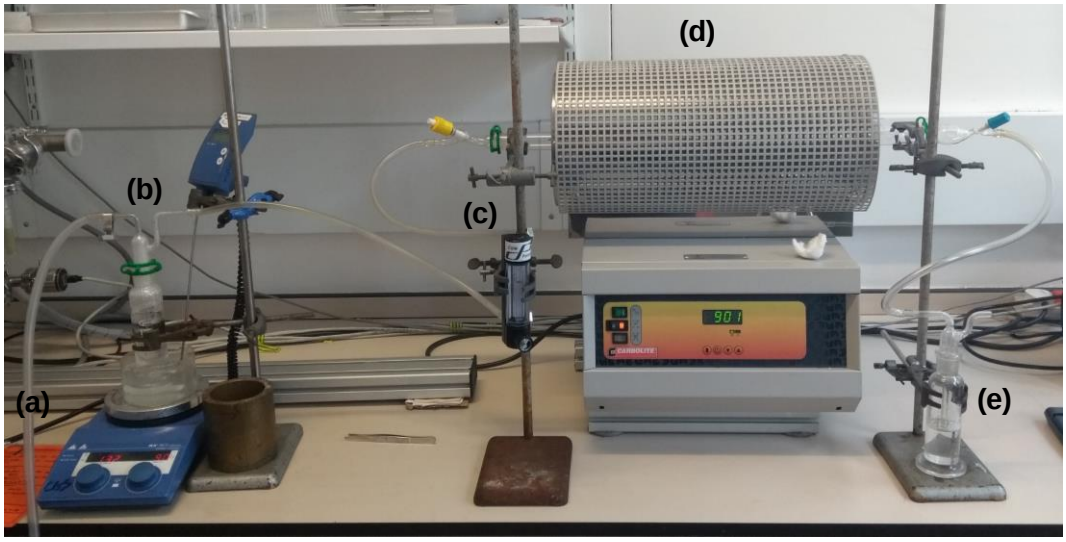

Figure 2.1 Steam Purification set-up. (a) Tube connecting the apparatus to a nitrogen cylinder. (b) Dreschel flask filled with distilled water and kept at 343 K. (c) Flow controller set to 100 mL min^{-1}. (d) Tube furnace at 1173 K. (e) Dreschel flask filled with oil to prevent any back flow of air.

This should provide gentle oxidation to help remove amorphous carbon and the tips of the SWCNTs following this reaction:

$$C + H_2O \rightarrow CO + H_2 \qquad [2.1]$$

The tips of the SWCNTs are more prone to oxidation, due to the higher strain of forming the hemispherical end cap and the presence of 5 membered rings, as opposed to the cylinder walls which allows for their opening without too much tube wall damage.[2] A second heat treatment at 723 K in air, and held for 30 min, is used to ensure the complete opening of the SWCNTs following this reaction:

$$C + O_2 \rightarrow CO_2 \qquad [2.2]$$

Once the tubes have cooled, they are refluxed in 6 M HCl for 2.5 h before being washed and filtered on a 0.2 μm polycarbonate membrane with distilled water until the washings are neutral.

2.2.2 Opening of CoMoCAT and HiPCO SWCNTs

CoMoCAT and HiPCO SWCNTs purchased were deemed pure enough to forego an additional purification procedure. CoMoCAT SWCNTs were purchased from Sigma, product number 704121, and HiPCO SWCNTs were purchased from Nanointegris, in their Purified grade powder form. They were therefore heated to 673 K in air to open the tips and allow filling. No other purification step was used.

2.3 Filling Single-Walled Carbon Nanotubes

2.3.1 White Phosphorus

White phosphorus was purified by sublimation and loaded onto a sublimation probe. The probe can then be transferred into a flask containing SWCNTs (50 mg) which have been pre-heated to 473 K under high-vacuum to fully dry and evacuate the SWCNTs before their filling. The SWCNTs were placed in a long alumina boat which is contained within a quartz vacuum tube. The vacuum tube is fitted with a quartz KF24 fitting which is fitted to a turbo vacuum system via a butterfly valve horizontally. The tube furnace can be slid over the vacuum tube and allow the system to be heated and evacuated under reduced pressure. The butterfly valve can seal the vacuum tube, so it remains under vacuum whilst it is transferred to a glove box in which the SWCNTs can be removed and placed into a Schlenk flask which already contains a magnetic stirrer bar. The sublimation probe can be added to the Schlenk flask without the risk of any unwanted oxidation of the white phosphorus. Hot water is used to melt the white phosphorus onto the SWCNTs. In other filling experiments, the two materials are usually ground to a homogenous mixture before heating. This step has been omitted due to the waxy nature of the phosphorus which makes this process almost impossible. The ability to stir the materials during the heating hopefully makes up for this omission. The mixture is heated to 323 K until the white phosphorus is completely molten and stirred for an hour. Whilst still heating, liquid nitrogen is used to sublime the excess white phosphorus from the SWCNTs until no more visible white phosphorus can be seen. 125 cm^3 distilled water is added and the mixture is sonicated for 5 min before bubbling air through the water, whilst stirring, using a sintered gas frit for two days. This is vital to remove any remaining excess white phosphorus which would ignite and destroy the sample otherwise. The sample is then filtered and washed with more distilled water and dried in a desiccator.

Capping of the filled tubes can be achieved by adding C_{60} which has dissolved in a solvent. This can be added after sublimation of the excess white phosphorus. The mixture is then stirred overnight before removing the solvent either by cannula or evaporation under reduced pressure. Water is then added to complete the work up as described above.

2.3.2 Red Phosphorus

20 mg SWCNTs and 20 mg red phosphorus, purchased from Sigma (part number 7723-14-0), were ground in an agar pestle and mortar for 5 minutes to create a homogenous mixture. The mixture was then placed in a long quartz ampoule which was pumped

down to 10^{-4} Pa using a turbo vacuum pump, heated to 473 K at 280 K min^{-1} and held for 2 hours. This was to ensure the material was fully dried and evacuated before sealing and is below the temperature at which the red phosphorus will sublime. The ampoule was sealed using a methane/oxygen gas mixture under dynamic vacuum by John Cowley. The seal was made at a narrow neck that had been designed to make this process easier and would also create a 200 mm long ampoule that is half the length of the tube furnace used to heat the ampoule in. Quartz was chosen to create the ampoules as they were created by extending an existing quartz piece that had the requisite KF40 fitting which allowed the ampoules to be connected to the turbo vacuum setup. Pyrex® or a similar high melting point glass could have also been used as the temperatures at which the ampoules were heated did not require the use of quartz, this system seemed to work incredibly well and was persisted with.

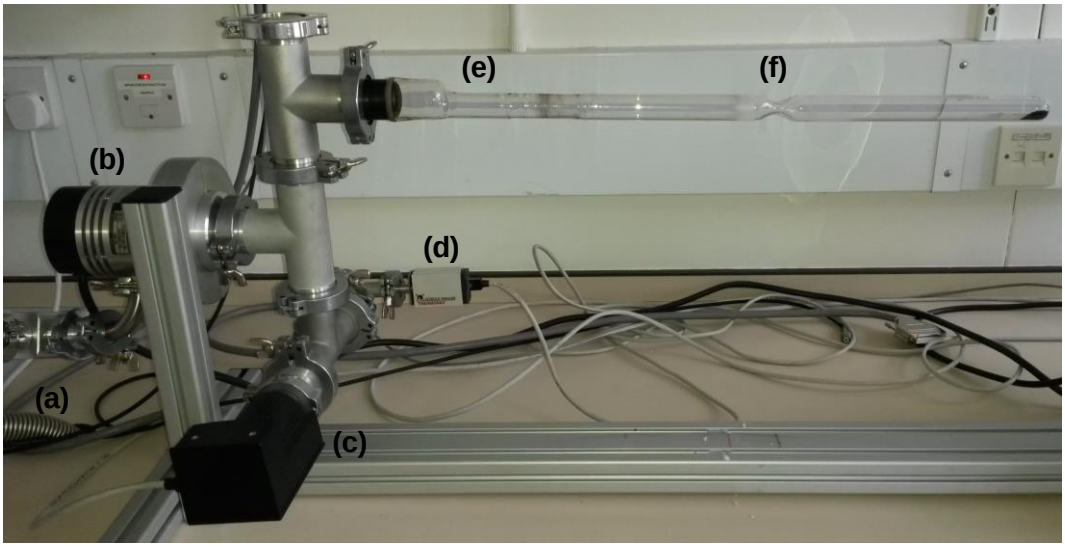

Figure 2.2 Ampoule experiment apparatus. (a) Bellows connecting the vacuum system to a double-stage rotary vane pump for initial evacuation. (b) Turbomolecular pump used to bring the pressure down to 10^{-4} Pa. (c) Cold cathode used for pressure low-monitoring. (d) Pirani gauge for pressure monitoring. (e) Quartz ampoule connected to the vacuum system with a KF40 joint. The sample can be seen at the end of the ampoule. (f) Neck used to seal the ampoule.

The ampoule is then heated in a tube furnace to 783 K at 283 K min^{-1} and held for 12 hours with the sample end in the centre of the furnace. Previous experiments have used 773 K as the reaction temperature.[3] The ampoule was reheated three more times, each time rotating the ampoule 180° to sublime the white phosphorus along the ampoule. The fourth and last heat treatment sublimed the white phosphorus onto to the SWCNTs located at the cool end of the ampoule.

After recovering the sample from the ampoule in a glove box, the excess white phosphorus was removed by bubbling air through water containing the sample.

2.3.3 Arsenic

20 mg SWCNTs and 20 mg grey arsenic, from lab 305 (UCL Chemistry Department), were ground for 5 minutes in an agar pestle and mortar to create a homogenous mixture. The mixture was then placed in a long quartz ampoule which was pumped down to 10^{-4} Pa using a turbo vacuum pump, heated to 473 K at 280 K min^{-1} and held for 2 hours. This was to ensure the material was fully dried and evacuated before sealing and is below the temperature at which the arsenic will sublime. The ampoule was sealed using a methane/oxygen gas mixture under dynamic vacuum by John Cowley. The seal was made at a narrow neck that had been designed to make this process easier and would also create a 200 mm long ampoule that is half the length of the tube furnace used to heat the ampoule in. Quartz was chosen to create the ampoules as they were created by extending an existing quartz piece that had the requisite KF40 fitting which allowed the ampoules to be connected to the turbo vacuum setup. Pyrex® or a similar high melting point glass could have also been used as the temperatures at which the ampoules were heated did not require the use of quartz, this system seemed to work incredibly well and was persisted with. The sample was heated in a tube furnace to 888 K at 283 K min^{-1} and held for 12 hours with the sample end in the centre of the furnace. This is the sublimation temperature of grey arsenic at atmospheric pressure so is more that hot enough to cause sublimation at a reduced pressure.[4] The ampoule was reheated three more times, each time rotating the ampoule by 180° to sublime the arsenic along the ampoule. The fourth heat treatment, therefore, allows the arsenic to sublime onto the SWCNTs located at the cool end of the ampoule. In some cases, an additional rotation and heat treatment was used to sublime the arsenic away from the SWCNTs.

After recovering the sample from the ampoule, excess arsenic was removed by stirring in 100 mL 0.5 M nitric acid solution for 4 hours followed by filtration and washing with water.

$$As + HNO_3 \rightarrow H_3AsO_4 + 5NO_2 + H_2O \qquad [2.3]$$

2.3.4 Antimony

30 mg SWCNTs and 30 mg antimony, from lab 305 (UCL Chemistry Department), were ground for 5 minutes in an agar pestle and mortar to create a homogenous mixture. The mixture was then placed in a long quartz ampoule which was pumped down to 10^{-4} Pa using a turbo vacuum pump, heated to 473 K at 280 K min^{-1} and held for 2 hours. This

was to ensure the material was fully dried and evacuated before sealing and is below the temperature at which the antimony will sublime. The ampoule was sealed using a methane/oxygen gas mixture under dynamic vacuum by John Cowley. The seal was made at a narrow neck that had been designed to make this process easier and would also create a 200 mm long ampoule that is half the length of the tube furnace used to heat the ampoule in. Quartz was chosen to create the ampoules as they were created by extending an existing quartz piece that had the requisite KF40 fitting which allowed the ampoules to be connected to the turbo vacuum setup. Pyrex® or a similar high melting point glass could have also been used as the temperatures at which the ampoules were heated did not require the use of quartz, this system seemed to work incredibly well and was persisted with. The ampoule was sealed under dynamic vacuum, heated in a muffle furnace to 973 K at 283 K min^{-1} and held for 66.5 hours. This temperature will cause sublimation of the antimony material.[5] After recovering the sample from the ampoule, excess arsenic was removed by stirring in 150 mL 1 M nitric acid solution for 4 hours followed by filtration and washing with water.

$$Sb + HNO_3 \rightarrow H_3SbO_4 + 5NO_2 + H_2O \qquad [2.4]$$

2.3.5 Aluminium Iodide

250 mg of aluminium iodide and 50 mg purified Tuball SWCNTs are ground together in a pestle and mortar in a glove box for five minutes until a homogenous mixture has formed. Aluminium iodide is purchased from Fisher Scientific at a >99.99% purity, catalogue number 11389399 . The mixture is placed into a 200 mm long quartz ampoule with a diameter of 12 mm. Pyrex® or a similar high melting point glass could have also been used as the temperature the ampoule is being heated to does not necessitate the use of quartz. The ampoule is pumped down until at least a pressure of 1 Pa is achieved before sealing with an oxygen fed blow torch. The ampoule is heated in a muffle furnace to 523 K at a ramp rate of 283 K min^{-1} for 24 h. The ampoule is opened within a glove box and placed into a round bottom flask with 15 wt% C_{60}. A needle and syringe are used to transfer 65 cm^3 of dry hexane and the mixture is stirred for 24 h. A filter cannula is used to remove the purple solution and 250 cm^3 of 1 M HCl is added. The mixture is sonicated for 5 min before refluxing for 2 h. The filled nanotubes are then washed and filtered with copious amounts of water.

2.4 X-ray Photoelectron Spectroscopy (XPS)

XPS is a pseudo-surface characterisation technique that can be used to identify both the elements present in samples and also their chemical states. This is achieved by

bombarding a sample with x-rays of a known energy to cause ionisation. A common energy used is the aluminium $K\alpha_1$ energy at 1486.6 eV. The photoelectrons that are emitted are detected and their kinetic energy is established. This allows the identification of the element which has emitted the photoelectron using this simple equation:

$$\text{X} - \text{ray Photon Energy} = \text{Binding Energy} + \text{Kinetic Energy of Photoelectron} \quad [2.5]$$

The X-ray photon energy is known, and the kinetic energy is measured by a photoelectron detector. By rearranging this equation the unique binding energy of the element is calculated.[6] From a vast number of experiments, the binding energies of each element became known and allows for their detection.

The binding energies of electrons are very sensitive to their environment and can change readily. For example, the higher the effective nuclear charge of the atom the higher the binding energy of the core electrons. This can be achieved either by electrons being closer to the nucleus, therefore electrons from the 1s orbital have higher binding energies than those from the 2s orbital, or electrons in higher proton number elements, therefore nitrogen 1s electrons will have a higher binding energy than carbon 1s electrons. The chemical state of the element will cause small changes to the expected value of binding energy for a given core electron. The oxidation state of the element has a significant impact on the binding energy. A sample with a positive oxidation state will give higher binding energies as it is harder to remove electrons from an oxidised element. Conversely, an element with a negative oxidation state will have a lower binding energy. It is this reason as to why the sample is often bombarded simultaneously with electrons, using a flood gun, as the ionisation of the sample from the x-rays will cause the binding energies to shift. Without this charge compensation, the binding energies will shift progressively higher. Elements next to more electronegative elements will also see a decrease in the binding energy as the electron is less tightly bound in this scenario. An element near to a less electronegative element will have a higher binding energy. These effects are less substantial than the oxidation state though.

The splitting of peaks is another common phenomenon and is caused by orbitals having a non-zero angular momentum number (l<0). This means all core orbitals, except for the s orbital, will have doublet peaks that have specific area ratios based on the degeneracy of each spin state. Table 2.1 shows how the *j* values for an orbital effect the area ratio of the doublet.[7]

Table 2.1 The effect the spin-orbit splitting of the j values effect the peak area ratios.

Subshell	*j* value	Area Ratio
s	1/2	n/a
p	1/2 3/2	1:2
d	3/2 5/2	2:3
f	5/2 7/2	3:4

Quantification of elements (except for H) is also possible by taking into account the area of each peak and the relative sensitivity factor of each element and orbital. These can be found in standards tables to allow for the simple quantification of the elements present in the sample. By fitting peaks, we can therefore get an accurate amount of each element and the quantity in each chemical state too, although not for hydrogen as it has no core electrons which can be photoionised.[8]

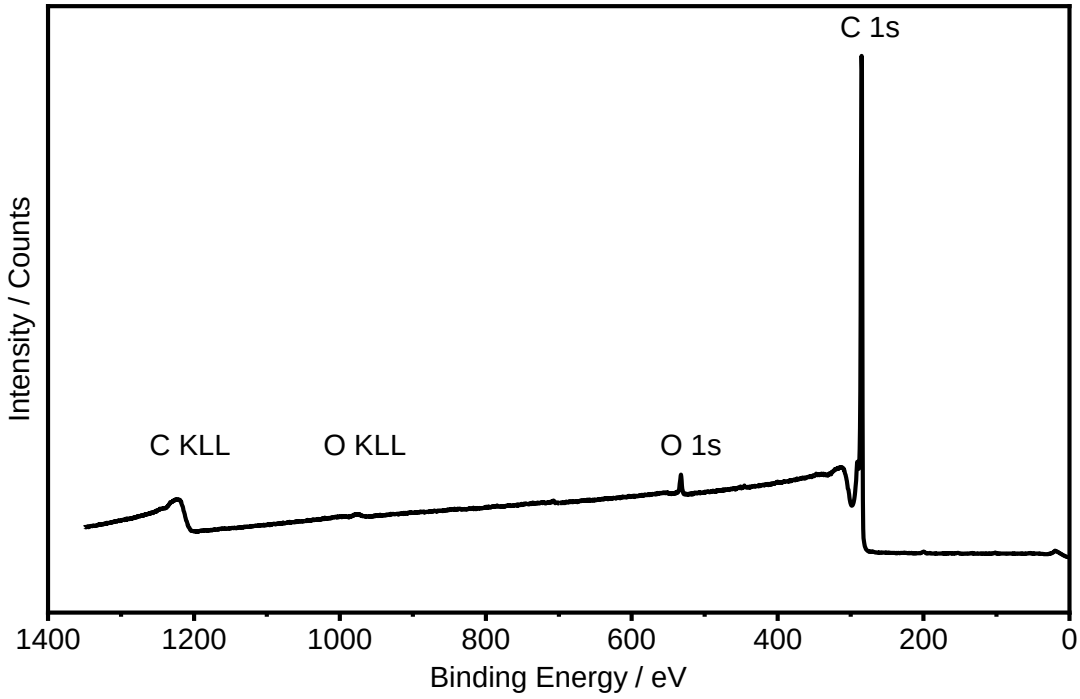

Figure 2.3 XPS survey spectrum of a steam purified Tuball SWCNT sample. Carbon and oxygen peaks have been highlighted.

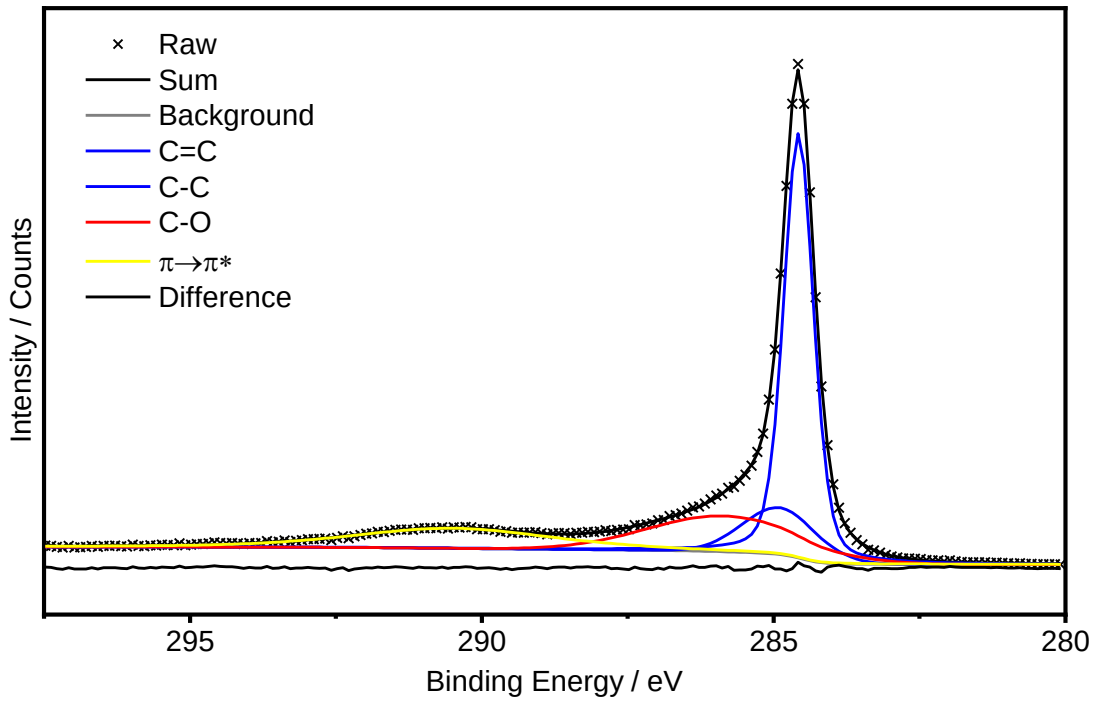

Figure 2.4 High resolution XPS spectrum of the carbon 1s region. By fitting the spectrum, we can get an understanding of the functional groups present in the sample.

Figure 2.3 shows the survey spectrum for a SWCNT. As expected, only carbon and oxygen are detectable. The oxygen can be present in the form of oxidation groups on the SWCNT and also from some residual water on the surface of the sample. Some additional peaks have also been detected which are caused by Auger electrons. These are caused by the relaxation of electrons into the hole created by the photoelectron.[6] The release of energy from this relaxation can cause the photoionisation of another electron in the atom which is detected as an Auger peak. The kinetic energy of the Auger electrons is independent of the x-ray energy and is equal to the energy difference between the energy transferred to it and its own binding energy.[6]

Figure 2.4 gives a high-resolution elemental scan of the carbon 1s region. This is fitted to show the oxidation states present in this sample. The main peak around at 284.57 eV is caused by the sp^2/sp^3 carbon present which makes up the bulk of a SWCNT. Due to their very similar binding energies, it is difficult to definitively separate their contributions. The peak at 285.99 eV is caused by C-O functional groups. The last peak at 290.45 eV is a shake-up peak caused by the π→π* electron excitation which occurs before the photoionisation. This reduces the kinetic energy of the photoion so appears at a higher binding energy.[9] Carboxyl C=O groups and carboxyl COOH groups will appear between the C-O and satellite peaks at 287.5 eV and 288.7 eV respectively.[10]

XPS was carried out using a Thermo Scientific K-Alpha XPS machine fitted with a monochromated Al K_α X-ray source. A double focussing 180° hemisphere analyser equipped with an 18-channel position sensitive detector is used to detect the photoelectrons. Charge accumulation in the sample is dealt with by a dual-beam flood gun which can emit either electrons or argon ions. The samples are prepared for XPS analysis by pressing the material into an indium substrate, that is affixed onto the analysis plate by carbon tape, in order to ensure that background contributions could not arise from the carbon tape. Survey scans were collected 3 times and coadded with a 1 eV resolution and pass energy of 200 eV. High-resolution elemental spectra were collected 10 times and coadded, with a 0.01 eV resolution and 50 eV pass energy. All scans used a 400 μm spot size and dwell time of 50 ms.

CasaXPS software was used to quantify the samples and export relevant spectra for fitting using XPSPEAK. Shirley backgrounds and Voigt functions were used to fit the spectra until a best fit could be achieved.

2.5 High-Resolution Transmission Electron Microscopy (HRTEM)

TEM is one of the most powerful microscopy techniques available and has been used extensively since its creation in 1931. By using electrons as the illuminating source instead of light, we can resolve images many times smaller than what is achievable using a light microscope.[11] An electron with an energy of 1 eV has a wavelength of 1.23 nm from de Broglie's theorem, a photon with the equivalent energy has a wavelength around 1000 times larger.

$$\lambda = \frac{h}{p} \qquad [2.6]$$

The electrons can be generated in numerous ways. Most commonly LaB_6 crystals or tungsten wires are used but field emission guns are becoming more commonplace due to the narrower beam of electrons produced, the narrower range of energies of electrons produced and also due to the brighter beam that can be created. The beam of electrons must then be focussed onto the sample using a series of electromagnetic coils to create a magnetic field which mimics the glass lenses used in optical microscopes. It is in fact the lenses used which is the limiting factor for the maximum resolution that can be achieved in electron microscopes. Any deviations in the radial symmetry of the lens will lead to aberrations such as spherical, chromatic and astigmatism which all reduce the resolution of the microscope. Apertures can be used to help remove stray electrons that

are not focussed down the centre of the microscope. Unfortunately, this reduces the intensity of the beam and can lead to darker images. Figure 2.5 shows a schematic of a TEM which shows how the various lenses and apertures can be used to manipulate the beam to ensure it is focussed correctly to produce an image on the fluorescent screen.

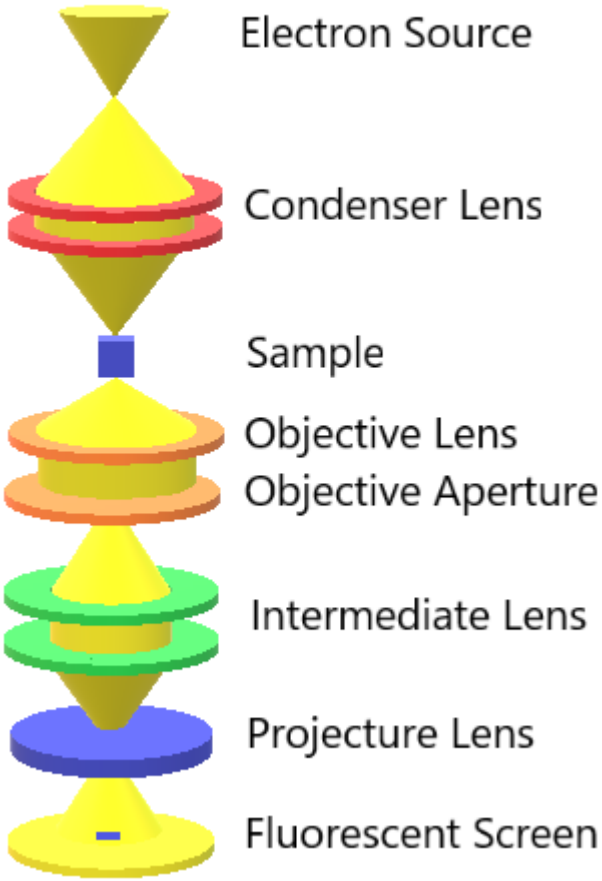

Figure 2.5 Schematic of a TEM showing its constituent parts.

TEM is conducted in UHV conditions to help reduce any unwanted scattering of the electron beam. The samples that can be imaged also have to be extremely thin, thinner than the mean free path of the electrons, to allow the electrons to pass through the sample.[12] The preparation of the sample is often more important for producing good images than the microscope itself. Samples must be clean and free of any dust or grease. Techniques such as ion milling are often used to help create thin and precise samples for imaging. Staining, freezing and etching are other techniques that can be used depending on the type of sample that needs imaging and the type of information that is required.

The interaction of the electrons with the sample allow an image to be generated. Electrons that are not scattered by the sample get detected and create the image. Thicker regions and heavier elements will scatter the electrons more and create darker areas in the image.[12] Some of these scattered electrons will still make it through the sample and be detected. These electrons will normally be inelastically scattered. By recording the energies of these electrons we can find out information about what element had scattered the electron.[13] This technique is called electron energy loss spectroscopy (EELS) and is a very powerful tool to microscopists as compositional information can now be used to map the elements in the sample.[14] We can also filter out any electrons that have been inelastically scattered to produce sharper images (zero loss imaging). A similar technique called energy dispersive x-ray spectroscopy (EDX) can also be used to map the elements in a sample. The electron beam may excite core electrons in the sample and create holes. As higher orbital electrons fill the hole, they give off x-rays which can be detected.[15] This technique is less sensitive than EELS so only elemental information can be detected. The chemical state of the element will be unknown.

The HRTEM conducted in this research was taken on the FEI Titan 80/300 TEM/STEM microscope fitted with a Cs (image) corrector at Imperial College London. The samples were prepared by sonicating >1 mg of sample in ethanol for 1 min and dropping a few drops of the dispersion onto a lacey carbon Agar 300 mesh copper TEM grid. The grid had been prepared by soaking in chloroform for a couple of minutes before allowing to dry under a lamp. The microscope was operated at 80 kV in order to reduce electron beam damage to the samples.[16] The image corrector was necessary to image the structure of the SWCNTs by reducing the effects of spherical aberrations. All images were taken with the image corrector corrected to at least 18 mrad.

Simulated TEM images were obtained using the SimulaTEM software[17] using an accelerating voltage of 80 kV, a defocus value of -310.271850 Å and a spherical aberration constant of 0.15 mm.

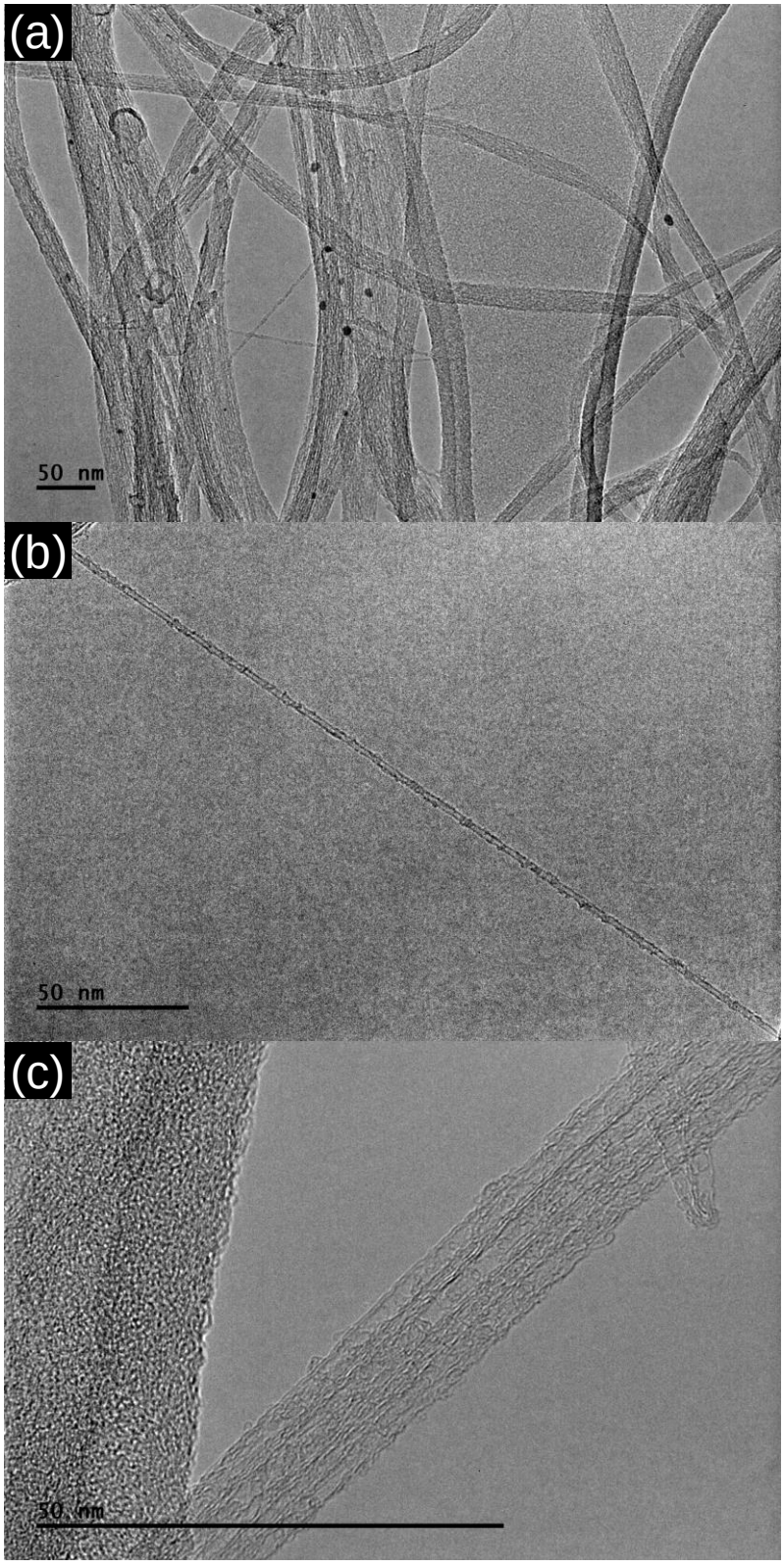

Figure 2.6 TEM micrographs of unfilled purified Tuball SWCNTs. (a) Image taken at x33000 magnification showing bundles of SWCNTs, some iron nanoparticles can still be seen which have survived the purification process. (b) Image taken at x40000 magnification showing a long straight SWCNT. (c) Image taken at x100000 magnification showing some of the amorphous carbon still present on the surface of the SWCNTs.

2.6 Thermogravimetric Analysis – Differential Scanning Calorimetry

TGA is a simple yet powerful tool that records the change of mass of a sample with temperature.[18] From this, we can record phase changes, decomposition, absorption, desorption and chemical reactions. A sample pan is placed onto a precise balance that is held within a furnace. Temperature programs are used to alter the rate is heating or to include any dwell times with isothermal heating.

TGA can be conducted with different flow gases to help understand different processes and can even be done under vacuum. Nitrogen is often used for air-sensitive samples that may decompose at higher temperatures.

By including a reference cell that is heated equally as the sample, energy changes can also be monitored to give calorimetry information. By either keeping the power supplied to both cells constant (power-compensated DSC) or the heat-flux constant (heat-flux DSC), energy changes in the sample can be monitored.[19] An exothermic process will require less power to the sample to keep its temperature constant with the reference cell. An endothermic process will require more power.

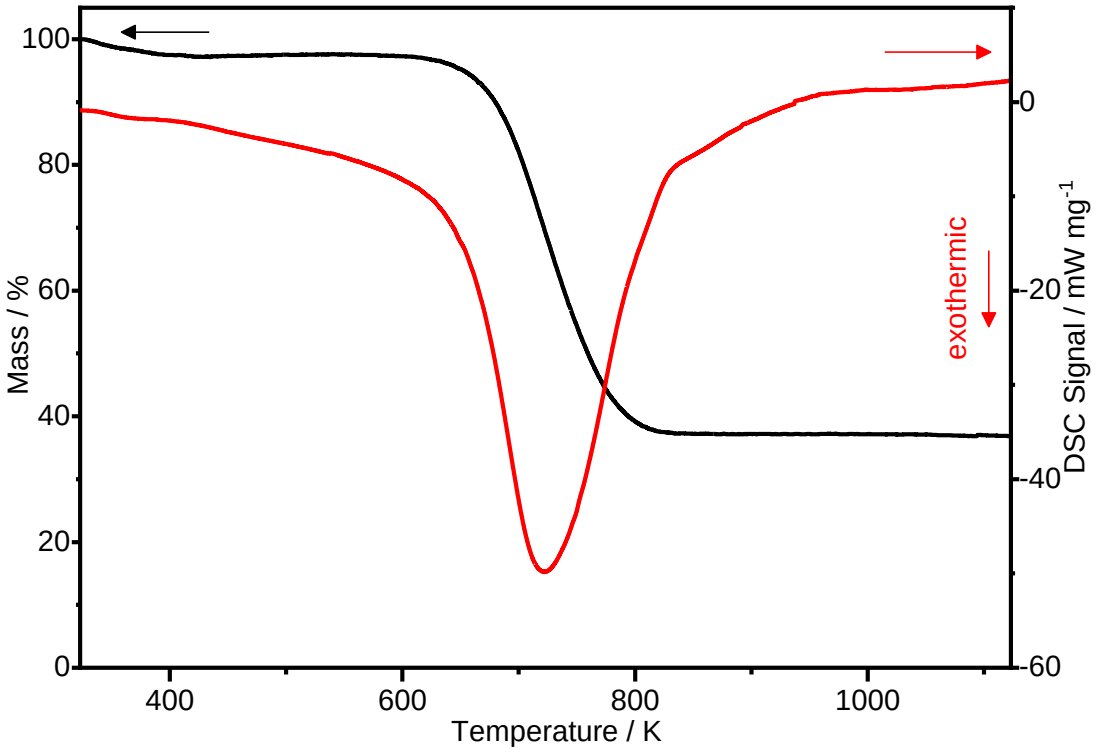

Figure 2.7 TGA/DSC scan of unfilled purified Tuball SWCNTs. The exotherm shows the enthalpy of combustion for the material as it loses mass.

The combination of TGA and DSC allows a complete understanding of the thermal character of a sample to be determined. For example, Figure 2.7 shows how the TGA/DSC scan reveals the thermal stability of the SWCNT to oxidation. It shows at which temperature the SWCNT will begin to oxidise in air to from either CO_2 or CO. an accompanying exotherm will give the enthalpy of combustion for the process. The remaining mass will be of any metal catalyst impurities which will have oxidised during the heating process. This gives a good indication of the purity of the sample.[20]

TGA/DSC measurements were taken on a Netsch STA 449 C Jupiter Thermogravimetric microbalance. The samples were heated from 20 to 1223 K at 283°C min^{-1} in air in alumina crucibles.

2.7 Powder X-ray Diffraction (PXRD)

PXRD is used to help determine the atomistic structure of a material. By measuring the angles at which x-rays are diffracted and the intensities of the peaks a three dimensional (3D) crystal structure of the material can be inferred. The x-rays interact with the electrons within the sample and scatter off of them.[21] The constructive interaction between the diffracted waves produce Bragg peaks as governed by Bragg's law:

$$n\lambda = 2d\sin\theta \qquad [2.7]$$

Where λ is the wavelength of the incident radiation, d is the interplanar spacing and θ is the incident angle. For constructive interference to occur, n must be an integer and the angle of diffraction must be correct. Figure 2.6 illustrates how Bragg's law can be derived.[22]

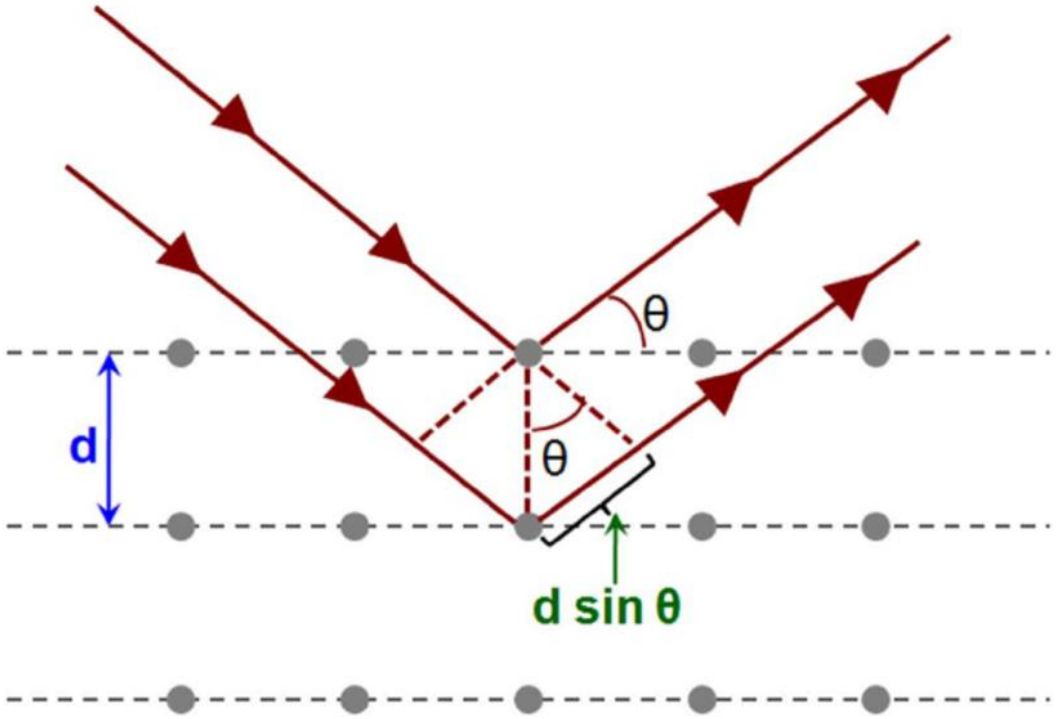

Figure 2.8 Diagram showing how Bragg's Law is derived. The constructive interference of incident x-rays can only occur when the difference between the distance travelled by each ray (2d sinθ) is equal to a whole number of wavelengths (nλ). Produced from permission from reference [21].

The wavelength of x-rays used in XRD is around 1 Å which is very similar to the spacings between atoms which tend to be on the 1-100 Å regime. This makes x-rays the perfect radiation to examine the structure of materials. For SWCNTs, the main feature which dominates is the inter-bundle spacing found between the SWCNTs.[23, 24]

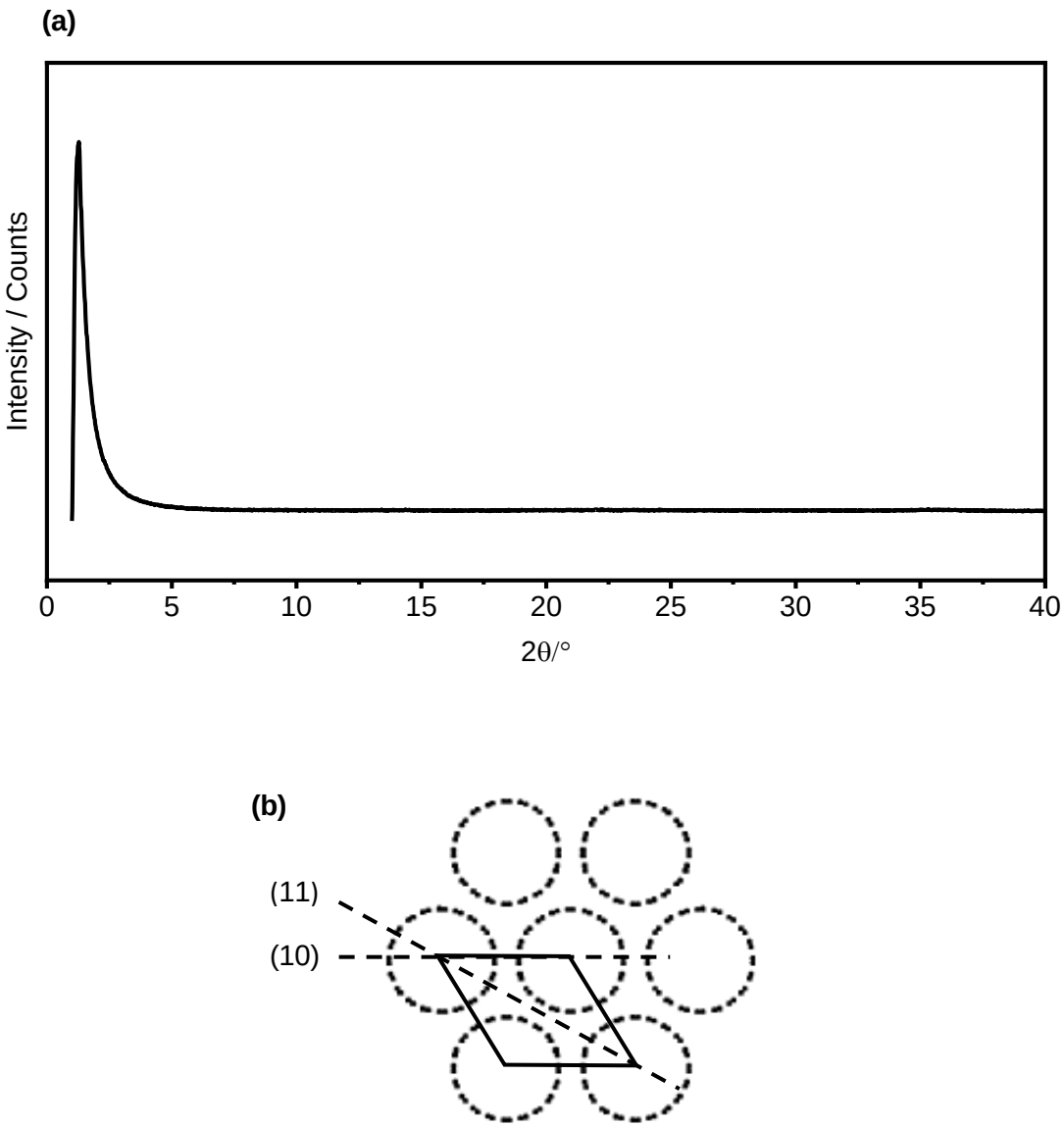

Figure 2.9(a) PXRD of unfilled HiPCO SWCNTs. The main feature seen is caused by the inter-SWCNT distance. (b) Bundle of SWCNTs showing its hexagonal crystal structure. Labelled are two different inter-SWCNT distances. Image reproduced with permission from reference [23].

Samples were prepared for PXRD by packing the material into a 0.6 mm or 0.8 mm borosilicate capillary. The diffraction patterns were collected on a Stoe Stadi P diffractometer using copper $K\alpha_1$ radiation at 40 kV, 30 mA and monochromated using a Ge 111 crystal. Patterns were collected using a Mythen 1K linear detector using a 2θ range of 1 – 40° with 0.05° steps at 15 s per step. Quantitative Rietveld analysis was carried out with the PowderCell program.[25]

2.8 Raman Spectroscopy

Raman spectroscopy is an extensive technique used to monitor the vibrational and rotational modes within a system by the inelastic interaction between a monochromatic light source and the sample. An emitted photon will have either more or less energy than the incident photon, and these differences, the Raman shift, can be used to help understand the chemical nature and symmetry of a material.[26] It has proved especially powerful for characterising carbon materials.[23]

Raman scattering is caused by the induced dipole moment within the system, due to the applied electric field of the incident photon. The electrons and nuclei will shift in response to the electric field and thus create a dipole moment. The induced dipole moment has three contributions, the elastic Rayleigh scattering and two inelastic modes, the Stokes and anti-Stokes scattering. An increase in the photon's energy gives rise to the Stokes shift and a decrease gives rise to the anti-Stokes shift, as can be demonstrated in Figure 2.7.

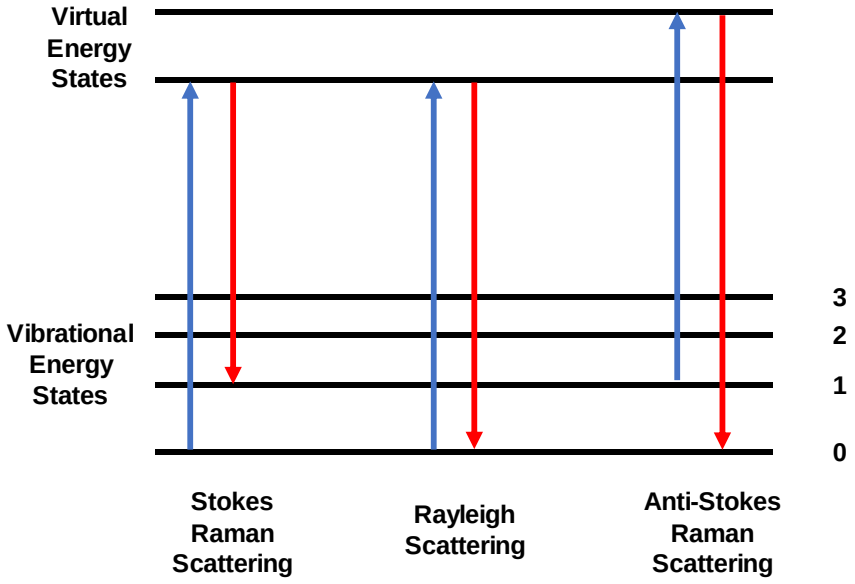

Figure 2.10 Energy level diagram showing the three transitions that can occur during elastic and inelastic light scattering.

SWCNTs have four well defined Raman scattering modes: The G-mode, D-mode, 2D-mode and the radial breathing modes (RBMs). The G-mode tends to be the most intense peak in a SWCNT sample and is caused by the tangential movement of the carbon atoms within the SWCNT. The more pristine the carbon, the higher the wavenumber is for the G-mode, hence graphene has a higher value than for SWCNTs. It is split into sub-bands, unlike in 2D graphene, due to the curvature of the SWCNT, with G+ and the G- sub-bands

for both semi-conducting and metallic SWCNTs. In semi-conducting SWCNTs, the G+ sub-band is representative of the related vibration in the direction parallel to the SWCNT elongation axis, whereas the G- sub-band is for the related vibration in the perpendicular direction to the SWCNT elongation axis. The opposite effect is seen in metallic SWCNTs due to electron-phonon coupling.[23] The G-band is often used to determine if charge transfer has occurred between the SWCNT and any dopant present. This can either be external or internal to the SWCNT wall or even if elements have been used to dope the SWCNT by embedding themselves within the SWCNT wall itself. N-doping leads to a blue shift, p-doping leads to a red shift in the G-mode.

The D-mode is often used to determine the defectiveness of a sample. It is caused by back scattering of the electrons by the phonon breathing mode. It can only be caused by the presence of defects in the sample as it requires a break in the symmetry of the sp^2 lattice to scatter the electron back to the K-point.[27] By taking the ratio of the G/D-mode intensity or area, a fairly accurate determination of the defectiveness of the sample can be determined.[28]

The 2D-mode is a second-order harmonic of the D-mode and occurs almost exactly at twice the wavenumber of the D-mode. It occurs by the excitation of electrons near the K-point into the conduction band of the SWCNTs. It is then scattered by a phonon vibration associated with the breathing mode of the lattice to an inequivalent K-point.[29] A secondary scattering event by another phonon vibration allows the electron (or hole) to recombine back at the K-point and emitting a photon.

The RBMs are caused by the expansion and contraction of the SWCNT. It is intrinsically linked to the diameter of the SWCNT that is being excited. Thus, it can be used to accurately identify the chirality of the SWCNT being excited. Larger diameter SWCNTs have a smaller Raman shift than narrow SWCNTs, but these can shift due to interactions with any filling material or external pressure. A relationship exists between frequency of the RBM peak and the diameter of the nanotube which is given in equation 2.8:

$$E_{ii} = \hbar v_F \left(\frac{4p}{3d_t}\right) \qquad [2.8]$$

where E_{ii} is the energy gap of van Hove singularities for a given transition, $\hbar$ is the reduced Planck constant, v_F is the Fermi velocity and p = 1, 2, 3, 4, 5 for $E_{11}^S, E_{22}^S, E_{11}^M, E_{33}^S$ and E_{44}^S respectively. The energy gap reduces as the nanotube diameter increases as the energy dispersion of the begins to approach that of graphene.[30]

Simplified versions of this equation exist in order to make the identification of the nanotube diameter more straightforward.[31]

Resonance in SWCNTs is a phenomenon exploited in order to achieve more intense Raman spectra. If the incident wavelength is close to the energy of an optical transition energy within the nanotube, the nanotube will resonate and produce very strong signals.[32] Thus, in order to get an accurate picture of all the nanotubes present in a sample, Raman spectra should be collected using as many different wavelengths of laser light possible.

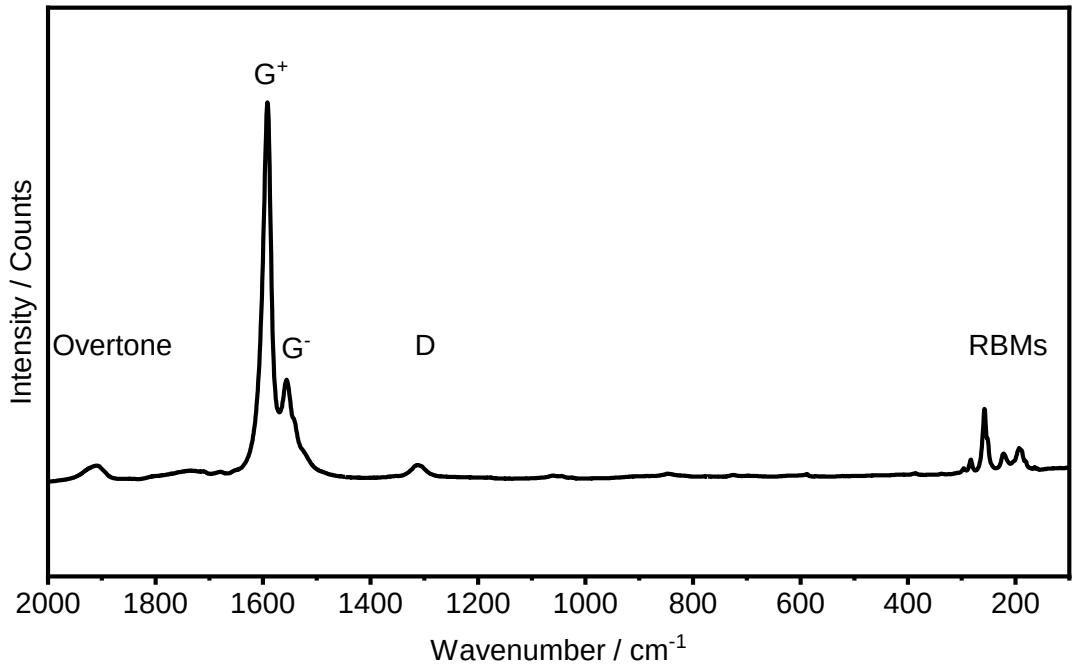

Figure 2.11 An example Raman spectrum of an unfilled HiPCO SWCNT taken using a laser wavelength of 633 nm. The key regions are highlighted.

Raman spectra of the SWCNT samples on glass slides were collected using a Renishaw Ramascope (632.8 nm HeNe laser) as well as a Renishaw InVia spectrometer (514.5 nm argon-ion laser and 785 nm diode laser). 50x ultra-long working distance objectives were used with both spectrometers. The laser powers were reduced to 25% in all cases and they are estimated to be around 1 mW at the sample for the 632.8 nm and 514.5 nm lasers, and about 5 mW for the 785 nm laser. To check for consistency, 3-5 spots on each sample were characterized with each of the lasers. Each spot was collected 4 times at 20 s each. Raman shifts were calibrated against a Ne discharge lamp.

Raman mapping was conducted on a Renishaw Reniscope equipped with a mapping stage. The samples were prepared by sonicating 2 mg of sample in water and filtered onto a polycarbonate membrane to ensure a flat even surface for mapping was created.

Raman spectra were collected using a 785 nm laser over an area of 1 mm^2. 100 static spectra were collected at 1200 cm^{-1}.

2.9 Fourier-Transform Infrared (FT-IR) Spectroscopy

FT-IR spectroscopy uses infrared radiation in the region of 4000-400 cm^{-1} to interact with matter to create spectra showing the fundamental vibrations associated with specific functional groups.

For a functional group to be IR active, the vibration must elicit a change in the dipole-moment within the group.[33] Bond vibrations can be described using a simple harmonic oscillator and thus the fundamental vibrational frequency can be determined:

$$\nu = \frac{1}{2\pi c}\sqrt{\frac{k}{\mu}} \qquad [2.9]$$

where k is the force constant (which is directly proportional to the bond strength) and μ is the reduced mass of the bond between the two atoms of mass m_1 and m_2 respectively:

$$\mu = \frac{m_1 \cdot m_2}{m_1 + m_2} \qquad [2.10]$$

By combining equations 2.9 and 2.10, simple observations about how bond strengths and the atomic masses of the bonds effect the fundamental vibration can be made. For example, a bond with a high bond strength (therefore a large k value) or a small reduced mass will cause the fundamental vibration to increase. It can be seen that strong bonds and bonds between lighter elements will have higher frequency vibrations than those between heavier elements. Figure 2.8 shows an example FT-IR spectrum for empty SWCNTs.

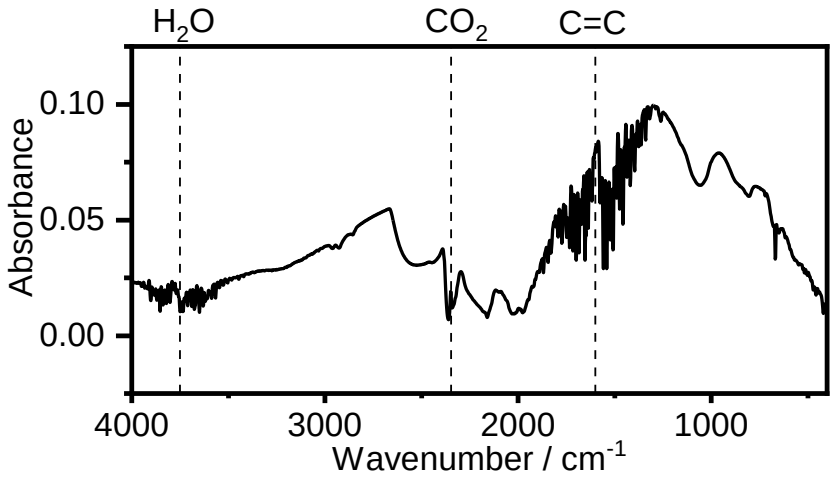

Figure 2.12 FT-IR spectra of empty SWCNTs (Tuball). Dashed lines highlight some of the features observed.

Tables of expected frequencies for functional groups can be found in many textbooks or websites describing FT-IR which makes interpretation of spectra quite straightforward.

FT-IR spectra were collected on a Bruker Tensor 27 FT-IT spectrometer in the attenuated total reflectance infrared spectroscopy mode (ATR-IR) and fitted with a room temperature DLaTGS detector at 4 cm^{-1} resolution and a diamond crystal as the internal reflection element. A background spectrum was collected for 256 scans before each sample is measured, again for another 256 scans.

2.10 Software

Software plays an integral part of the research process. For example, the construction of simulated TEM images has played a significant role in the identification of the structures adopted by the various confined materials. Here listed are key pieces of software used as part of this thesis.

Nanotube Modeler version 1.8.0, produced by JCrystalSoft, was used to create .cif files of SWCNTs of any chirality required.

SWCNTStructureRotation, written by Prof. C. G. Salzmann, was used to produce structures that have been rotated about the z-axis through 360°, generating a set of coordinates for every 10° rotation.

RANDROT, written by Prof. C. G. Salzmann, was used to produce a structure that had been rotated randomly about its origin.

CrystalMaker® X, produced by CrystalMaker Software Ltd., was used to analyse and manipulate atomic models of structures and to create .pdb files.

SimulaTEM[17] was used to create simulated TEM images.

Digital Micrograph® version 3.20.1314.0, produced by Gatan Inc., was used to analyse both real and simulated micrographs.

ImageJ version 1.50i, produced by Wayne Rasband, was used to create rotationally averaged images by taking the average intensity of image stacks.

CasaXPS version 2.3.16, produced by Casa Software Ltd., was used for analysis of XPS spectra.

XPSPEAK version 4.1, produced by Raymund W. M. Kwok, was used for fitting XPS high-resolution spectra in order to determine the ratios of the chemical states of the fitted elemental region.

RMCProfile is a reverse Monte Carlo software used to fit diffraction data.[34] The software was used to estimate the filling yield of *m*-P@Tuball samples. Simulations were run to allow the atoms to move freely whilst obeying the minimum distances defined between C-C (0 Å), C-P (5.06 Å) and P-P (6.0 Å) atom pairs. P_4 sphere was estimated to be 4.92 Å, a larger minimum distance was used to account for any dynamic behaviour of the molecules (such as rotations)[35]. Simulations were run for 1 min.

2.11 Density Functional Theory

DFT calculations have been performed by Ji Chen to help support the experimental data collected in this research. The primary aim was to create geometry-optimised structures that would fit within the cavity of a SWCNT.

DFT calculations were performed using the Vienna ab initio Simulation Package (VASP) where the core electrons were described with projector augmented wave (PAW) potentials.[36, 37] An energy cutoff of 400 eV was used to expand the wave functions. The optB86b-vdW van der Waals inclusive exchange correlation functional was used.[38, 39] *Ab initio* random structure searches (AIRSS)[40] were carried out with an interface to VASP. An empirical cylindrical confining potential was implemented to simulate the confinement of carbon nanotube following the procedure used in refs [41, 42]. The empirical potential has a Morse-type formula defined as: $V(x)=0.172[(1-\exp(-1.052(x-3.565)))^2-1]$ in eV, where x is the distance of a pnictogen atom to the carbon nanotube in Å. The parameters used were fitted to the DFT interaction between a P_4/As_4/Sb_4 molecule and graphene.

The activation energy for the reaction pathway from P_4/As_4 molecules to the *trans* butterfly chain was obtained using the climbing-image nudged-elastic-band (cNEB) method with a fixed size of the unit cell.[43]

The electronic density of states were also calculated for the structures and also for the free-standing structures. These were created by applying geometry optimisation without the presence of the confining potential. The DOS were performed using the Heyd-Scuseria-Ernzerhof hybrid exchange correlation functional[44] on structures obtained with the optB86b-vdW functional.

2.12 References

1. Tobias, G.; Shao, L. D.; Salzmann, C. G.; Huh, Y.; Green, M. L. H., Purification and opening of carbon nanotubes using steam. *J. Phys. Chem. B* **2006,** *110* (45), 22318-22322.

2. Ajayan, P. M.; Ebbesen, T. W.; Ichihashi, T.; Iijima, S.; Tanigaki, K.; Hiura, H., Opening carbon nanotubes with oxygen and implications for filling. *Nature* **1993,** *362*, 522.
3. Zhang, J.; Zhao, D.; Xiao, D.; Ma, C.; Du, H.; Li, X.; Zhang, L.; Huang, J.; Huang, H.; Jia, C.-L.; Tomanek, D.; Niu, C., Assembly of Ring-Shaped Phosphorus within Carbon Nanotube Nanoreactors. *Angew. Chem. Int. Ed.* **2017,** *56* (7), 1850-1854.
4. Lisak, A.; Fitzner, K., Vapor pressure measurements of arsenic and arsenic trioxide over condensed phases. *J. Phase Equil.* **1994,** *15* (2), 151-154.
5. Aldred, A. T.; Pratt, J. N., Vapor Pressures or Zinc, Cadmium, Antimony, and Thallium. *J. Chem. Engin. Dat.* **1963,** *8* (3), 429-431.
6. Hufner, S., *Photoelectron Spectroscopy: Principles and Applications*. Springer Verlag: 1995.
7. Briggs, D.; Grant, J. T., *Surface analysis by Auger and x-ray photoelectron spectroscopy*. Chichester : IM publications: 2003.
8. Stojilovic, N., Why Can't We See Hydrogen in X-ray Photoelectron Spectroscopy? *J. Chem. Edu.* **2012,** *89* (10), 1331-1332.
9. The Nature of X-ray Photoelectron Spectra. http://www.casaxps.com/help_manual/XPSInformation/IntroductiontoXPS.htm (accessed 11/04/2018).
10. Okpalugo, T. I. T.; Papakonstantinou, P.; Murphy, H.; McLaughlin, J.; Brown, N. M. D., High resolution XPS characterization of chemical functionalised MWCNTs and SWCNTs. *Carbon* **2005,** *43* (1), 153-161.
11. Girit, C. O.; Meyer, J. C.; Erni, R.; Rossell, M. D.; Kisielowski, C.; Yang, L.; Park, C. H.; Crommie, M. F.; Cohen, M. L.; Louie, S. G.; Zettl, A., Graphene at the Edge: Stability and Dynamics. *Science* **2009,** *323* (5922), 1705-1708.
12. Williams, D. B.; Carter, C. B., *Transmission Electron Microscopy: A Textbook for Materials Scientists*. Springer: 2009.
13. Egerton, R. F., Electron energy-loss spectroscopy in the TEM. *Rep. Prog. Phys.* **2009,** *72* (1).
14. Goode, A. E.; Hine, N. D. M.; Chen, S.; Bergin, S. D.; Shaffer, M. S. P.; Ryan, M. P.; Haynes, P. D.; Porter, A. E.; McComb, D. W., Mapping functional groups on oxidised multiwalled carbon nanotubes at the nanometre scale. *Chem. Comm.* **2014,** *50* (51), 6744-6747.
15. Goldstein, J., *Scanning Electron Microscopy and X-Ray Microanalysis*. Springer: 2003.
16. Smith, B. W.; Luzzi, D. E., Electron irradiation effects in single wall carbon nanotubes. *J. App. Phys.* **2001,** *90* (7), 3509-3515.
17. Gómez-Rodríguez, A.; Beltrán-del-Río, L. M.; Herrera-Becerra, R., SimulaTEM: Multislice simulations for general objects. *Ultramicroscopy* **2010,** *110* (2), 95-104.
18. Coats, A. W.; Redfern, J. P., Thermogravimetric analysis. A review. *Analyst* **1963,** *88* (1053), 906-924.
19. Hoehne, G. W. H.; Hemminger, W. F.; Flammersheim, H. J., *Differential Scanning Calorimetry*. 2003.
20. Liu, X.; Bian, H.; Zhou, H.; Gao, L.; Jiang, S. J.; Zhang, Y. F., Effective Purification of SWNTs Based on Combined Method. *Full. Nano. Carb. Nanostruct.* **2015,** *23* (1), 78-82.
21. Clegg, W., *Crystal Structure Determination (Oxford Chemistry Primer)*. Oxford: Oxford University Press: 1998.
22. Baskaran, S., *Structure and Regulation of Yeast Glycogen Synthase*. 2010.
23. Monthioux, M., *Carbon Meta-Nanotubes: Synthesis, Properties and Applications*. Wiley: 2012.
24. Qian, D.; Liu, W. K.; Ruoff, R. S., Load transfer mechanism in carbon nanotube ropes. *Comp. Sci. Tech.* **2003,** *63* (11), 1561-1569.

25. Kraus, W.; Nolze, G., POWDER CELL - a program for the representation and manipulation of crystal structures and calculation of the resulting X-ray powder patterns. *J. Appl. Cryst.* **1996,** *29* (3), 301-303.
26. Ferrari, A. C.; Basko, D. M., Raman spectroscopy as a versatile tool for studying the properties of graphene. *Nature Nanotechnology* **2013,** *8* (4), 235-246.
27. Dresselhaus, M. S.; Jorio, A.; R.Saito, Characterizing Graphene, Graphite, and Carbon Nanotubes by Raman Spectroscopy. *Ann. Rev. Cond. Mat. Phys.* **2010,** *1* (1), 89-108.
28. Eckmann, A.; Felten, A.; Verzhbitskiy, I.; Davey, R.; Casiraghi, C., Raman study on defective graphene: Effect of the excitation energy, type, and amount of defects. *Phys. Rev. B* **2013,** *88* (3), 035426.
29. Ferrari, A. C.; Meyer, J. C.; Scardaci, V.; Casiraghi, C.; Lazzeri, M.; Mauri, F.; Piscanec, S.; Jiang, D.; Novoselov, K. S.; Roth, S.; Geim, A. K., Raman Spectrum of Graphene and Graphene Layers. *Phys. Rev. Let.* **2006,** *97* (18), 187401.
30. Saito, R.; Dresselhaus, G.; Dresselhaus, M. S., Trigonal warping effect of carbon nanotubes. *Phys. Rev. B* **2000,** *61* (4), 2981-2990.
31. Maultzsch, J.; Telg, H.; Reich, S.; Thomsen, C., Radial breathing mode of single-walled carbon nanotubes: Optical transition energies and chiral-index assignment. *Phys. Rev. B* **2005,** *72* (20), 16.
32. Popov, V. N.; Henrard, L.; Lambin, P., Resonant raman intensity of the radial breathing mode of single-walled carbon nanotubes within a nonorthogonal tight-binding model. *Nano Let.* **2004,** *4* (9), 1795-1799.
33. Atkins, P.; de Paula, J., *Elements of Physical Chemistry*. OUP Oxford: 2013.
34. Playford, H. Y.; Owen, L. R.; Levin, I.; Tucker, M. G., New Insights into Complex Materials Using Reverse Monte Carlo Modeling. *Ann. Rev. Mat. Res., Vol 44*, Clarke, D. R., Ed. 2014; Vol. 44, pp 429-449.
35. Boden, N.; Folland, R., Nuclear magnetic spin-lattice relaxation and molecular motion in solid white phosphorus and in liquid phosphorus. *Molec. Phys.* **1971,** *21* (6), 1123-&.
36. Kresse, G.; Furthmüller, J., Efficient iterative schemes for ab initio total-energy calculations using a plane-wave basis set. *Phys. Rev. B* **1996,** *54* (16), 11169-11186.
37. Kresse, G.; Joubert, D., From ultrasoft pseudopotentials to the projector augmented-wave method. *Phys. Rev. B* **1999,** *59* (3), 1758-1775.
38. Jiří, K.; David, R. B.; Angelos, M., Chemical accuracy for the van der Waals density functional. *J. Phys.: Cond. Matt.* **2010,** *22* (2), 022201.
39. Klimeš, J.; Bowler, D. R.; Michaelides, A., Van der Waals density functionals applied to solids. *Phys. Rev. B* **2011,** *83* (19), 195131.
40. Chris, J. P.; Needs, R. J., Ab initio random structure searching. *J. Phys.: Cond. Matt.* **2011,** *23* (5), 053201.
41. Chen, J.; Schusteritsch, G.; Pickard, C. J.; Salzmann, C. G.; Michaelides, A., Two Dimensional Ice from First Principles: Structures and Phase Transitions. *Phys. Rev. Lett.* **2016,** *116* (2), 025501.
42. Hart, M.; White, E. R.; Chen, J.; McGilvery, C. M.; Pickard, C. J.; Michaelides, A.; Sella, A.; Shaffer, M. S. P.; Salzmann, C. G., Encapsulation and Polymerization of White Phosphorus Inside Single-Wall Carbon Nanotubes. *Angew. Chem. Int. Ed.* **2017,** *56* (28), 8144-8148.
43. Henkelman, G.; Uberuaga, B. P.; Jónsson, H., A climbing image nudged elastic band method for finding saddle points and minimum energy paths. *J. Chem. Phys.* **2000,** *113* (22), 9901-9904.
44. Heyd, J.; Scuseria, G. E.; Ernzerhof, M., Erratum: “Hybrid functionals based on a screened Coulomb potential” [J. Chem. Phys. 118, 8207 (2003)]. *J. Chem. Phys.* **2006,** *124* (21), 219906.

3 Filling Single-Walled Carbon Nanotubes with Phosphorus

3.1 Introduction

Phosphorus is the most well-known and explored of all the pnictogens. It is also one of the most structurally diverse elements on the periodic table which is one of the many reasons as to why it has been so widely and consistently studied for the past three centuries! The allure of the gentle glow of white phosphorus is still just as captivating now as it must have been when it was first isolated, and that characteristic smell of garlic as it oxidises is one that few forget. Despite the mixed reception that phosphorus elicits nowadays, it cannot be mistaken that phosphorus is still an integral element and material to modern life, with its uses ranging from making fertilisers to the creation of steels and coppers.[1]

White phosphorus is the culprit for giving phosphorus its bad name. Its use in munitions has led to much suffering throughout the years. The allotrope is comprised of tetrahedral P_4 molecules that can pack together in three different ways; named α, β and γ. The α-phase is the room temperature modification. It is a plastic crystal with the molecules rotating about their centres of gravity in an α-Mn structure.[2, 3] The β-phase occurs around 196 K.[4] It is a reversible transformation but occurs at irregular temperatures. The crystal structure for β-P_4 is that of γ-Pu,[5] with the P_4 molecules replacing the Pu atoms. Lastly, the γ-phase can be formed by supercooling the α-phase and slowly warming the sample, at which point a strong exothermic event occurs at 98 K to form the γ-phase.[4] The β→γ transition is not observed upon cooling. The γ-phase has a simple body-centred cubic arrangement.[6] As phosphorus vapour is comprised of P_4,[7] it is simple to prepare white phosphorus. Simply condensing phosphorus vapour onto a cold surface will create a film of pure white crystals.[8]

Red phosphorus is the set of allotropes that is unique to phosphorus amongst the pnictogens. Neither arsenic, antimony or bismuth show these types of structures, despite the other similarities they share. It is commonly accepted that there are five distinct varieties of red phosphorus, Type I (amorphous phosphorus), Type II, Type III, Type IV (fibrous red phosphorus) and Type V (Hittorf's phosphorus).[9] Type I can be produced from the gradual conversion of white phosphorus either by an irradiation source or by

heating. The other types can be formed by recrystallizations of the Type I structure from melts or within the presence of metal catalysts. It is also been shown that the pentagonal tubular motif that defines Types IV and V is also present in amorphous phosphorus.[10] Less is known about Types II and III due to difficulties in isolating good crystals, but it has been shown that nanorods of red phosphorus can be made using the Type II crystal.[11] Types IV and V are made from pentagonal tubes of phosphorus atoms that are linked together in different ways.[12] Novel structures with similar tubular motifs to the five red phosphorus types have also been synthesised using copper and iodine stabilising atoms.[13] Phosphorus confined in MWCNTs have also shown similar structures.[14]

Little is still known about the mechanisms for the formations of the various phosphorus allotropes. Pauling has reasoned that a logical first step in the white to red conversion would be the breaking of one bond per tetrahedral unit which then allows the molecular units to link up.[15] The opening of the tetrahedral unit has been observed in many complexes that have tried to incorporate phosphorus tetrahedra.[16]

Black phosphorus is the current darling of the materials chemistry world. This material, which in the wake of graphene, has garnered new interest due to its layered composition which have now been separated to form phosphorene.[17] Black phosphorus is the most thermodynamically stable phosphorus allotrope and has an orthorhombic crystal structure made up of puckered honeycomb layers.[7, 18] At high pressures, black phosphorus will convert into a rhombohedral structure which has the same structure as grey arsenic and antimony.[19] Black phosphorus can be made in two ways, either heating to 473 K under pressures of 1.2 gPa,[20] or from the recrystallisation of red phosphorus in the presence of mercury or tin.[21-23] The property that interests chemists is its tuneable bandgap. The bulk material has a band gap of 0.3 eV but this can be increased to 1.5 eV if exfoliated to a monolayer.[24]

Phosphorene can be synthesised using many of the standard procedures used to synthesis other monolayered materials. Mechanical cleavage (scotch tape method)[17] and liquid exfoliation (sonication in a solvent)[24] have been shown to generate small scale yields of true monolayered phosphorene. Epitaxy has been able to produce few layered black phosphorus, but true monolayers have been difficult to synthesis with this method.[25]

Blue phosphorus is one of the newer allotropes that has been synthesised.[26] It is another layered allotrope that has been grown by molecular beam epitaxy. The material

is a semiconductor and although it has a smaller band gap than phosphorene, it gives materials scientists even more diversity in order to create bespoke electronic components.[27] This is one of the many variations of layered pnictogens that have been theorised, all of which have band gaps, though, their size and nature may differ.[28]

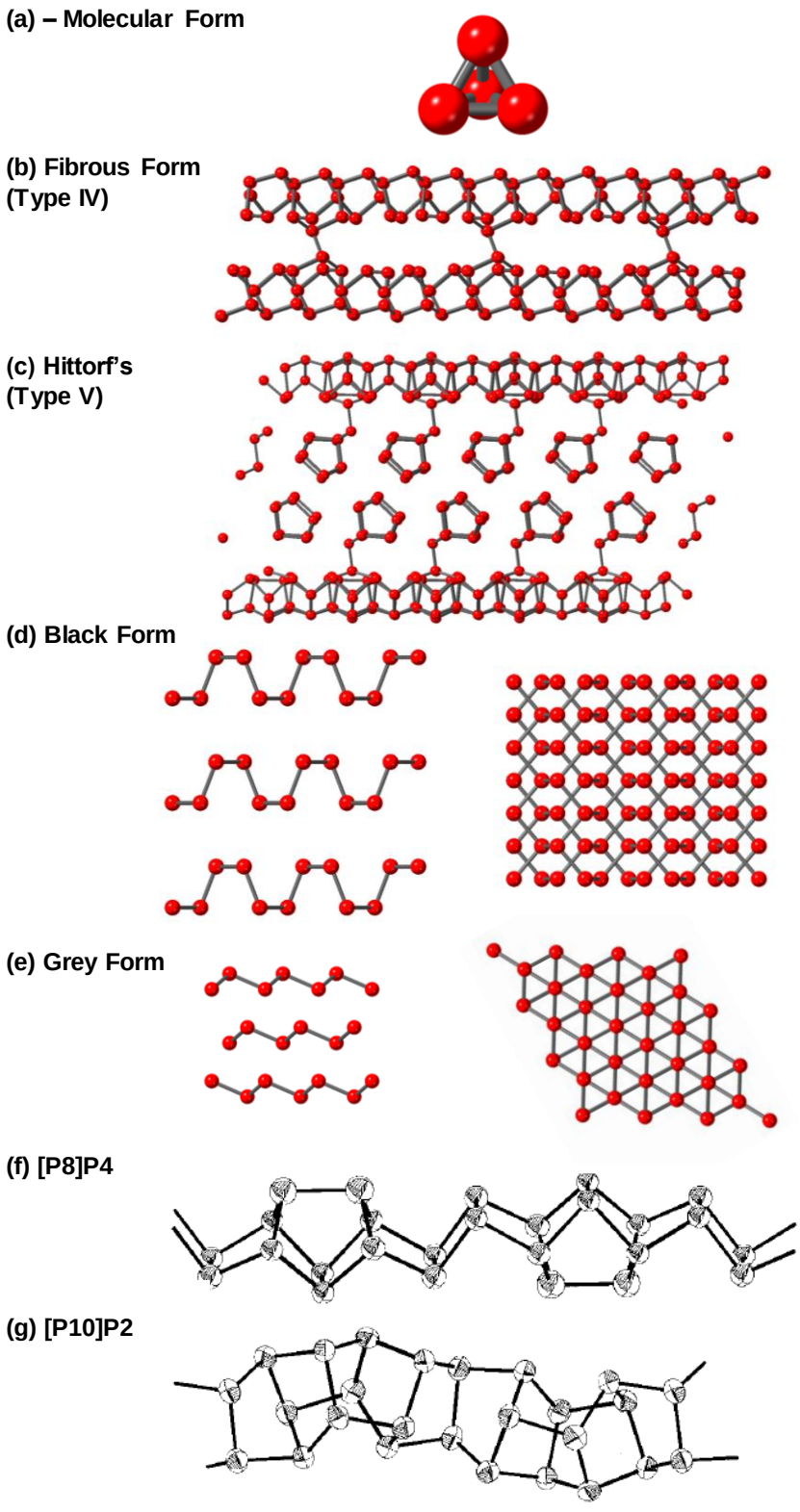

Figure 3.1 The various allotropes of phosphorus. (a) Molecular "white" Phosphorus, (b) Fibrous Phosphorus (Type IV), (c) Hittorf's Phosphorus (Type V), (d) Black Phosphorus, (e) Grey Phosphorus, (f) [P8]P4, (g) [P10]P2. (f) and (g) reproduced from reference [12].

Stabilising P_4 has been a goal of chemists for a long time. Having the ability to safely contain and release P_4 molecules without any risk to the user would be a great

achievement. P_4 has successfully been immobilised between crystallised C_{60} molecules from CS_2 solvent.[29] The P_4 molecules occupied the trigonal prismatic sites of the hexagonal C_{60} array, but they retain their dynamic nature. ^{31}P NMR showed a narrow singlet caused by the P atoms which would broaden as the sample was cooled due to the slowing of the dynamic processes. No charge transfer was observed for the sample, the phosphorus resonance occurred at -490 ppm which was only slightly higher than the expected value of -462 ppm for bulk white phosphorus. The sample showed good stability to oxidation, with PXRD still detecting P_4 features after a week. A similar example of this type of entrapment was discovered recently with the stabilisation of P_4 within activated carbon using a similar process of recrystalising from a solvent, though it was shown that after a few weeks, the NMR signal began to diminish and a growing feature associated with oxide products was evident.[30]

P_4 molecules have been traditionally stabilised by coordinating to metal complexes. Ginsberg *et al.* showed that P_4 will coordinate to a variety of Rh(I) or Ir(I) complexes in the form of MXL_3 by displacing one of the ligands to form $MX(P_4)L_2$.[31] Originally, it was thought that the phosphorus molecules are η^2-coordinated to the metal, with back-bonding causing the lengthening of the P-P bond that is bonded to the metal centre, but more recent work has shown that in fact very little P-P bond remains in the coordinated edge making the P_4 molecule closer in structure to the butterfly molecular unit.[32] True η^2-bonding was seen in silver-phosphorus complexes which can contain one or two P_4 molecules and truly retains the P_4 molecular species.[32] P_4 has also been η^1-coordinated to rhenium complexes and has been shown to act as a bridging ligand to create a binuclear rhenium complex.[33]

A more recent method used for stabilising P_4 molecules involves constructing cages or supramolecular structures around the phosphorus molecule. This prevents oxidation from occurring as the supramolecular structure cannot accommodate the larger P_4O_{10} molecule.[34] This system was constructed from polymeric chains, with Fe^{2+} ions found at the corners of the tetrahedral cage. The material was found to be stable for an indefinite period of time, but could release the P_4 molecule if a suitably sized guest molecule was introduced, such as benzene. This self-assembled method of entrapment has inspired similar methods, from a completely organic cage created from an imine condensation scheme that wraps around the P_4 molecule,[35] to an anion-coordinated based cage that uses PO_4^{3-} as the coordination centre instead of a more commonly used transition metal.[36] This complex also makes use of favourable σ-π interactions between the guest and host molecules which provides further protection of the P_4 molecule from

oxidation. Theoretical calculations have showed two mechanisms that cause this, first, the active orbitals of the P_4 molecule are shielded by the π conjugate orbitals of the ligand and second, the lone-pair orbitals of P_4 are correlated with the π orbitals of the aryl rings.

Considering the widespread use of phosphorus as a dopant, and the amount of research predicting that SWCNTs will be used within the electronics industry, it is of no surprise that phosphorus has been encapsulated within SWCNTs before. Both SWCNTs and MWCNTs have all been filled with phosphorus using red phosphorus as the phosphorus feedstock.[14, 37] The previous P@SWCNT samples have been synthesised with mixed success, some do not even show any elemental phosphorus in their XPS analysis![38] TEM has revealed some encapsulation though, but due to the low resolution, it is hard to decipher the structure adopted by the phosphorus. It was hypothesised that the phosphorus has filled as small clusters within the nanotube, but without any simulated micrographs and considering the width of the nanotube imaged, this seems doubtful.[38] There is definitely no evidence that the phosphorus has remained as tetrahedral molecules. The P@MWCNT sample showed a familiar phosphorus structure containing P_8 and P_2 units producing a ring that is reminiscent of other red phosphorus allotropes.[14]

These materials were created to try and tune the band structure of the SWCNTs. Raman spectra have shown blue-shifts in the G-bands which would indicate that the SWCNTs have been p-doped.[38, 39] However, as so much phosphorus oxide is present, the shifts in the G-band are most likely caused by interactions with the external phosphorus material. A P@MWCNT sample has been prepared as an anode for lithium ion batteries.[40] The material showed excellent cyclability and retained most of its charge after its 15th cycle. The presence of phosphorus oxide helped prevent the lithium ions from reacting with the internal phosphorus and forming Li_xP compounds which have been shown previously to drastically decrease the charge of P@SWCNTs in similar studies.[41]

3.2 Outline of Chapter

This chapter presents the investigation into filling SWCNTs with P_4 molecules. The key question is whether the carbon sheath can provide a suitable environment to stabilise the elemental phosphorus without oxidation. A variety of SWCNT types and ways of filling have been investigated in order to understand how the filling yield varies with nanotube diameter and to see how the diameter of the cavity and method of filling can

affect the types of phosphorus structures possible when confined. DFT calculations conducted by Ji Chen will be used to support the findings in this chapter.

The chapter will be split into three sections based on the diameter of the carbon nanotubes used, and also by the filling process. In order to give a comprehensive review of how the diameter and filling process effects the filling yield and structures produced.

3.3 Filling Large-Diameter SWCNTs

Tuball SWCNTs have been used primarily due to the high proportion of SWCNTs in the sample given their price.[42] The future of composites using SWCNTs will be married to the ability to produce high quality but cheap SWCNTs and with lots of experiments planned they seemed like an excellent material to work with. Their large diameters should also offer good loading compared to narrower SWCNTs and would hopefully allow phase transitions of the white phosphorus to be seen under HRTEM.

Initial experiments were focussed on creating an air-stable composite material, which would not ignite and destroy the sample. Various approaches, including using hydrogen peroxide solutions, to remove the excess white phosphorus material were inconsistent until a reliable method was formalised. The key step was removing as much white phosphorus as possible by sublimation before the final work up. Once this had been achieved, work began on trying to create purer materials.

3.3.1 Capping – Which solvent?

The capping of filled carbon nanotubes has been tentatively described in the literature.[43, 44] The fact it is not more commonly utilised shows the general thoughts towards this method. Commonly, a solvent in which the C_{60} molecules are insoluble is used to help create an environment that favours the fullerene entering the nanotube. A series of experiments were conducted to determine the best solvent for this particular system. The initial experiments were used to determine if a solvent was needed at all. By adding the fullerenes whilst the white phosphorus was molten, the use of solvents could be avoided altogether to make for a simpler and quicker synthesis procedure.

It can be seen from Figure 3.2 (d) that the C_{60} added to just molten white phosphorus does not disperse within the molten phosphorus. Although the molten phosphorus appears slightly brown, this is just the appearence of molten white phosphorus. The lack of dispersion should favour the capping process, as the fullerenes will prefer to be confined within the tube as opposed to being within the melt.[45] The XPS results showed that this technique is be quite inconsistent, Figure 3.2 (c). The composites produced had

high levels of impurities as can be seen from the large P(Ox) feature at ~135 eV, insets of Figure 3.2 (a) and (b). Fitting this region and combining with the quantities of elements present from survey spectra allows the determination of the proportion of oxidised to elemental phosphorus. The sensitivity of phosphorus to oxygen provides a convenient method of calculating the filling yield of the sample. Internal material will remain protected from the atmosphere, whilst external material will oxidise.

An estimated maximal filling yield determined using RMCProfile was calculated at 8.3 at% for a 1.8 nm SWCNT. This was calculated by simplifying the phosphorus tetrahedral molecules to spheres and allowing them to move within a SWCNT. Minimum distance parameters kept the molecules apart and away from the nanotube sidewall using the van der Waal radii. If the minimum distances were disobeyed, then too many molecules were in the simulation. A helical structure was achieved. This is logical as spheres pack most efficiently as a helix when confined to a cylinder, Figure A3.1 (a).

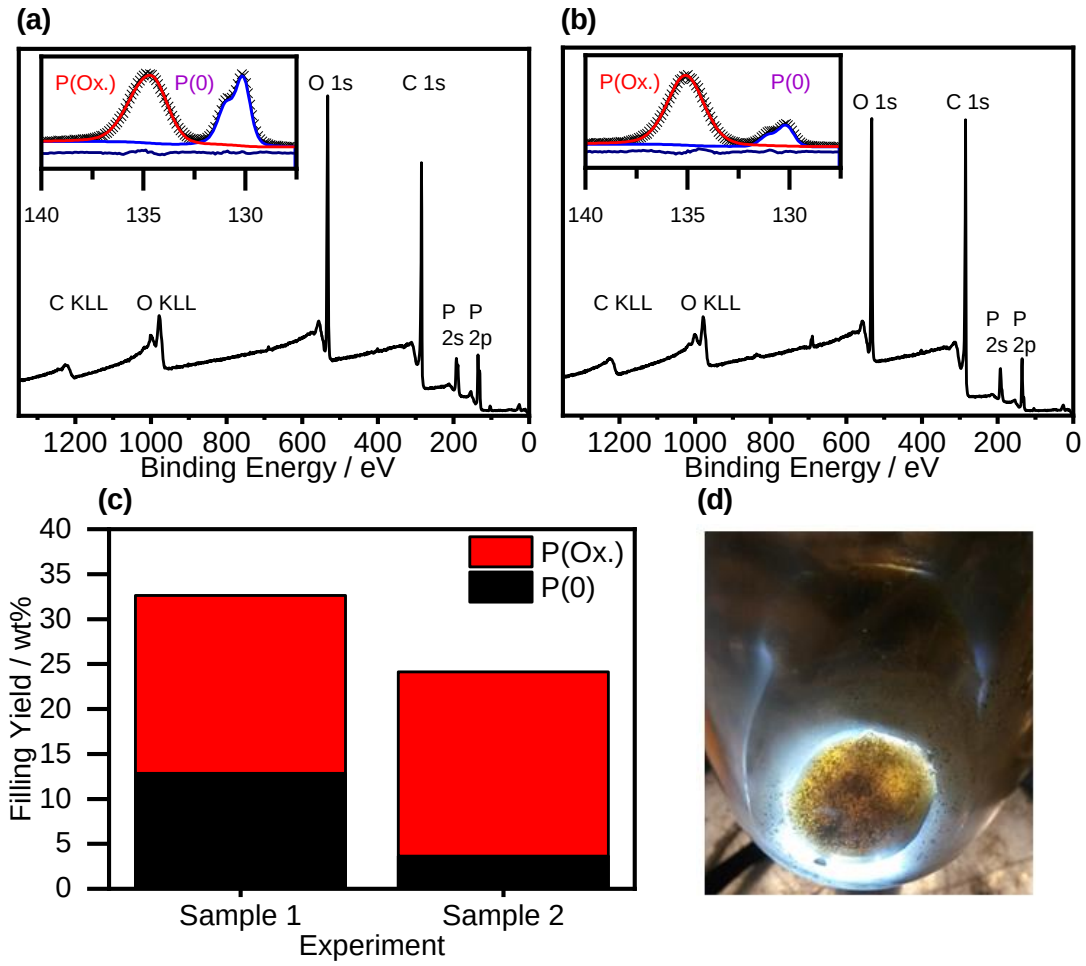

Figure 3.2 XPS overview of some capping experiments. (a, b) Survey spectra and high-resolution XPS spectra (inset) of samples where C_{60} is added whilst the white phosphorus is still molten. High-resolution XPS spectra have been fitted to produce the results in (c).

(c) Filling yield overview. (d) Image taken of C_{60} in molten white phosphorus showing that no dispersion has been created.

Experiments began on a more conventional approach, using a capping solvent in which to stir the filled SWCNTs in. The solvents used had a variety of solubility values for C_{60} from ethanol with the lowest solubility to CS_2 with the highest.[46] Each experiment was carried out with a control experiment where no capping agent was used. Instead the work up stage was carried out after the sublimation step as described in the standard procedure.

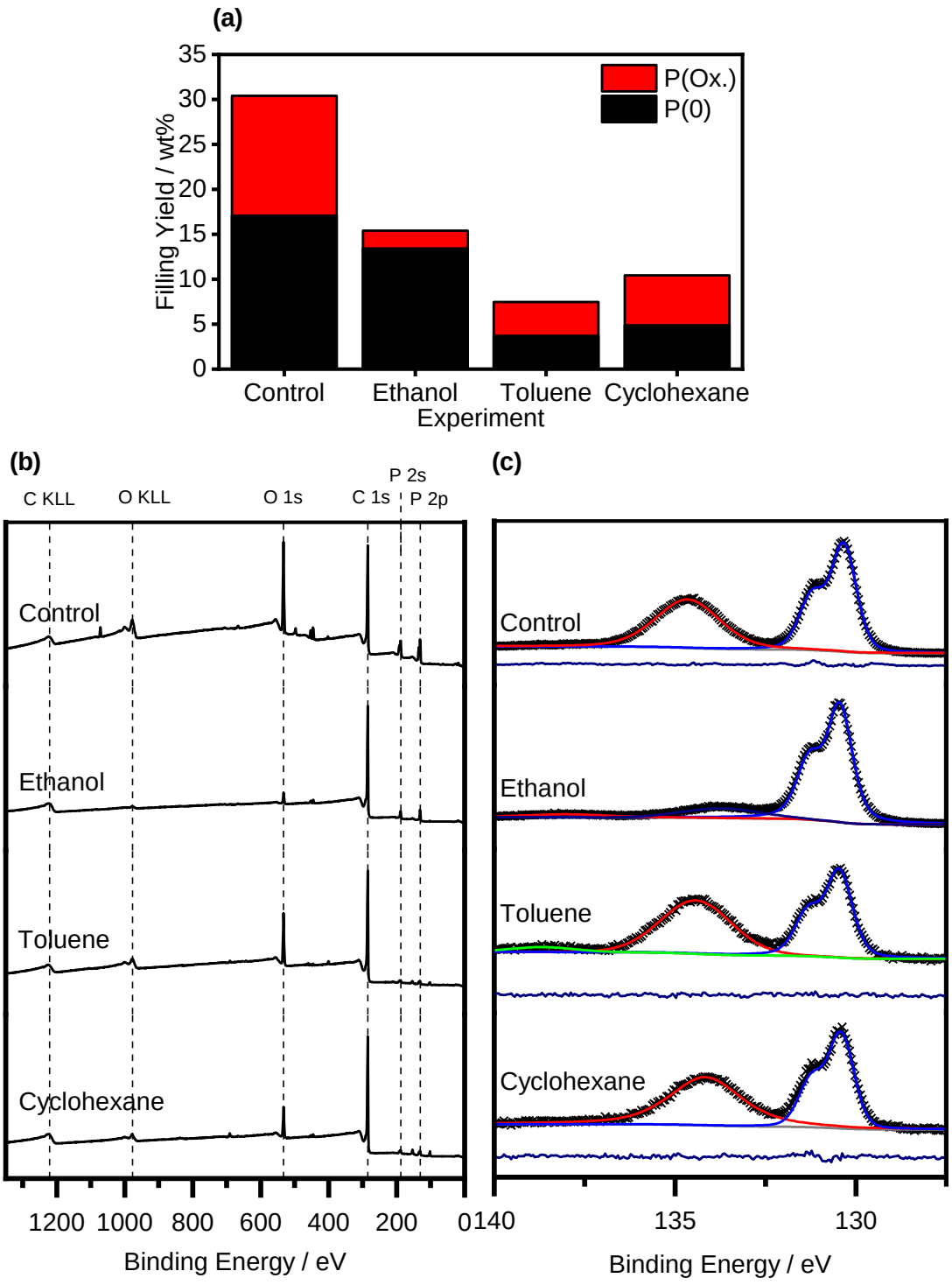

Figure 3.3 XPS overview of a set of capping experiments. The filled sample was split into four samples of equal mass. Three are capped with C_{60} and the last is kept as a control experiment which is not capped. (a) Filling yield overview, (b) survey spectra and (c) high-resolution XPS spectra that have been fitted to produce the results in (a).

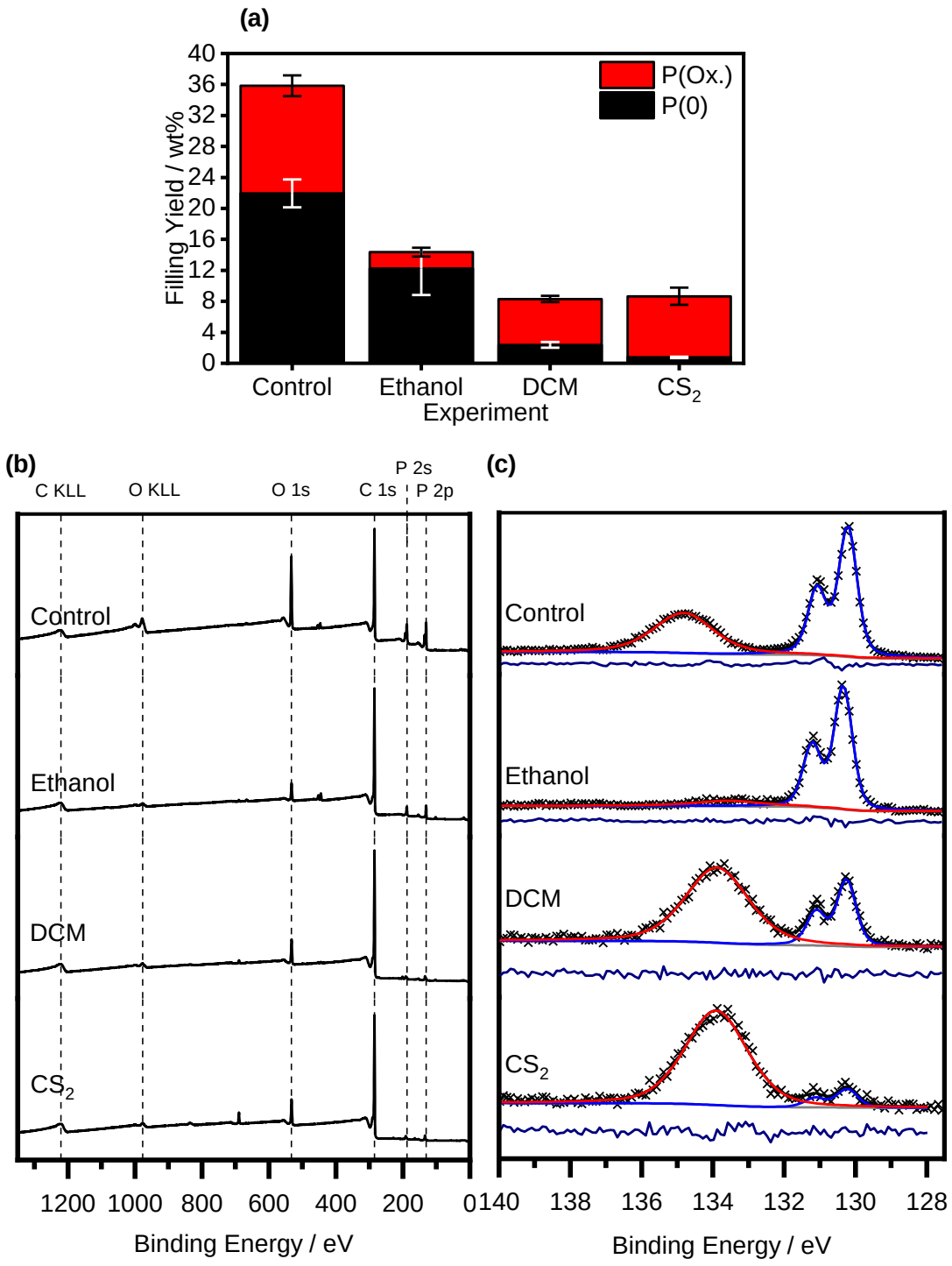

Figure 3.4 XPS overview of a second set of capping experiments. The filled sample was split into four samples of equal mass. Three are capped with C_{60} and the last is kept as a control experiment which is not capped. (a) Filling yield overview, (b) survey spectra and (c) high-resolution XPS spectra that have been fitted to produce the results in (a).

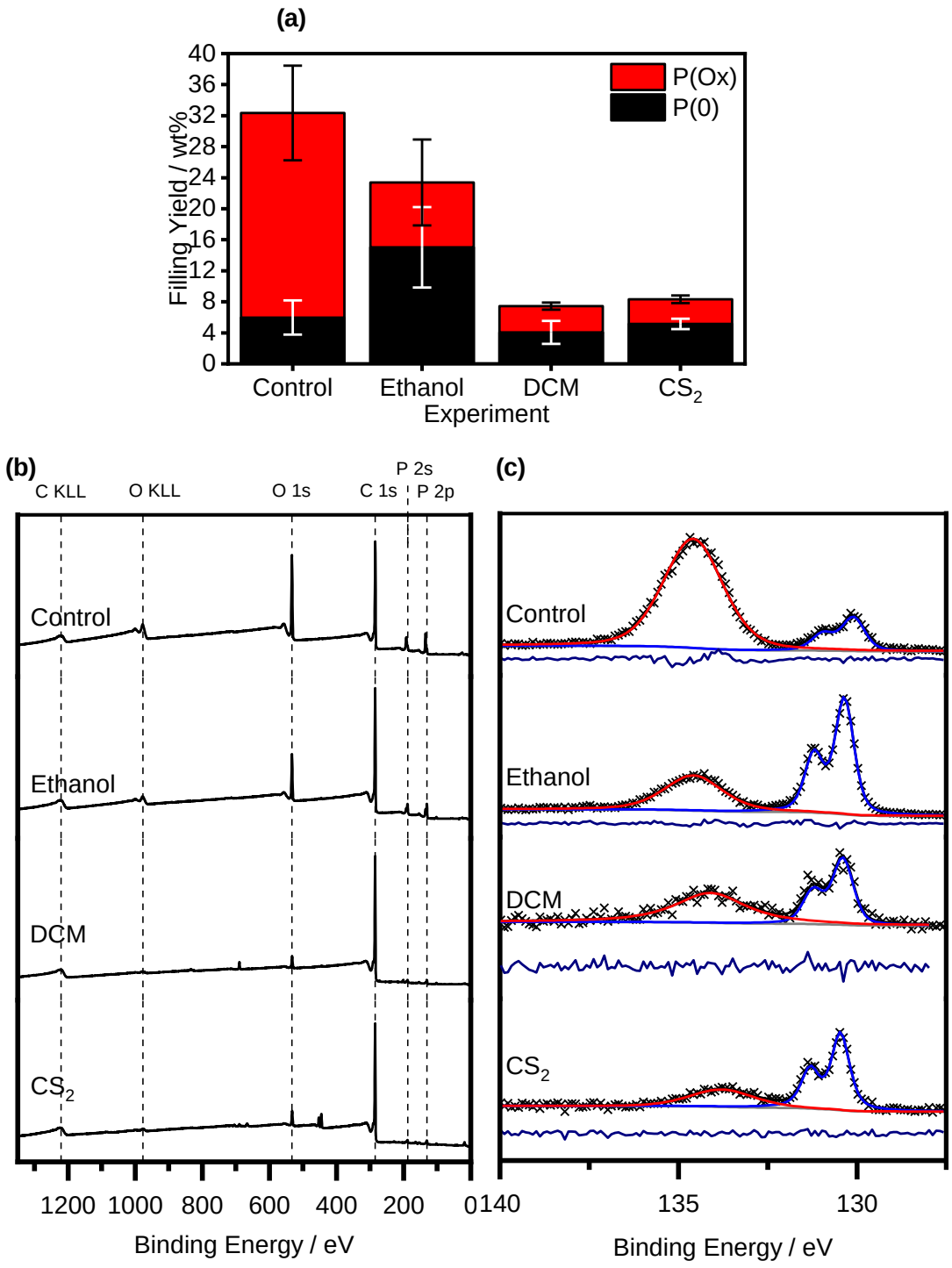

Figure 3.5 XPS overview of a third set of capping experiments. The filled sample was split into four samples of equal mass. Three are capped with C_{60} and the last is kept as a control experiment which is not capped. (a) Filling yield overview, (b) survey spectra and (c) high-resolution XPS spectra that have been fitted to produce the results in (a).

A consistent pattern has emerged which shows that the capped samples all have lower filing yields than the control sample, with one exception. Figure 3.5 shows that the C_{60} capped sample, using ethanol as the solvent, had a higher filling yield than the uncapped sample. This seems to indicate that the C_{60} is competing with the white phosphorus for

encapsulation within the cavity. The capped samples also show better ratios between elemental and oxidised phosphorus. This shows that capping is able to protect the filling material whilst allowing the external material to be removed. The solubility of the white phosphorus within the solvents used also seems to have played a part. White phosphorus is very soluble in carbon disulphide and also in dichloromethane.[47] These solvents performed particularly badly in terms of filling yield. It is feasible that the solvents helped remove some of the filled material and then displace them with C_{60} fullerenes. Studies in the literature have shown it is possible for the filling material to be removed almost completely by solvents so this result is not surprising.[43, 48] Ethanol consistently gave the best balance between filling yield and purity. This is due to both C_{60} and white phosphorus' insolubility in the solvent. Ethanol is the most commonly used solvent for these types of experiments and these results confirm this to be the best solvent for this system as well.

It can be seen from the data that the filling yield can be very variable. With seemingly identical experiments, the elemental phosphorus presence has a broad range. It is proposed that this variation is caused during the stirring of the nanotubes within the molten phosphorus. The material regularly sticks to the walls of the flask and gets pushed away from the molten phosphorus pool by the stirrer bar. The nanotubes that remain in the pool do not disperse within the phosphorus "solvent" either, which will also increase heterogeneity within the sample.

This variation can also be seen in the position and shape of the oxidised phosphorus region. The broad peak shape indicates that a variety of phosphorus oxidation states exist, and an average value of 134.3 ± 0.5 eV for the peak falls firmly between the III (133.1 eV) and V (135.2 eV) oxidation states.[49] It seems the limited oxygen supply

during the work up of the sample prevents the complete oxidation of the phosphorus. The formation of these oxides is described in the below equations:

$$P_4 + 3O_2 \rightarrow P_4O_6 \quad [3.1]$$

$$P_4O_6 + 2O_2 \rightarrow P_4O_{10} \quad [3.2]$$

These oxides can in turn form a myriad of acids,[50] with a couple highlighted below upon exposure to water:

$$P_4O_6 + 6\,H_2O \rightarrow 4\,H_3PO_3 \quad [3.3]$$

$$P_4O_{10} + 6\,H_2O \rightarrow 4\,H_3PO_4 \quad [3.4]$$

It alludes to a system in which a variety of oxides and acids can be present and vary depending on the unpredictable nature of the filling and purification.

3.3.2 Thermal Stability

The filled carbon nanotubes help stabilise the phosphorus to ambient conditions. The point at which they ignite and release their cargo has been investigated using TGA/DSC.

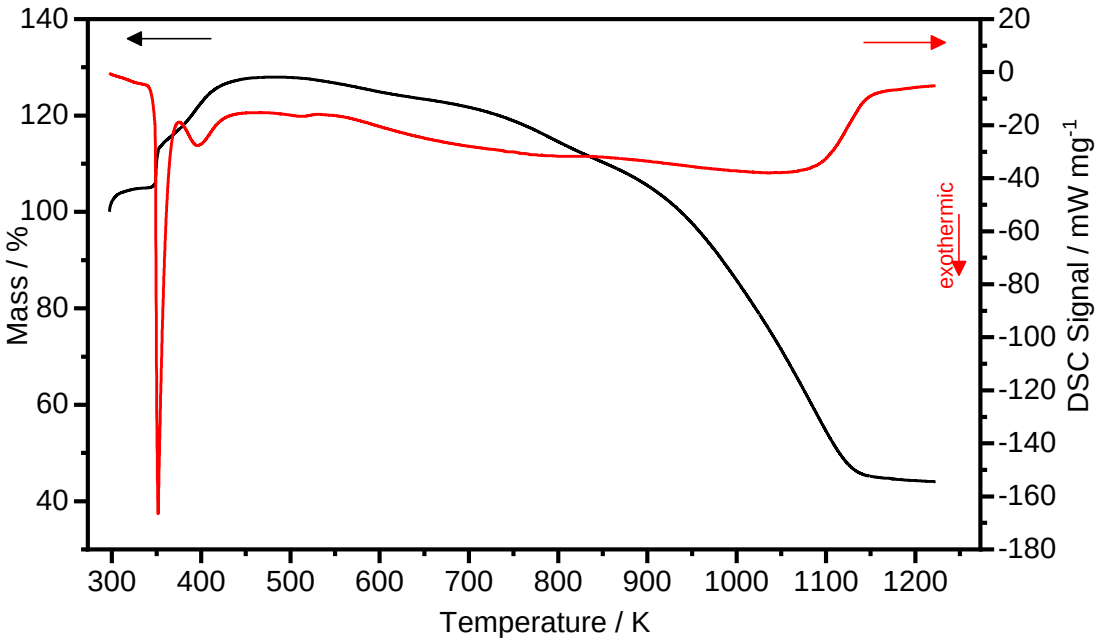

Figure 3.6 TGA/DSC scans of m-P@Tuball.

Figure 3.6 shows a quintessential TGA/DSC scan for a capped *m*-P@Tuball sample. This particular sample has a filling yield of 5 at% P(0) and 0.5 at% P(Ox). A small buoyancy artefact occurs at the start before a sharp mass increase with accompanying exotherm at 352 K. Several other exotherms and mass increases can be seen up to 483 K. This is caused by the oxidation of the white phosphorus which has leaked out of the nanotube.

The mass increases due to the uptake of oxygen and water forming phosphorus pentoxide and phosphoric acid respectively, equations 3.1 – 3.4 show some of the oxides and acids that can be produced. The presence of species in the III oxidation state, as seen in the XPS, may also oxidise further and will also form acids too. This combination of processes and the magnitude of phosphorus oxide acids that exist has made it difficult to fully understand this mass increase.

The temperature at which the initial leakage occurs varies between 323-373 K, with a high of 422 K. There seems to be no correlation with the filling yield or presence of oxidative species and the temperature of this feature. This seems to corroborate with the variation in the samples which XPS has also revealed. This type of behaviour has been evident in other systems, with water having been shown to melt at over 100°C depending on the diameter of nanotube used. [51], [52]

Raman spectroscopy has been used to see if any of the white phosphorus Raman features could be detected and to determine if any charge transfer has occurred. White phosphorus is very Raman active, with the main feature being the symmetric breathing mode of the molecule, $\nu_1(\alpha_1)$.[53] This feature appears at around 600 cm^{-1}, but no evidence could be determined for this feature. A noticeable shift in the G-band was detected though which indicates that charge transfer between the SWCNT and filling material has occurred, although not in the direction that is expected. The blue shift of the G-band, when the sample is illuminated with the 785 nm and 514 nm lasers in Figure 3.17, indicates that the SWCNT has "donated" electrons to the filling material.[54] This is a consistent pattern regardless of the wavelength used, with a shift of up to 14 cm^{-1} observed when the shortest wavelength is used. Previous evidence of this exists in the literature with samples with a high presence of phosphorus oxides.[14, 38, 39] It was expected that the lone pairs of the P_4 molecules would cause charge transfer to the SWCNTs, and thus cause a red-shift of the G-band, but it appears that hole-doping from the presence of phosphorus oxide is the dominating factor and causes the blue-shift observed.[38]

Another factor that makes it hard to truly understand what processes are ongoing is that it is only assumed that the phosphorus filling material has maintained its tetrahedral structure. TEM micrographs in Figure 3.9 depict a cage-like structure which have been induced by the energy of the electron beam. The electronic properties of these structures are unknown, and it would not be wholly unfeasible for these structures to be generated by the laser energy. It is known that white phosphorus is sensitive to x-rays and light, and shows discolouring when exposed for too long, so the Raman laser could have the

same effect. This may also explain why no features were observed for the P_4 breathing mode as they had already transitioned to a new allotrope.

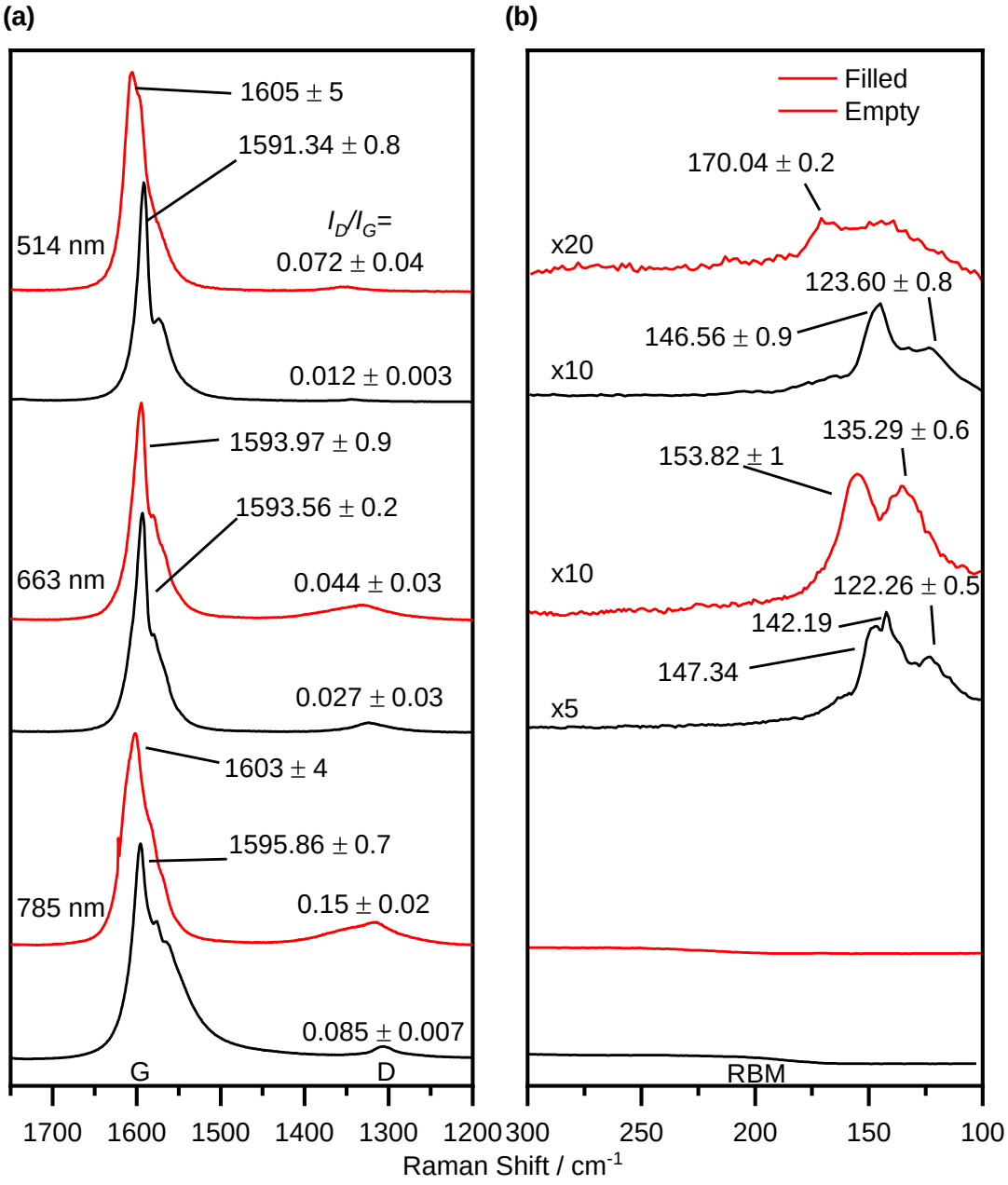

Figure 3.7 Raman spectra of m-P@Tuball and empty SWCNTs showing the (a) G and D bands and (b) the radial breathing modes when excited by 514 nm, 633 nm and 785 nm lasers. The spectra are normalised with respect to the G band and shifted vertically for clarity. Average values for the G band, D band, RBM and D/G band ratios have been calculated from the average of 3 spots. The RBM spectra are magnified by the given values to make the spectra clearer.

3.3.3 Structure

As discussed in the previous chapters, one of the fundamental reasons for filling nanotubes is to study how confinement effects the structure of the material.

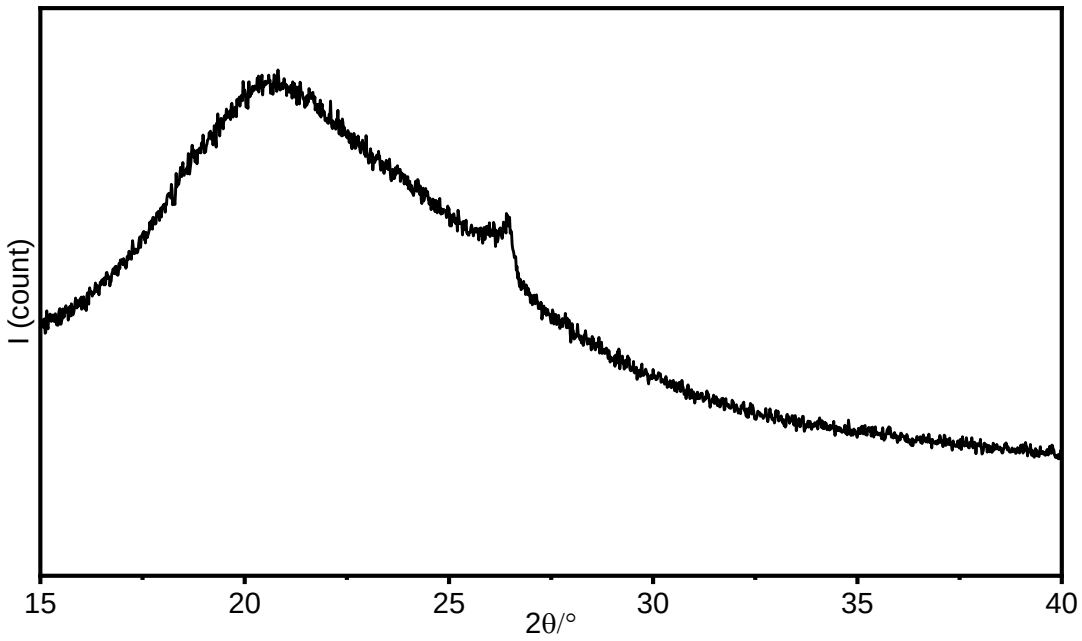

Figure 3.8 PXRD pattern of m-P@Tuball.

PXRD, Figure 3.8, shows a remarkable dearth of features. The amorphous feature is caused by the glass capillary. A small feature at 2θ=28° is caused by some residual graphite which seems to have survived the purification.[55] To further understand why no features have been seen, HRTEM of the samples have been conducted.

Figure 3.9 shows a collection of micrographs depicting filled SWCNTs. The features seem to show amorphous and potentially cage-like structures confined within SWCNTs. No signs of bead-like features were detected which could indicate that tetrahedral molecules are present. It seems that the freedom of movement afforded by the large diameter SWCNTs and the exposure to the electron beam have allowed the molecules to rearrange themselves into structures that mould themselves to the confines of the cavity.

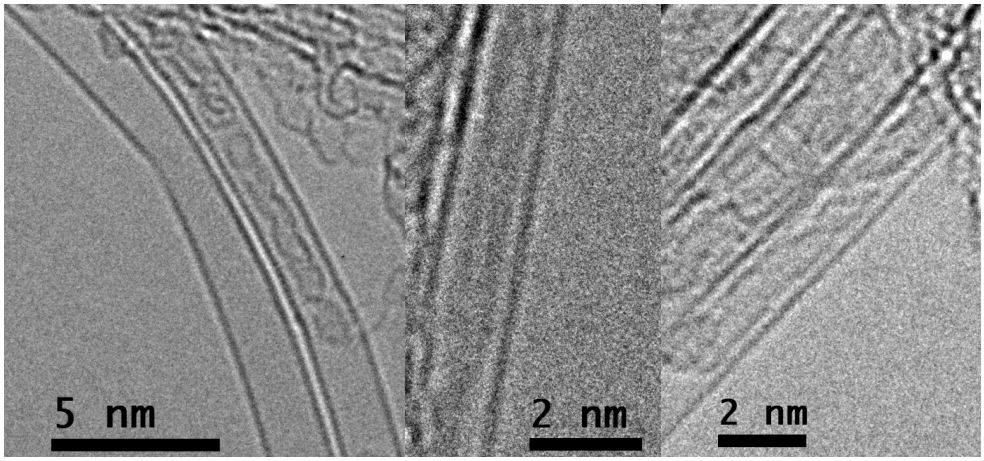

Figure 3.9 HRTEM micrographs of m-P@Tuball.

Attempts were made to try and prevent this rearrangement by using an environmental TEM grid holder to cool the sample. However, the sample vibrated and drifted heavily when at the magnification level needed to acquire the images. Another problem with imaging the Tuball filled samples is that the C_{60} fullerenes, used as the capping agent, were often mistaken for white phosphorus molecules due to their very similar appearance to what could be expected of confined white phosphorus. This can be clearly seen in Figure 3.10.

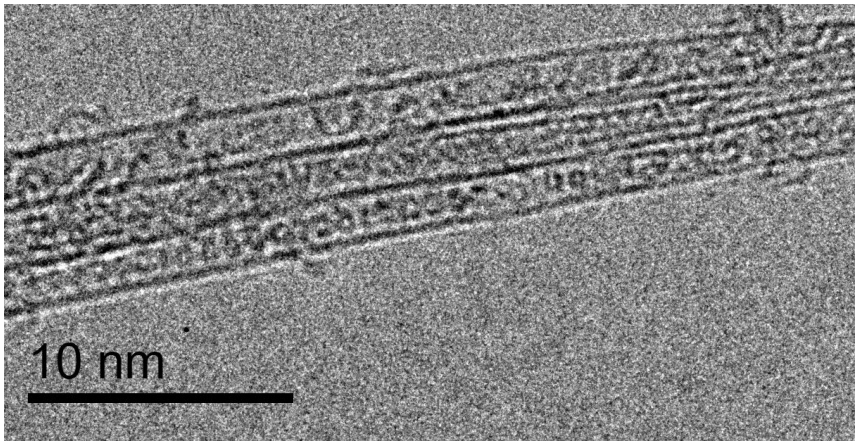

Figure 3.10 HRTEM micrograph of m-P@Tuball capped with C_{60} showing the fullerenes in the classic "peapod" formation.

3.4 Filling Narrower Diameter SWCNTs with Phosphorus

Due to the imaging problems discussed above, narrower diameter SWCNTs were used to try and confine the white phosphorus tetrahedra to one-dimension and to hopefully preserve their shape.

Both CoMoCAT and HiPCO SWCNTs were used for these experiments and the filled samples will be referred to as *m*-P@CoMoCat and *m*-P@HiPCO respectively. Initially, CoMoCat SWCNTs were examined as the diameter range they provide should perfectly encapsulate the white phosphorus tetrahedra. HiPCO nanotubes were examined as well, to see how the confined material may behave in a slightly larger environment.

3.4.1 Filling Yield

CoMoCat and HiPCO SWCNTs showed very similar filling yields to what was achieved using the Tuball material, as can be seen in Figure 3.11. A lot more oxide was present though as no capping agent can be used for such small SWCNTs. The van der Waals radius of a C_{60} molecule is 1.1 nm, which is too large to fit inside these nanotubes.[56]

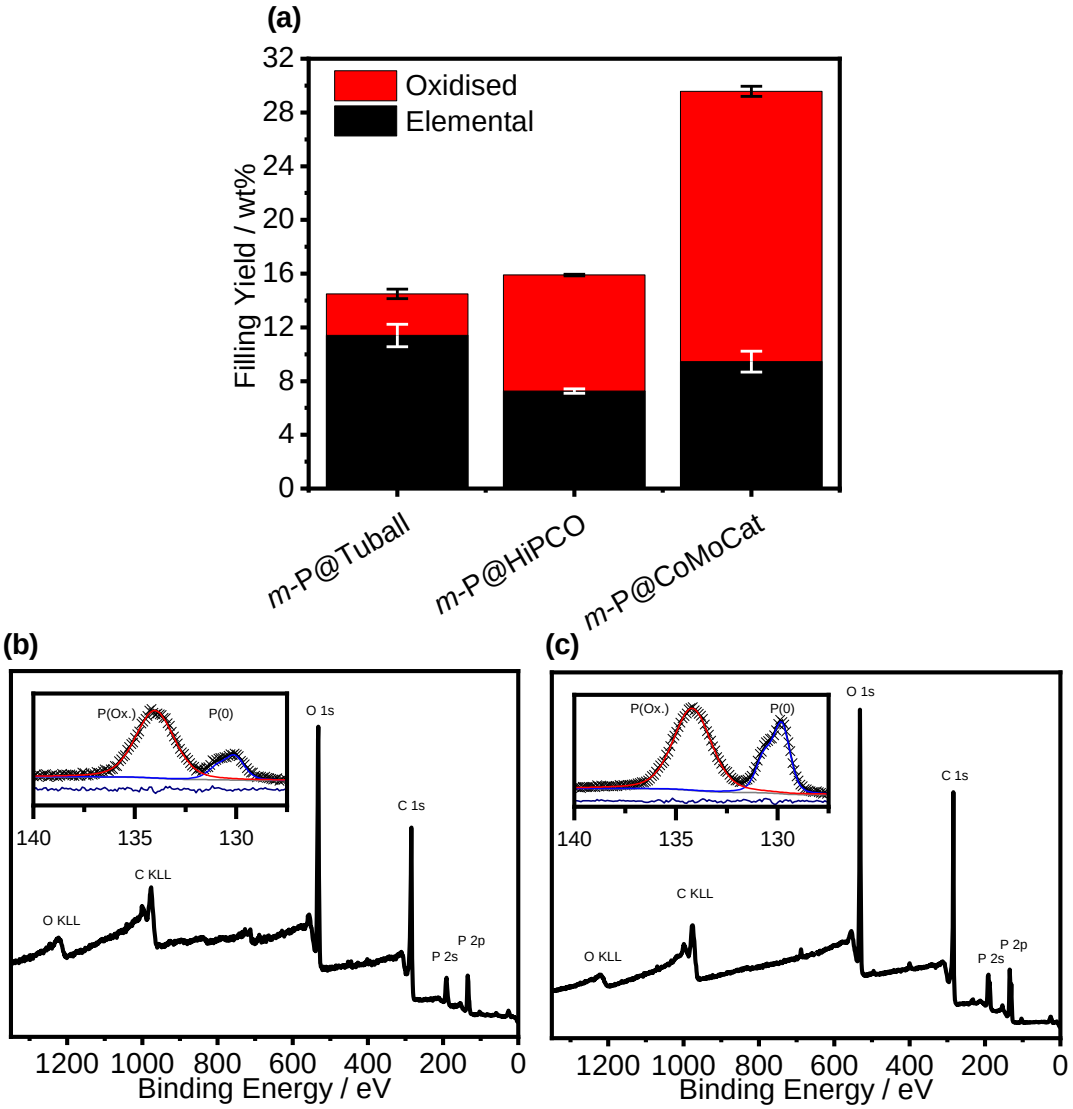

Figure 3.11 XPS overview comparing the filling yields for m-P@Tuball, m-P@HiPCO and m-P@CoMoCat. (a) Filling yield overview, (b) survey spectra and (c) high-resolution XPS spectra that have been fitted to produce the results in (a).

Filling yield estimates in Figure 3.13, created using DFT optimised and confined structures calculated by Ji Chen (Figure 3.12), show that the filling yields of the *m*-P@HiPCO and *m*-P@CoMoCat samples are slightly below what is expected. The filling yield estimates for confined phosphorus ranges from 15 wt% to 24 wt% depending on the structure and nanotube diameter. It is interesting to see, though, that as the average diameter increased from 7-8 Å (CoMoCat) to 9-10 Å (HiPCO), that the filling yield fell as predicted from the DFT calculations. The amorphous structures observed in the Tuball SWCNTs (Figure 3.9) would be expected to pack better, hence the increased filling yield compared to the HiPCO and CoMoCat filled materials. Overall, from these calculations, the SWCNTs are only around 50% filled.

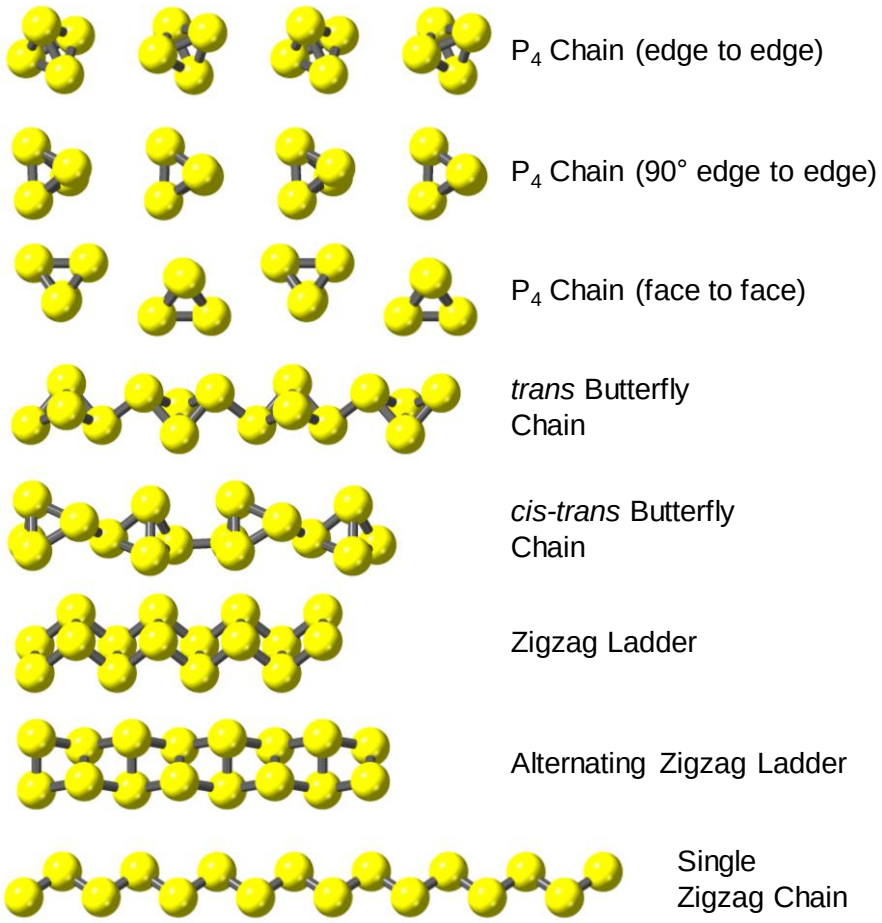

Figure 3.12 Geometry-optimised phosphorus structures created by Ji Chen using DFT techniques.

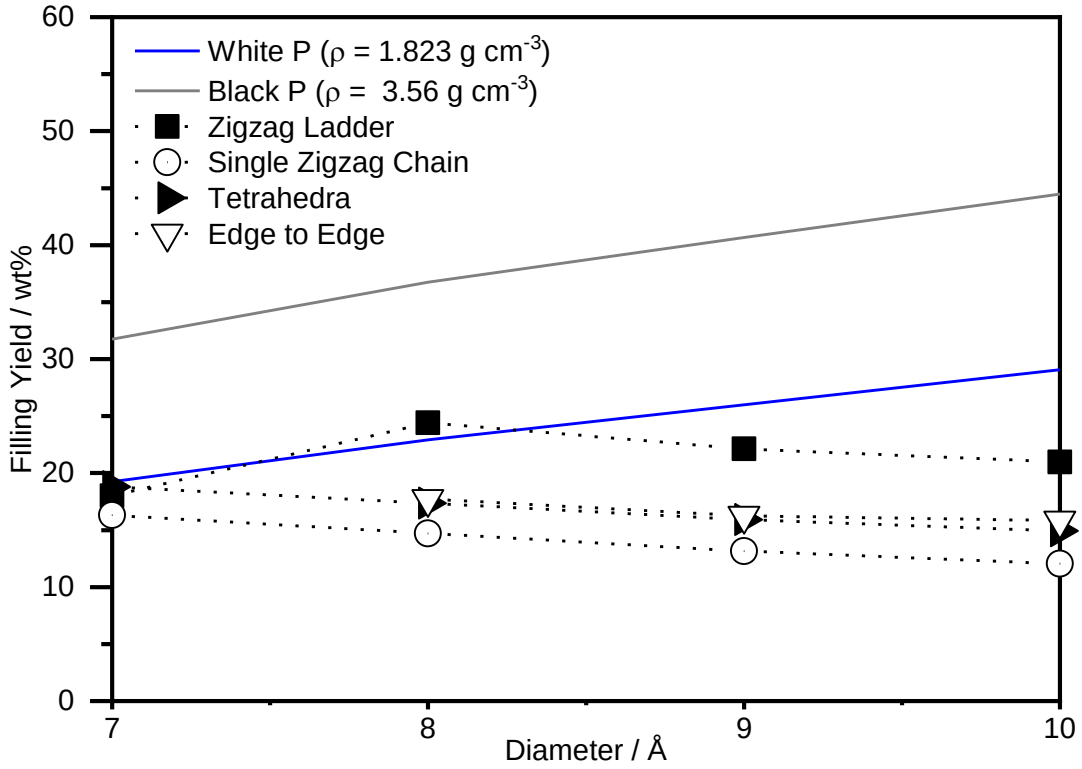

Figure 3.13 Filling yield estimates based on structures created from DFT by Ji Chen in Figure 3.12. The filling yield was calculated by filling a 50 Å length of SWCNT with the largest number of unit cells of the filling material without causing any of the filling material to exit the end of the tube. The proportion of each atom type could then be used to calculate a filling yield.

3.4.2 Micro-Structures

HRTEM has been used to examine the filled narrow SWCNTs to determine if the tighter confinement has helped preserve the tetrahedral structures. DFT has been used in conjunction with these measurements to help identify the structures seen within the SWCNTs in Figure 3.15.

The structures created and examined in Figure 3.12 were the result of logical assumptions as well as structure searching to find stable possibilities. The various tetrahedral structures represent the possible alignments each molecule can have relative to one another. Although, in all likelihood, the tetrahedra will rotate about their centre of masses when thermally excited or exposed to an electron beam.[3] The butterfly chains potentially show the first stages of polymerisation, with one bond breaking in each tetrahedra and linking up with the adjacent molecule. This is based on the predictions made by Pauling of the first step in the transformation of white phosphorus to red phosphorus.[15] This structure has also been synthesised and stabilised in a number of molecular compounds.[57-59] Two variations of this allotrope exist, with the *trans* butterfly formed from face-to-face tetrahedra (therefore, the bond that breaks in

adjacent molecules are on the opposite sides to one another) and the *cis-trans* as a result of edge-to-edge tetrahedra (therefore, the bond that breaks in adjacent molecules occur on the same side as one another). The ladder structures are formed from more bond-breaking and rearrangement. These are the narrowest structures that phosphorus can adopt whilst each atom retains its trivalency and can be observed as a motif in some of the red phosphorus structures, as shown in Figure 3.1.[12, 60, 61] Finally, the single zigzag chain is formed from the complete breakage of the tetrahedra and is the only structure which has free valencies, as only two bonds are needed to construct the structure.

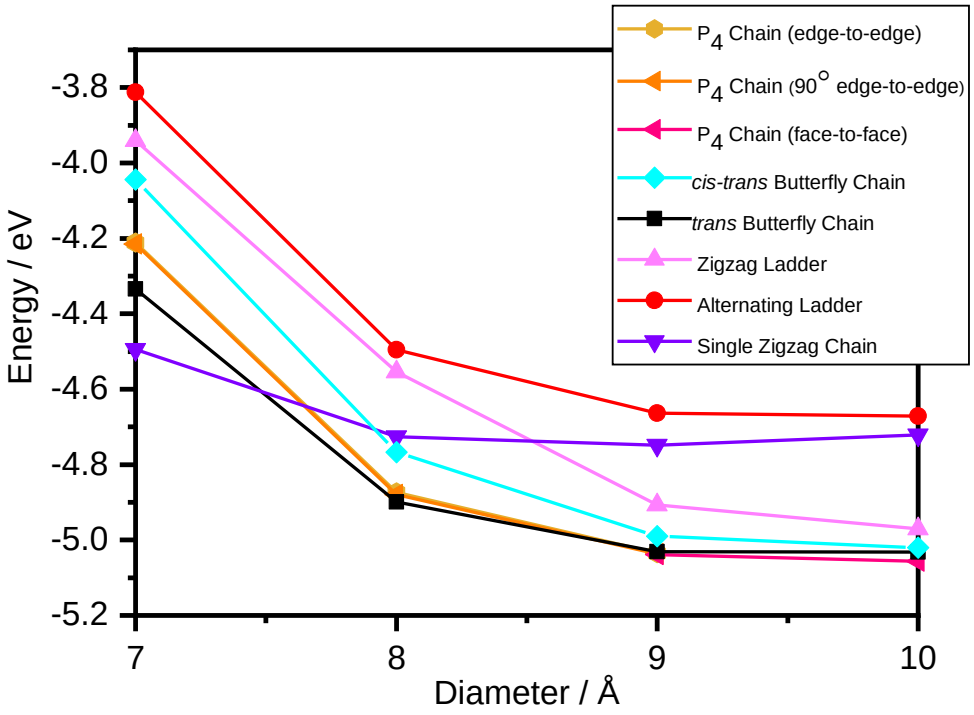

Figure 3.14 DFT analysis of confined phosphorus structures. Energies of the structures, shown in Figure 3.12, as a function of the nanotube diameter. Energy is defined as the per-atom binding energy relative to an isolated phosphorus atom plus the confining energy. Calculations performed by Ji Chen.

The DFT analysis reveals that the *trans* butterfly structure is the most stable allotrope when confined. The various tetrahedral chains are also very similar in energy, which is not surprising given the similarities of the structures. The alternating ladder is never low in energy, especially compared to the zigzag ladder. It can be reasoned that if this type of structure is observed within a SWCNT that it will most likely be the zigzag ladder and not the alternating ladder due to its much higher energy. The zigzag ladder though is only relatively stable at the larger diameters, and is not expected to be a preferred structure below 9 Å. Conversely, the single zigzag chain only becomes the most preferred

structure at the narrowest of diameters. Only at these diameters will the phosphorus atoms be able to maintain only two bonds.

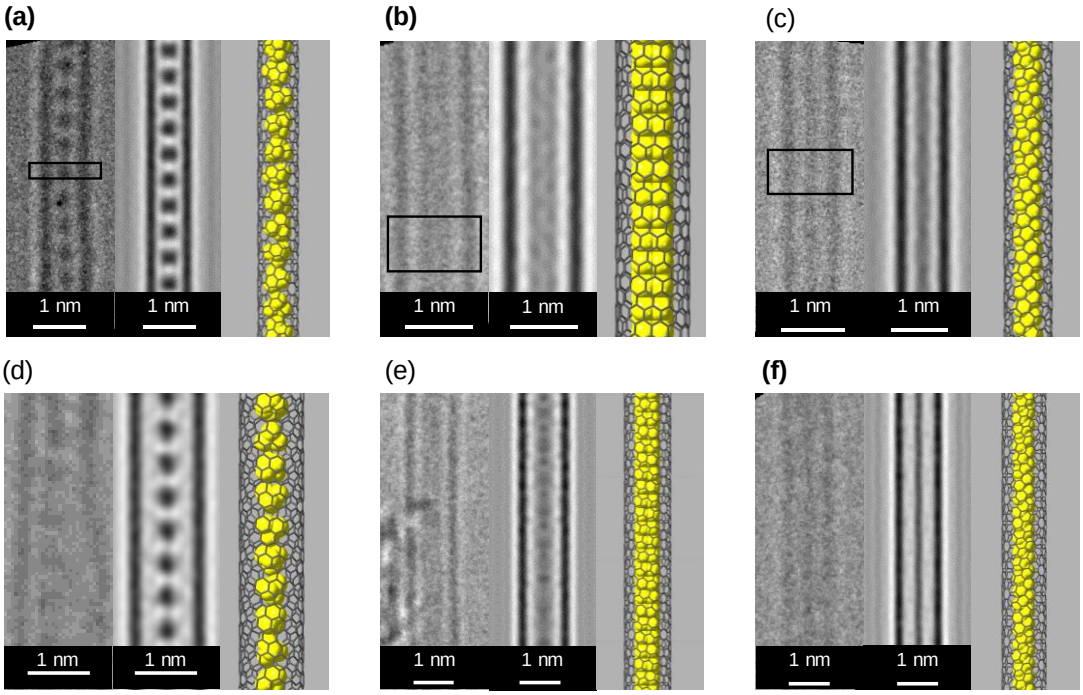

Figure 3.15 A range of structures observed during HRTEM sessions. (a, d) Tetrahedra observed within CoMoCat and HiPCO respectively. (b, e) Zigzag ladders observed within CoMoCat and HiPCO respectively. (c, f) Single zigzag chains observed within CoMoCat and HiPCO respectively. Areas marked in (a), (b) and (c) show the regions taken for the line profiles in Figure 3.16.

Figure 3.15 shows that the confined phopshorus could adopt the same structures within the different SWCNTs. This is not at all surprising given the range of diameters that each SWCNT type possesses. Tetrahedra, zigzag ladders and single zigzag chains were all observed within the SWCNTs.

In order to help identify the types of structures observed, line profiles taken across the nanotube were taken. Although the tetrahedra were quite easy to observe, the differences between the zigzag ladder and single zigzag chain could be subtler. Figure 3.16 shows the line profiles. The zigzag ladder shows a characteristic gap caused by the two parallel phosphorus chains. This feature helped identify the zigzag ladder structure. The gap showed an average value of 0.236 nm ± 0.03 nm for the *m*-P@CoMoCat sample and 0.266 nm ± 0.07 nm for the *m*-P@HiPCO sample. Plotting this gap as a function of diameter, Figure 3.17 (a), showed a slight trend for the gap to widen as the nanotube diameter increased which shows how flexible the filling material is at adopting a structure that fits within the cavity the best. The calculated structure shows a slight increase of gap size but not to the same degree as observed. This perhaps shows some

of the limitations of this method of DFT simulated structures, such as not taking into account exposure to an electron beam.

No trend could be observed for the tetrahedral repeat unit distance as a function of nanotube diameter, Figure 3.17 (b). It seems clear, though, that the repeat distance for the CoMoCat filled samples had a smaller repeat distance than the HiPCO samples. The DFT calculated repeat distance shows a downward trend. This is caused by the molecules being able to move laterally due to the larger diameter nanotube and therefore can get closer together.

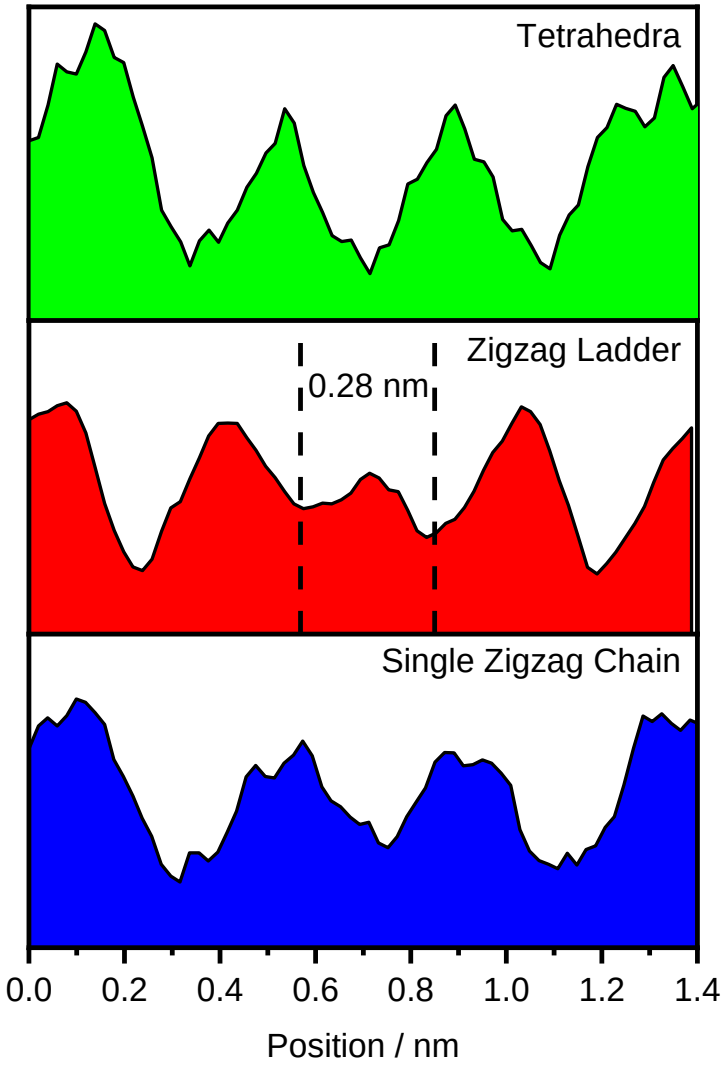

Figure 3.16 Line profiles taken of the m-P@CoMoCat sample in Figure 3.15 showing the differences between the tetrahedra (from Figure 3.15 (a)), zigzag ladder (from Figure 3.15 (b)) and the single zigzag chain (from Figure 3.15 (c)). The zigzag ladder shows a characteristic gap created by the two parallel chains.

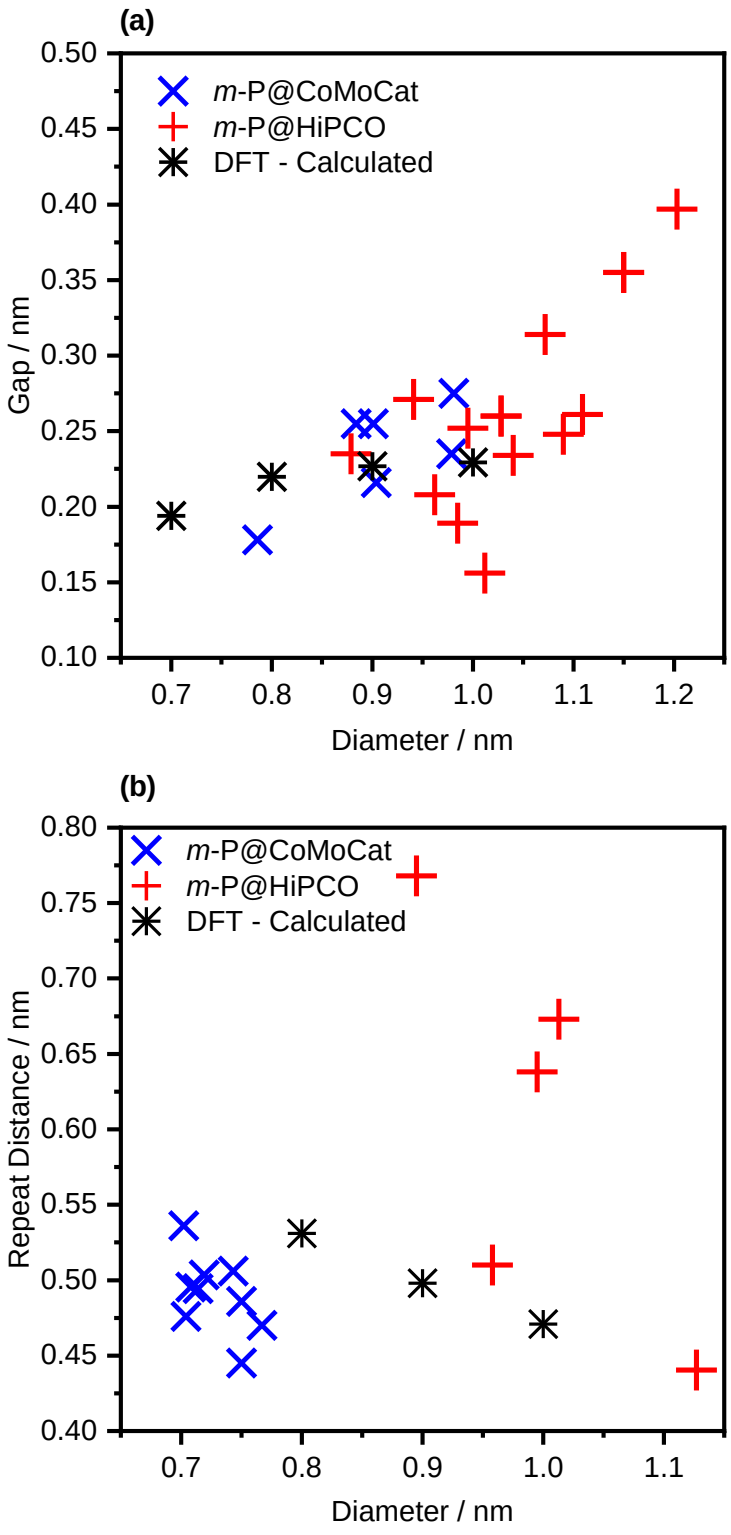

Figure 3.17 (a) Zigzag ladder gap as a function of SWCNT diameter. (b) Tetrahedral unit repeat distance as a function of SWCNT diameter.

Once the structures could be reliably identified, distributions of each type and the nanotube diameter they are observed in could be created, Figure 3.18. The first observation is that the overall distribution of the SWCNTs are what is expected for

CoMoCat and HiPCO SWCNTs. The majority of the SWCNTs recorded are in the 7-9 Å range for WP@CoMoCat compared with 9-11 Å for WP@HiPCO.

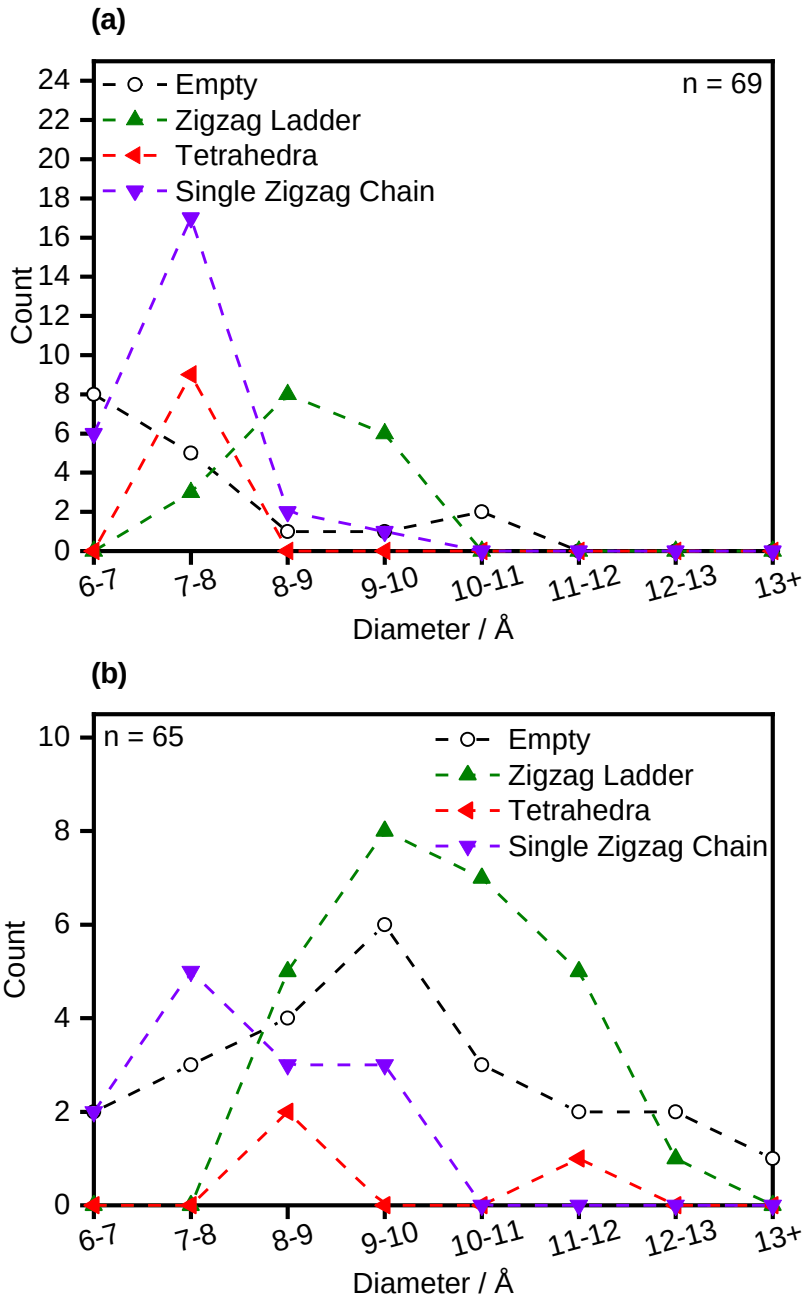

Figure 3.18 Distributions of observed structure against the nanotube diameter for (a) m-P@CoMoCat and (b) m-P@HiPCO.

The nanotube diameter at which each structure will most likely be found is remarkably consistent across both materials. The tetrahedra and single zigzag chains are both most frequently found below 9 Å whilst the zigzag ladder is most commonly found from 9 Å and above. This is also consistent with the DFT results. Overall, 75% of CoMoCat SWCNTs are filled and 65% HiPCO SWCNTs are filled. These values are both greater than what the XPS data has shown, but the distributions do not consider that some sections of the

SWCNT could be empty and that there is an element of luck as to what the HRTEM session reveals at the time.

No evidence of either butterfly structures has been seen, despite the DFT calculations predicting that they are the most preferential structures to be adopted in the medium diameter range. From the simulated image, Figure 3.19(a), the structure shows a blurring of the main bead-like features. It can be hard to discern the differences between the two structures and it is most likely that the tetrahedra are in an equilibrium with the butterfly structure. Nudged-elastic band computational methods, calculated by Ji Chen, have determined that the energy barrier the tetrahedra need to overcome in order to transform into the butterfly structure is only 0.07 eV mol^{-1}. It is entirely possible that exposure to the electron beam during the imaging could cause the structures to dynamically switch between the two. Some entropic factors may also play a part as to why tetrahedra seem to be more favourable which have not been included in the DFT calculations. The tetrahedra are able to rotate about their centre of mass, whereas the chain allotropes can only rotate about the tube axis. This extra freedom of movement will be entropically favoured and hence may result in why the tetrahedra are more frequently observed than the butterfly structures.

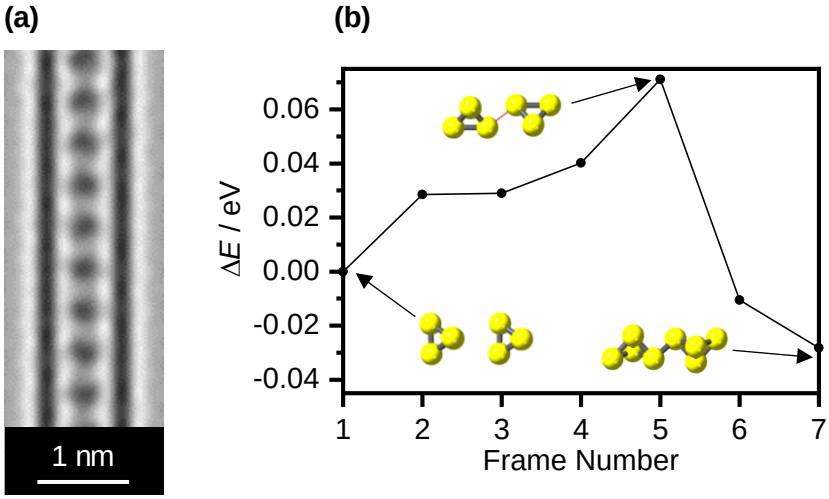

Figure 3.19 (a) Rotationally averaged simulated image of the butterfly structure confined within a 0.9 nm SWCNT. (b) Nudged-elastic band calculations showing the relative energy differences between the P_4 face-to-face starting structure and butterfly ending structure showing the optimum reaction pathway between both.

More evidence that the confined structures are rotating can be seen from the stills of the simulated structures in Figure 3.20. The stills show fine features and extra details that are not observed in the micrographs themselves. Figure 20 (a) clearly shows the orientation of each tetrahedral unit. The micrographs depict spherical units which can

only be obtained from their rotation. Figure 3.20 (b) and (c) show that unless the internal structure is in a certain orientation to the electron beam, the structures will appear to have a very defined zigzag characteristic which again has never been observed. The chances that the confined materials are always in this orientation whilst being imaged is very low, and it is much more likely that the structures are rotating which can be confirmed by the simulated images in Figure 3.15 which give the best comparison to the micrographs.

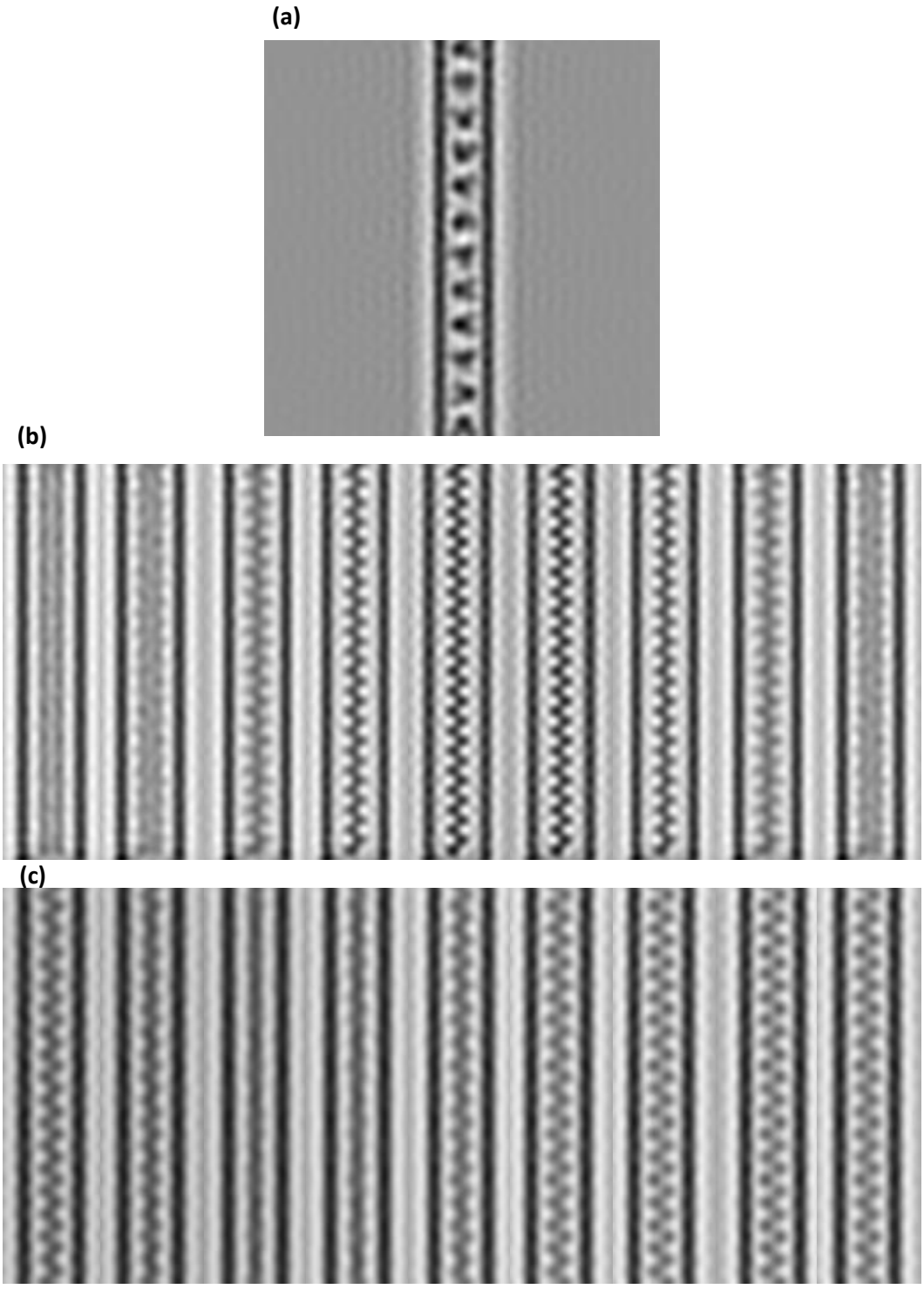

Figure 3.20 (a) Individual frame of unrotated confined tetrahedra. (b) Frames from 0°-160° of every 20° rotation for the confined zigzag ladder structure. (c) Frames from 0°-160° of every 20° rotation for the confined single zigzag chain structure.

An example of the dynamic behaviour of the phosphorus filling material can be seen in Figure 3.21. A series of images show how the chain is excited by the electron beam and causes the chain to split from one strand (Figures 3.21 (a-b)) into two strands in Figure 3.21 (c). The strands remain separate for a few images and then look to recombine in

Figure 3.21 (f). This is reminiscent of behaviour seen in iodine filled nanotubes which explicitly show strands of iodine wrapped around each other.[62]

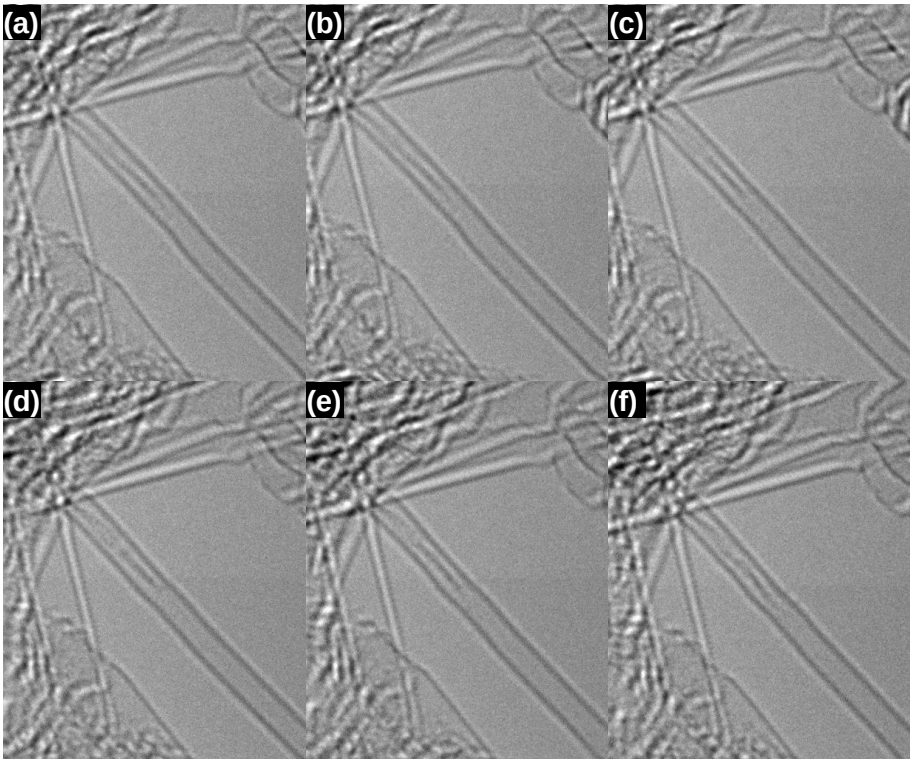

Figure 3.21 A series of images showing the dynamic behaviour of the confined phosphorus chain. (c) The chain splits into two chains. (f) The strands recombine into one chain again.

3.4.3 Further Characterisation of the narrow filled SWCNTs

Further characterisation has been completed in order to draw further comparisons between the two materials.

Similarly, to the Tuball filled sample, there were concerns of any external material coating the SWCNTs being detected. PXRD, Figure 3.22, of the two materials shows a very similar result with no external crystalline material detected. This further confirms the assertion that external material will combust to form an oxide which will either be washed away or may linger in small amounts either between SWCNTs or at the tips.

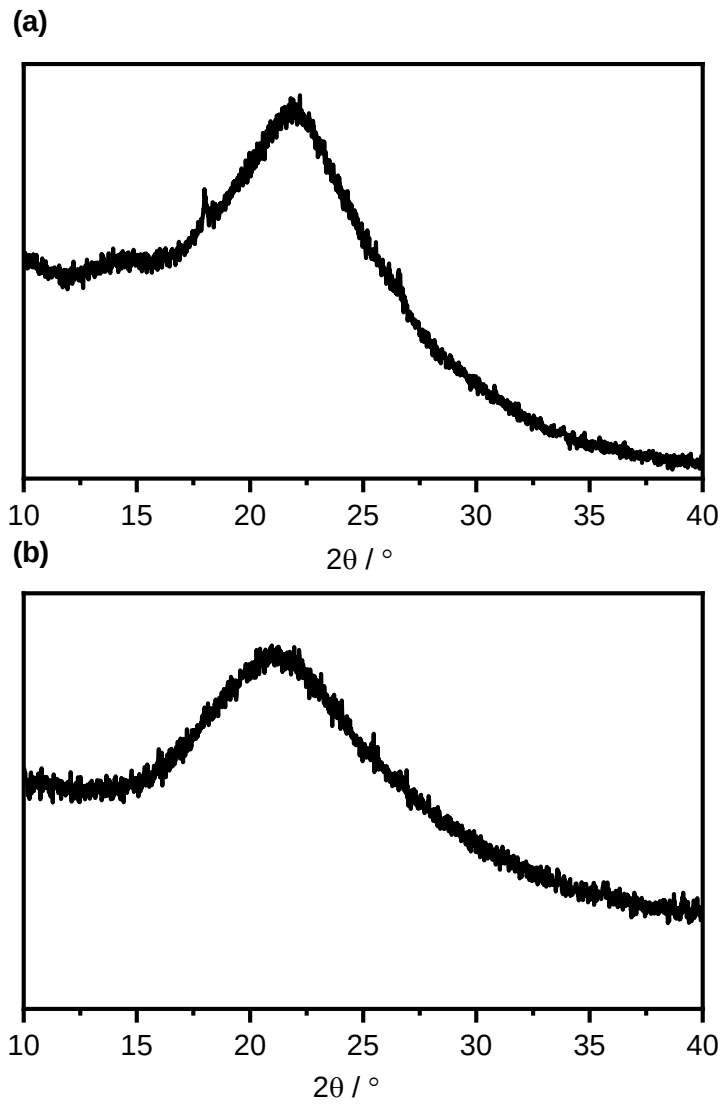

Figure 3.22 (a) PXRD of m-P@COMoCat. (b) PXRD of m-P@HiPCO.

The thermal characteristics of the CoMoCat and HiPCO filled samples, Figure 3.23, gave a similar result to that of the Tuball material. TGA/DSC scans show an exothermic feature accompanied by a mass increase caused by the leakage and then oxidation of the internal material. For the CoMoCat sample, this event occurs at 323 K, with two smaller features at 383 K and 473 K caused by further oxidation of either some red phosphorus formed or from any phosphorus being shielded by oxide formation. Analysis of this exothermic region shows that -2.77 J mg^{-1} of energy is released. The combustion enthalpy of white phosphorus is given as -23.98 J mg^{-1},[63] meaning that the sample is filled with 11.6 wt% from this analysis. This is in very good agreement with the filling yield obtained from XPS of 9.5 wt%. At 573 K the carbon begins to burn as shown by the mass decrease and small exotherm.

Analysis of the HiPCO sample shows that the main exothermic event begins at 396 K. The exotherm is much broader than observed for the CoMoCat sample and the mass increase is not as large. Analysis of this feature reveals that only 2 wt% of the sample is comprised of phosphorus, which is vastly different from the XPS data. The sample may have deteriorated between collecting the XPS and TGA data. The carbon burned at 853 K, which is a higher temperature than observed for the CoMoCat sample. This is due to the slightly larger diameter range of HiPCO SWCNTs making them slightly more resilient to oxidation.

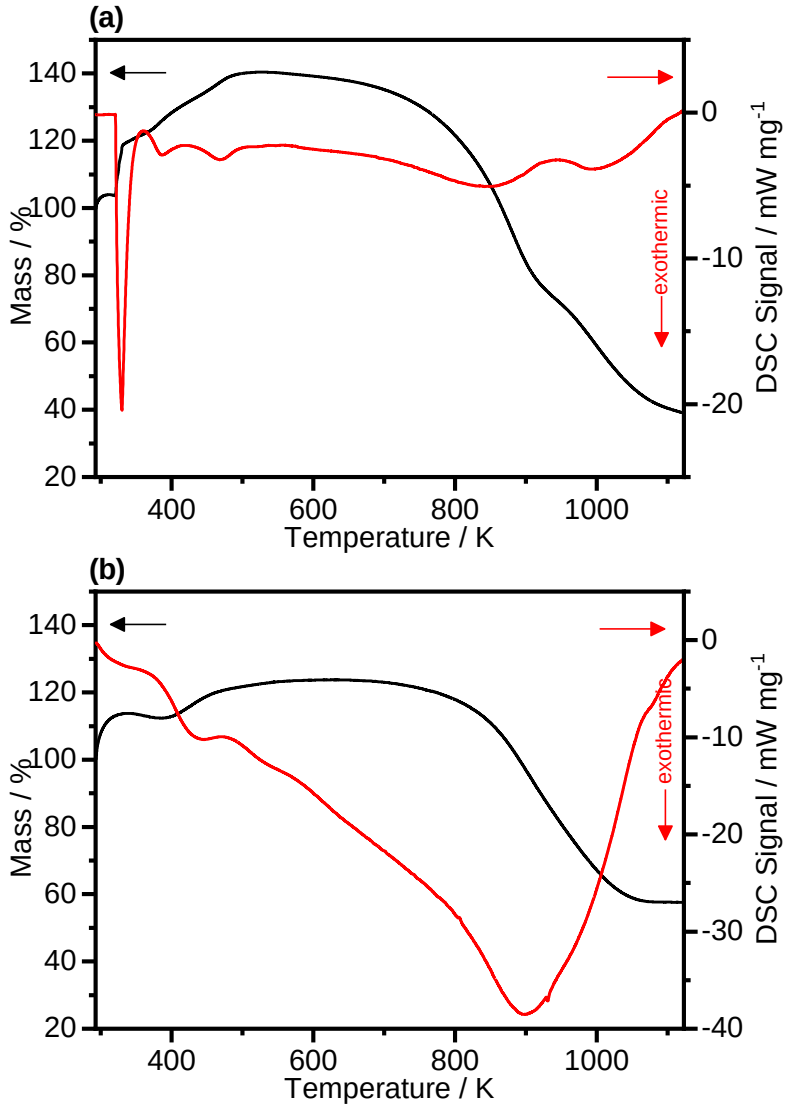

Figure 3.23 (a) TGA/DSC scan of m-P@CoMoCat. (b) TGA/DSC scan of m-P@HiPCO.

Raman spectroscopy of the *m*-P@CoMoCat sample in Figure 3.24 revealed very similar behaviour to the *m*-P@Tuball sample. Blue shifts of the G-band occurred when the sample was illuminated with the 785 nm and 633 nm lasers which is caused by charge

transfer from the SWCNT to the filling material, or more likely caused by electron holes created by phosphorus oxides. The 514 nm laser showed a red shifted G-band which is what would have been expected for this sample. This perhaps shows the heterogeneity of the sample. XPS has showed variable filling across the sample and the Raman has also shown some variation in the G-band position between the spots analysed. One laser shows a differing result that could be due to hitting areas of the sample with low amounts of oxide present which would not compete with the charge transfer from the sample to the SWCNT. No peaks associated with P_4 molecules could be detected either.

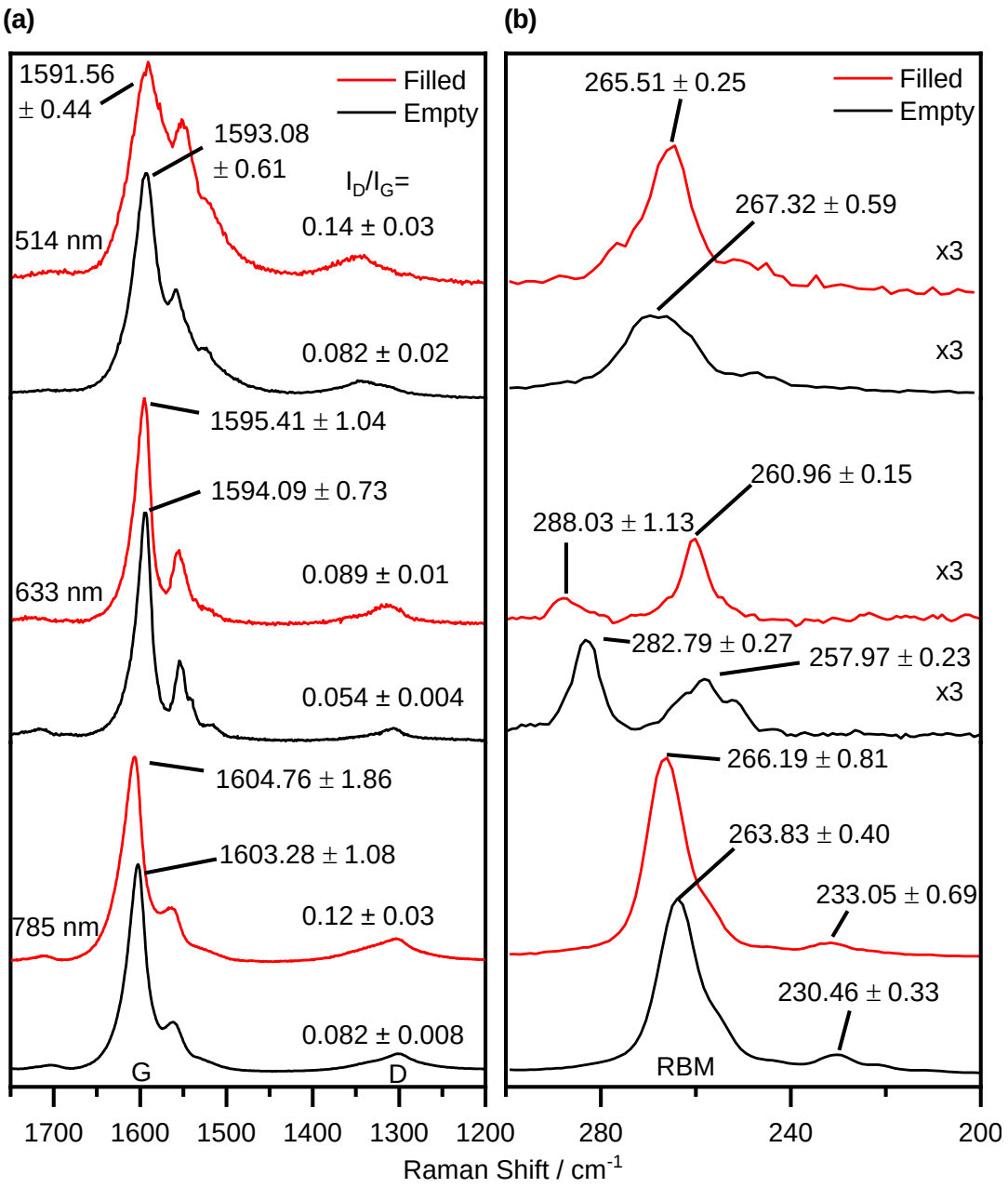

Figure 3.24 Raman spectra of m-P@CoMoCat and empty SWCNTs showing the (a) G and D bands and (b) the radial breathing modes when excited by 514 nm, 633 nm and 785 nm lasers. The spectra are normalised with respect to the G band and shifted vertically for clarity. Average values for the G band, D band, RBM and D/G band ratios have been calculated from the average of 5 spots.

XPS can also reveal if charge transfer has occurred. The fit of the carbon 1 s region can reveal if any of the contributing regions have shifted which can indicate if charge transfer has occurred.[54] A small shift in the C(0) region can be detected between the empty and filled samples as shown in Figure 3.25. The average position of this peak is 284.01 eV and 284.17 eV for the empty and filled sample respectively, which shows that there is some slight donor doping behaviour from either the filling or external material to the

SWCNT, converse to the Raman findings.[54] Additionally, the peaks have the same shape, with no broadening or narrowing seen for the filled sample to signal the increased semi-conducting or metallic behaviour of the SWCNTs.

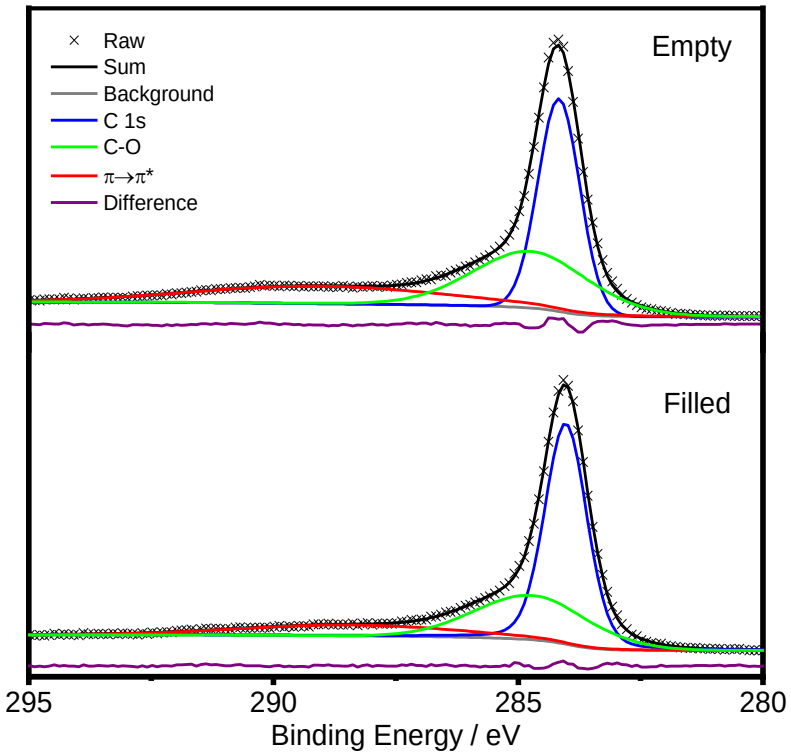

Figure 3.25 High-resolution XPS spectra of the C 1s region for both empty SWCNTs and the m-P@CoMoCat sample.

Figure 3.26 shows the Raman result for the *m*-P@HiPCO sample, and yet again the G-band has undergone blue shifts and no P_4 modes have been detected either. The presence of the oxide seems to be dominating the Raman behaviour. However, as discussed above, the filling material is very sensitive and can form a variety of structures when excited. These structures will have different electronic structures and so will dope the SWCNT in different ways. The band gaps of the various structures, Figure 3.28, have been calculated from their electronic density of states (Figure A.32) and reveal that the phosphorus allotropes range from semi-conducting to metallic depending on the degree of polymerisation. The two P_4 chain structures are semi-conducting, with band gaps of 2.60 eV and 2.54 eV for the face-to-face and edge-to-edge (90°) structures respectively, as expected for individual molecules. The band gap drops dramatically when the *trans* butterfly structure is formed. The bond created to link the adjacent broken tetrahedral molecules brings the molecules much closer together and will help with electron hopping between the molecules. The zigzag ladder has a small band gap and then the alternating zigzag ladder and single zigzag chain have metallic behaviour. Considering

the evidence of dynamic behaviour of the filling material when illuminated by the electron beam it would be very tricky to determine which structures the laser could induce during the measurement so predicting the expected G-band shift, whilst taking into account the phosphorus oxide present as well, may in fact be a futile exercise.

High-resolution XPS spectra in Figure 3.27 shows that again there is very little difference between the empty and filled sample. With average positions of 284.46 eV and 284.51 eV for the filled and empty respectively, no significant shift has occurred which corroborates the findings from the Raman spectroscopy.

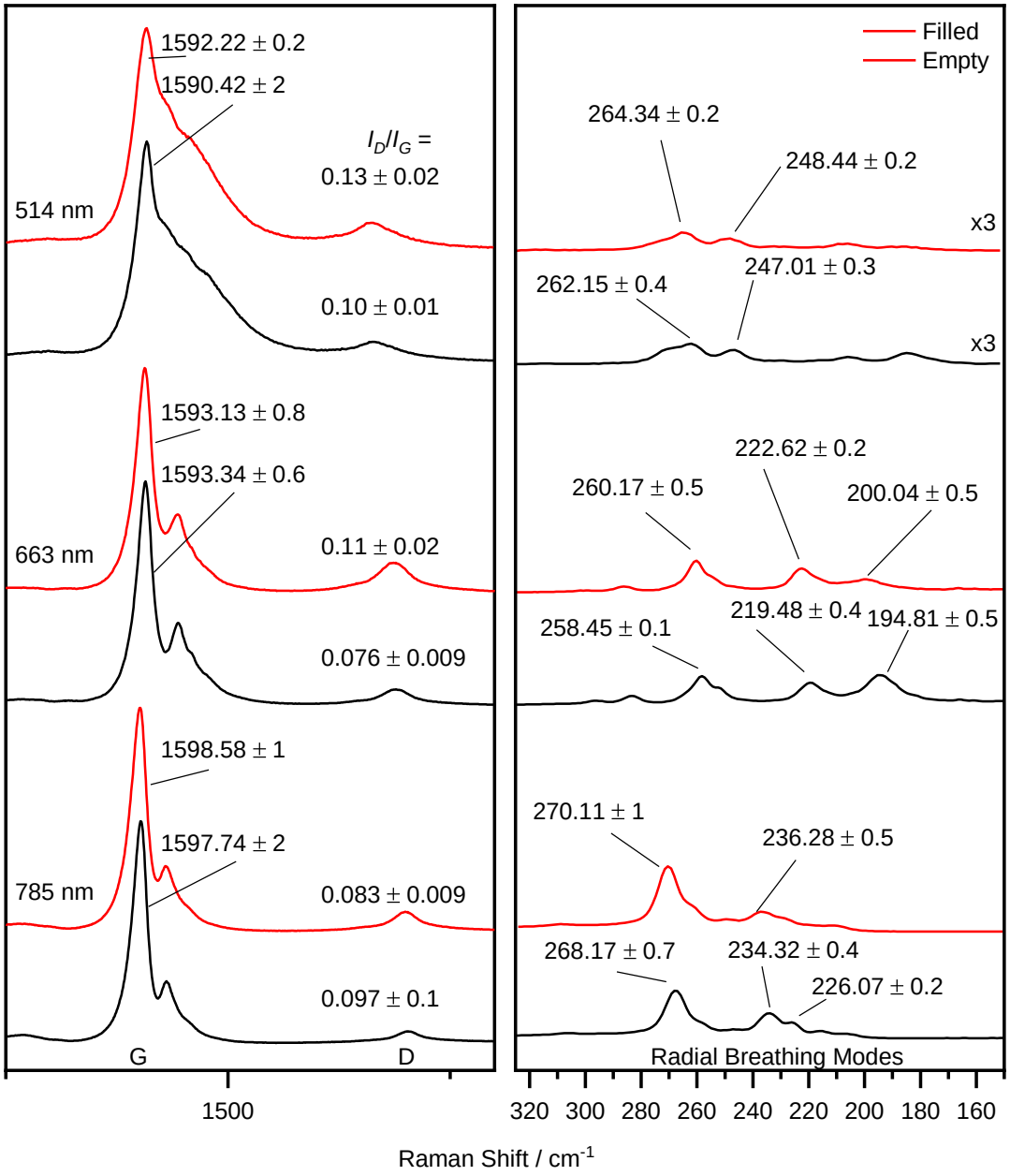

Figure 3.26 Raman spectra of m-P@HiPCO and empty SWCNTs showing the (a) G and D bands and (b) the radial breathing modes when excited by 514 nm, 633 nm and 785 nm lasers. The spectra are normalised with respect to the G band and shifted vertically for clarity. Average values for the G band, D band, RBM and D/G band ratios have been calculated from the average of 3 spots.

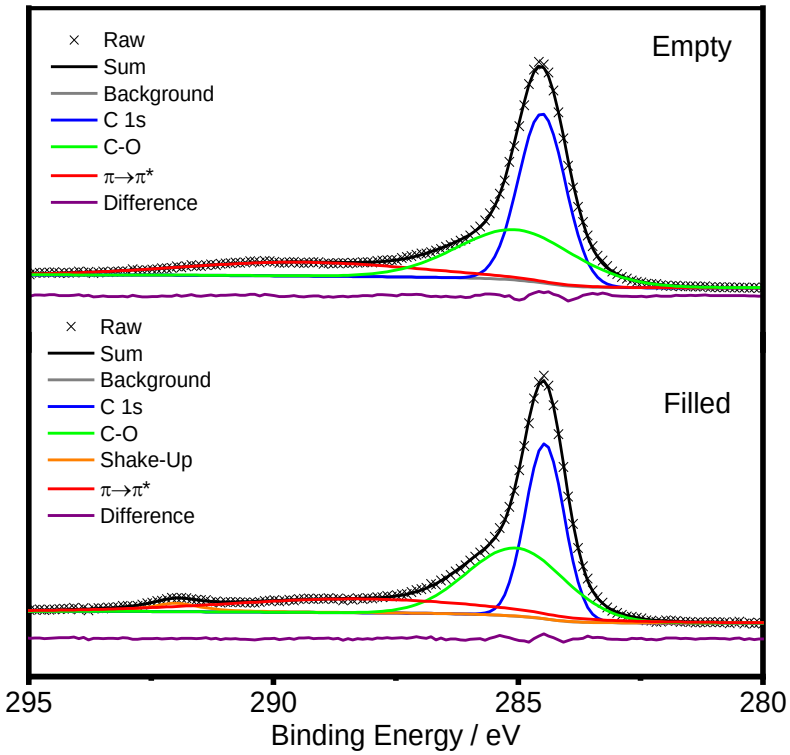

Figure 3.27 High-resolution XPS spectra of the C 1s region for both empty SWCNTs and the m-P@HiPCO sample.

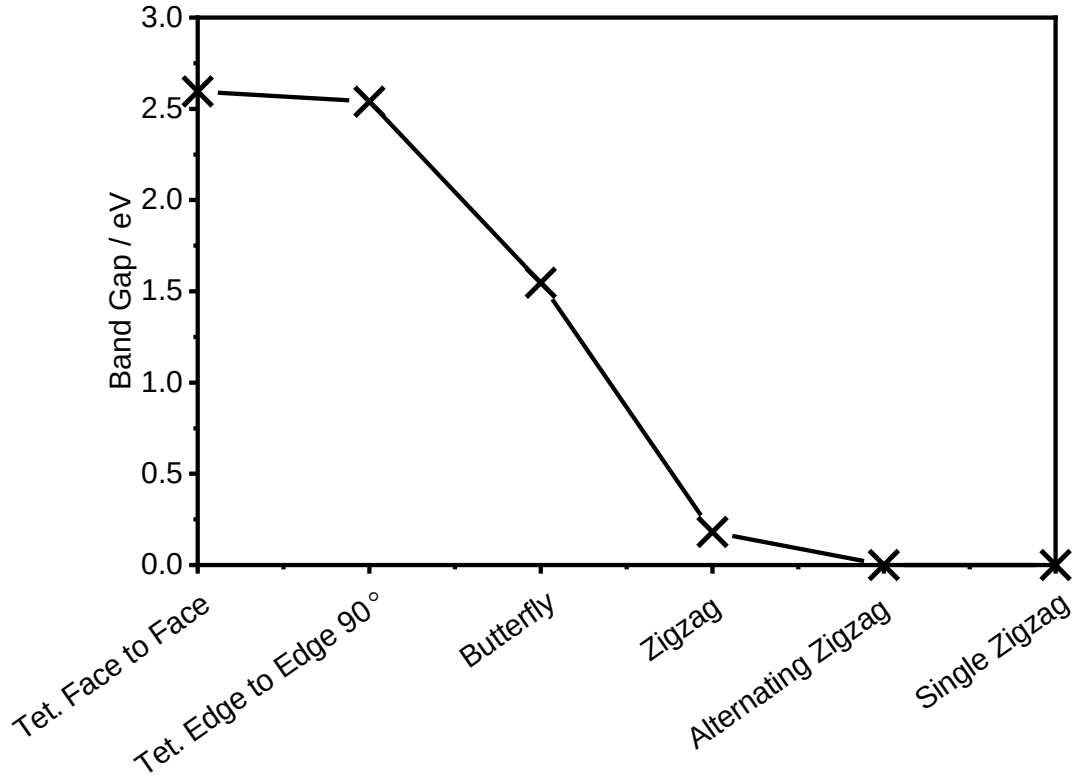

Figure 3.28 Band gaps of the potential structures of the filling materials generated from Density of States calculations performed by Ji Chen.

3.5 Comparisons between Liquid-Phase Filling and Vapour-Phase Filling

So far, a liquid-phase filling procedure has been employed. One of the first general papers of how to fill nanotubes advocates for this method due to the ability to agitate the SWCNT material during the filling process.[64] The low melting point of white phosphorus and the ability to stir the sample during the filling process were very appealing traits for employing this method (putting aside the ridiculous idea of working with molten white phosphorus in the first place!). However, there is an alternative way of creating P_4 molecules. Phosphorus vapour is comprised of P_4 molecules; at higher temperatures both P_2 diatoms and P atoms can be obtained.[7] Using red phosphorus as the feedstock and employing more conventional filling techniques, a comparison between the two methods could be examined. SWCNTs have been filled in this method previously,[37, 39, 41] however, the characterisation of these materials leaves much to be desired, (some samples showing no evidence of elemental phosphorus at all) and most importantly, no evidence of tetrahedra were found![39]

The main difference between the two methods is that the vapour phase filling is performed in an ampoule and conducted at much higher temperatures. The ampoule

contains a ground SWCNTs and red phosphorus mixture and is heated in a tube furnace to 500°C for 12 h. This process is repeated 3 more times, each time rotating the ampoule to allow the phosphorus material to move across the SWCNTs and fill them. The crude material is purified by bubbling air through the sample whilst submerged in water whilst stirring, the same way in which the *m*-P@CNT samples were purified. Full details can be found in Chapter 2.

Both CoMoCat and HiPCO SWCNTs were investigated and similar techniques were used to fully characterise the materials. These samples will be referred to as *v*-P@CoMoCat and *v*-P@HiPCO respectively.

3.5.1 Filling Yield Results

Figure 3.30 shows the filling yields achieved for the new materials, and also includes the filling yields for all the previous materials for comparison. Immediately it can be seen that the vapour phase method has produced the highest filling yield sample. The *v*-P@HiPCO sample contains 14 wt% elemental phosphorus which is double the amount achieved when a melt phase procedure is used. From the filling yield estimates in Figure 3.12, the sample is almost 75% fully filled! The ratio of oxide to elemental material is also superior. It is reasoned that the vapour coats the SWCNTs in a finer layer of phosphorus than when submerged in the melt. Figure 3.29 shows that the ampoule and SWCNTs are coated with the phosphorus vapour, so less is needed to be removed and makes for a purer product.

Figure 3.29 Crude schematic of the SWCNTs within the ampoule during the filling process. The phosphorus coats not only the SWCNTs but also the ampoule wall.

The same cannot be said about the CoMoCat sample. It has achieved only 1.5 wt% phosphorus filling, which is calculated as only 7.5% filled. This result is unexpected as the CoMoCat SWCNTs showed good filling yields when exposed to the molten white phosphorus. Potentially, the narrowness of the SWCNTs coupled with the lower exposure to P_4 molecules in the vapour (when compared to being submerged within the melt) has led to a much lower filling yield than expected.

Due to the poor filling of the *v*-P@CoMoCat sample, the rest of this chapter will focus on the *v*-P@HiPCO sample in comparison with the other phosphorus filled SWCNTs.

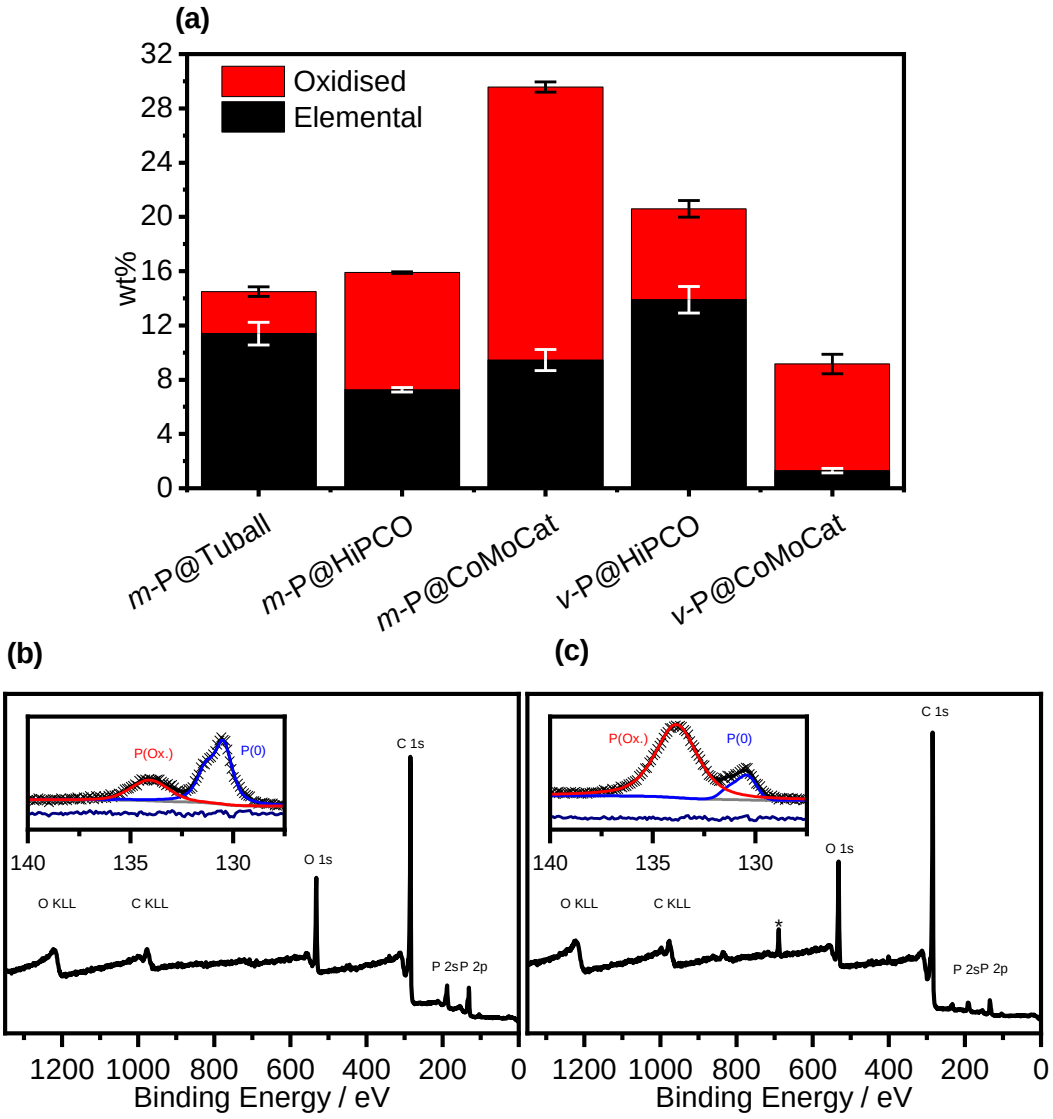

*Figure 3.30 (a) Comparative filling yields for all phosphorus filled SWCNT samples. Filling yields calculated from the fitted XPS spectra in the insets of (b) and (c). (b) Survey and high-resolution XPS spectra (inset) for v-P@HiPCO. (c) Survey and high-resolution XPS spectra (inset) for v-P@CoMoCat. *Impurity present in (c) caused by fluorine.*

3.5.2 Microstructure

HRTEM images in Figure 3.31 once again show the same three structures appearing for the *v*-P@HiPCO sample. The distributions of the structure type, though, are much more interesting. The distributions, Figure 3.31 (d), reveal that 78% of the SWCNTs show evidence of filling. The filling yield for this sample is almost 15 wt%, and is therefore 75% full based on the filling yield predictions. The tetrahedral and single zigzag chains appear consistently across all diameters, unlike in the melt samples which showed a preference for appearing in the smaller diameters. The zigzag chain dominates, with over 65% of the SWCNTs filled with this structure. The increased occurrence of this structure is thought to be caused by the filling procedure. The white phosphorus samples

are never exposed to temperatures higher than 323 K and are held at this temperature for only a few hours during the filling and sublimation steps. The red phosphorus sample is held at 773 K for a total of 24 h during the rotations of the ampoule. It is likely that the tetrahedra will convert to the other structures during this process. The exposure of the sample to high temperatures during the synthesis procedure may also partially anneal some of the nanotubes, which may also help prevent leakage during the experiment and help maintain the high filling yields.[65] More examples of filled nanotubes can be found in Figure 3.33.

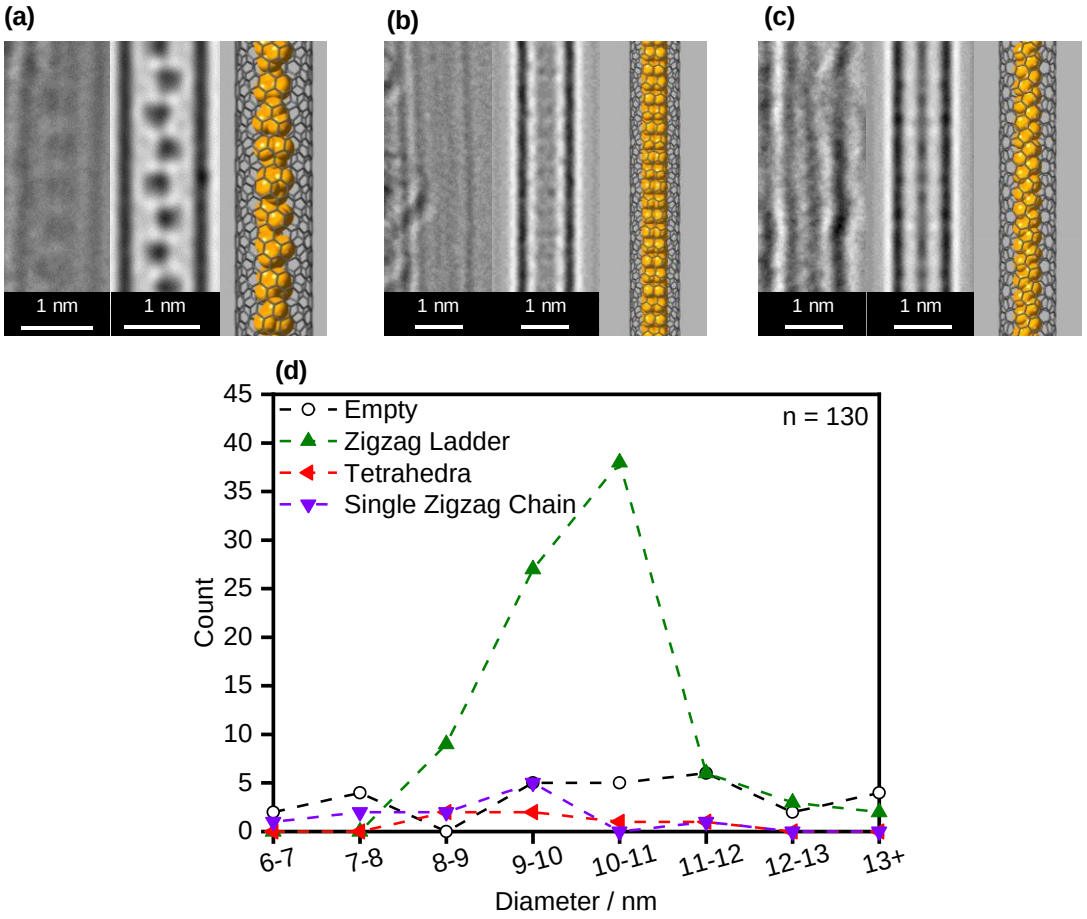

Figure 3.31 The same group of structures observed in the m-P@CoMoCAT and m-P@HiPCO samples have also been observed within the v-P@HiPCO sample. (a) Tetrahedral molecules confined within HiPCO. (b) Zigzag ladder and (c) the single zigzag chain. (d) Distributions of the three structures as a function of tube diameter.

The average gap of the zigzag ladder is 0.252 nm, firmly between the gaps recorded for the melt filled samples. There seems to be little correlation between the gap and the diameter of the nanotube with most of the values grouped around the average, Figure 3.32 (a). The average repeat distance for the tetrahedra is 0.582 nm, which is comparable to the values observed for the melt filled samples as well. No correlation could be observed for the repeat distance against the nanotube diameter.

Table 3.1 Average values for the zigzag ladder gap and tetrahedral repeat distances measured for the various samples.

Sample	Zigzag Ladder Gap / nm	Repeat Distance / nm
***m*-P@CoMoCat**	0.236	0.490
***m*-P@HiPCO**	0.266	0.606
***v*-P@HiPCO**	0.252	0.583

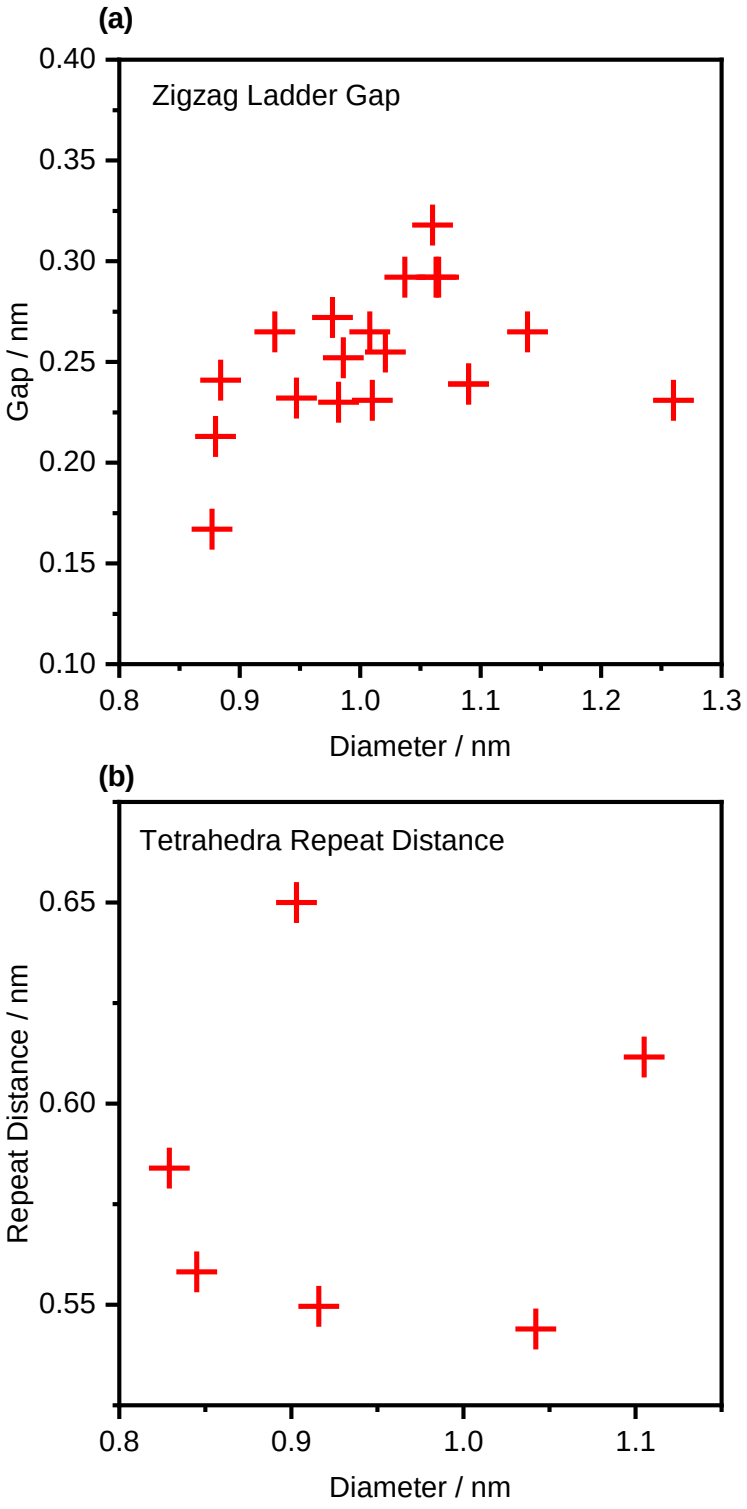

Figure 3.32 (a) Zigzag ladder gap as a function of SWCNT diameter for the v-P@HiPCO sample. (b) Tetrahedral unit repeat distance as a function of SWCNT diameter for the v-P@HiPCO sample.

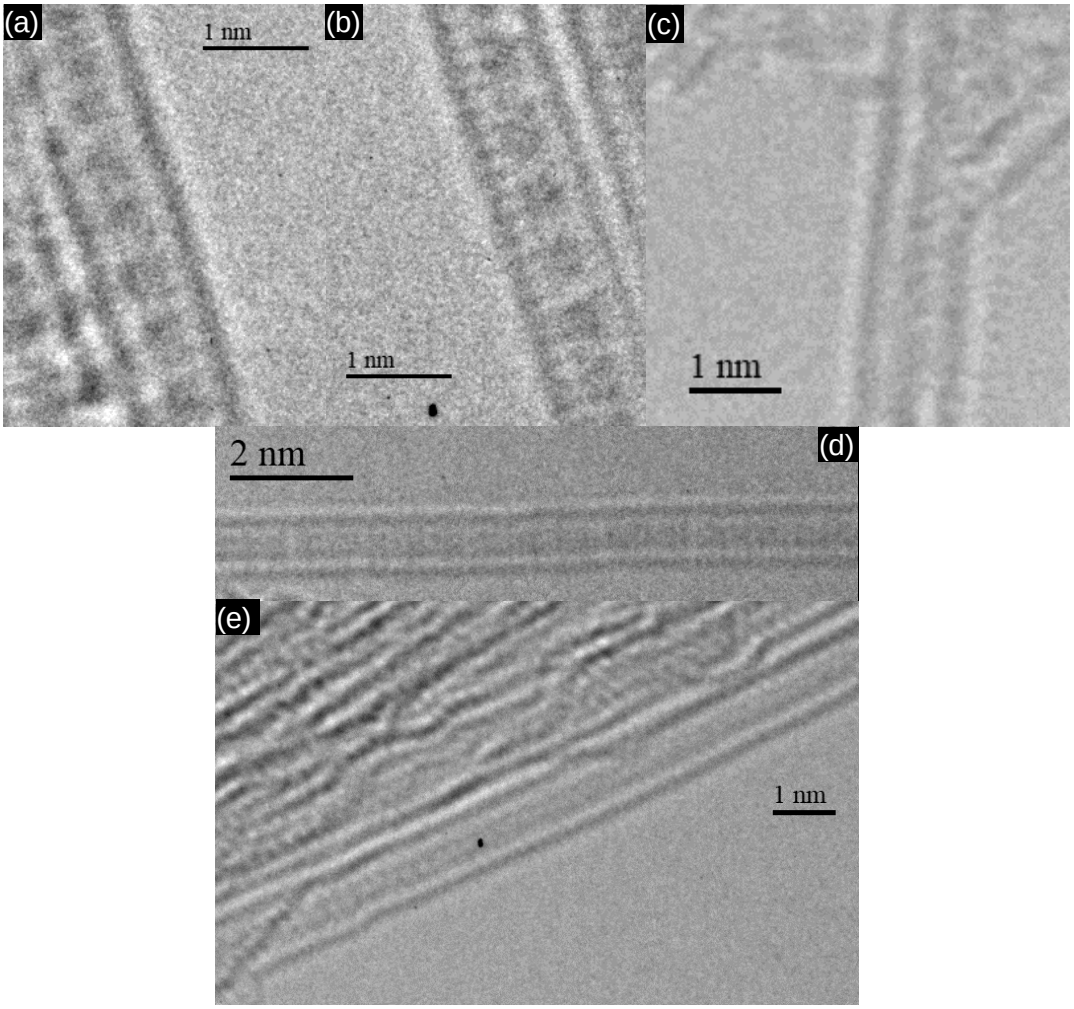

Figure 3.33 Additional examples of the structures confined phosphorus can adopt within HiPCO SWCNTs. (a-b) Tetrahedra, (c) single zigzag chain and (d, e) zigzag ladders.

3.5.3 Further Characterisation

PXRD, TGA and Raman have all been conducted to complete our understanding of this material.

PXRD, Figure 3.34, shows that no external phosphorus material could be detected. The small peak at 2θ=26.7° is caused by some residual graphite that has persisted through the purification of the SWCNTs.[55]

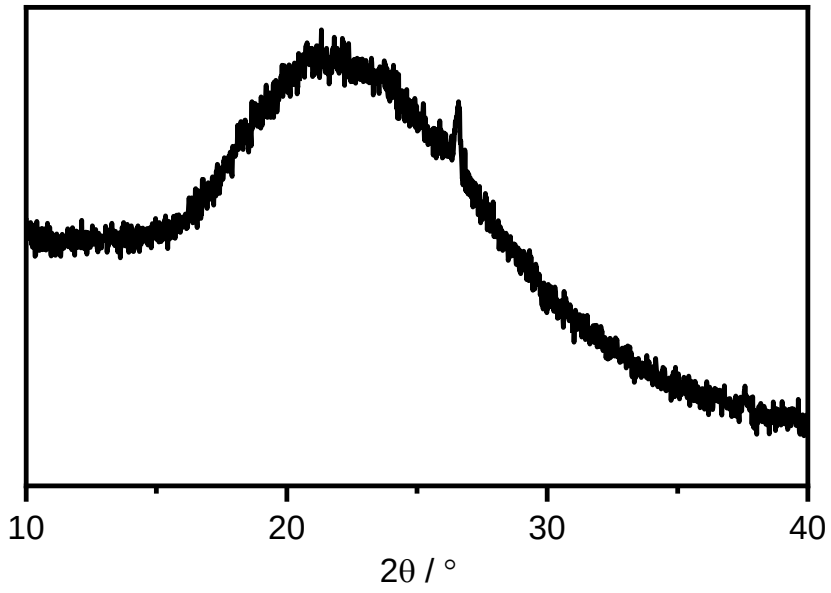

Figure 3.34 PXRD of v-P@HiPCO.

The TGA/DSC scan in Figure 3.35 gave an unexpected result based on the observations from the previous samples. No sharp exotherm can be seen at around 323 K. Instead, the scan shows a broad feature, starting at 543 K and ending at 643 K, coupled with a gradual mass increase which is most likely caused by the delayed leakage and oxidation of the internal phosphorus material. There are a couple of explanations that may clarify this result. The first is that any annealing of the SWCNTs that may have occurred during the filling procedure has prevented the phosphorus from leaking out. Once some of the tips have burnt away, the phosphorus can leak out and oxidise. The carbon burning would normally happen at slightly higher temperatures though, somewhere in the region of 673-773 K which makes this theory less likely.[66] A more probable idea is that the phosphorus within the SWCNTs is not in the form of tetrahedra, which would be unexpected to leak out of the SWCNTs at the melting point of white phosphorus and has been observed in the liquid filled samples. The TEM analysis in Figure 3.31 (d) shows an overwhelming majority of polymerised phosphorus structures, thought to be caused by the exposure to elevated temperatures. These structures will need to transform back to tetrahedra before leakage can occur, which seems to start at 543 K based on the thermogram. The white phosphorus filled samples appear to be predominantly filled with tetrahedra and only undergo polymerisation once exposed to the electron beam and hence, when heated to the melting point of white phosphorus, the DSC scan shows such a sharp feature at this temperature.

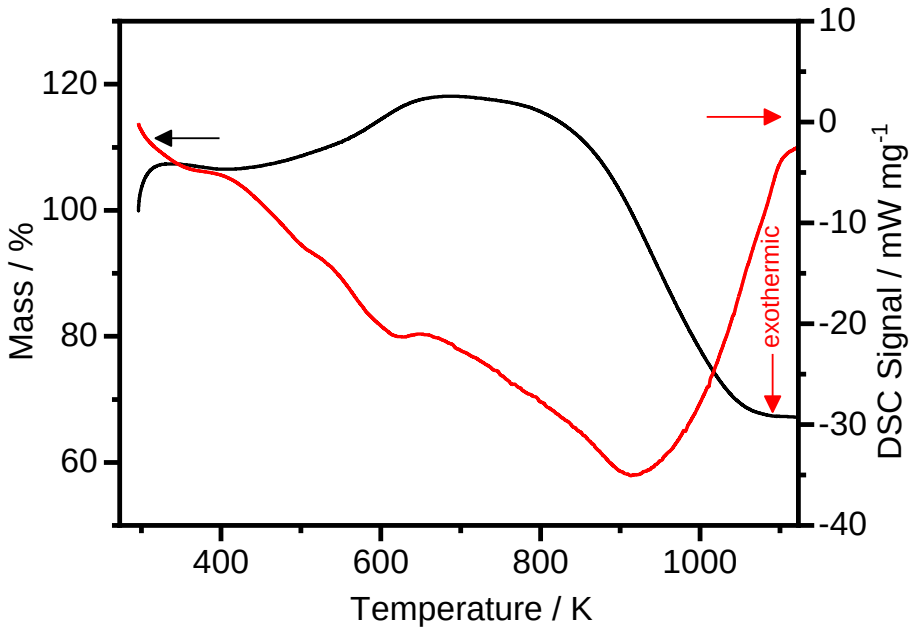

Figure 3.35 TGA/DSC scan of v-P@HiPCO showing a different behaviour to the previous samples. The initial mass increase at the start of the thermogram is caused by buoyancy effects.

Finally, Raman spectra has been collected of the *v*-P@HiPCO sample. The G-bands of the filled samples appear to be in very similar positions compared to the empty sample, with only the 785 nm laser showing the same blue-shifted G-band of the previous samples. The ratio of oxidised to elemental phosphorus is much better for this sample compared to the others which may explain why the blue-shift is less pronounced. The high-resolution spectra in Figure 3.37 reveal C(0) peaks at 284.51 eV and 284.56 eV for the filled and empty samples respectively. This again confirms that no charge transfer has been detected by XPS. With the competing doping properties of the phosphorus oxide present and the various structures that the filling material can adopt, it is probably not surprising that nothing significant has been detected.

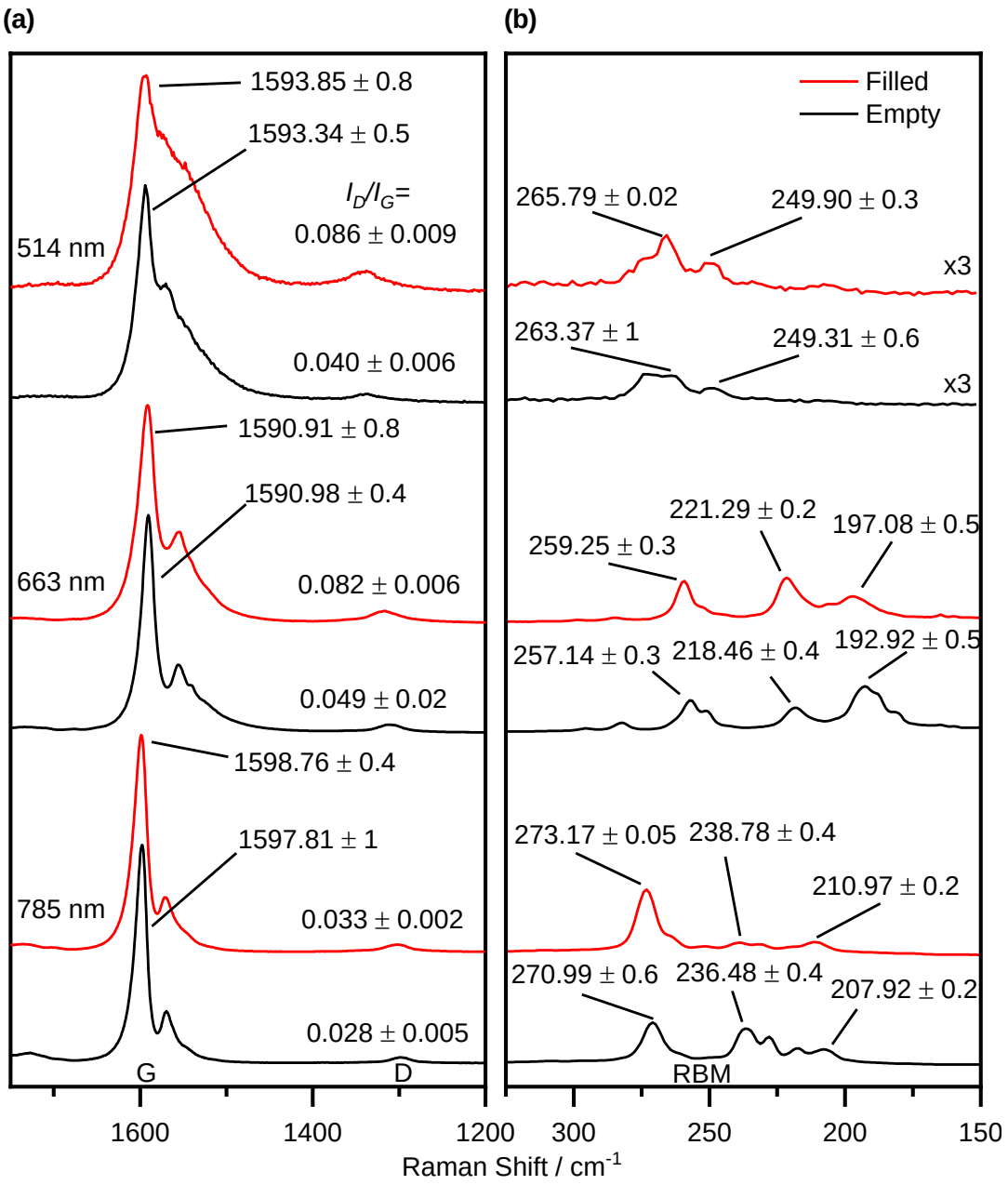

Figure 3.36 Raman spectra of v-P@HiPCO and empty SWCNTs showing (a) the G and D-bands and (b) the radial breathing modes when excited by 514 nm, 633 nm and 785 nm lasers. The spectra are normalised with respect to the G band and shifted vertically for clarity. Average values for the G band, D band, RBM and D/G band ratios have been calculated from the average of 5 spots.

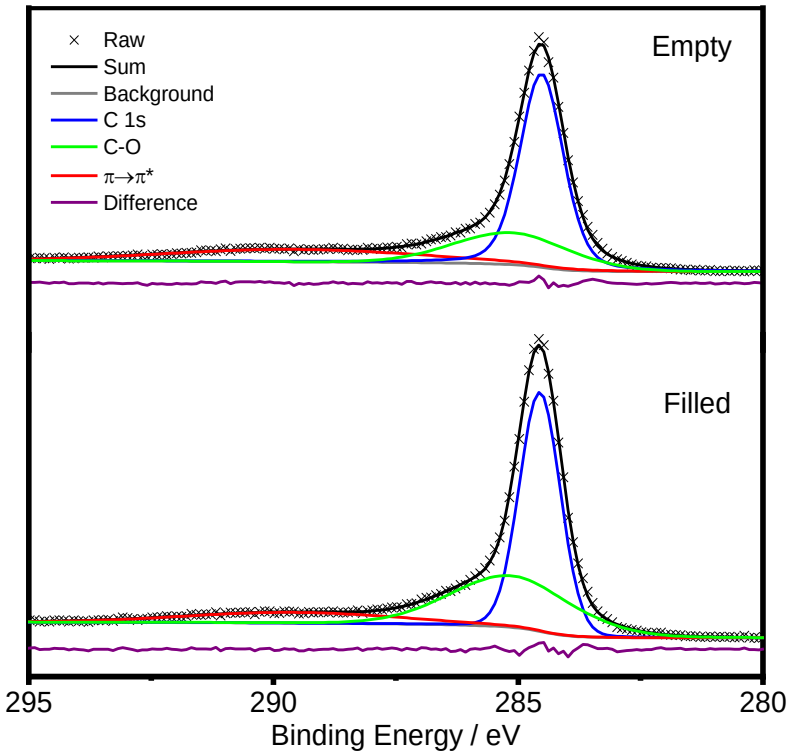

Figure 3.37 High-resolution XPS spectra of the C 1s region for both empty and filled samples.

3.6 Conclusion

In summary, a range of SWCNTs, with differing diameters, have been filled with phosphorus either from the liquid or vapour phase. *v*-P@HiPCO had the highest filling yield of all samples, followed by *m*-P@Tuball and *m*-P@CoMoCat. Rather oddly, the *m*-P@CoMoCat sample showed much more success than the *v*-P@CoMoCat sample, yet the behaviour was not repeated for the *m*-P@HiPCO sample. It is presumed that some annealing of the *v*-P@HiPCO sample, causing the SWCNTs to partially repair and also induce polymerisation of the internal material, prevented the leakage of the filling material during the work-up stages. TGA analysis of this sample seems to confirm this result as no oxidation is seen at 50°C unlike for the melt samples.

TEM has revealed that when the wide diameter nanotubes are filled, large amorphous structures are created within the cavity. The electron beam seams to cause the P_4 molecules to breakdown and form structures which fill the space afforded them by the cavity. The narrower nanotubes all showed the same three structures, tetrahedra chains, zigzag ladders and single zigzag chains regardless of the filling procedure. The distributions of the structures did change though. Although the zigzag ladder dominated, the melt filled samples showed larger amounts of the tetrahedra and single zigzag chain.

The *v*-P@HiPCO sample had a much larger proportion of zigzag ladder structures. The annealing process can account for this as well, as exposure to the high temperatures may induce the polymerisation.

Full characterisation of the samples was completed including PXRD showing no external material was present for any of the samples, with only a little residue graphite present in some of the samples. Raman spectroscopy predominantly showed blue-shifts of the G-bands signifying charge transfer from the SWCNTs to either the filling material, or more likely to the phosphorus oxide coating the walls of the SWCNTs. Similar behaviour has already been reported in the literature before, so at least these results are consistent with the literature.

3.7 References

1. In Their Element. In *Phosphorus, Smoke and Lightning*, Sella, A., Ed. BBC: BBC Radio 4, 2018.
2. Vonschnering, H. G., Homoatomic bonding of main group elements. *Angew. Chem. Int. Ed.* **1981,** *20* (1), 33-51.
3. Boden, N.; Folland, R., Nuclear magnetic spin-lattice relaxation and molecular motion in solid white phosphorus and in liquid phosphorus. *Molec. Phys.* **1971,** *21* (6), 1123-&.
4. Simon, A.; Borrmann, H.; Horakh, J., On the polymorphism of white phosphorus. *Chem. Ber. Rec.* **1997,** *130* (9), 1235-1240.
5. Simon, A.; Borrmann, H.; Craubner, H., Crystal-structure of ordered white phosphorus (beta-p). *Phos. Sulf. Silic. Rel. Elem.* **1987,** *30* (1-2), 507-510.
6. Okudera, H.; Dinnebier, R. E.; Simon, A., The crystal structure of gamma-P-4, a low temperature modification of white phosphorus. *Zeit. Kristal.* **2005,** *220* (2-3), 259-264.
7. Schlesinger, M. E., The thermodynamic properties of phosphorus and solid binary phosphides. *Chem. Rev.* **2002,** *102* (11), 4267-4301.
8. Winchester, R. A. L.; Whitby, M.; Shaffer, M. S. P., Synthesis of Pure Phosphorus Nanostructures. *Angew. Chem. Int. Ed.* **2009,** *48* (20), 3616-3621.
9. Bachhuber, F.; von Appen, J.; Dronskowski, R.; Schmidt, P.; Nilges, T.; Pfitzner, A.; Weihrich, R., The Extended Stability Range of Phosphorus Allotropes. *Angew. Chem. Int. Ed.* **2014,** *53* (43), 11629-11633.
10. Olego, D. J.; Baumann, J. A.; Kuck, M. A.; Schachter, R.; Michel, C. G.; Raccah, P. M., The microscopic structure of bulk amorphous red phosphorus - a raman-scattering investigation. *Solid State Comm.* **1984,** *52* (3), 311-314.
11. Winchester, R. A. L.; Whitby, M.; Shaffer, M. S. P., Synthesis of Pure Phosphorus Nanostructures. *Angew. Chem. Int. Ed.* **2009,** *48* (20), 3616-3621.
12. Ruck, M.; Hoppe, D.; Wahl, B.; Simon, P.; Wang, Y. K.; Seifert, G., Fibrous red phosphorus. *Angew. Chem. Int. Ed.* **2005,** *44* (46), 7616-7619.
13. Pfitzner, A.; Bräu, M. F.; Zweck, J.; Brunklaus, G.; Eckert, H., Phosphorus Nanorods—Two Allotropic Modifications of a Long-Known Element. *Angew. Chem. Int. Ed.* **2004,** *43* (32), 4228-4231.
14. Zhang, J.; Zhao, D.; Xiao, D.; Ma, C.; Du, H.; Li, X.; Zhang, L.; Huang, J.; Huang, H.; Jia, C.-L.; Tomanek, D.; Niu, C., Assembly of Ring-Shaped Phosphorus within Carbon Nanotube Nanoreactors. *Angew. Chem. Int. Ed.* **2017,** *56* (7), 1850-1854.

15. Pauling, L.; Simonetta, M., Bond orbitals and bond energy in elementary phosphorus. *J. Chem. Phys.* **1952,** *20* (1), 29-34.
16. Scherer, O. J.; Swarowsky, M.; Wolmershauser, G., Synthesis and structure of the cobaltatetraphosphatricycloalkanes (eta-5-C5Me5)(CO)CoP4 and (eta-5-C5Me5)2(CO)2Co2P4. *Organometallics* **1989,** *8* (3), 841-842.
17. Liu, H.; Neal, A. T.; Zhu, Z.; Luo, Z.; Xu, X.; Tomanek, D.; Ye, P. D., Phosphorene: An Unexplored 2D Semiconductor with a High Hole Mobility. *Acs Nano* **2014,** *8* (4), 4033-4041.
18. Hultgren, R.; Gingrich, N. S.; Warren, B. E., The atomic distribution in red and black phosphorus and the crystal structure of black phosphorus. *J. Chem. Phys.* **1935,** *3* (6), 351-355.
19. Jamieson, J. C., Crystal structures adopted by black phosphorus at high pressures. *Science* **1963,** *139* (356), 1291-&.
20. Zhao, M.; Niu, X. Y.; Guan, L.; Qian, H. L.; Wang, W.; Sha, J.; Wang, Y. W., Understanding the growth of black phosphorus crystals. *Crystengcomm.* **2016,** *18* (40), 7737-7744.
21. Lange, S.; Schmidt, P.; Nilges, T., Au3SnP7@Black Phosphorus: An Easy Access to Black Phosphorus. *Inorg. Chem.* **2007,** *46* (10), 4028-4035.
22. Bridgman, P. W., Two new modifications of phosphorus. *J. Am. Chem. Soc.* **1914,** *36*, 1344-1363.
23. Brown, A.; Rundqvist, S., Refinement of crystal structure of black phosphorous. *Acta Crystal.* **1965,** *19*, 684-+.
24. Guo, Z.; Zhang, H.; Lu, S.; Wang, Z.; Tang, S.; Shao, J.; Sun, Z.; Xie, H.; Wang, H.; Yu, X.-F.; Chu, P. K., From Black Phosphorus to Phosphorene: Basic Solvent Exfoliation, Evolution of Raman Scattering, and Applications to Ultrafast Photonics. *Adv. Fun. Mat.* **2015,** *25* (45), 6996-7002.
25. Xu, H.; Han, X.; Li, Z.; Liu, W.; Li, X.; Wu, J.; Guo, Z.; Liu, H., Epitaxial Growth of Few-Layer Black Phosphorene Quantum Dots on Si Substrates. *Adv. Mat. Inter.* **2018,** *5* (21), 1801048.
26. Zhang, J. L.; Zhao, S.; Han, C.; Wang, Z.; Zhong, S.; Sun, S.; Guo, R.; Zhou, X.; Gu, C. D.; Yuan, K. D.; Li, Z.; Chen, W., Epitaxial Growth of Single Layer Blue Phosphorus: A New Phase of Two-Dimensional Phosphorus. *Nano Let.* **2016,** *16* (8), 4903-4908.
27. Xia, F.; Wang, H.; Jia, Y., Rediscovering black phosphorus as an anisotropic layered material for optoelectronics and electronics. *Nat. Commun.* **2014,** *5*.
28. Nahas, S.; Bajaj, A.; Bhowmick, S., Polymorphs of two dimensional phosphorus and arsenic: insight from an evolutionary search. *Phys. Chem. Chem. Phys.* **2017,** *19* (18), 11282-11288.
29. Douthwaite, R. E.; Green, M. L. H.; Heyes, S. J.; Rosseinsky, M. J.; Turner, J. F. C., Synthesis and characterization of the inclusion complex ((P-4)(2)C-60). *J. Chem. Soc. Chem. Comm.* **1994,** (11), 1367-1368.
30. Seitz, A. E.; Hippauf, F.; Kremer, W.; Kaskel, S.; Scheer, M., Facile storage and release of white phosphorus and yellow arsenic. *Nat. Commun.* **2018,** *9*.
31. Ginsberg, A. P.; Lindsell, W. E.; McCullough, K. J.; Sprinkle, C. R.; Welch, A. J., Preparation and properties of tetrahedro-tetraphosphorus complexes of rhodium and iridium - molecular and electronic-structure of RhCl(ETA-2-P4)(PPH3)2. *J. Am. Chem. Soc.* **1986,** *108* (3), 403-416.
32. Krossing, I.; van Wullen, L., Superweak complexes of tetrahedral P-4 molecules with the silver cation of weakly coordinating anions. *Chem.-a Euro. J.* **2002,** *8* (3), 700-711.
33. Peruzzini, M.; Marvelli, L.; Romerosa, A.; Rossi, R.; Vizza, F.; Zanobini, F., Synthesis and characterisation of tetrahedro-tetraphosphorus complexes of rhenium - Evidence for the first bridging complex of white phosphorus. *Euro. J. Inorg. Chem.* **1999,** (6), 931-933.

34. Mal, P.; Breiner, B.; Rissanen, K.; Nitschke, J. R., White Phosphorus Is Air-Stable Within a Self-Assembled Tetrahedral Capsule. *Science* **2009,** *324* (5935), 1697-1699.
35. Jiao, T. Y.; Chen, L.; Yang, D.; Li, X.; Wu, G. C.; Zeng, P. M.; Zhou, A. K.; Yin, Q.; Pan, Y. J.; Wu, B.; Hong, X.; Kong, X. Q.; Lynch, V. M.; Sessler, J. L.; Li, H., Trapping White Phosphorus within a Purely Organic Molecular Container Produced by Imine Condensation. *Angew. Chem. Int. Ed.* **2017,** *56* (46), 14545-14550.
36. Yang, D.; Zhao, J.; Yu, L.; Lin, X. S.; Zhang, W. Y.; Ma, H. W.; Gogoll, A.; Zhang, Z. B.; Wang, Y. Y.; Yang, X. J.; Wu, B., Air- and Light-Stable P-4 and As-4 within an Anion-Coordination-Based Tetrahedral Cage. *J. Am. Chem. Soc.* **2017,** *139* (16), 5946-5951.
37. Zhu, Y.; Wen, Y.; Fan, X.; Gao, T.; Han, F.; Luo, C.; Liou, S.-C.; Wang, C., Red Phosphorus Single-Walled Carbon Nanotube Composite as a Superior Anode for Sodium Ion Batteries. *Acs Nano* **2015,** *9* (3), 3254-3264.
38. Xu, J.; Guan, L., Toward understanding the active site for oxygen reduction reaction on phosphorus-encapsulated single-walled carbon nanotubes. *RSC Adv.* **2013,** *3* (16), 5577-5582.
39. Xu, J.; Guan, L., Diameter-Selective Band Structure Modification of Single-Walled Carbon Nanotubes by Encapsulated Phosphorus Chains. *J. Phys. Chem. C* **2009,** *113* (34), 15099-15101.
40. Tojo, T.; Yamaguchi, S.; Furukawa, Y.; Inada, R.; Sakurai, Y., Electrochemical Characterization of Phosphorus Encapsulated in Drilled Carbon Nanotubes as Anode Material for Lithium Ion Batteries. *ECS Trans.* **2017,** *75* (20), 39-44.
41. Ishii, Y.; Sakamoto, Y.; Song, H. Y.; Tashiro, K.; Nishiwaki, Y.; Al-Zubaidi, A.; Kawasaki, S., Alkali metal ion storage properties of sulphur and phosphorous molecules encapsulated in nanometer size carbon cylindrical pores. *AIP Advances* **2016,** *6* (3).
42. Clancy, A. J.; White, E. R.; Tay, H. H.; Yau, H. C.; Shaffer, M. S. P., Systematic comparison of conventional and reductive single-walled carbon nanotube purifications. *Carbon* **2016,** *108*, 423-432.
43. Luksirikul, P.; Ballesteros, B.; Tobias, G.; Moloney, M. G.; Green, M. L. H., pH-triggered release of materials from single-walled carbon nanotubes using dimethylamino-functionalized fullerenes as removable "corks". *Carbon* **2010,** *48* (7), 1912-1917.
44. Ren, Y.; Pastorin, G., Incorporation of hexamethylmelamine inside capped carbon nanotubes. *Adv. Mat.* **2008,** *20* (11), 2031-+.
45. Ulbricht, H.; Moos, G.; Hertel, T., Interaction of C-60 with carbon nanotubes and graphite. *Phys. Rev. Lett.* **2003,** *90* (9), 4.
46. Ruoff, R. S.; Tse, D. S.; Malhotra, R.; Lorents, D. C., SOLUBILITY OF C-60 IN A VARIETY OF SOLVENTS. *J. Phys. Chem.***1993,** *97* (13), 3379-3383.
47. Groot, C.; Hildebrand, J. H., THE SOLUBILITY RELATIONS OF WHITE PHOSPHORUS. *J. Am. Chem. Soc.* **1948,** *70* (11), 3815-3818.
48. Shao, L. D.; Tobias, G.; Huh, Y.; Green, M. L. H., Reversible filling of single walled carbon nanotubes opened by alkali hydroxides. *Carbon* **2006,** *44* (13), 2855-2858.
49. Dake, L. S.; Baer, D. R.; Friedrich, D. M., AUGER PARAMETER MEASUREMENTS OF PHOSPHORUS-COMPOUNDS FOR CHARACTERIZATION OF PHOSPHAZENES. *J. Vac. Sci. Tech. Vac. Sur. Films* **1989,** *7* (3), 1634-1638.
50. Phosphoric acids and phosphates. https://en.wikipedia.org/wiki/Phosphoric_acids_and_phosphates (accessed 18/12/2018).
51. Agrawal, K. V.; Shimizu, S.; Drahushuk, L. W.; Kilcoyne, D.; Strano, M. S., Observation of extreme phase transition temperatures of water confined inside isolated carbon nanotubes. *Nat. Nano.* **2017,** *12* (3), 267-+.

52. Fujimori, T.; Morelos-Gomez, A.; Zhu, Z.; Muramatsu, H.; Futamura, R.; Urita, K.; Terrones, M.; Hayashi, T.; Endo, M.; Hong, S. Y.; Choi, Y. C.; Tomanek, D.; Kaneko, K., Conducting linear chains of sulphur inside carbon nanotubes. *Nat. Commun.* **2013,** *4*, 8.
53. Beattie, I. R.; Ozin, G. A.; Perry, R. O., The gas-phase Raman spectra of P4, P2, As4, and As2. The resonance fluorescence spectrum of 80Se2. Resonance fluorescence–Raman effects in the gas-phase spectra of sulphur and I2. The effect of pressure on the depolarization ratios for I2. *J. Chem. Soc. A: Inorg., Phys., Theo.* **1970,** (0), 2071-2074.
54. Kharlamova, M. V., Advances in tailoring the electronic properties of single-walled carbon nanotubes. *Prog. Mat. Sci.* **2016,** *77*, 125-211.
55. Zhang, K.; Zhang, Y.; Wang, S., Enhancing thermoelectric properties of organic composites through hierarchical nanostructures. *Sci. Rep.* **2013,** *3*, 3448.
56. Qiao, R.; Roberts, A. P.; Mount, A. S.; Klaine, S. J.; Ke, P. C., Translocation of C60 and Its Derivatives Across a Lipid Bilayer. *Nano Let.* **2007,** *7* (3), 614-619.
57. Giffin, N. A.; Masuda, J. D., Reactivity of white phosphorus with compounds of the p-block. *Coord. Chem. Rev.* **2011,** *255* (11-12), 1342-1359.
58. Power, M. B.; Barron, A. R., The interaction of tri-tert-butylgallium with white phosphorus - isolation of an unusual gallium phosphorus cluster. *Angew. Chem. Int. Ed. in English* **1991,** *30* (10), 1353-1354.
59. Riedel, R.; Hausen, H. D.; Fluck, E., BIS(2,4,6-tri-tert-butylphenyl)bicyclotetraphosphane. *Angew. Chem. Int. Ed. in English* **1985,** *24* (12), 1056-1057.
60. Hittorf, W., Zur Kenntniss des Phosphors. *Anna. Phys.* **1865,** *202* (10), 193-228.
61. Baudler, M., Contributions to the chemistry of phosphorus .118. chain and ring phosphorus-compounds - analogies between phosphorus and carbon-chemistry. *Angew. Chem. Int. Ed.* **1982,** *21* (7), 492-512.
62. Fan, X.; Dickey, E. C.; Eklund, P. C.; Williams, K. A.; Grigorian, L.; Buczko, R.; Pantelides, S. T.; Pennycook, S. J., Atomic Arrangement of Iodine Atoms inside Single-Walled Carbon Nanotubes. *Phys. Rev. Lett.* **2000,** *84* (20), 4621-4624.
63. Holmes, W. S., Heat of combustion of phosphorus and enthalpies of formation of P4O10 and H3PO4. *Trans. Far. Soc.* **1962,** *58* (478), 1916-&.
64. Harris, P. J. F.; Tsang, S. C., A simple technique for the synthesis of filled carbon nanoparticles. *Chem. Phys. Let.* **1998,** *293* (1-2), 53-58.
65. Geng, H. Z.; Zhang, X. B.; Mao, S. H.; Kleinhammes, A.; Shimoda, H.; Wu, Y.; Zhou, O., Opening and closing of single-wall carbon nanotubes. *Chem. Phys. Let.* **2004,** *399* (1-3), 109-113.
66. Kierkowicz, M.; Gonzalez-Dominguez, J. M.; Pach, E.; Sandoval, S.; Ballesteros, B.; Da Ros, T.; Tobias, G., Filling Single-Walled Carbon Nanotubes with Lutetium Chloride: A Sustainable Production of Nanocapsules Free of Nonencapsulated Material. *ACS Sustain. Chem. Eng.* **2017,** *5* (3), 2501-2508.

4 One-Dimensional Arsenic Allotropes

4.1 Introduction

The great success seen in filling SWCNTs with phosphorus and observing its excellent ability in stabilising the air-sensitive P_4 molecule, attempts moved onto pushing the limits of confining sensitive materials even further by trying to stabilise the even more notorious As_4 molecule. Such is its instability to both oxygen and light that as yet, no crystallographic data for the bulk material exists.[1]

Despite the reputation that arsenic has developed due to its devious history, arsenic has found its way into being an essential element to everyday life. Semi-conductors frequently use arsenic as a dopant to alter the bandgap of the material,[2-4] and batteries contain arsenic to help strengthen its lead components.[5] In fact, it seems that arsenic is even an essential element for healthy human life![6] Now, with the recent interest in 2d materials, attention has shifted to trying to find other uses and allotropes from this element.

Grey arsenic is the most common form of arsenic. It is a layered material comprised of 2d sheets that possess a rhombohedral crystal structure. The sheets of black arsenic, in contrast, possess an orthorhombic crystal structure, the differences can be seen in Figure 3.1. Grey arsenic is also the most thermodynamically stable of the various allotropes that arsenic can form,[7] which is one of arsenic's main differences to phosphorus, as black phosphorus is the most stable allotrope of phosphorus. Black arsenic has yet to be conclusively shown to exist without the use of impurities potentially stabilising the material.[8] A material synthesised in the presence of mercury did show the same structure as its phosphorus counterpart but was not 100% pure.[9] Such is their structural and chemical similarity that a hybrid material was made from both phosphorus and arsenic which possessed the "black" structure.[10] This remarkable material also showed that by varying the arsenic and phosphorus content the experimenters had excellent control of the band gap. Structures for the grey, black and molecular forms of arsenic can be found in Chapter 3.

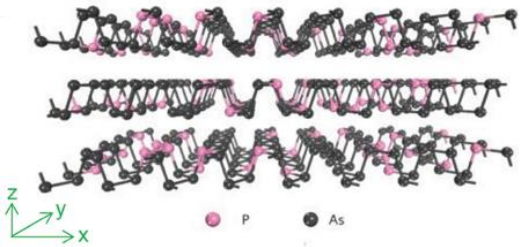

Figure 4.1 A hybrid black phosphorus-arsenic material highlighting the similarity between the chemical and structural properties of phosphorus and arsenic. Reproduced with permission from reference [10].

Examinations of the electronic structure of bulk grey arsenic in comparison to its monolayer counterpart have already shown some interesting results. Grey arsenic exists as a semi-metal,[11] but when reduced to a single layer a band gap of 2.49 eV emerges.[12] This band gap dramatically shrinks to 0.37 eV when an additional layer is added and becomes metallic in behaviour once it becomes a tri-layer material. It is proposed that the high level of inter-planar interaction between the layers causes the metallic behaviour. Once it is reduced to only a single layer, there is no longer any interaction and therefore it behaves as a semi-conductor. Studies have also shown that arsenene nanoribbons have a controllable band gap by varying the width of the material.[13] These properties and level of control already make arsenic a more enticing material to electronic engineers than its "big brother" graphene.

Arsenene has been created, although it is still in its infancy. Exfoliation of grey arsenic in a solution of sodium cholate using a kitchen blender did yield arsenene.[14] The sheets were quite large, and only a few layers thick but they only had a yield of 3.9% which is low. Oxidation of the surface was also present from analysis of XPS spectra collected for the material. A more conventional approach used ultrasonication to break the bulk material into nanosheets and dots.[15] The solvent used seemed key to which material is produced, with NMP forming nanosheets and toluene forming the nanodots. AFM revealed that the nanosheets were mainly in the 6-12 layer range, with the occasional mono- and bi-layer being detected. Band gap measurements revealed that the material had a band gap of 2.3 eV which is very similar to calculated values.[12] Despite all the computational work, there seems to have been very little progress in synthesising arsenene. There is an abundant number of mono-layered materials being synthesised that the material has to be very exciting in order to spend time and money researching.

Alternative 2D materials have also been examined, six new polymorphs have been proposed to add to the grey and black arsenic materials.[16, 17] Two of these are comprised of new arrangements of the six-membered rings found in grey arsenic whilst the others are made from eight-membered rings and seven-membered clusters.[16] Similarly, to the other monolayer arsenic materials, these are all semi-conducting too. With the creation of blue phosphorus,[18] perhaps these new 2D structures may also be created soon.

Yellow arsenic consists of tetrahedral As_4 molecules. It can be synthesised from grey arsenic by subliming the vapour onto a cold surface whilst in a dark room or within a cold solvent for use as a reagent.[19] It is incredibly unstable and will readily convert back to the grey form with any exposure to heat or light.[1] The mechanism of this transformation has been proposed to go through an As_8 dimer which forms the hexagonal motif which makes up grey arsenic.[20]

There have been many attempts to stabilise the yellow arsenic material. Confinement within a polymeric environment prevented the oxidation and conversion of the molecules due to light exposure.[21] The reaction of CuCl with [Cp*Fe(η^5-P_5)], when in the presence of As_4, forms $[Cu_2Cl_2\{Cp^*Fe(\eta^5\text{-}P_5)\}_2]_\infty \cdot (0.75As_4)_n$, which traps the As_4 molecule between four pairs of As···P(P_5) intermolecular contacts and numerous CH_3···As contacts. Only three quarters of the available sites were occupied due to the declining concentration of As_4 molecules in the solution as they are taken up. The methyl groups in the Cp* ligands lock the molecule in place and prevents any rotation. The material was so stable in this configuration that the first ever diffraction pattern of the tetrahedral molecule was recorded. The pattern showed very little distortion of the bond lengths in the molecule occurred when compared to other studies. This confirms that there is only a weak interaction between the host and guest molecules. Since then, As_4 has been found to exist without risk of oxidation or transformation in activated carbon,[22] and a range of other supramolecular chains.[23, 24] These materials have also been shown to release their arsenic loadings for use in further reactions.[22, 24]

Arsenic clusters have also been created but tend to require additional stabilising atoms to exist. Arsenic allotropes smaller than As_4 do exist, with As, As_2 and even As_3 being found in arsenic vapour,[25] but tend to form anionic clusters beyond As_4. A five-membered cluster has been observed though which did not need these additional atoms, but was in the form of an anion.[26] No cluster above the this size has been found experimentally stable.[27] One of the largest clusters observed experimentally contained 10 atoms. This was formed from the reaction of yellow arsenic with silyene.[28] The As_{10} structure comprised of a core cluster of As_7, taking the form of nortricyclane, which was

stabilised by arsasilene moietes bound to the unsaturated arsenic atoms within this core cluster. Interestingly, P_4 did not show the same behaviour and instead formed a linear chain of four phosphorus atoms. It was proposed that the weaker bond of As_4 allowed an additional unit to react with an intermediate species and form a larger cluster size.

Mid-sized arsenic clusters in the range of $6 \leq n \leq 28$ have been examined extensively by computational methods to predict the types of structures they could exhibit. It has been shown that for larger As_n ($n \geq 14$) clusters, As_2 bridging units are used to join As_4, As_6 and As_8 units together,[27] with As_{20}, As_{24} and As_{28} superclusters starting to appear very similar to red phosphorus fibres.[29] Debate as to the stability of these superclusters remain to be seen. 28 atoms would be enough to form a small fragment of a grey arsenic sheet, though, would the instability caused by dangling bonds allow for these structures to become the preferential structure. Novel carbon structures have been observed during the growth of graphene, perhaps this may help unlock these new superclusters.[30]

4.2 Outline of Chapter

This chapter will be concerned with the confinement of arsenic within single-walled carbon nanotubes using vapour filling techniques. Optimisation of the filling yield is attempted before trying to establish if the As_4 molecule can be stabilised within the SWCNT using HRTEM. The final material will be fully characterised to determine the thermal stability of the material, to investigate if any evidence of external material can be seen and finally to see if any charge transfer has occurred between the filling material and the SWCNT. Where possible, these results will be corroborated with computational studies. Density of states calculations will be calculated to help determine the likeliness of any charge transfer effects and new confined structures will be searched for and examined for suitability from DFT calculations.

4.3 Results and Discussion

4.3.1 Maximising the Filling Yield

CoMoCat SWCNTs were initially used for the confinement of arsenic based on the previous success with white phosphorus. Although arsenic has a larger van der Waals diameter than phosphorus; the size of the yellow arsenic molecule should still be within the range of diameters that CoMoCat SWCNTs possess. Taking into account the As-As bond length (2.49 Å), the van der Waals radius (1.85 Å)[31] and simplifying the tetrahedron to a sphere, a rough dimeter of the molecule can be estimated as 5.31 Å,

which should fit within the larger diameter CoMoCat SWCNTs. For comparison, P_4 has a diameter of 4.92 Å.

In order to determine the success of the filling, estimated filling yield calculations were performed using structures, in Figure 4.2, created by Ji Chen. These were generated in the same way as for the phosphorus structures in the previous chapter. Figure 4.3 shows that for SWCNTs within the 8-9 Å diameter range, we can expect a filling yield from anywhere between 0.24 wt% to 0.42 wt%. These filling yield estimates have been calculated by counting the number of atoms in the structure that would fit into a 50 Å length of the appropriately sized diameter SWCNT. This value is then converted into a wt% value which can be used to compare with the XPS results. The values for bulk grey and yellow arsenic have been plotted too. These have been calculated using the density of these materials and the volume within the SWCNT, accounting for the van der Waals' radius of the carbon atom.

As we go to larger diameters, the filling yield decreases for most of the structures, apart from the bulk materials which rise as expected given the increasing volume of the wider nanotubes. Despite the extra room afforded by the wider diameters, the structures' shapes are already optimised at 7 Å. Therefore, structures cannot pack any more effectively to offset the extra carbon atoms within the larger SWCNTs.

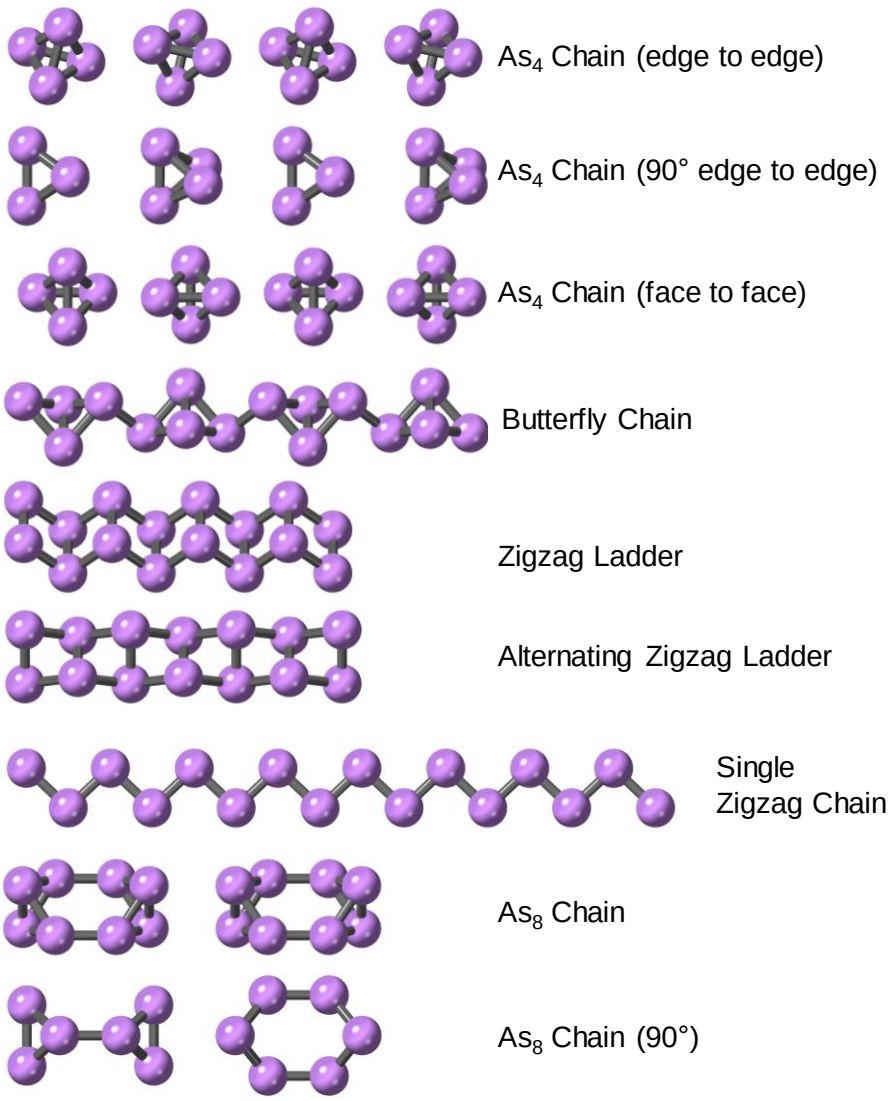

Figure 4.2 Geometry-optimised arsenic structures produced by Ji Chen.

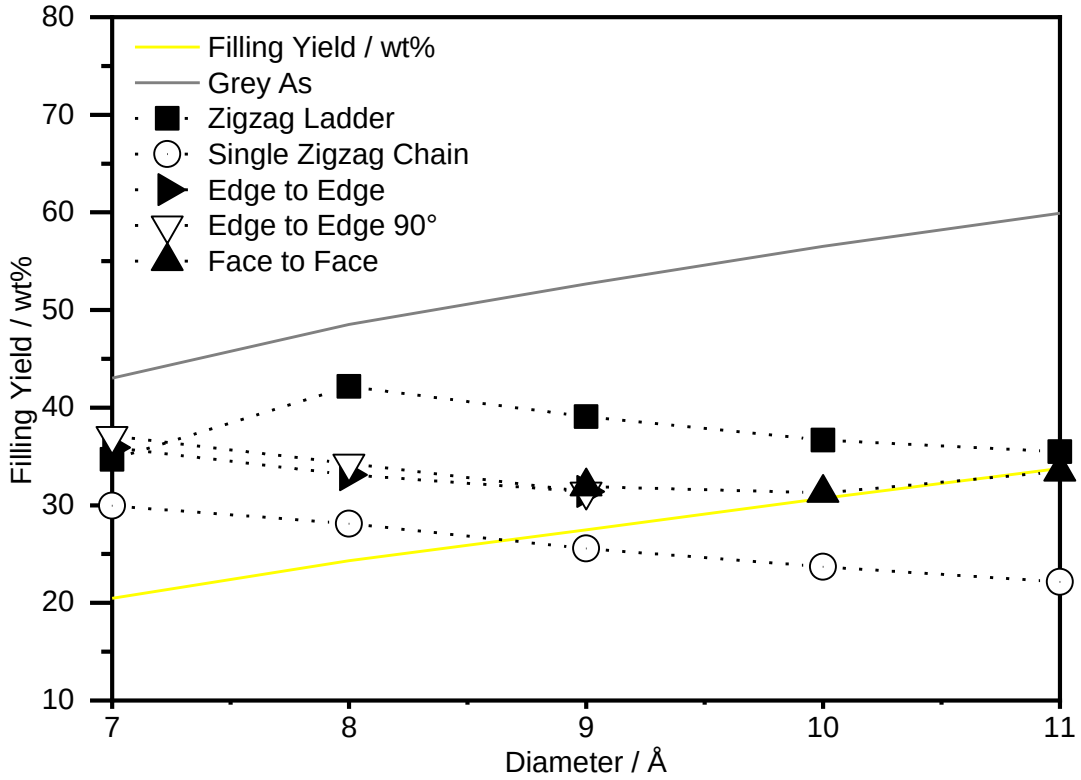

Figure 4.3 Filling yield estimates based on DFT structures generated by Ji Chen. The filling yield is calculated by filling a 50 Å SWCNT with the largest number of unit cells of the filling material without it exiting the end of the tube. The proportion of each atom type can be then used to calculate the filling yield of the material.

The only exceptions to this are the zigzag ladder, which can narrow its bond angle from 180° at 7 Å to 98.61° at 8 Å to allow a higher yield, and the face to face tetrahedra, which can pack more laterally and therefore more tightly at 11 Å. This result can be seen in the respective increases in filling yield in Figure 4.3.

Although ampoules have been used to perform the filling procedure, it is hoped that that similar techniques developed from filling SWCNTs with white phosphorus can be applied here. Subliming the excess material away from the SWCNTs proved to be a vital step for filling SWCNTs with white phosphorus in order to create pure samples. This step was initially replicated by rotating the ampoule containing the As/SWCNT mixture within the tube furnace so that the As vapour sublimes to the end containing no SWCNTs.

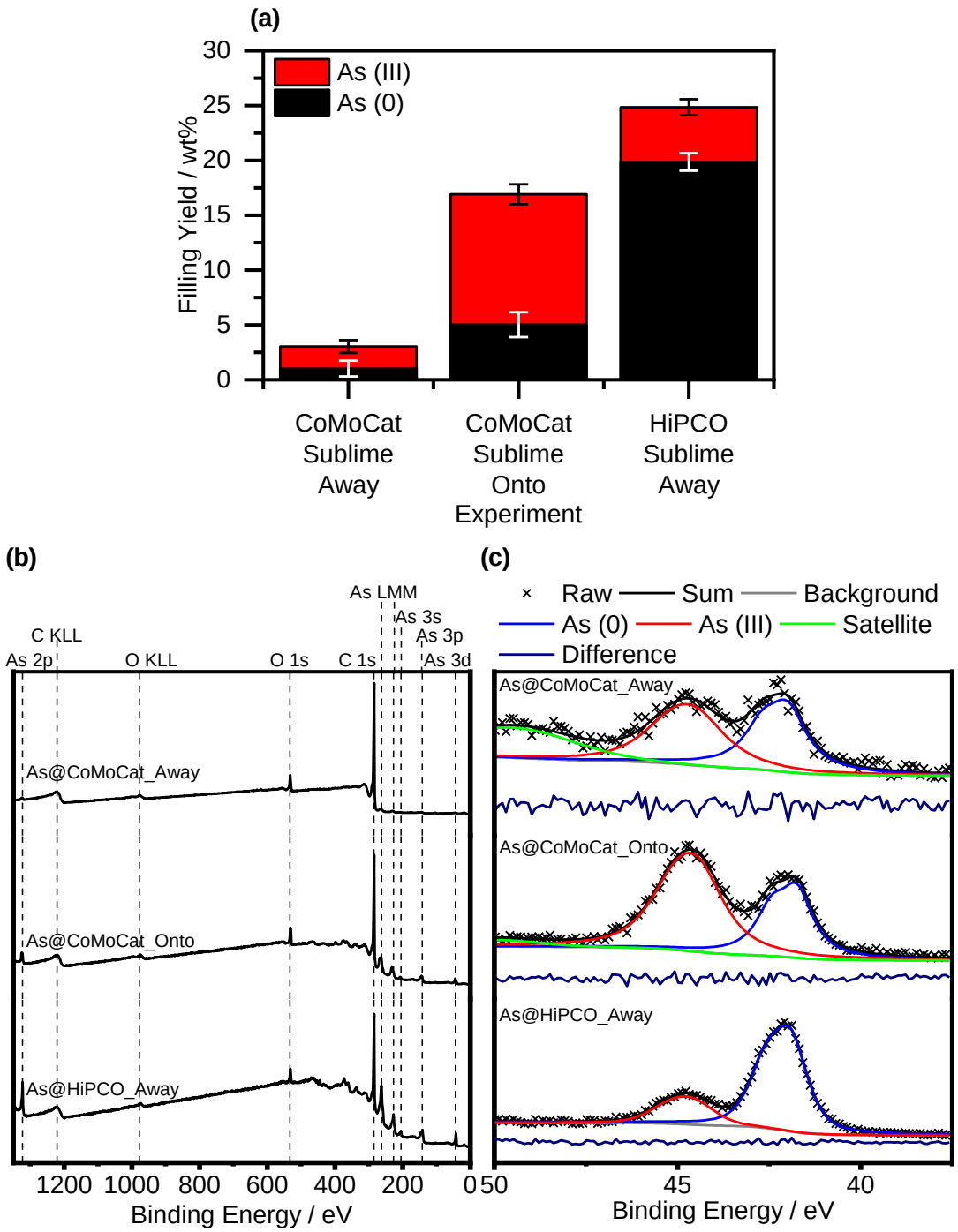

Figure 4.4 (a) Overview of arsenic filling experiments showing the improvement in filling yield as the procedure became more refined. (b) Survey spectra for the various samples. (c) High resolution spectra of the As 3d region for the various samples showing the change in ratio between the elemental and oxidised arsenic in each sample.

Figure 4.4 shows an overview for the filling yields achieved. These values have been generated from the survey spectra and accurate fitting of the As 3d region (shown in Figure 4.4 (c)) in the same way as described in the previous chapter. When the arsenic

material is sublimed away from the SWCNTs, a low filling yield is achieved. This is much lower than the estimated 30 wt%. It may be that the much stronger vacuum achieved within the sealed ampoule, compared to within a Schlenk flask, may have caused any filled material to evacuate the SWCNTs and cause the lower filling yield.

A second attempt sublimed the arsenic material onto the SWCNTs as the last step. This saw a significant improvement in the filling yield. The large amount of arsenic (III) oxide present also confirms that subliming the arsenic onto the SWCNTs coats them thoroughly with arsenic material. A trade-off between the filling yield and the purity has been achieved which shows the level of control we have over this system.

Larger diameter HiPCO SWCNTs were used to try and improve the filling yield, with the same filling method used as before. Although the arsenic tetrahedra should fit within the CoMoCat SWCNTs, any additional room that can be created without losing the confining ability will be beneficial. The diameter ranges for CoMoCAT and HiPCO are <1nm[32] and 0.8-1.3 nm[33] respectively. It is hoped that the extra few Ångströms of room will hopefully make it easier for the molecules to fill the SWCNT without being too large as reduce its ability to confine the molecules and prevent leakage or oxidation. HiPCO offers a large range of diameters too, and also overlaps with the diameter range for CoMoCat, so it should still be possible to explore the structure of confined arsenic within the size of nanotube that CoMoCat offers. An immediate increase in the filling yield has been achieved using these HiPCO SWCNTs. It seems as if the larger diameter tubes have made it much easier for the arsenic molecules to enter the SWCNT.

As shown in Figure 4.4, when the arsenic material is sublimed away from the SWCNTs, a low filling yield was achieved. The emptying of SWCNTs is not well understood. There are papers showing success in emptying nanotubes,[34] but it has not been thoroughly researched with contrasting reports showing the stability of SWCNTs filled with other water soluble materials.[35] The emptying of As@HiPCO was attempted by heating the sample under vacuum. The filling yield of the heat-treated sample shows a clear reduction in the arsenic presence by almost 85% leaving a sample with a comparable arsenic and oxide presence to the initial arsenic filling experiment where the arsenic material was sublimed away from the CoMoCat SWCNTs as the last stage of the filling procedure.

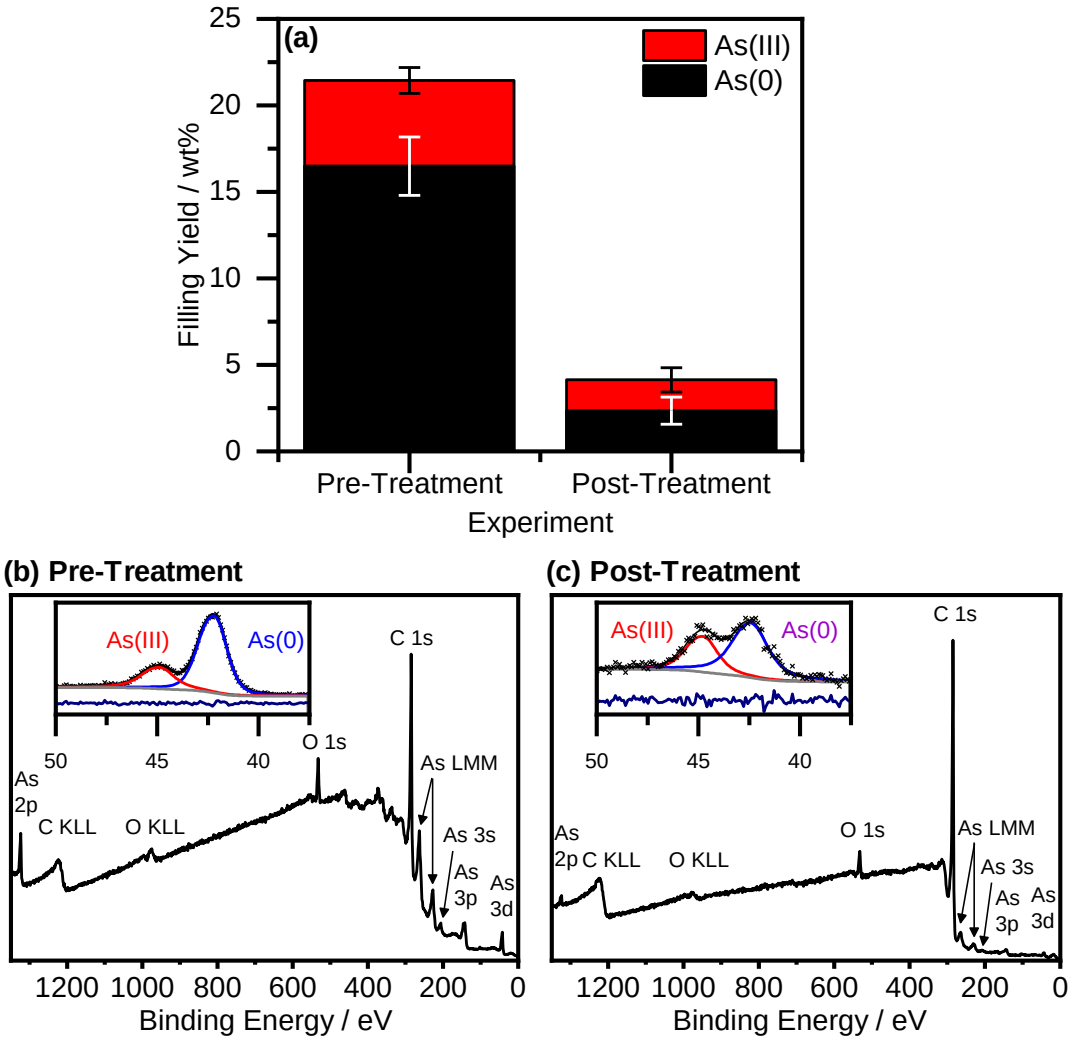

Figure 4.5 XPS data showing the emptying of arsenic filled SWCNTs. (a) Filling yield comparison for the pre- and post-treated samples. (b) Survey and high-resolution XPS spectra for the pre-treated sample. (c) Survey and high-resolution XPS spectra for the post-treated sample.

Raman spectroscopy was attempted on the sublimed arsenic material, which can be seen in Figure 4.6. Good agreement can be seen between the Raman spectrum collected and the what can be found in the literature confirming that this is amorphous arsenic.[36] The way it was created also suggests that this material is amorphous arsenic.[7] The shiny appearance of the arsenic is also very reminiscent of the arsenic mirror produced in the Marsh test, again confirming that it is indeed amorphous arsenic.[37]

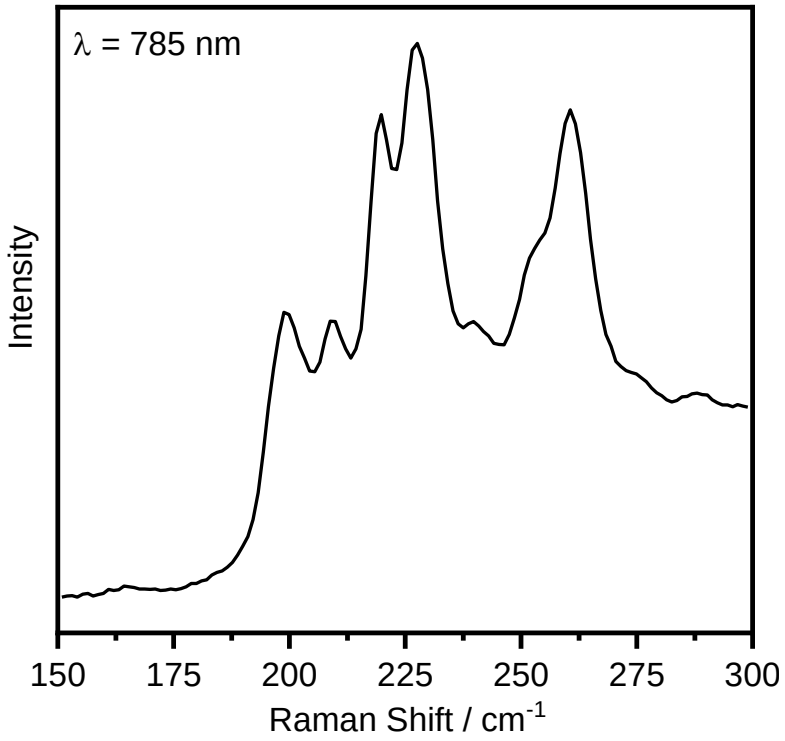

Figure 4.6 Raman spectrum for the amorphous arsenic grown in Figure 4.7. Good agreement can be seen with examples in the literature.[36]

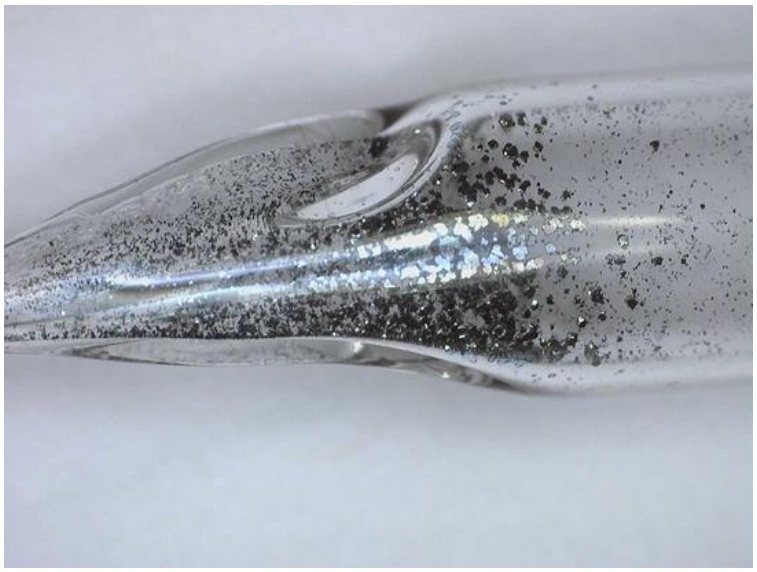

Figure 4.7 Image of the sublimed arsenic after heat treatment of the filled sample.

4.3.2 Identification and Classification of One-Dimensional Arsenic Allotropes

HRTEM has been used to confirm the inclusion of arsenic within the SWCNT cavity. It has also helped in identifying the structure of the confined material. This work has been aided by the use of simulated micrographs which have been created with the use of

CrystalMaker, Nanotube Modeler and SimulaTEM software,[38] as well as DFT optimised structures generated by Ji Chen.

The possible arsenic structures that could be adopted within the SWCNT cavity has been explored by Ji Chen and can be seen in Figure 4.8. The structures that were investigated are based on the structures identified for confined phosphorus due to their chemical similarity. As with those calculations, these calculations do not use an explicit SWCNT, but instead use a confining potential to mimic the SWCNT environment. This is based on a similar approach used to confine ice between graphene layers.[39] The various As_4 chains investigated show the different repetitions that the tetrahedra can adopt, although, it is most likely that the tetrahedra will be rotating and make these structures unrealistic, in the same way as seen in white phosphorus.[40] Two additional structures have been investigated, the As_8 chain and As_8 chain (90°). These dimers may link arsenic tetrahedra to the grey arsenic sheets and act as the first step of polymerisation.[41] The two ladder structures are the narrowest structures that can be created whilst keeping three bonds between the atoms that is seen in the variety of clusters that arsenic can adopt.[42]

As expected, the energies of the structures increase as the nanotube diameter narrows. This has been seen in many systems so confirms that the calculations, at first glance, seem reasonable.[43] The *trans* butterfly structure and various As_4 chains all show the widest range of stability, and specifically the lowest energies at the average diameter of the HiPCO SWCNTs of 9 Å. Although the As_4 chains are never the most stable, as the arsenic is expected to fill the SWCNT in this form from the vapour phase, so it can be reasoned that they may exist in a metastable state. At the narrowest diameter, the single zigzag chain becomes the most stable. This shows the stabilising effect that a SWCNT can provide to these one-dimensional allotropes and is why a variety of other elements, such as selenium and iodine, have shown this behaviour within narrow diameter nanotubes.[43-45] It becomes increasingly unstable compared to the other structures as the diameter increases which shows the preference of the element to want to form more bonds and more complex structures. The zigzag ladder only becomes comparatively stable to the other structures at the larger diameter nanotubes. The alternating ladder and As_8 chains are never comparatively stable. It can be reasonably assumed that if the filling material exhibits a ladder-like structure, that it will be of the zigzag ladder structure and not the alternating alternative.

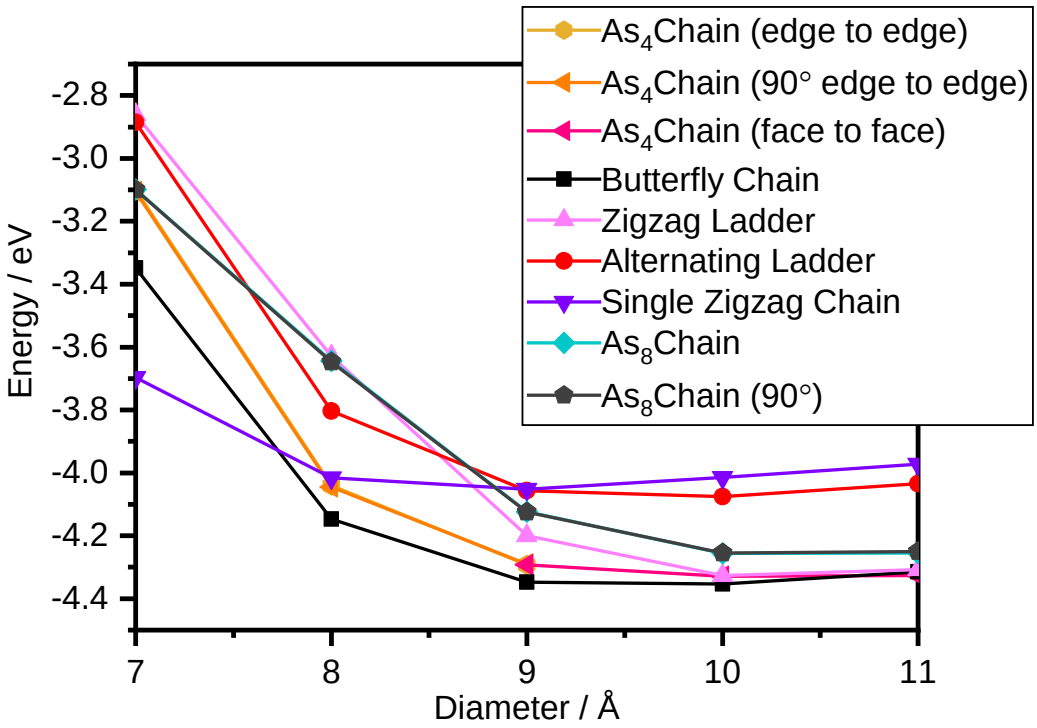

Figure 4.8 DFT analysis of confined arsenic structures. Energies of the structures shown in Figure 4.2 as a function of the nanotube diameter. Energy is defined as the per-atom binding energy relative to an isolated arsenic atom plus the confining energy. Calculations performed by Ji Chen.

Figure 4.9 shows the three different structures that have been observed confined within SWCNTs. There is good agreement between the micrographs taken and the simulations produced using the structures generated from DFT calculations. The atomic models show that tetrahedra, zigzag ladder and single zigzag chain structures have been observed. The simulations have been created by rotating the structures, either about their centre of mass (tetrahedra) or about the nanotube axis (zigzag ladder and single zigzag chain). The chain structures have been rotated in steps of 10° for a full revolution with a simulated image taken for rotation. The 36 images produced have been averaged using the ImageJ z-projection feature to create the final image. These steps have been shown to be a necessary procedure as the stills of the structures show very defined features that have not been observed during the TEM sessions. Dynamic behaviour, such as rotation, has also been observed previously in SWCNTs filled with graphene nanoribbons so this behaviour is not unexpected.[46]

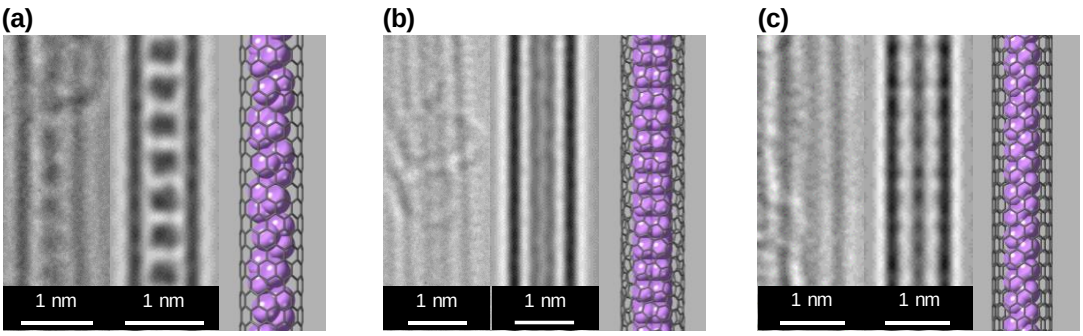

Figure 4.9 HRTEM images (left), simulations (centre) and atomic models (right) of different arsenic structures found confined within SWCNTs. (a) Tetrahedra, (b) zigzag ladder and (c) single zigzag chain.

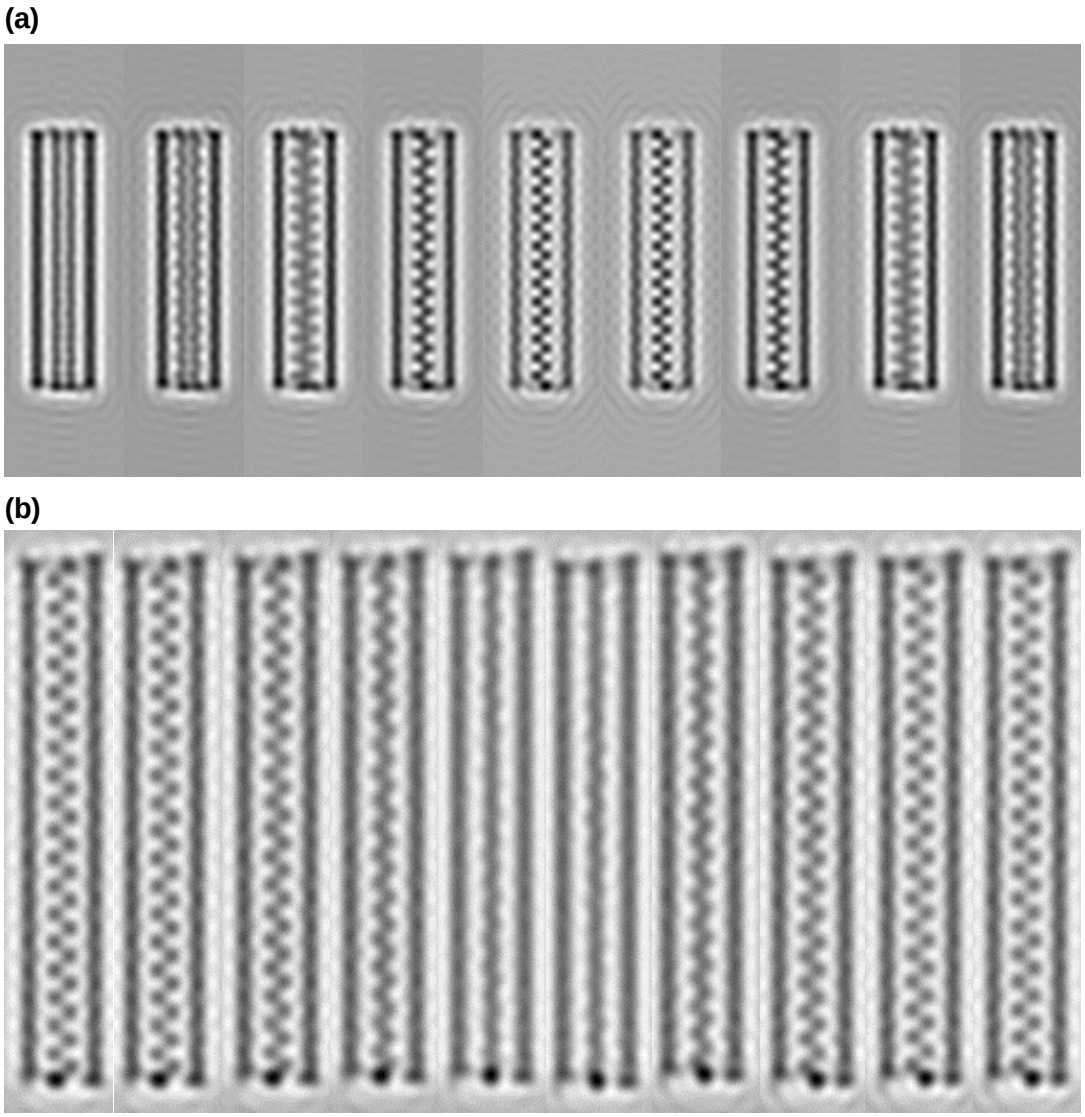

Figure 4.10 (a) HRTEM simulation stills showing the rotation of the arsenic zigzag ladder about the z-axis of the SWCNT. Stills are shown of every 20° rotations from 0 – 180°. (b) HRTEM simulation stills showing the rotation of the arsenic single zigzag chain about the z-axis of the SWCNT. Stills are shown of every 20° rotation from 0 – 180°.

The tetrahedra have an average repeat distance of 0.55 nm which is slightly longer to the repeat distance measured in the simulation of 0.51 nm. In fact, the repeat distances measured in the sample are all slightly longer than what is predicted from the simulations, as can be seen in Figure 4.11. This is most likely caused by the energy imparted into the molecules by the electron beam inducing dynamic behaviour within the molecules which cannot be replicated by the DFT calculations. In fact, there seems to be an opposite trend between the simulated calculations and the sample. There is a slight positive correlation between the repeat distance and the nanotube diameter in the As@HiPCO sample whereas the simulations show a negative correlation. The simulations show that the tetrahedra can move laterally as the nanotube widens, so can pack together tighter and cause the smaller repeat distance, especially when packed in the fact-to-face arrangement. It would be expected that the sample would show a similar pattern, but it seems the opposite is true.

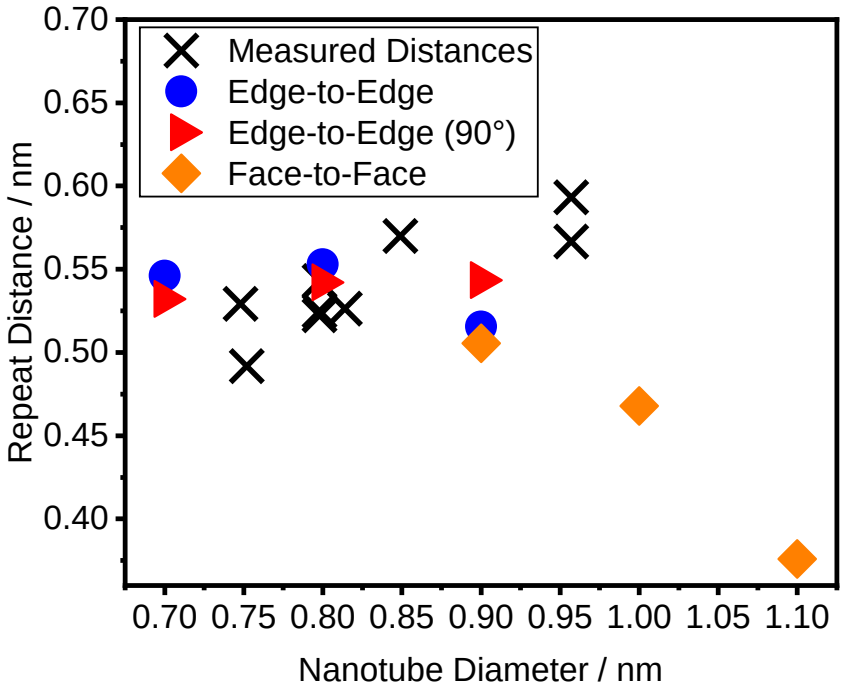

Figure 4.11 Tetrahedra repeat distance as a function of nanotube diameter for sample As@HiPCO. Repeat distances generated from simulated images of DFT generated structures are also included.

More examples of the structures adopted by confined arsenic can be found in Figure 4.12.

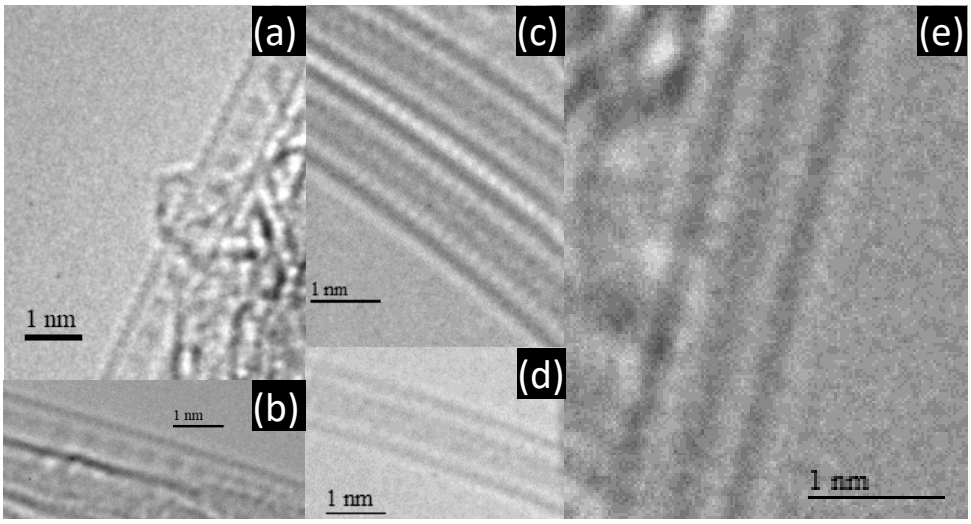

Figure 4.12 Additional examples of the structures confined arsenic can adopt within HiPCO SWCNTs. (a-b) Tetrahdera, (c-d) zigzag ladders and (e) single zigzag chains.

Recognising these structures can be tricky, however, some fine structure can be detected which makes their identification easier. The zigzag ladder appears as a broad line within the SWCNT whilst the single zigzag chain appears as a narrow line. The zigzag chain can also show a faint gap along its centre, as shown in Figure 4.13. Line profile analysis reveals that this gap has an average width of 2.32 Å which is in good agreement with the gap measured in the simulated image, at 9 Å. Figure 4.13 (e) shows that there is a trend for the zigzag ladder gap width to increase as the nanotube gets wider. A similar trend is seen in the DFT simulated structures, but not to the same degree. This shows that the filling material is flexible enough to expand or contract to best fit into the available space.

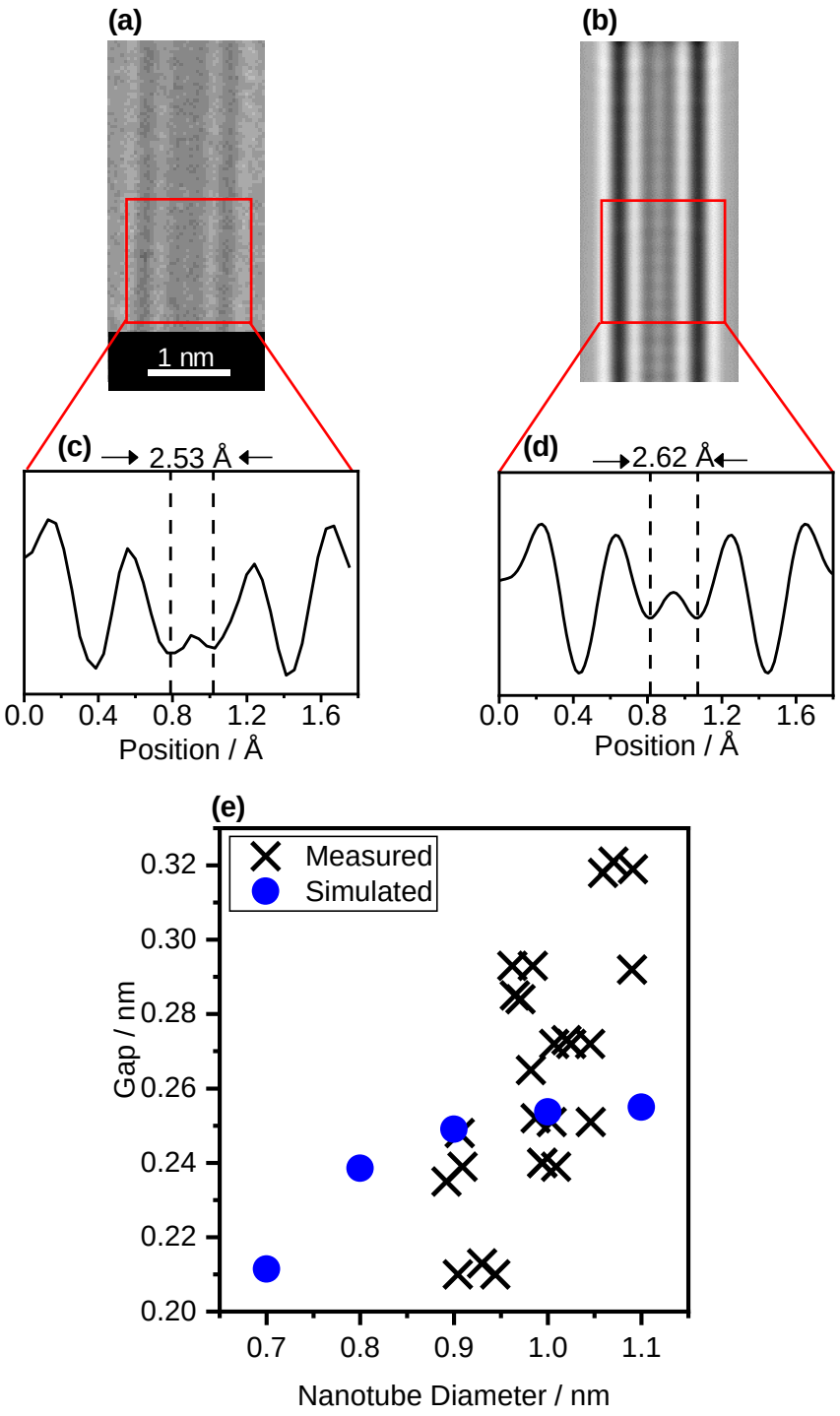

Figure 4.13 (a) HRTEM image of the zigzag ladder confined within a SWCNT. (b) Simulation of (a). (c) Line profile taken across highlighted area in (a). (d) Line profile taken across highlighted area in (b). (e) Comparison of measured zigzag ladder gap values and simulated values.

Although the DFT results predict the butterfly structure as being the most stable, the simulated images of the rotationally averaged structure (Figure 4.14(a)) has shown features that have so far been undetected whilst imaging the sample in TEM. Climbing-image nudged-elastic band calculations have shown a very small activation energy exists

for the conversion between a face-to-face tetrahedral structure and the butterfly chain in Figure 4.14(b). At just over 0.05 eV separating the two structures, it would be entirely possible for the two structures to rapidly switch between each other. The entropic advantage gained for the arsenic atoms existing as tetrahedra as opposed to the polymerised structures may also help preserve the tetrahedral molecules and cause the conversion from the butterfly back to the tetrahedral units. The tetrahedra can rotate about three axes, as opposed to one when polymerised. Unfortunately, these entropic factors have not been incorporated into the DFT calculations but remain a highly plausible theory as to why the butterfly structure has so far been undetected.

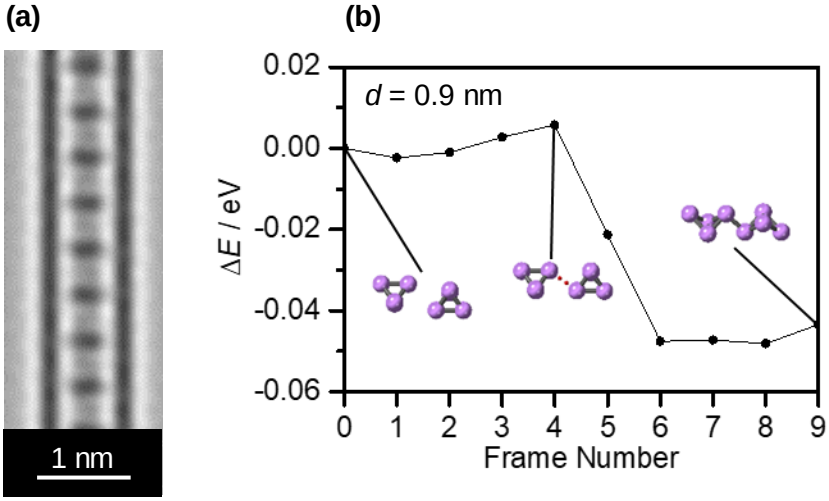

Figure 4.14 (a) Simulated image of the butterfly structure confined within a 0.9 nm SWCNT. (b) Nudged-elastic band calculations showing the relative energy differences between the As_4 face-to-face starting structure and butterfly ending structure showing the optimum reaction pathway between both.

These techniques have helped create a comprehensive understanding of the different types of structures observed and their frequency. Figure 4.15 shows the occurrence of these structures as a function of the nanotube diameter. This analysis has also revealed that the most commonly observed SWCNT diameter is between 0.8 nm and 1.2 nm, which is reassuring as this corresponds with what is expected for HiPCO SWCNTs.[47] The most frequent structure seen within this range is the zigzag ladder. Tetrahedral units and the single zigzag ladder are observed at smaller diameters. This is reflected well in the DFT results in Figure 4.7. It is reasoned that the arsenic atoms need room in order to rearrange themselves into the zigzag ladder. At the smallest diameters there is not enough room for this to occur, and as such the tetrahedra and single zigzag chain are stabilised. As so few structures are also seen above 1.1 nm, it implies that the arsenic is more prone to leakage or oxidation. It is only through their tight confinement within the SWCNT that their removal from the nanotube can be prevented. This seems to confirm

that there is a very fine margin for success. If the SWCNTs are too narrow, such as CoMoCat SWCNTs, the As_4 molecules struggle to fill the nanotubes. If the SWCNTs are too wide, leakage and oxidation may occur. The tight confinement is essential for the tetrahedra to maintain their shape as can be evidenced by other attempts at stabilising the molecules.[23] By confining the As_4 within tetrahedral cages that are just large enough to wrap around the molecule, the molecules remain stable to both light and oxidation as there is not enough room for the molecules to rearrange themselves or form new As-O bonds. These attempts allow for the 0D isolation of As_4 molecules. The benefits of As@CNT is that 1D chains of As_4 molecules can be produced allowing for much larger loadings.

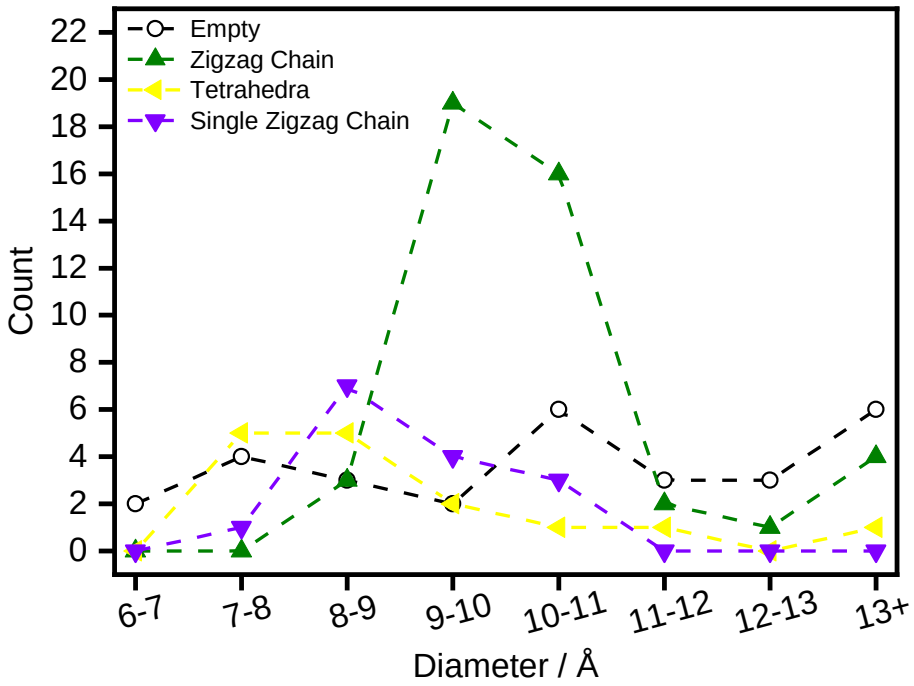

Figure 4.15 Statistical analysis of the arsenic structures observed within HiPCO SWCNTs as a function of the nanotube diameter.

Lastly, the statistical analysis shows that 73% of all observed nanotubes show some evidence of filling. This is approximate to the value determined through XPS.

4.3.3 Further Characterisation

Further characterisation has been completed in order to help fully understand the material. As the HiPCO filled sample showed the highest filling yield, the rest of this chapter will focus on this material.

TGA/DSC analysis has been conducted in air. A small mass increase at 403 K could signal the oxidation of the leaked yellow arsenic, although with such a high arsenic content, this

peak would be expected to be larger. It is most likely some further oxidation of the arsenic (iii) oxide present on the outside of the sample. The gradual mass loss from 573 K to 773 K shows the sublimation of the internal arsenic present. Mass loss only begins at 673 K and is much sharper for the empty SWCNTs which helps prove that the earlier mass loss seen in the filled sample is caused by leakage of the arsenic material. A mass loss of ~20 wt% corroborates the filling yield determined by XPS. Integration of the large DSC feature, peaking at 823 K, shows that -22.8 J are released per milligram of sample at this temperature range. This is caused by the combustion of the SWCNTs and given the enthalpy of combustion of graphitic carbon is -33.2 J mg^{-1},[48] it can be estimated that the sample is ~70 wt% carbon, again confirming the results derived from the XPS analysis. The TGA analysis also corroborates what has been seen when annealing the sample, that the material will leak out of the SWCNTs when exposed to high temperatures.

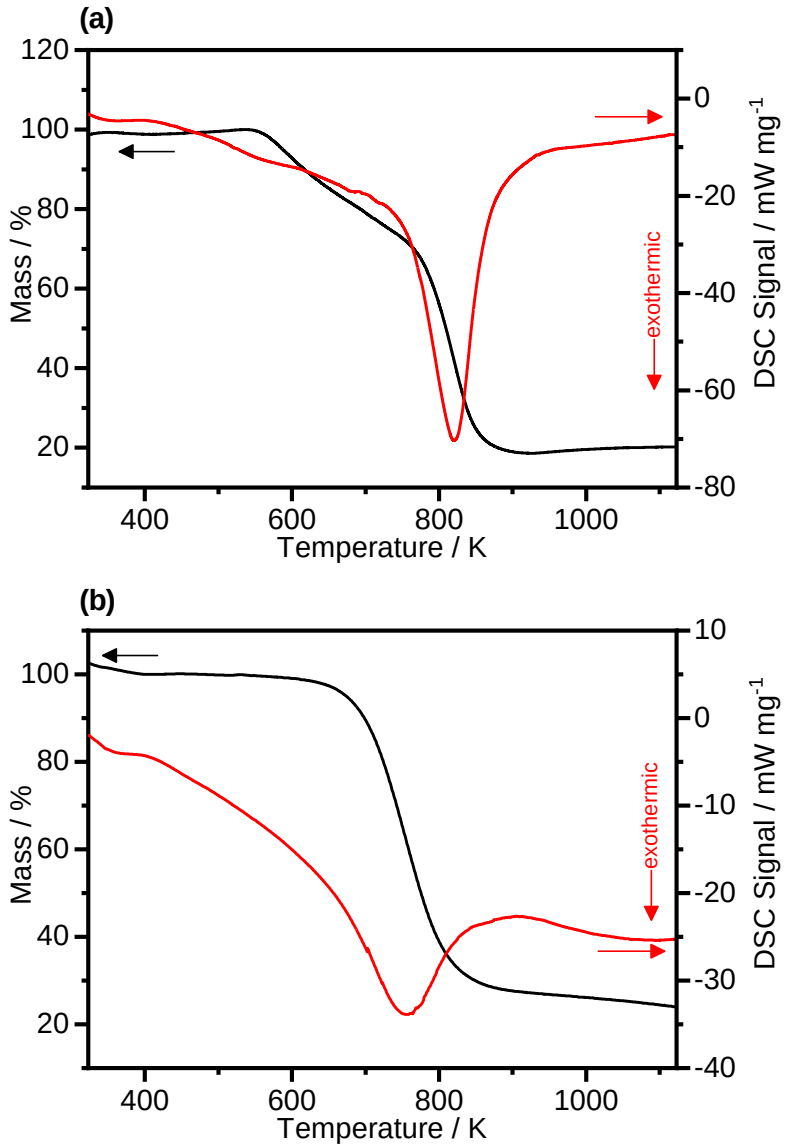

Figure 4.16 (a) TGA/DSC analysis of the arsenic filled HiPCO SWCNTs. (b) TGA/DSC analysis of empty HiPCO SWCNTs for reference.

Although efforts have been made to remove the external arsenic from the sample by washing in dilute nitric acid, there are always concern that some material may still be present. The reaction of arsenic with nitric acid is given in the equation below:

$$As + HNO_3 \rightarrow H_3AsO_4 + 5NO_2 + H_2O \qquad [4.1]$$

PXRD has been used to check for this and to potentially see any new features arising from the confined arsenic. Grey arsenic was observed in the PXRD, as well as iron arsenide, so an internal standard was added in the form of sodium chloride. As the amount of sodium chloride weighed in is known (0.2 mg), it can be used to give an estimate to the amount of other substances present in the sample. Fitting the data shows that only around 1.2 wt% of the elemental arsenic detected by XPS is in the form of

external grey arsenic. The iron diarsenide present seems to have formed from the reaction of the iron catalyst nanoparticles and arsenic vapour. Based on previous literature on the growth of $FeAs_2$ crystals, this method of synthesis seems very reasonable and explains the presence of the compound.[49]

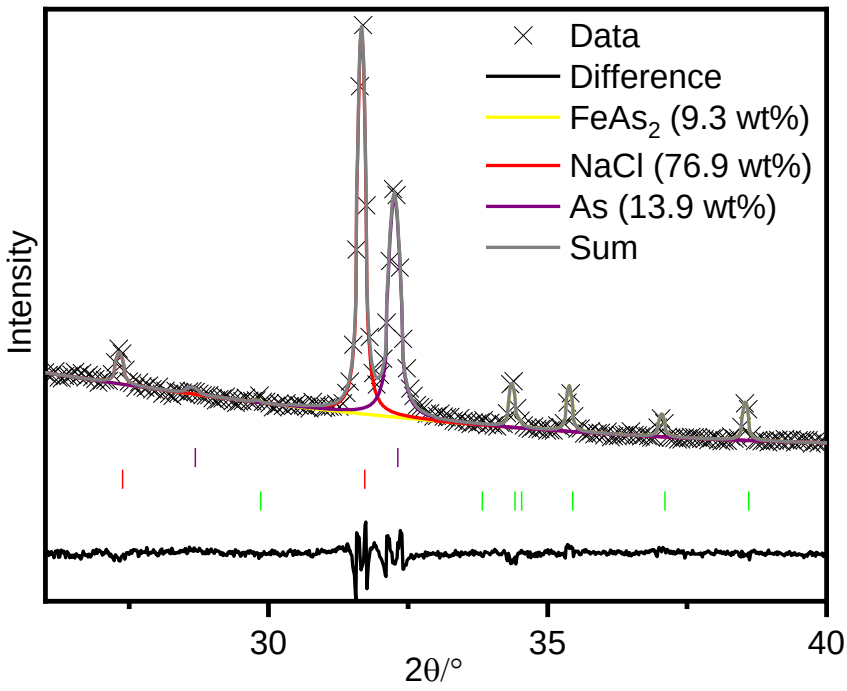

Figure 4.17 Quantitative PXRD analysis of the As@HiPCO/NaCl mixture.

Raman spectroscopy has also been performed to determine if any charge transfer has occurred between the filling material and the SWCNTs, from shifts in the G-band, and to also see if any changes have occurred to the size of the SWCNTs from the inclusion of the arsenic, by shifts in the RBMs. The first thing to note is the lack of any additional new features that may have been caused by the encapsulated arsenic. It is expected that a sharp feature at 340 cm^{-1} should be observed which is caused by the breathing mode of the tetrahedral molecules.[50] Other confined materials have shown very intense new features when examined by Raman spectroscopy.[43, 46] The lack of any new features can be caused by a couple of reasons. One, the laser energy is absorbed by the carbon wall and unable to excite the arsenic material. A variety of wavelengths (514 nm, 633 nm and 785 nm) were tested to try and overcome this issue, but no differences can be seen. Two, the laser energy is causing the polymerisation of the tetrahedra in the same way the electron beam in HRTEM and the x-rays in PXRD do. The D/G band ratio shows that there is little to no additional disorder caused from the degradation of the SWCNTs during the filling procedure. It may also be reduced potentially by some annealing of the SWCNTs during the heat treatments. Although the experiments were only conducted at 888 K,

which is a little low for annealing SWCNTs, it is not unreasonable to suggest that this process may have occurred.[51]

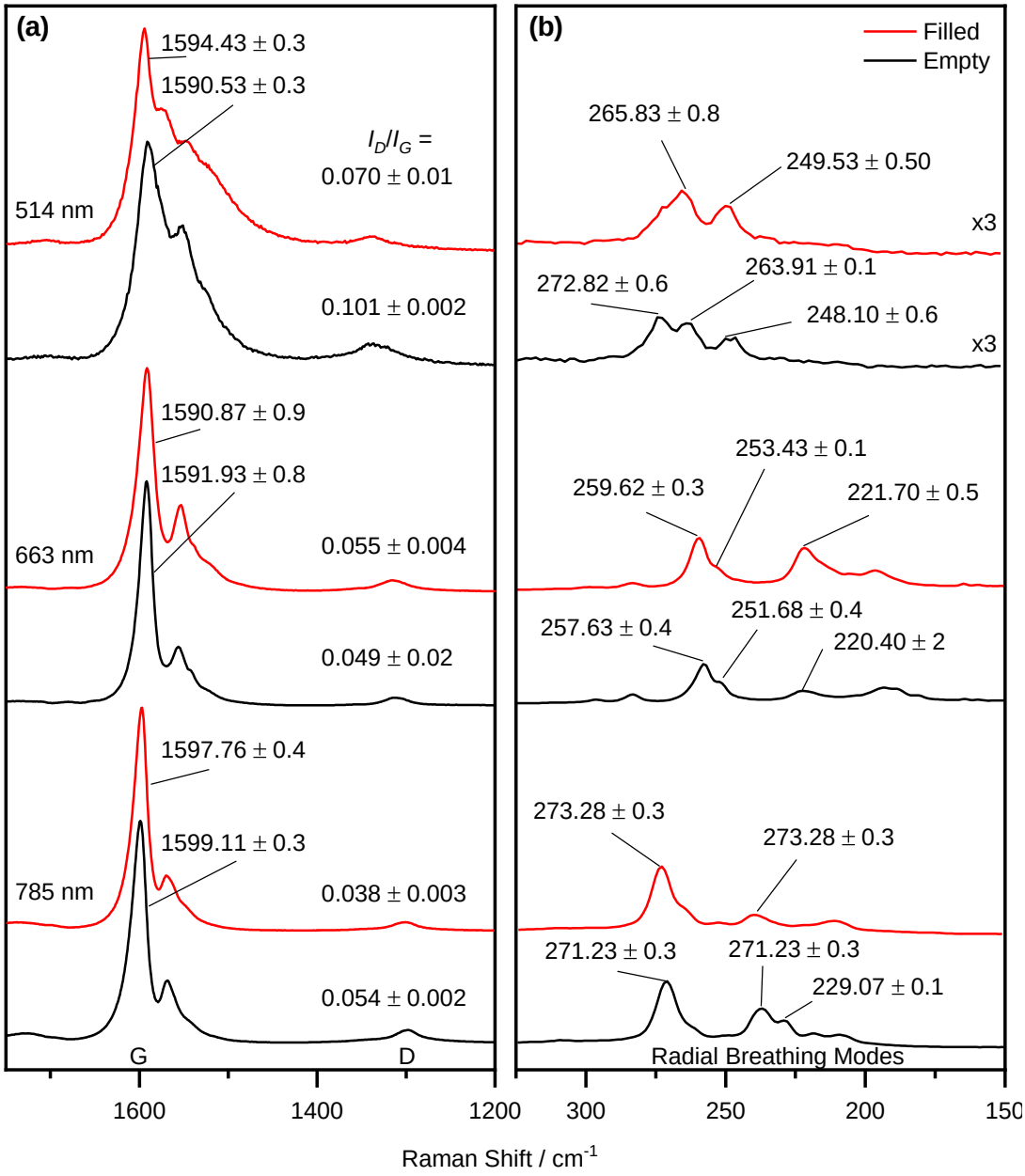

Figure 4.18 Raman spectra of As@HiPCO showing the G-band and RBM regions with prominent peaks highlighted, collected using three different excitation wavelengths.

Evidence to show that charge transfer has occurred between the SWCNTs and filling material seems doubtful. Inconsistent shifts in the G-band can be seen between the empty and filled samples, when excited by the different lasers, which suggests that no charge transfer has occurred. Density of states calculations, performed by Ji Chen, on the potential structures adopted by the confined arsenic show that both metallic and semi-conducting structures can exist within the SWCNTs. These structures will have

competing charge transfer effects with the SWCNTs, with semi-conducting materials accepting charge from the SWCNTs and metallic structures transferring charge to the SWCNTs.[52] Evidence of charge transfer is also accompanied by changes in the peak shapes of the G-band. For example, the narrow and symmetrical G-bands seen for both filled and empty samples, when excited by the 785 nm and 633 nm lasers, shows predominantly semi-conducting SWCNTs are excited.[53] If charge transfer had occurred, the G-band would be expected to a shift to a higher frequency and show a broadening of the peak caused by the semi-conducting SWCNTs behaving more akin to metallic ones. Overall, the Raman data collected suggests that no charge transfer has occurred between the two materials, or at least has not detected if any has occurred.

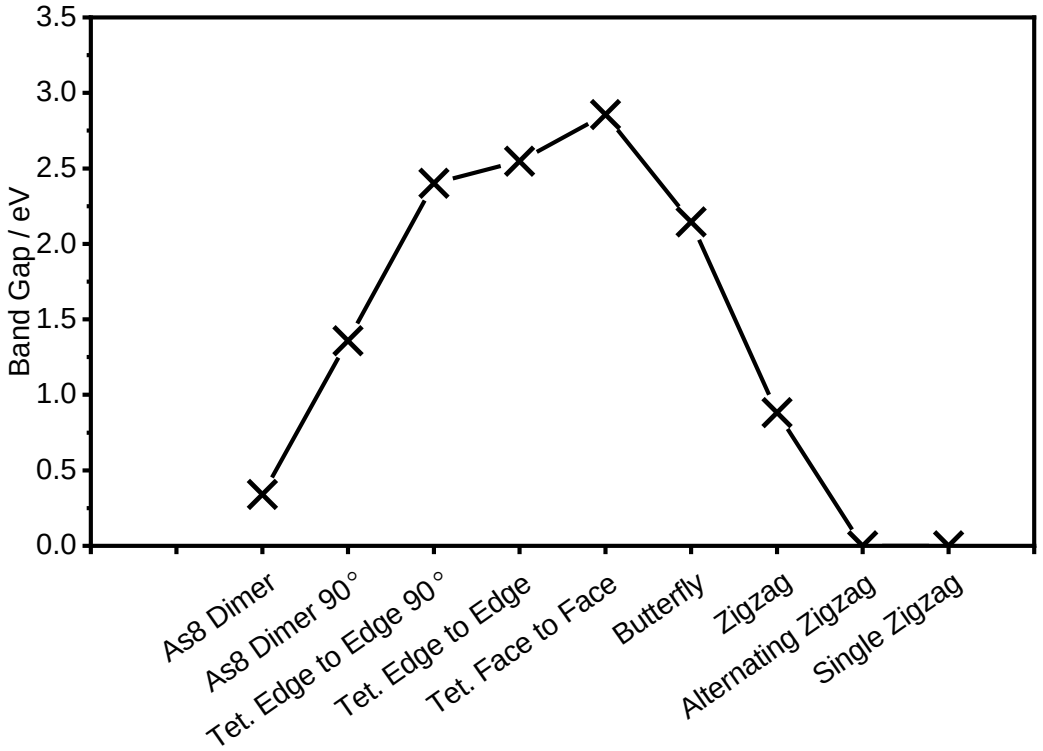

Figure 4.19 Band gaps of the potential structures of the filling materials generated from Density of States calculations performed by Ji Chen.

XPS can also reveal if charge transfer has occurred. The fit of the carbon 1 s region can reveal if any of the contributing regions have shifted which can indicate if charge transfer has occurred.[54] No shift in the C(0) region can be detected between the empty and filled samples as shown in Figure 4.20. The average position of this peak is 284.20 eV and 284.24 eV for the empty and filled sample respectively. Additionally, the peaks have the same shape, with no broadening or narrowing seen for the filled sample to signal the increased semi-conducting or metallic behaviour of the SWCNTs. This coupled with the Raman data confirms that charge transfer has not occurred in this material.

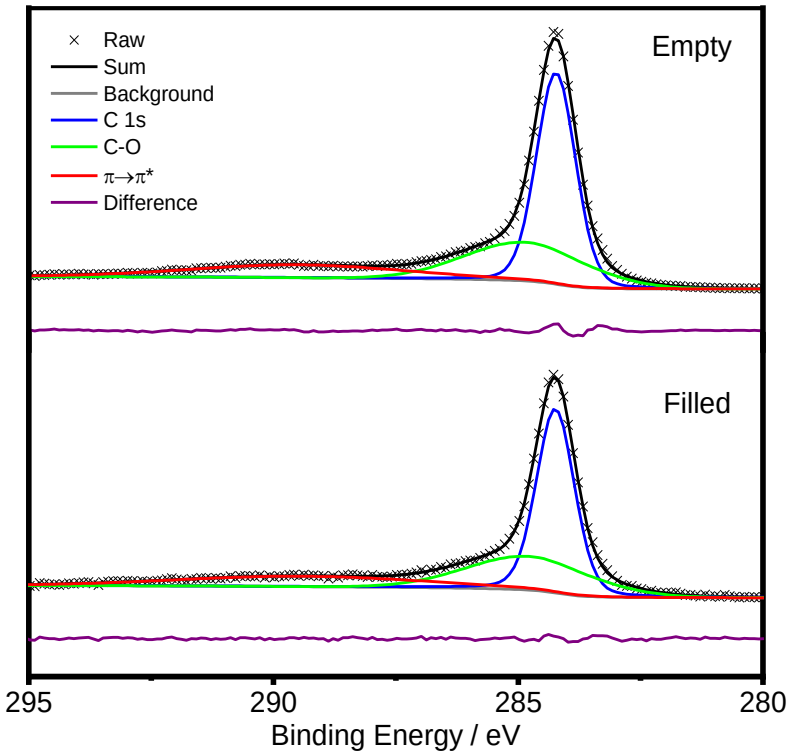

Figure 4.20 High-resolution XPS spectra of the C 1s region for both empty and filled samples.

4.4 Conclusion

Single-Walled Carbon Nanotubes have shown themselves to be excellent containers for the highly poisonous and sensitive arsenic element. They show much higher weight loadings than has been achievable through the use of supramolecular methods[21] and can be emptied conveniently through high temperature and vacuum annealing. Whilst confined, the arsenic can exist in a variety of phases but seem to fill as tetrahedral units and then rearrange into different allotropes depending on the diameter of nanotube in which it resides. DFT has confirmed the identity of the structures seen and reveals that the tetrahedra exist in a metastable state, compared to more stable structures, and may be stabilised due to entropic factors. The two new one-dimensional structures observed may help provide the missing links to between small arsenic clusters and the larger grey and black arsenic sheets. Further characterisation has shown excellent purity of the material, with minimal amounts of oxides being detected and over 90% of the arsenic detected by XPS being confined within the SWCNTs. Initial experiments into the electronic properties of the material have been attempted using Raman and XPS, however, DOS calculations have shown differing characteristics between the nano-structures, from insulating tetrahedral chains, semi-conducting zigzag ladders and metallic single zigzag chain structures. These results demand more thought and

experimentation, with confinement within insulating boron nitride SWCNTs a possibility to truly understand the potential of this material.

4.5 References

1. Rodionov, A.; Kalendarev, R.; Eiduss, J., Photostimulated structural changes in yellow arsenic. *J. Phys.: Con. Mat.* **1995,** *7* (29), 5805.
2. Blakemore, J. S., Semiconducting and other major properties of gallium arsenide. *J. App. Phys.* **1982,** *53* (10), R123-R181.
3. Milnes, A. G.; Polyakov, A. Y., Indium arsenide: a semiconductor for high speed and electro-optical devices. *Mat. Sci. Engin.: B* **1993,** *18* (3), 237-259.
4. Whitaker, J., Electrical properties of n-type aluminium arsenide. *Sol.-State Elec.* **1965,** *8* (8), 649-652.
5. Bagshaw, N. E., Lead alloys: past, present and future. *J. Pow. Sour.* **1995,** *53* (1), 25-30.
6. Mayer, D. R.; Kosmus, W.; Pogglitsch, H.; Mayer, D.; Beyer, W., Essential trace-elements in humans - serum arsenic concentrations in hemodialysis-patients in comparison to healthy controls. *Bio. Trace Elem. Res.* **1993,** *37* (1), 27-38.
7. Greaves, G. N.; Elliott, S. R.; Davis, E. A., Amorphous arsenic. *Adv. Phys.* **1979,** *28* (1), 49-141.
8. Osters, O.; Nilges, T.; Bachhuber, F.; Pielnhofer, F.; Weihrich, R.; Schöneich, M.; Schmidt, P., Synthesis and Identification of Metastable Compounds: Black Arsenic—Science or Fiction? *Angew. Chem. Int. Ed.* **2012,** *51* (12), 2994-2997.
9. Smith, P. M.; Leadbetter, A. J.; Apling, A. J., Structures of orthorhombic and vitreous arsenic. *Philos. Mag.* **1975,** *31* (1), 57-64.
10. Liu, B.; Köpf, M.; Abbas, A. N.; Wang, X.; Guo, Q.; Jia, Y.; Xia, F.; Weihrich, R.; Bachhuber, F.; Pielnhofer, F.; Wang, H.; Dhall, R.; Cronin, S. B.; Ge, M.; Fang, X.; Nilges, T.; Zhou, C., Black Arsenic–Phosphorus: Layered Anisotropic Infrared Semiconductors with Highly Tunable Compositions and Properties. *Ad. Mat.* **2015,** *27* (30), 4423-4429.
11. Kelly, M. J.; Bullett, D. W., Calculation of the electronic structure of crystalline and amorphous arsenic. *Sol. State Comm.* **1976,** *18* (5), 593-595.
12. Zhang, S. L.; Yan, Z.; Li, Y. F.; Chen, Z. F.; Zeng, H. B., Atomically Thin Arsenene and Antimonene: Semimetal-Semiconductor and Indirect-Direct Band-Gap Transitions. *Angew. Chem. Int. Ed.* **2015,** *54* (10), 3112-3115.
13. Kou, L.; Ma, Y.; Tan, X.; Frauenheim, T.; Du, A.; Smith, S., Structural and Electronic Properties of Layered Arsenic and Antimony Arsenide. *J. Phys. Chem. C* **2015,** *119* (12), 6918-6922.
14. Gusmao, R.; Sofer, Z.; Bousa, D.; Pumera, M., Pnictogen (As, Sb, Bi) Nanosheets for Electrochemical Applications Are Produced by Shear Exfoliation Using Kitchen Blenders. *Angew. Chem. Int. Ed.* **2017,** *56* (46), 14417-14422.
15. Vishnoi, P.; Mazumder, M.; Pati, S. K.; Rao, C. N. R., Arsenene nanosheets and nanodots. *New J. Chem.* **2018,** *42* (17), 14091-14095.
16. Nahas, S.; Bajaj, A.; Bhowmick, S., Polymorphs of two dimensional phosphorus and arsenic: insight from an evolutionary search. *Phys. Chem. Chem. Phys.* **2017,** *19* (18), 11282-11288.
17. Mardanya, S.; Thakur, V. K.; Bhowmick, S.; Agarwal, A., Four allotropes of semiconducting layered arsenic that switch into a topological insulator via an electric field: Computational study. *Phys. Rev. B* **2016,** *94* (3).
18. Zhang, J. L.; Zhao, S.; Han, C.; Wang, Z.; Zhong, S.; Sun, S.; Guo, R.; Zhou, X.; Gu, C. D.; Di Yuan, K.; Li, Z.; Chen, W., Epitaxial Growth of Single Layer Blue Phosphorus: A New Phase of Two-Dimensional Phosphorus. *Nano Let.* **2016,** *16* (8), 4903-4908.

19. Curley, J. J.; Piro, N. A.; Cummins, C. C., A Terminal Molybdenum Arsenide Complex Synthesized from Yellow Arsenic. *Inorg. Chem.* **2009,** *48* (20), 9599-9601.
20. Rodionov, A.; Kalendarev, R.; Eiduss, J.; Zhukovskii, Y., Polymerization of molecular (yellow) arsenic. *J. Mol. Struc.* **1996,** *380* (3), 257-266.
21. Schwarzmaier, C.; Schindler, A.; Heindl, C.; Scheuermayer, S.; Peresypkina, E. V.; Virovets, A. V.; Neumeier, M.; Gschwind, R.; Scheer, M., Stabilization of Tetrahedral P4 and As4 Molecules as Guests in Polymeric and Spherical Environments. *Angew. Chem. Int. Ed.* **2013,** *52* (41), 10896-10899.
22. Seitz, A. E.; Hippauf, F.; Kremer, W.; Kaskel, S.; Scheer, M., Facile storage and release of white phosphorus and yellow arsenic. *Nat. Comm.* **2018,** *9* (1), 361.
23. Yang, D.; Zhao, J.; Yu, L.; Lin, X. S.; Zhang, W. Y.; Ma, H. W.; Gogoll, A.; Zhang, Z. B.; Wang, Y. Y.; Yang, X. J.; Wu, B., Air- and Light-Stable P-4 and As-4 within an Anion-Coordination-Based Tetrahedral Cage. *J. Am. Chem. Soc.* **2017,** *139* (16), 5946-5951.
24. Spitzer, F.; Sierka, M.; Latronico, M.; Mastrorilli, P.; Virovets, A. V.; Scheer, M., Fixation and Release of Intact E-4 Tetrahedra (E = P, As). *Angew. Chem. Int. Ed.* **2015,** *54* (14), 4392-4396.
25. Lippa, T. P.; Xu, S. J.; Lyapustina, S. A.; Nilles, J. M.; Bowen, K. H., Photoelectron spectroscopy of As-, As-2(-), As-3(-), As-4(-), and As-5(-). *J. Chem. Phys.* **1998,** *109* (24), 10727-10731.
26. Bai, X.; Zhang, Q. C.; Gao, A. F.; Yang, J. C., Arsenic clusters As-n (n=6-16) and their anions: Structures, thermochemistry, and electron affinities. *Comp. Theo. Chem.* **2013,** *1009*, 94-102.
27. Zhao, J. J.; Zhou, X. L.; Chen, X. S.; Wang, J. L.; Jellinek, J., Density-functional study of small and medium-sized As-n clusters up to n=28. *Phys. Rev. B* **2006,** *73* (11), 10.
28. Seitz, A. E.; Eckhardt, M.; Sen, S. S.; Erlebach, A.; Peresypkina, E. V.; Roesky, H. W.; Sierka, M.; Scheer, M., Different Reactivity of As-4 towards Disilenes and Silylenes. *Angew. Chem. Int. Ed.* **2017,** *56* (23), 6655-6659.
29. Ruck, M.; Hoppe, D.; Wahl, B.; Simon, P.; Wang, Y.; Seifert, G., Fibrous red phosphorus. *Angew. Chem. Int. Ed.* **2005,** *44* (46), 7616-9.
30. Gao, J.; Yuan, Q.; Hu, H.; Zhao, J.; Ding, F., Formation of Carbon Clusters in the Initial Stage of Chemical Vapor Deposition Graphene Growth on Ni(111) Surface. *Journal of Physical Chemistry C* **2011,** *115* (36), 17695-17703.
31. Bondi, A., van der Waals Volumes and Radii. *J. Phys. Chem.* **1964,** *68* (3), 441-451.
32. Bachilo, S. M.; Balzano, L.; Herrera, J. E.; Pompeo, F.; Resasco, D. E.; Weisman, R. B., Narrow (n,m)-distribution of single-walled carbon nanotubes grown using a solid supported catalyst. *J. Am. Chem. Soc.* **2003,** *125* (37), 11186-11187.
33. O'Connell, M. J.; Bachilo, S. M.; Huffman, C. B.; Moore, V. C.; Strano, M. S.; Haroz, E. H.; Rialon, K. L.; Boul, P. J.; Noon, W. H.; Kittrell, C.; Ma, J. P.; Hauge, R. H.; Weisman, R. B.; Smalley, R. E., Band gap fluorescence from individual single-walled carbon nanotubes. *Science* **2002,** *297* (5581), 593-596.
34. Shao, L. D.; Tobias, G.; Huh, Y.; Green, M. L. H., Reversible filling of single walled carbon nanotubes opened by alkali hydroxides. *Carbon* **2006,** *44* (13), 2855-2858.
35. Brown, G.; Bailey, S. R.; Novotny, M.; Carter, R.; Flahaut, E.; Coleman, K. S.; Hutchison, J. L.; Green, M. L. H.; Sloan, J., High yield incorporation and washing properties of halides incorporated into single walled carbon nanotubes. *Appl. Phys. A-Mater. Sci. Process.* **2003,** *76* (4), 457-462.
36. Lannin, J. S., Raman-scattering properties of amorphous As and Sb. *Phys. Rev. B* **1977,** *15* (8), 3863-3871.
37. Marsh, J., New Edinburgh Philos. J: 1836.

38. Gómez-Rodríguez, A.; Beltrán-del-Río, L. M.; Herrera-Becerra, R., SimulaTEM: Multislice simulations for general objects. *Ultramicroscopy* **2010,** *110* (2), 95-104.
39. Chen, J.; Schusteritsch, G.; Pickard, C. J.; Salzmann, C. G.; Michaelides, A., Two Dimensional Ice from First Principles: Structures and Phase Transitions. *Phys. Rev. Lett.* **2016,** *116* (2).
40. Boden, N.; Folland, R., NUCLEAR MAGNETIC SPIN-LATTICE RELAXATION BY SPIN-ROTATIONAL INTERACTION IN PLASTIC CRYSTALLINE WHITE PHOSPHORUS. *Chem. Phys. Let.* **1971,** *10* (2), 167-&.
41. Rodionov, A. N.; Zhukovskii, Y. F.; Kalendarev, R. I.; Eiduss, J. A., Formation of As-8 dimers in molecular solid-state arsenic. *J. Mol. Struc.* **1997,** *410*, 361-364.
42. Vonschnering, H. G., HOMOATOMIC BONDING OF MAIN GROUP ELEMENTS. *Angew. Chem. Int. Ed.* **1981,** *20* (1), 33-51.
43. Shi, L.; Rohringer, P.; Suenaga, K.; Niimi, Y.; Kotakoski, J.; Meyer, J. C.; Peterlik, H.; Wanko, M.; Cahangirov, S.; Rubio, A.; Lapin, Z. J.; Novotny, L.; Ayala, P.; Pichler, T., Confined linear carbon chains as a route to bulk carbyne. *Nat Mater* **2016,** *15* (6), 634-639.
44. Fujimori, T.; dos Santos, R. B.; Hayashi, T.; Endo, M.; Kaneko, K.; Tománek, D., Formation and Properties of Selenium Double-Helices inside Double-Wall Carbon Nanotubes: Experiment and Theory. *ACS Nano* **2013,** *7* (6), 5607-5613.
45. Fujimori, T.; Morelos-Gómez, A.; Zhu, Z.; Muramatsu, H.; Futamura, R.; Urita, K.; Terrones, M.; Hayashi, T.; Endo, M.; Young Hong, S.; Chul Choi, Y.; Tománek, D.; Kaneko, K., Conducting linear chains of sulphur inside carbon nanotubes. *Nat. Comm.* **2013,** *4*, 2162.
46. Kuzmany, H.; Shi, L.; Kürti, J.; Koltai, J.; Chuvilin, A.; Saito, T.; Pichler, T., The growth of new extended carbon nanophases from ferrocene inside single-walled carbon nanotubes. *Physic. Stat. Sol. (RRL)* **2017,** *11* (8), 1700158-n/a.
47. Kuwahara, S.; Kuwahara, Y.; Shinohara, H., Quantitative Analysis of Isolated Single-Wall Carbon Nanotubes with Their Molar Absorbance Coefficients. *J. Nano.* **2014**.
48. Plummer, W. B., Heat of combustion of carbon. *Ind. Engin. Chem.* **1930,** *22*, 630-632.
49. Fan, A. K. L.; Rosenthal, G. H.; Wold, A.; McKinzie, H. L., PREPARATION AND PROPERTIES OF FEAS2 AND FESB2. *J. Sol. State Chem.* **1972,** *5* (1), 136-+.
50. Ozin, G. A., Gas-phase raman spectroscopy of phosphorus, arsenic, and saturated sulphur vapours. *J. Chem. Soc. D-Chem. Comm.* **1969,** (22), 1325-&.
51. Serpell, C. J.; Rutte, R. N.; Geraki, K.; Pach, E.; Martincic, M.; Kierkowicz, M.; De Munari, S.; Wals, K.; Raj, R.; Ballesteros, B.; Tobias, G.; Anthony, D. C.; Davis, B. G., Carbon nanotubes allow capture of krypton, barium and lead for multichannel biological X-ray fluorescence imaging. *Nat. Comm.* **2016,** *7*.
52. Kharlamova, M. V.; Volykhov, A. A.; Yashina, L. V.; Egorov, A. V.; Lukashin, A. V., Experimental and theoretical studies on the electronic properties of praseodymium chloride-filled single-walled carbon nanotubes. *J. Mat. Sci.* **2015,** *50* (16), 5419-5430.
53. Brown, S. D. M.; Corio, P.; Marucci, A.; Dresselhaus, M. S.; Pimenta, M. A.; Kneipp, K., Anti-Stokes Raman spectra of single-walled carbon nanotubes. *Phys. Rev. B* **2000,** *61* (8), R5137-R5140.
54. Kharlamova, M. V.; Niu, J. J., Comparison of metallic silver and copper doping effects on single-walled carbon nanotubes. *Appl. Phys. A-Mater. Sci. Process.* **2012,** *109* (1), 25-29.

5 Comparison of One-Dimensional Pnictogen Allotropes

5.1 Introduction

The pnictogen group is one of the most interesting groups of elements. No other elemental group shares the same variety of structures (excluding nitrogen!), which makes them an excellent group to compare how they behave when confined within a SWCNT. Molecular, black, grey and amorphous variants exist for all, with only the red phosphorus chains being unique to phosphorus. The common structures found for phosphorus and arsenic are displayed in Chapters 3 and 4 respectively. This combination of similarities and unique properties makes the pnictogens interesting to study as the limits of their similarities can be pushed until their unique properties begin to dominate the behaviour seen. The only pnictogens excluded from this study are nitrogen and bismuth. Although bismuth shares the same rhombohedral crystal structure of arsenic and antimony, its metallic nature and high surface tension would not make it favourable to fill nanotubes. An overview of the structures that phosphorus and arsenic possess can be found in chapters 3 and 4.

Antimony is most sought after as a flame retardant, with 60% of the antimony produced in the world being used as flame retardants.[1] Halogenated antimony will react with hydrogen and oxygen which will inhibit fires.[2] Similarly to arsenic, antimony is also used to strengthen lead and can also improve the charging characteristics of lead too making it a useful element for battery manufacturers.[3, 4] It is also interestingly used to produce antifriction alloys which are needed for bearings and other such items.[5]

Antimony, like arsenic, is classed as a metalloid which gives it both metallic and non-metallic characteristics. It is also most thermodynamically stable as the grey allotrope, similarly to arsenic.[6] Black antimony and yellow antimony are the two other main allotropes, and have the same structures as their phosphorus and arsenic equivalents. Molecular antimony can be formed from the oxidation of stibine, SbH_3. This reaction must occur at no higher than 183 K as yellow antimony will convert to grey antimony above this.[7] It is also light sensitive. Antimony vapour has also been proven to exist as Sb_4 molecules up to around 973 K,[8] which is lower than phosphorus and arsenic, which do not show signs of disintegration until 1173 K, and is another example of its increased

instability. Yellow antimony seems to only exist in the vapour phase and has never been condensed. When yellow antimony was attempted to be grown on HOPG, by condensation, only small clusters of antimony located around defect sites in the HOPG could be formed, such is its sensitivity.[9]

Black antimony can be formed from rapidly cooling antimony vapour onto a cool surface. This is also very sensitive and may ignite in air. It also gradually converts back to the grey form over time. The generic structures for the molecular, grey and black allotropes of phosphorus, arsenic and antimony can be found in Chapter 3.

Antimony has a unique "explosive" allotrope which sets it apart from the other pnictogens.[10] This can be formed from the electrolysis of antimony trichloride and will explode when scratched to reform the grey allotrope. This form is in fact amorphous, and the explosion is caused by the recrystallisation of the amorphous antimony. The scratch removes a film of $SbCl_3$ which allows more of the amorphous material to contact each other. Above a critical amount, the antimony recrystallises and explodes. The crystallisation is accompanied by a change in the electronic structure of the material, from semiconducting to semi-metallic.[11]

These are the main 3D allotropes that have been isolated for antimony. Some research has been conducted on 2D antimonene. Like phosphorene and arsenene, antimonene is the 2D layer of antimony that may refer to either a single layer of the grey modification (rhombohedral, β) or the black modification (orthorhombic, α).[6] Monolayers of β-Sb are predicted to show an indirect bandgap, and similarly to arsenic, this will change to a direct bandgap under some strain.[12] Attempts have been made to synthesise antimonene, using both mechanical (scotch tape method) and liquid exfoliation (sonication in an IPA/water solution) techniques.[13, 14] These procedures could produce monolayer antimonene, although the yields of true monolayers was low as expected of these types of techniques. Vapour deposition attempts have shown a variety of results ranging from small clusters of antimony to monolayers of antimony.[9, 15] It has not been until recently that large isolated monolayer antimonene could be grown, using epitaxial methods.[16]

Antimony has seemingly never been stabilised by confinement of any kind. Some very early work claims to have created antimony-filled carbon nanotubes, but due to poor TEM micrographs it is hard to say what structure the encapsulated antimony has adopted.[17] These samples have been formed from arc discharge methods so it is unlikely they "filled" the nanotubes as Sb_4 molecules but were grown in unison.

Considering the success of trapping P_4 and As_4 molecules within polymeric chains,[18] it is surprising that trapping Sb_4 molecules using similar methods has not been attempted.

5.2 Outline of Chapter

The aim of this chapter is to bring together the results from the previous two chapters and to try and draw some comparisons between arsenic and phosphorus filled SWCNTs. Antimony-filled nanotubes will also be introduced to complete the pnictogen filled nanotubes research.

5.3 Results and Discussion

From the data in the previous chapters, and with the inclusion of antimony filled nanotubes, a comprehensive study of the inclusion of pnictogens within different SWCNTs has been achieved. A wide variety of SWCNT diameter ranges have been filled to give a full illustration of the diameter dependence of the filling materials, with CoMoCAT providing <1nm[19] diameters, HiPCO 0.8-1.3nm[20] and Tuball >1.5 nm.[21] The only experiment excluded was filling CoMoCAT with antimony due to the very large radius of the antimony atom.[22] Liquid phase filling experiments using yellow arsenic were not attempted either due to the instability of the material. As the HiPCO filled SWCNTs achieved the highest filling yields; these samples will be used for the bulk of the comparisons.

Many samples have been created in this thesis and will be discussed in this chapter. Below is a reminder of how to understand the sample moniker:

m-P@CNT – SWCNTs filled from the melt of white phosphorus using air sensitive techniques.

v-P@CNT – SWCNTs filled from the vapour of red phosphorus in an ampoule.

v-As@CNT - SWCNTs filled from the vapour of grey arsenic in an ampoule.

m-Sb@CNT - SWCNTs filled from the melt of antimony in an ampoule.

v-Sb@CNT - SWCNTs filled from the vapour of antimony in an ampoule.

The type of SWCNT filled is signified in the name of the sample, for example, *m*-P@Tuball is a sample of Tuball SWCNTs that have been filled with white phosphorus in a melt-phase experiment.

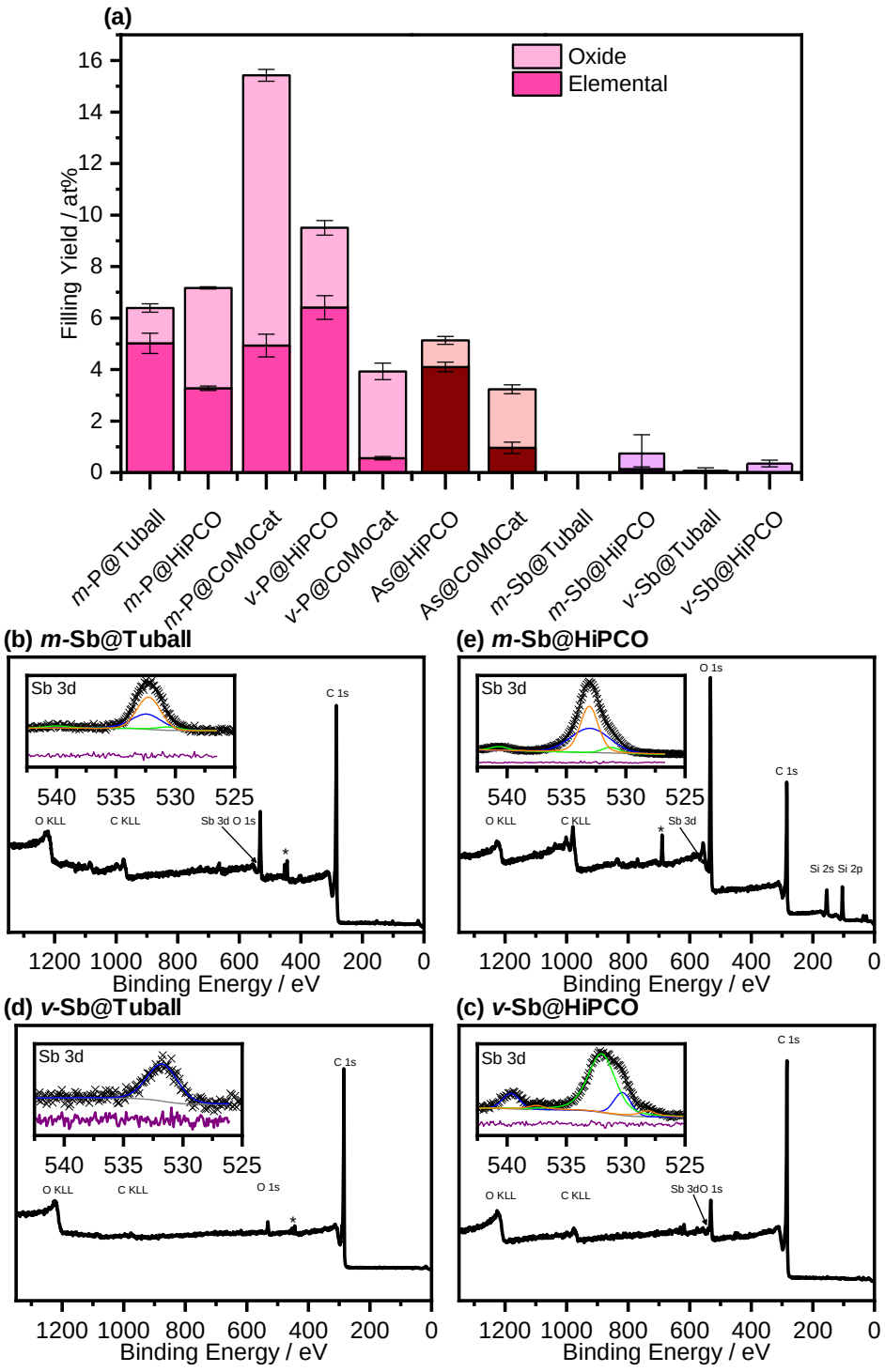

Figure 5.1 (a) Overview of the filling success of pnictogens in various single-wall carbon nanotube types. Filling yields for arsenic and phosphorus samples calculated from fitted XPS spectra in the previous chapters. Filling yields for Sb@CNT generated from fitted XPS spectra in (b-e).

The filling yields for these samples have been calculated from fitted XPS spectra. Due to the sensitivity of these elements to oxygen, or in arsenic and antimony's case to nitric acid, it can be concluded that the oxidised regions for these elements are caused by

external material. The As@HiPCO sample was the only material that showed any external elemental material. This was detected using PXRD and detailed analysis given in Chapter 4 shows that this forms only a small percentage of the arsenic present in the sample. Iron arsenide was also detected but as crystals of $FeAs_2$ have been grown previously from the vapour reaction of iron and arsenic so this result is not unexpected.[23] Despite oxides being consistently present in the samples, they are in a low enough presence to not cause any to be detected by PXRD, so it follows that the overall purity of the samples remains high regardless of the procedure used. No features relating to the internal structures could be detected from this analysis.

With theoretical filling yields of 17 wt% for P and 30 wt% for As in a 9 Å SWCNT, assuming the filling materials retain their tetrahedral molecular structure, both *v*-P@HiPCO and As@HiPCO samples achieve the highest overall filling success of 82% and 67% respectively. However, the results show the various conditions needed to maximise the filling yield depending on the nanotube that is hoped to be filled. For example, when HiPCO SWCNTs are intended to be filled, a vapour-phase experiment seems to outperform the melt-phase procedures, as the comparison between *v*-P@HiPCO and *m*-P@HiPCO shows. When CoMoCAT nanotubes are used though, the liquid phase experiments achieve a better result.

Table 5.1 Filling yield comparison with theoretical values and overall success.

Sample	Filling Yield / wt%	Theoretical / wt%	Filling Success / %
m-P@HiPCO	7	17	41
v-P@HiPCO	14	17	82
As@HiPCO	20	30	67
m-Sb@HiPCO	1	33	3

Melt and vapour phase fillings have been attempted in order to fill SWCNTs with antimony, with neither being successful regardless of which type of nanotube is used. The very low filling yields observed for antimony can be attributed to a number of factors. An obvious observation would be that the size of Sb_4 molecules are much larger than that of the other elements which makes the inclusion more difficult. By approximating the tetrahedra to spheres, the diameter for each pnictogen molecule increases from 4.92 Å to 5.31 Å to 6.12 Å for phosphorus, arsenic and antimony respectively. The arsenic molecule has an 8 % larger diameter than phosphorus, but

antimony has a 15% larger diameter than arsenic. This is a substantial increase and may explain the poor filling yield.

Table 5.2 Atomic radii, bond lengths and tetrahedral diameters for the pnictogens studied in this thesis.

	Atomic Radius / Å	**Bond Length / Å**	**Diameter of Tetrahedron / Å**
Phosphorus	1.80	2.21	4.92
Arsenic	1.85	2.49	5.31
Antimony	2.09	2.91	6.12

However, when larger SWCNTs are used, which should accommodate the tetrahedra comfortably, it still performs poorly. Another reason could be that the surface tension of molten antimony is too high for successful encapsulation. The surface tension for molten antimony is 368 mN m^{-1},[24] and exceeds the theoretical limit for the filling of SWCNTs, 200 mN m^{-1}.[25] Both melt and vapour phase filling of SWCNTs with antimony have been attempted with no great success. Previous attempts at trying to isolate molecular antimony on HOPG resulted in the growth of an eclectic selection of structures around defect sites.[9] This shows the sensitivity and difficulty of controlling this element compared to arsenic and phosphorus and perhaps is why higher filling yields have not been achieved for this element.

Both phosphorus and arsenic have been observed to adopt the same three nanostructures within the SWCNT cavity. These are chains of beads formed by the tetrahedral molecules of P_4 or As_4, a zigzag ladder made from two parallel zigzag chains of atoms and a single zigzag chain. These observations have been confirmed by comparing to HRTEM simulations of the systems created using structures generated from DFT calculations.

The different polymerised structures can be identified by the broadness of the filling material. The zigzag ladder is depicted as a broad feature with a gap visible between the two parallel strands whereas the single zigzag chain can be identified as a very narrow strand. The gap measured is on average 2.38 Å wide for As@HiPCO and 2.43 Å for *v*-P@HiPCO which is converse to what would have been expected. With a shorter bond length and smaller atomic radius, it would have been expected that the phosphorus would have a smaller gap. It seems that because of the larger atomic radius of arsenic, the atoms are forced closer together when confined. Similar results have been observed

in crystals which have shown bond lengths being altered in unexpected ways.[26] Bond lengths have both lengthened and shortened when confined and it seems that the filling material will change its bond lengths in a manner which makes best use of the space available within the cavity.

The structure distributions for each phosphorus and arsenic filled nanotubes can be found in Chapters 3 and 4. Due to the low filling yield of the antimony filled nanotubes, very few examples of filling were observed. As such, it was felt that making similar analysis would be unnecessary. At first glance, it gives confirmation that the SWCNTs that have selected are comprised of the appropriately sized SWCNTs that is expected. The CoMoCAT sample is predominantly made up of SWCNTs within the 0.6 – 0.9 nm range whilst the HiPCO samples show a range of 0.9-1.1 nm. The percentage of filled nanotubes observed matches quite well with the XPS results, with only the white phosphorus filled samples showing much disparity.

Table 5.3 Comparison between the filling yields calculated from TEM and XPS.

Sample	**Filled SWCNTs – TEM / %**	**Filled SWCNTs – XPS / %**
m-P@CoMoCAT	75 (n = 69)	56
m-P@HiPCO	65 (n = 65)	42
v-P@HiPCO	78 (n = 130)	75
As@HiPCO	73 (n = 108)	66

The results gathered from the HRTEM sessions gives reassurances to the DFT calculations (Figures 3.12 (b) and 4.8 (b)). The expected structures for both phosphorus and arsenic at smaller and larger diameters match well with what is seen from TEM with the single zigzag chain being most frequently observed in the 0.7-0.8 nm range and the zigzag ladder dominating at diameters above this. Although these results are, broadly speaking, true, some subtleties can be found between the samples, namely between the *m*-P@HiPCO and *v*-P@HiPCO samples. Despite both procedures being expected to fill the nanotubes with P_4 molecules, differences can be seen between the structure distributions. *m*-P@HiPCO shows only a slight preference for the zigzag ladder to be observed, whereas *v*-P@HiPCO is predominantly filled with zigzag ladder structures; 65% of the filled tubes were filled with the zigzag ladder allotrope. It is presumed that the much higher heat treatment that the sample is exposed to during the filling procedure has caused the filled material to polymerise. In fact, the As@HiPCO sample

has an uncannily similar structure distributions as the *v*-P@HiPCO which is most probably also as a result of the same filling procedure being used for both. This could also cause the much higher filling yields seen in these samples, as at these temperatures the annealing of the SWCNTs becomes a possibility which will prevent an oxidation and leakage of the internal phosphorus during the work up of the sample.[27] If yellow arsenic were more stable, it would have been very interesting to see if the melt filling procedure using yellow arsenic would give a similar result to the *m*-P@HiPCO sample.

Very few examples of SWCNTs filled with antimony were imaged. The micrographs taken, though, seem to indicate that the antimony has adopted a zigzag ladder structure with a clearly defined gap that had an average width of 0.33 nm. This is much larger than the values obtained for phosphorus and arsenic. Considering the much longer bond lengths for antimony and the larger atomic radius (Table 5.2), it makes sense that this value is larger. The nanotube diameters measured for these examples is no larger than what has been recorded for the phosphorus and arsenic samples, and considering the arsenic zizag ladder showed a narrower gap, it would have been expected that the antimony zigzag ladder would follow suit. Another interesting feature is that Figure 5.2 (b) clearly shows two parallel rows of dots. Previously, the filling material has been shown to rotate, due to the blurring of any fine features in the micrographs, with only a faint gap being observed. These rotations will also reduce the size of the gap observed. The presence of dots could only be achieved by a static filling material that is held in position leng enough for an image to be taken and also results in a larger gap being measured. Another reason for the lack of rotation could be caused by the much tighter fit of the antimony in the cavity. This could lead to a distortion of the nanotube itself, to form an elliptical cross-section around the filling material which helps fix the filling material in place. Similar behaviour has been observed before which shows the distortion of the nanotube caused by the filling material.[28]

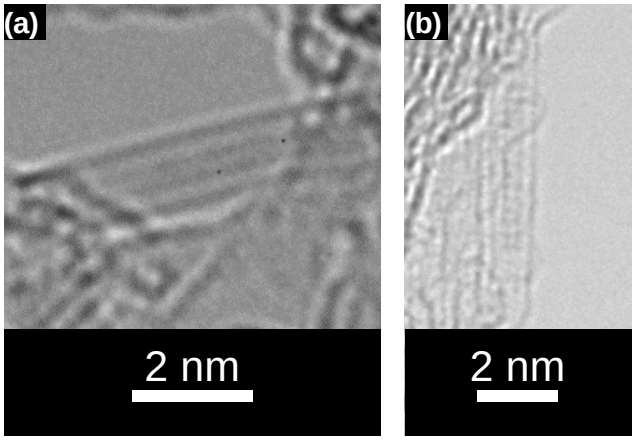

Figure 5.2 Examples of antimony-filled SWCNTs. (a) 1.086 nm diameter SWCNT. (b) 0.963 nm diameter SWCNT.

The relative energies calculated for the structures and for their element can be seen in Figure 5.3. The overall trend shows that energy increases for each structure as the atomic number increases. This also reflects trends observed in the bulk structures. The molecular form becomes increasingly unstable down the pnictogen group. This can be simply explained by the increasing size of the atomic radii putting the bonds within the tetrahedra under greater strain. This allows the conversion to the more stable "grey" allotropes to occur under increasingly less demanding conditions.

The energies for each allotrope tends to increase as the confinement diameter decreases, which is to be expected, as other studies have shown.[29] In fact, stable allotropes of antimony could not even be found at 7 Å due to its instability. The only exception is the single zigzag chain which increases in energy above 9 Å. The structure must be tightly confined in order to exist. The atoms will prefer to form other allotropes which is mirrored in the DFT results. The energy of the single zigzag chain is higher than both other structures from 9 Å so any observations of this structure at larger diameters must be caused by some metastability, especially considering the energy provided by the electron beam.

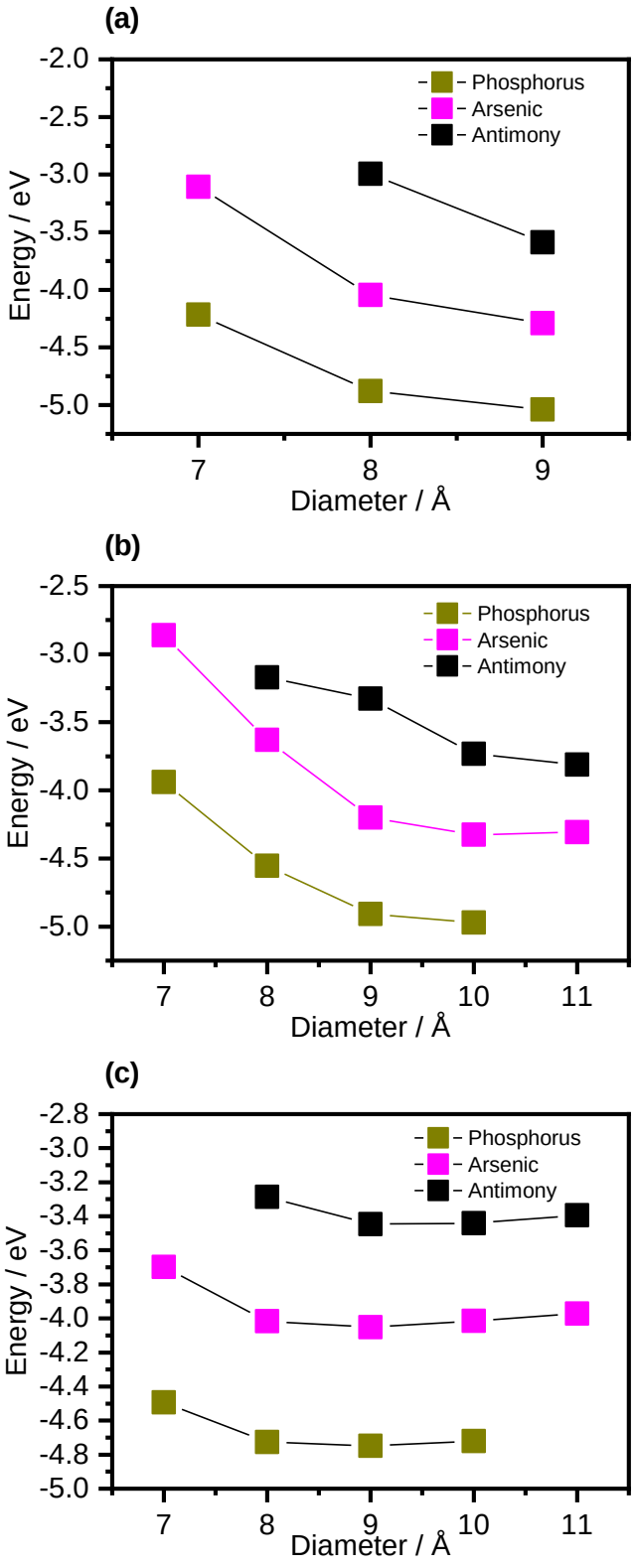

Figure 5.3 DFT analysis showing the energy of the pnictogen allotropes as a function of their confinement for (a) tetrahedra, (b) zigzag ladder and (c) the single zigzag chain. The values for antimony when confined to 7 Å could not be calculated for each structure due to their instability at this confinement.

Electronic band gaps have been calculated for each of the structures, using electronic density of states generated for each structure, which can be found in the appendix. The phosphorus and arsenic allotropes show very similar trends, with the various tetrahedral structures being the most insulating of the allotropes and the structures gradually becoming more metallic as the structure changes from the tetrahedra to the single zigzag chain. Antimony has a slightly different behaviour, although the most transformed structures are still metallic. The *trans* butterfly structure for antimony has the largest band gap. This is thought to be caused by the increased distance between the tetrahedral units after they have bonded to form the *trans* butterfly allotrope.

For both phosphorus and arsenic, adjacent atoms, within neighbouring tetrahedral molecules, are brought closer when they convert to the *trans* butterfly structure. This will aid electron hopping between adjacent atoms in the molecules, due to their closer proximity, which causes a reduction in the band gap. The opposite behaviour is seen for antimony, as the bond length is much longer for antimony. This pushes the adjacent atoms in neighbouring molecules away during the conversion and hinders the electron hopping process, causing a larger band gap.

It had been hoped that these results would help shed light on any charge transfer effects that may have been discovered through Raman spectroscopy. However, as seen from the previous chapters, there appears to have been little to no evidence of any charge transfer effects. This has been justified by the presence of oxides causing opposing effects which may dwarf any charge transfer occurring between the filling material and SWCNT. The evidence of dynamic behaviour from TEM also confuses matters. The electronic behaviour of the various structures ranges from semi-conducting to metallic which will have contrasting charge transfer effects which adds an extra level of difficulty in assessing the results.

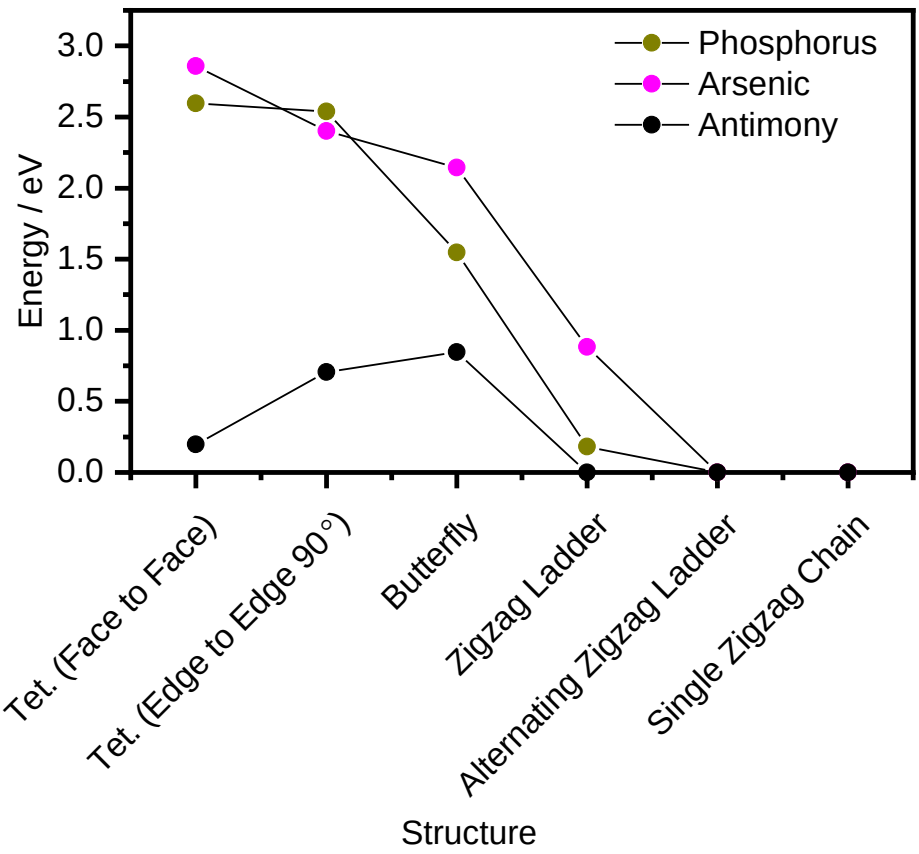

Figure 5.4 Electronic band gaps of the confined structures generated from Density of States calculations that can be found in the Appendix.

5.4 The Single Zigzag Chain

With the addition of three new encapsulated elements, it is perhaps a good time to reflect on other elements that have been confined and their similarities.

The examples shown throughout this thesis have shown that phosphorus, arsenic and antimony all undergo reactions within the SWCNT to form chains of atoms. Reactions within SWCNTs are nothing new. One of the very first publications showed how ruthenium can be reduced by the action of hydrogen.[30] However, the structures of most confined materials are generally very similar to the bulk material.[26] The need to maintain the stoichiometry of the material may be the driving force as to why the confined crystals do not differ too much, providing enough room exists.[31]

Elemental species do not have this constraint. The various clusters and allotropes that have been created show that pure elements have more flexibility when it comes to the types of structures that they can form.[32, 33] It is here that the true potential of SWCNTs as moulds can be seen. Carbon has been contained within CNTs in many forms, most notably as C_{60} fullerenes.[34] These peapods are prone to break down and form new

structures that fit within the cavity of the SWCNT.[35] When carbon is confined within narrower nanotubes, linear chains can form.[29] Nano-diamonds have also been created in mid-sized nanotubes from the polymerisation of halogenated diamantane.[36]

As carbon has the most bulk allotropes, it is not surprising that this is also reflected in the types of structures that have been detected in SWCNTs. Most other main block elements have shown chains of atoms, from one strand to up to three strands. Iodine was the first to show such features,[37] but sulfur,[38] selenium,[39] tellurium and now phosphorus and arsenic can be added.[40] S@CNTs has shown very similar structures to P@CNT and As@CNT, with a single zigzag chain being observed. In the very narrowest of cavities, that of a DWCNT, a straight linear chain is observed. Perhaps with similar nanotubes the same could be created but with P and As.

Some key non-metal elements have yet to be encapsulated within SWCNTs. Bromine has been predicted to be stable as helical chains within SWCNTs,[41] and has been found within the interstitial sites of nanotube bundles as polymeric chains.[42] Chlorine seems to have also not been encapsulated yet and perhaps surprisingly, boron has yet to be confined in SWCNTs either. This means that the vast bulk of the main group elements have now been encapsulated and have shown to show the same variation of structures.

5.5 Conclusion

The confined phosphorus and arsenic display similar structures with tetrahedra, zigzag ladders and single zigzag chains all being observed within the nanotubes. Confined antimony has also been achieved for the first time, although in very low filling yields, and seems to also adopt the zigzag ladder. Differences within the features of the structures observed seem to indicate that the zigzag ladder that antimony adopts may not be rotating, but instead has distorted the nanotube into an ellipse to accommodate the structure.

The occurrence of each structure when observed by HRTEM has been corroborated with DFT calculations of the confined structures, when some consideration of the energy of the electron beam is accounted for. New amorphous phosphorus structures have also been achieved when confined within larger SWCNTs that allow more freedom of movement for the atoms. The energies of these structures show trends that would be expected of the pnictogens, with the phosphorus structures being the most stable allotropes and antimony the least. The electronic properties of these new structures have also begun to be examined and show the genral trend that the most polymerised structures are metallic. These can have profound effects in the doping of SWCNTs and

adds to the vast number of filling materials that show similar behaviour. More experimenting needs to be conducted to confirm this but it shows the potential these materials have and the expands the potential library of filled nanotubes that can be used to create bespoke electronic devices based on the level of doping that is required.

5.6 References

1. Butterman, W. C.; Carlin Jr, J. F. *Mineral Commodity Profiles: Antimony*; 2003-19; 2004.
2. Weil, E. D.; Levchik, S. V., *Flame Retardants for Plastics and Textiles: Practical Applications*. Hanser: 2009.
3. Grund, S. C.; Hanusch, K.; Breunig, H. J.; Wolf, H. U., *Antimony and Antimony Compounds*. 2006.
4. Kiehne, H. A., *Battery Technology Handbook*. CRC Press: 2003.
5. Williams, R. S., *Principles of Metallography*. Read Books: 2007.
6. Pumera, M.; Sofer, Z., 2D Monoelemental Arsenene, Antimonene, and Bismuthene: Beyond Black Phosphorus. *Ad. Mat.* **2017,** *29* (21).
7. Stock, A.; Guttmann, O., Concerning antimony hydrogen and yellow antimony. *Berichte Der Deutschen Chemischen Gesellschaft* **1904,** *37*, 885-900.
8. Rosenblatt, G. M., The composition of antimony vapor. *J. Phys. Chem.* **1962,** *66* (11), 2259-2260.
9. Kushvaha, S. S.; Yan, Z.; Xiao, W.; Wang, X. S., Surface morphology of crystalline antimony islands on graphite at room temperature. *J. Phys.-Cond. Mat.* **2006,** *18* (13), 3425-3434.
10. Aymerich, F. M.; Delunas, A., Explosive semiconductor-semimetal transition of antimony. *Phys. Stat. Sol. a-App. Res.* **1975,** *31* (1), 165-170.
11. Taft, E.; Apker, L., Fermi level in amorphous antimony films. *Phys. Rev.* **1954,** *96* (6), 1496-1497.
12. Zhang, S.; Yan, Z.; Li, Y.; Chen, Z.; Zeng, H., Atomically Thin Arsenene and Antimonene: Semimetal-Semiconductor and Indirect-Direct Band-Gap Transitions. *Angew. Chem. Int. Edit.* **2015,** *54* (10), 3112-3115.
13. Ares, P.; Aguilar-Galindo, F.; Rodriguez-San-Miguel, D.; Aldave, D. A.; Diaz-Tendero, S.; Alcami, M.; Martin, F.; Gomez-Herrero, J.; Zamora, F., Mechanical Isolation of Highly Stable Antimonene under Ambient Conditions. *Ad. Mat.* **2016,** *28* (30), 6332-+.
14. Gibaja, C.; Rodriguez-San-Miguel, D.; Ares, P.; Gomez-Herrero, J.; Varela, M.; Gillen, R.; Maultzsch, J.; Hauke, F.; Hirsch, A.; Abellan, G.; Zamora, F., Few-Layer Antimonene by Liquid-Phase Exfoliation. *Angew. Chem. Int. Edit.* **2016,** *55* (46), 14343-14347.
15. Kim, S. H.; Jin, K. H.; Park, J.; Kim, J. S.; Jhi, S. H.; Yeom, H. W., Topological phase transition and quantum spin Hall edge states of antimony few layers. *Sci. Rep.* **2016,** *6*, 7.
16. Ares, P.; Palacios, J. J.; Abellan, G.; Gomez-Herrero, J.; Zamora, F., Recent Progress on Antimonene: A New Bidimensional Material. *Ad. Mat.* **2018,** *30* (2), 27.
17. Loiseau, A.; Pascard, H., Synthesis of long carbon nanotubes filled with Se, S, Sb and Ge by the arc method. *Chem. Phys. Lett.* **1996,** *256* (3), 246-252.
18. Schwarzmaier, C.; Schindler, A.; Heindl, C.; Scheuermayer, S.; Peresypkina, E. V.; Virovets, A. V.; Neumeier, M.; Gschwind, R.; Scheer, M., Stabilization of Tetrahedral P4 and As4 Molecules as Guests in Polymeric and Spherical Environments. *Angew. Chem. Int. Ed.* **2013,** *52* (41), 10896-10899.

19. Bachilo, S. M.; Balzano, L.; Herrera, J. E.; Pompeo, F.; Resasco, D. E.; Weisman, R. B., Narrow (n,m)-distribution of single-walled carbon nanotubes grown using a solid supported catalyst. *J. Am. Chem. Soc.* **2003,** *125* (37), 11186-11187.
20. O'Connell, M. J.; Bachilo, S. M.; Huffman, C. B.; Moore, V. C.; Strano, M. S.; Haroz, E. H.; Rialon, K. L.; Boul, P. J.; Noon, W. H.; Kittrell, C.; Ma, J. P.; Hauge, R. H.; Weisman, R. B.; Smalley, R. E., Band gap fluorescence from individual single-walled carbon nanotubes. *Science* **2002,** *297* (5581), 593-596.
21. Clancy, A. J.; White, E. R.; Tay, H. H.; Yau, H. C.; Shaffer, M. S. P., Systematic comparison of conventional and reductive single-walled carbon nanotube purifications. *Carbon* **2016,** *108*, 423-432.
22. Bondi, A., van der Waals Volumes and Radii. *J. Phys. Chem.* **1964,** *68* (3), 441-451.
23. Fan, A. K. L.; Rosenthal, G. H.; Wold, A.; McKinzie, H. L., Preparation and properties of FeAs2 and FeSB2. *J. Sol. State Chem.* **1972,** *5* (1), 136-+.
24. Moser, Z.; Gasior, W.; Pstrus, J.; Ishihara, S.; Liu, X. J.; Ohnuma, I.; Kainuma, R.; Ishida, K., Surface tension and density measurements of Sn-Ag-Sb liquid alloys and phase diagram calculations of the Sn-Ag-Sb ternary system. *Mat. Trans.* **2004,** *45* (3), 652-660.
25. Dujardin, E.; Ebbesen, T. W.; Hiura, H.; Tanigaki, K., Capillarity and wetting of carbon nanotubes. *Science* **1994,** *265* (5180), 1850-1852.
26. Sloan, J.; Friedrichs, S.; Meyer, R. R.; Kirkland, A. I.; Hutchison, J. L.; Green, M. L. H., Structural changes induced in nanocrystals of binary compounds confined within single walled carbon nanotubes: a brief review. *Inorg. Chim. Acta* **2002,** *330*, 1-12.
27. Geng, H. Z.; Zhang, X. B.; Mao, S. H.; Kleinhammes, A.; Shimoda, H.; Wu, Y.; Zhou, O., Opening and closing of single-wall carbon nanotubes. *Chem. Phys. Lett.* **2004,** *399* (1-3), 109-113.
28. Kuzmany, H.; Shi, L.; Kurti, J.; Koltai, J.; Chuvilin, A.; Saito, T.; Pichler, T., The growth of new extended carbon nanophases from ferrocene inside single-walled carbon nanotubes. *Phys. Status Solidi-Rapid Res. Lett.* **2017,** *11* (8), 7.
29. Shi, L.; Rohringer, P.; Suenaga, K.; Niimi, Y.; Kotakoski, J.; Meyer, J. C.; Peterlik, H.; Wanko, M.; Cahangirov, S.; Rubio, A.; Lapin, Z. J.; Novotny, L.; Ayala, P.; Pichler, T., Confined linear carbon chains as a route to bulk carbyne. *Nat Mater* **2016,** *15* (6), 634-639.
30. Sloan, J.; Hammer, J.; Zwiefka-Sibley, M.; Green, M. L. H., The opening and filling of single walled carbon nanotubes (SWTs). *Chem. Comm.* **1998,** (3), 347-348.
31. Sloan, J.; Kirkland, A. I.; Hutchison, J. L.; Green, M. L. H., Aspects of crystal growth within carbon nanotubes. *Comptes Rendus Physique* **2003,** *4* (9), 1063-1074.
32. Vonschnering, H. G., HOMOATOMIC BONDING OF MAIN GROUP ELEMENTS. *Angew. Chem.-Int. Edit.* **1981,** *20* (1), 33-51.
33. Hoffmann, R.; Kabanov, A. A.; Golov, A. A.; Proserpio, D. M., Homo Citans and Carbon Allotropes: For an Ethics of Citation. *Angew. Chem. Int. Ed.* **2016,** *55* (37), 10962-10976.
34. Smith, B. W.; Monthioux, M.; Luzzi, D. E., Encapsulated C-60 in carbon nanotubes. *Nature* **1998,** *396* (6709), 323-324.
35. Luzzi, D. E.; Smith, B. W., Carbon cage structures in single wall carbon nanotubes: a new class of materials. *Carbon* **2000,** *38* (11-12), 1751-1756.
36. Nakanishi, Y.; Omachi, H.; Fokina, N. A.; Schreiner, P. R.; Kitaura, R.; Dahl, J. E. P.; Carlson, R. M. K.; Shinohara, H., Template Synthesis of Linear-Chain Nanodiamonds Inside Carbon Nanotubes from Bridgehead-Halogenated Diamantane Precursors. *Angew. Chem.-Int. Edit.* **2015,** *54* (37), 10802-10806.
37. Guan, L.; Suenaga, K.; Shi, Z.; Gu, Z.; Iijima, S., Polymorphic Structures of Iodine and Their Phase Transition in Confined Nanospace. *Nano Let.* **2007,** *7* (6), 1532-1535.

38. Fujimori, T.; Morelos-Gómez, A.; Zhu, Z.; Muramatsu, H.; Futamura, R.; Urita, K.; Terrones, M.; Hayashi, T.; Endo, M.; Young Hong, S.; Chul Choi, Y.; Tománek, D.; Kaneko, K., Conducting linear chains of sulphur inside carbon nanotubes. *Nat. Comm.* **2013,** *4*, 2162.
39. Fujimori, T.; dos Santos, R. B.; Hayashi, T.; Endo, M.; Kaneko, K.; Tománek, D., Formation and Properties of Selenium Double-Helices inside Double-Wall Carbon Nanotubes: Experiment and Theory. *ACS Nano* **2013,** *7* (6), 5607-5613.
40. Medeiros, P. V. C.; Marks, S.; Wynn, J. M.; Vasylenko, A.; Ramasse, Q. M.; Quigley, D.; Sloan, J.; Morris, A. J., Single-Atom Scale Structural Selectivity in Te Nanowires Encapsulated Inside Ultranarrow, Single-Walled Carbon Nanotubes. *Acs Nano* **2017,** *11* (6), 6178-6185.
41. Yao, Z.; Liu, C. J.; Lv, H.; Yang, X. B., Package of double helical bromine chains inside single-walled carbon nanotubes. *Mod. Phys. Lett. B* **2016,** *30* (29), 11.
42. Liu, B. B.; Cui, Q. L.; Yu, M.; Zou, G. T.; Carlsten, J.; Wagberg, T.; Sundqvist, B., Raman study of bromine-doped single-walled carbon nanotubes under high pressure. *J. Phys. Cond. Mat.* **2002,** *14* (44), 11255-11259.

6 Filling Single-Walled Carbon Nanotubes with Aluminium Iodide

6.1 Introduction

Despite the fantastic properties that SWCNTs have, one of their main failings is that they can be quite challenging to functionalise. A pristine SWCNT has two distinct regions with different reactivity to functionalisation, the sidewalls and the tips. Due to the network of sp^2-hybridised carbon in the sidewall, strong conditions are required to break these double bonds.[1] The tips present an easier challenge due to their curvature, inducing strain,[2] and the presence of 5-membered rings.[3] Functionalisation is a necessary process for producing composite materials and for tuning the electronic properties of the nanotube itself. Unmodified SWCNTs are also only soluble in a limited number of solvents which not only limits their potential but these solvents are not within the accepted solvent list that green chemistry tries to promote.[4] There are a number of ways to make SWCNTs more processable though but they generally fall within two approaches: oxidation and then functionalisation or altering of the electronic properties.[1, 5]

The covalent functionalisation of SWCNTs is an extensive field, but two main routes seem to have been developed. First, the amidation or esterification of oxidised SWCNTs and second, using addition chemistry.[1]

Any oxygen containing functional groups (carbonyl, carboxyl, hydroxyl etc.) can be manipulated for further functionalisation. The oxidation of SWCNTs aims to create oxygen containing functional groups along the walls and tips of the SWCNT which can be further manipulated. This can be achieved through thermal or chemical means. Air, CO_2 and H_2O have all been shown to be effective atmospheres in which to cause thermal oxidation.[6-8] Treatment with oxidising acids or peroxides are also commonly used to oxidise SWCNTs and introduce these types of groups onto SWCNTs.[9] The range of modifications using these types of reactions is extensive and many reviews have been written that covers the array of modifications that have been achieved.[10, 11] Unfortunately, although this method is consistent and adaptable, it is at the expense of the integrity of the SWCNT. The more oxidised the SWCNTs are, the more they are

damaged. Control of which tubes get oxidised, and by how much is also a factor that must be accounted for, making these procedures less homogenous.[12]

It must be said though, that the side-walls of the SWCNTs are not always directly functionalised in this way. Oxidised debris, carboxylated carbonaceous fragments,[13] coat the surface of SWCNTs and seem to be the main contributor to the presence of carboxyl- groups in SWCNTs, and are therefore the main species which is effected by functionalisation experiments. The removal of these fragments, by washing in NaOH,[14] lead to highly pure SWCNTs with little presence of these oxidised functional groups. Due to the strong interaction between the oxidised debris and the SWCNTs though, it seems that these washing steps may not be required if the outcome of a functionalisation experiment remains the same regardless of which part is actually functionalised.

Addition directly to the SWCNT is a trickier proposition, but the presence of five membered rings in the tips and defect sites in the sidewall provide points which can be exploited for functionalisation. Chemical modification in this way does require stronger chemicals though.[1] For example, fluorination is a route to creating more reactive sidewalls. By first treating the SWCNTs with fluorine gas at 673 K,[15] the SWCNTs can be functionalised using Grignard reagents and organolithium chemicals.[16] Free-radical reactions have shown promise too, with various species being directly bonded to the sidewall such as organic peroxides, aromatic ketones and perfluorooctyl groups to name a few.[17-20]

A new route that is becoming very popular is to reduce the SWCNT first using Birch reductions,[21] or by using a one-step process, negating the need to use liquid ammonia and sodium to make this an even easier method.[22] SWCNTs in the presence of sodium naphthalide and dimethylacetamide can create nanotubide material that can be functionalised via alkyl halides. In fact, the choice of how to functionalise nanotubide material is broad enough that comparative studies to show the best route to grafting a particular species to SWCNTs can be achieved.[23] In this example, poly(vinyl acetate) was grafted to reduced SWCNTs using either azide, diazonium or bromide terminated polymers to show the effectiveness of each, with the brominated polymer achieving he highest grafting.

Being able to selectively target particular chiralities, diameters, electronic species or even position along the sidewall for functionalisation is a growing trend.[12] For example, diazonium salt additions are seen to cause adjacent sites to the first covalent bond to become more reactive and therefore prone to further functionalisation.[24] The reductive

chemistries described above tend to functionalise metallic SWCNTs,[25] whereas oxidative procedures, especially those concerning hydrogen peroxide, selectively functionalise semi-conducting ones.[26]

Kharlamova *et al.* have shown real progress in how filling SWCNTs with various materials can induce charge transfer effects. Filling SWCNTs with $PrCl_3$,[27] a Lewis acid, shows charge transfer occurring from the SWCNT to the filling material and filling SWCNTs with metals such as copper and silver have shown the reverse.[28] Such is the sensitivity of the SWCNT to charge transfer that a significant difference in the charge transfer effects can be seen between the copper and silver filling. Taking inspiration in the work by Cambré *et al.* developed by separating SWCNTs through ultracentrifugation,[29] Kharlamova *et al.* have been able to create batches of filled tubes that show clear electronic differences to the empty samples.[30] This is a step forward in terms of thinking how filled SWCNTs could be used in an industrial process. If 100% filling cannot be achieved (and increasingly it looks an unlikely prospect, except for fullerene peapods),[31] then filling and removing the empty nanotubes is a compromise that may have to be made.

A comprehensive overview of materials that can have either accepting or donating behaviour when incorporated into SWCNTs is given in Kharmalova's 2016 review.[32] The majority of the acceptor-behaving materials take the form of fullerenes or metal halides. Donor doping materials tend to be either metals or organometallic molecules. Some materials have also shown to have no noticeable charge transfer effects, SnTe being an example where the electronic structures of both materials are left undisturbed.[33]

Much of this work makes use of Raman spectroscopy, optical absorption spectroscopy and XPS to show the charge transfer effects. The G-band shift is a key signifier for charge transfer. Blue-shifts indicate charge transfer from the SWCNT to the filling material and red-shifts indicate the opposite behaviour.[32] The shape of the peak can also reveal the type of doping that has occurred.[27] The broadening of a G-band can indicate that the sample has a more metallic behaviour due to the suppression of the semi-conducting SWCNTs that have undergone charge transfer. The opposite is also true, with a narrower G-band being observed after filling with electron acceptors. This suppresses the metallic components of the G-band and causes the change detected.[34]

Optical absorption spectroscopy cannot reveal the direction of charge transfer, but it can reveal its presence. Peaks in the spectrum often disappear after filling, but the reason for

their disappearance needs corroborating with other data. For example, the disappearance of the E_{11}^{S} peak can be caused by either the downshift of the Fermi level of the SWCNT and the first van Hove singularity of the valence band of the semi-conducting SWCNTs to empty or the Fermi level upshifts and the first van Hove singularity fills completely.[35] This ambiguity makes this technique less useful for understanding charge transfer.

As mentioned earlier, XPS can also be used to show the effects of charge transfer. The C 1s peak can show shifts, broadenings and increases in asymmetry if charge transfer has occurred.[36] The filled samples can show more components caused by the presence of both empty and filled SWCNTs in the sample. Shifts to lower binding energies can be caused by the lowering of the Fermi level due to charge transfer from the SWCNT to the filling material.[32] The reverse can be said too.[28] The reporting of differences between the C 1s peak for semi-conducting and metallic SWCNTs makes the analysis of doping much easier.[37] Up to 5 components can now be used to understand doped SWCNTs, empty and filled semi-conducting nanotubes, empty and filled metallic nanotubes and a fifth being caused by local interactions between the SWCNT and filling material.[38]

6.2 Outline of Chapter

The first aim of this work is to fill SWCNTs with aluminium iodide, a Lewis acid. This material will be fully characterised using the same combination of techniques as described previously. The filling material should induce charge transfer from the SWCNT to the filling material which is theorised to make the SWCNT more attractive to nucleophiles. This should make functionalisation of the material by use of a simple Grignard reagent more effective. It is predicted that the areas of SWCNT wall that are functionalised should take place where the nanotube has been filled. There is also potential for a Moiré pattern to develop where the attached groups follow the crystal structure of the filling material. This could lead onto the ability to control where functionalisation occurs. By changing the filling material to a Lewis acid with a shorter or longer repeat distance, the location of the functional groups should hopefully change to match the filling material.

6.3 Results and Discussion

6.3.1 Maximising the Filling Yield

Tuball SWCNTs were used in these experiments for the same reasons as outlined previously: they are high quality, inexpensive and have a large diameter which can help

with loading. Initial experiments used 10:1 and 5:1 AlI_3 to SWCNT mass ratios and were worked up with water. Although as Figure 6.1 shows, no significant difference in the amount of filling was achieved. XPS has been used to determine the extent of filling once again. For reference, a 1.4 nm wide SWCNT is predicted to have a maximum iodine presence of 8.5 at%. The filling yield is determined from the iodine presence in the sample as the iodine should be present in the Lewis acid. A third of the I at% gives the expected amount of aluminium in the form of the Lewis acid, and the difference between this and the overall aluminium detected are any aluminium impurities that are formed during the purification. As the oxidation state of the aluminium remains unchanged, XPS cannot be used to identify the aluminium impurity, although it should either be an oxide or hydroxide of aluminium.

Figure 6.1 also shows that large amounts of aluminium impurities remain after the purification step. To try and reduce the amount of impurities present, washings in HCl (0.01 M), NaOH (0.01 M) and ethanol were attempted after the filling stage instead of just water. As the 5:1 mass ratio worked equally well to the 10:1 mass ratio, and used less material, this ratio will be continued with for the rest of these experiments. Both base and acid washes have worked well in terms of reducing the impurities but at the expense of lower filling yields. Ethanol was also used as a washing agent. As it is a bulkier solvent than water, it was thought it may create bulkier products that might block the nanotube tips and prevent any hydrolysis of the internal filling material. No improvement was made over the water washings though as seen by the comparable presence of aluminium impurities to the water washings in Figure 6.1.

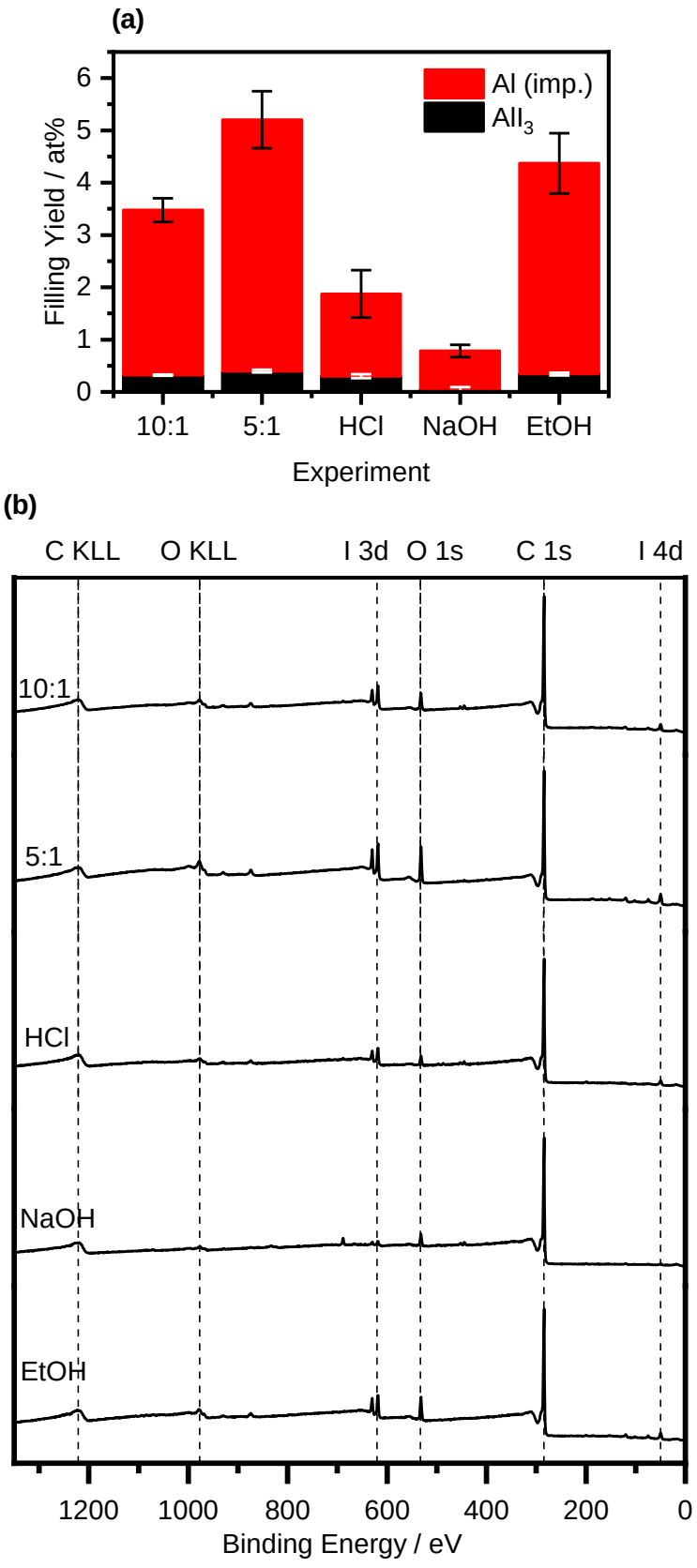

Figure 6.1 (a) Filling yield results for the initial filling experiments using a variety of experiment conditions. (b) XPS survey spectra for initial experiments used to create (a).

ATR-IR has been conducted on a series of samples with a variety of impurity levels and show no noticeable difference to a sample of empty SWCNTs. There is no evidence for any O-H stretching which would signify the presence of $Al(OH)_3$. The only noticeable features are some associated peaks for some background water and carbon dioxide and the C=C stretching for the carbon in the SWCNT. This would make it seem that the impurities present are in the form of aluminium (III) oxide, Al_2O_3.

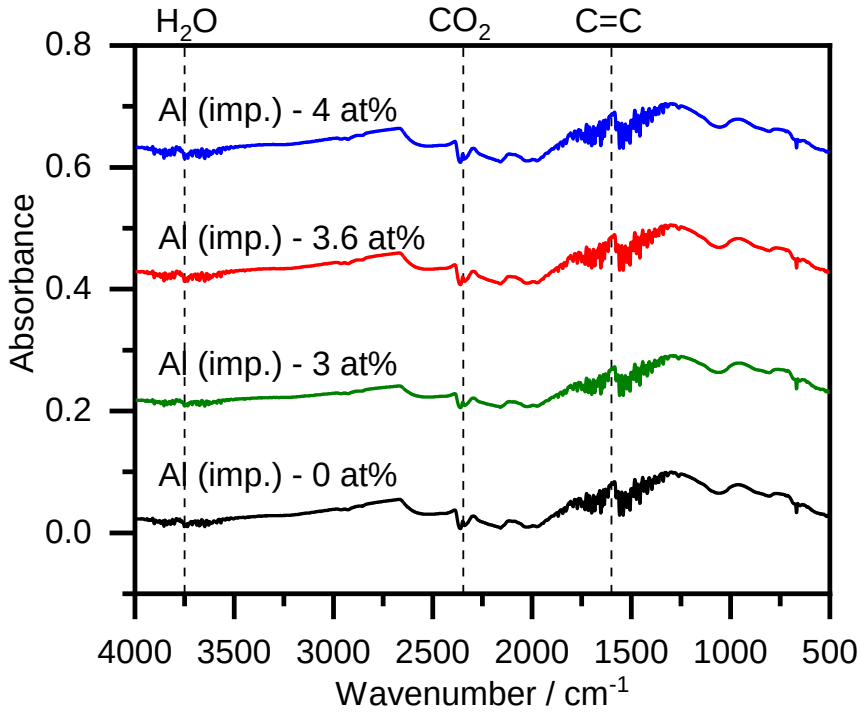

Figure 6.2 Absorbance FT-IR spectra of a range of AlI_3@Tuball samples in comparison to an empty sample of SWCNTs. No discernible difference can be seen between the samples and no noticeable -OH stretching can be detected. This signifies that the aluminium impurities are unlikely to be in the form of $Al(OH)_3$.

The filling material has shown great sensitivity to the purification procedure and so a capping agent is needed to try and provide protection for the filling material during the purification step. C_{60} fullerenes will be used again as they performed well when used to cap the WP@Tuball samples. Ethanol performed the best out of the solvents examined for that work, however, it has just been shown in Figure 6.1 that ethanol will react with the filling material and create lots of aluminium impurities, so a new solvent will be needed. Ideally, both the filling material and fullerenes should have low solubilities in the solvent, but as the Lewis acid will react with any oxygen or nitrogen containing atoms, this limits the possibilities. Aliphatic solvents seemed to be a compromise, and the XPS results in Figure 6.3 reveal that these samples had improved results compared to the non-capped samples. The amount of AlI_3 present in the hexane and cyclohexane

samples were higher than in the uncapped samples in Figure 6.1. The cyclohexane control also confirms this. There are still large amounts of aluminium impurities present in these samples, so the samples were refluxed in HCl. Although there has been a reduction in the AlI_3, there has been a large reduction in the impurities. When comparing the ratio of AlI_3 to the impurities in these refluxed samples with the HCL washed sample in Figure 6.1, it is clear that the capping has helped create improved samples.

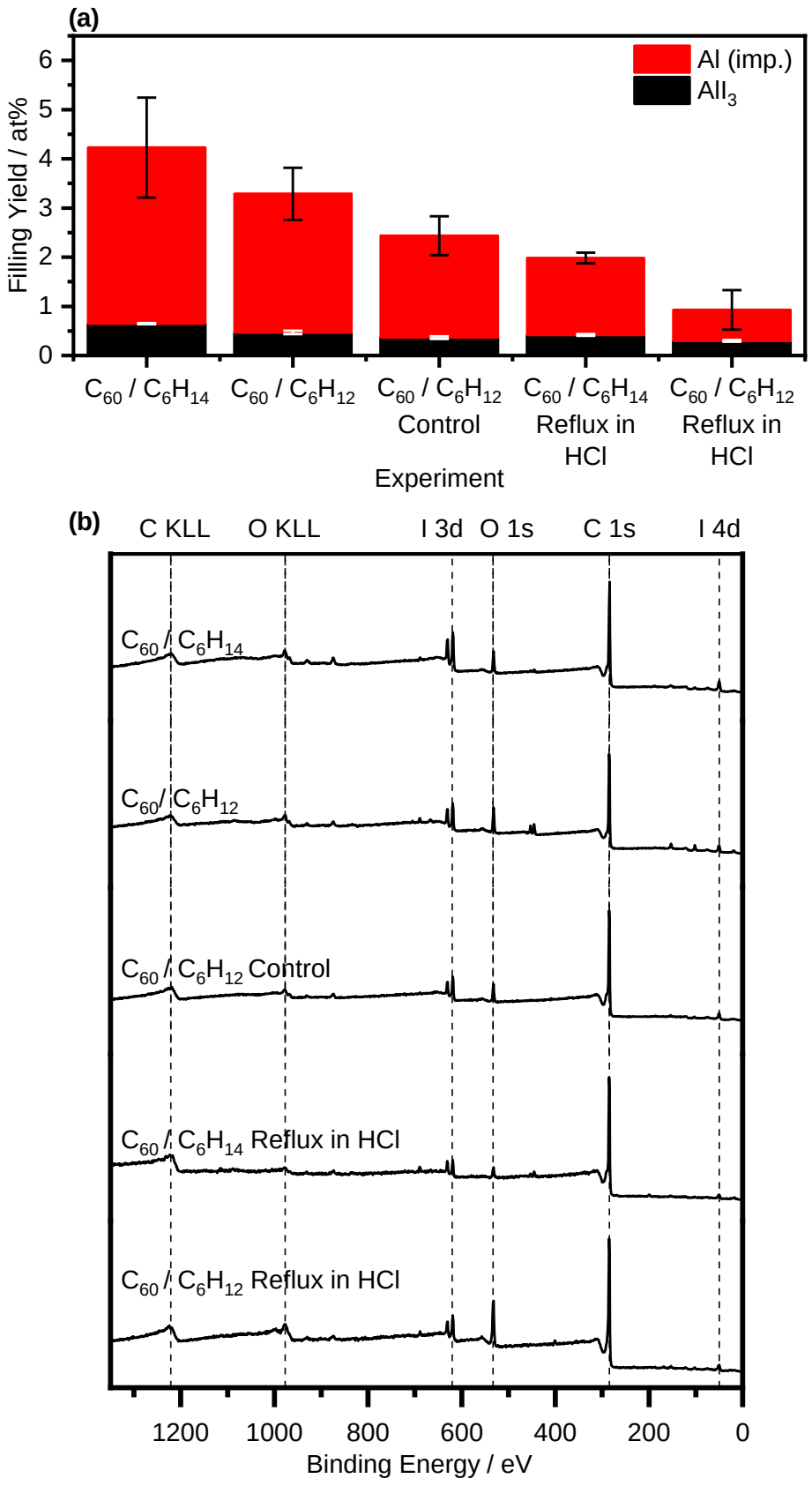

Figure 6.3 (a) Filling yield results for initial capping experiments. (b) XPS survey spectra for capping experiments used to create (a).

Figure 6.4 shows that capping the sample and then refluxing in HCl gives a consistent result. Although the filling yield is low, the ratio of impurity to AlI_3 is the best that could be achieved. Currently, the limiting factor is finding a solvent that will have no interaction with the Lewis acid, either dissolving or reacting with it, to use during the capping step. The solvents used both dissolved some of the AlI_3 which would have affected the filling yield. It has also been shown in the *m*-P@Tuball work that the C_{60} molecules seem to displace some of the filling material which may have also have had an effect here too.

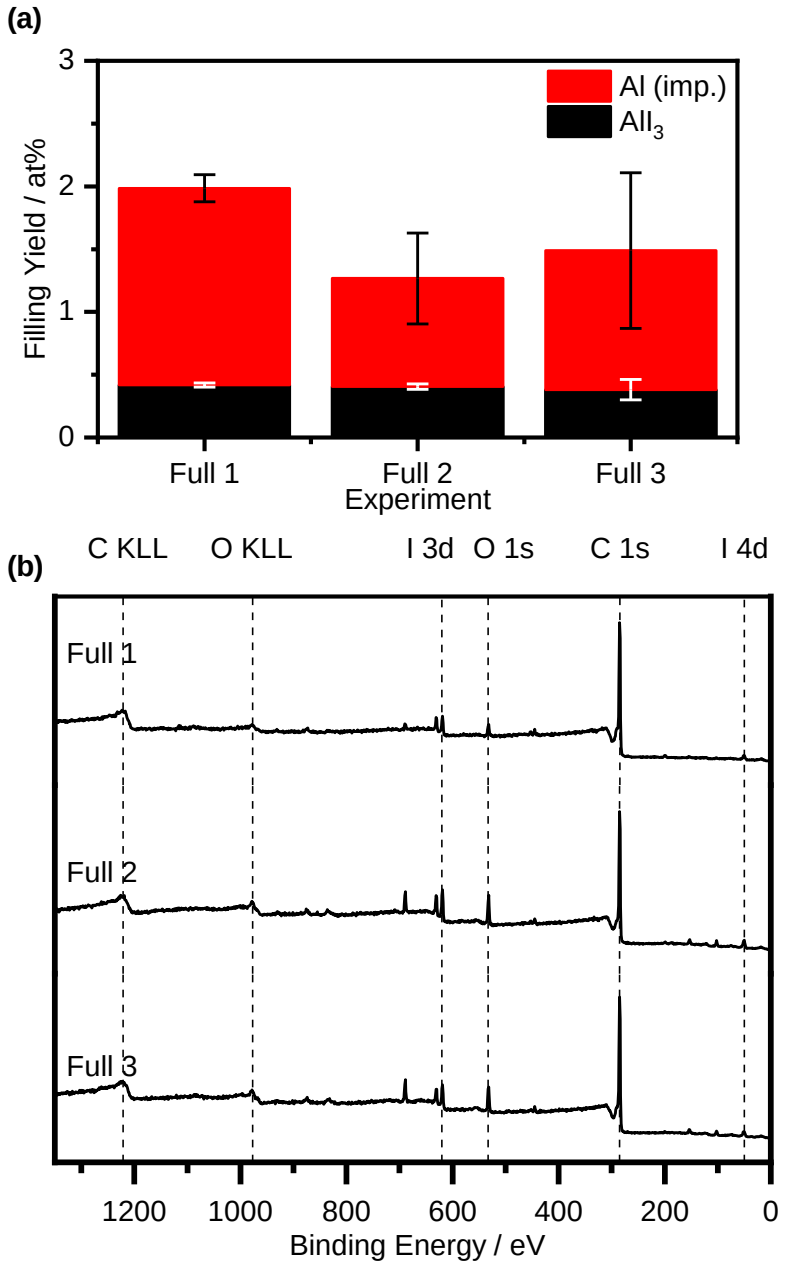

Figure 6.4 (a) Filling yield results for the final procedure. Consistent results have been found when the filled nanotubes are capped with C_{60} and then refluxed in HCl. (b) XPS survey spectra used to generate (a).

6.3.2 Further Characterisation

TGA/DSC of AlI_3@CNT in Figure 6.5 shows a gradual mass loss from the start of the thermogram. The initial mass rise at the very start of the thermogram is caused by buoyancy effects. A drop occurs around 573 K which is above the melting point of the bulk material of 464 K and could be signs of the filling material leaking out.[39] The carbon then begins burning at 823 K.

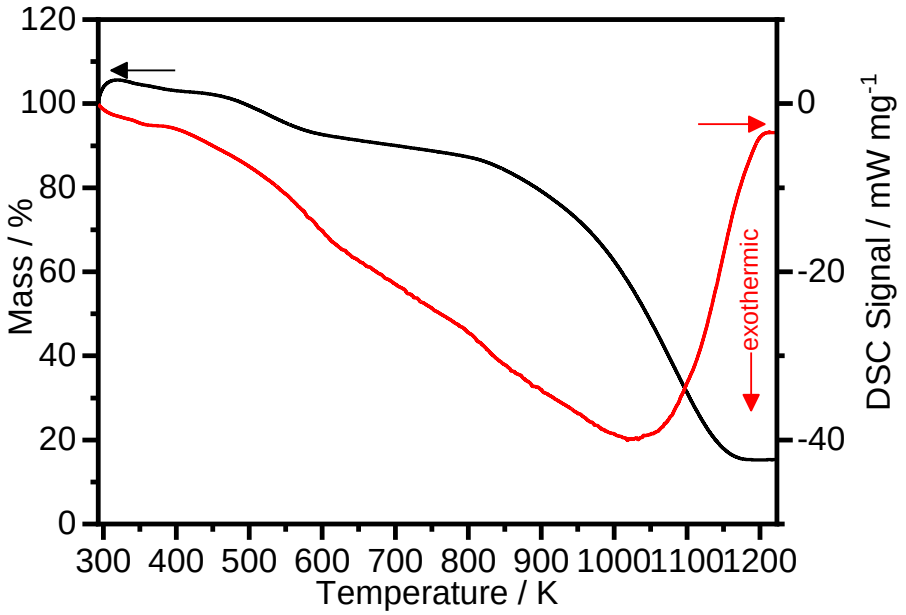

Figure 6.5 TGA/DSC of AlI_3@CNT

PXRD, Figure 6.6, has revealed no crystalline features in this material. Due to the crystalline nature of the filling material and the much heavier elements compared to the previous filling materials, it was hoped that potentially some of the filling material could be detected with this method. The low filling yields most likely account for the lack of peaks. No peaks associated with the aluminium impurity could be detected either.

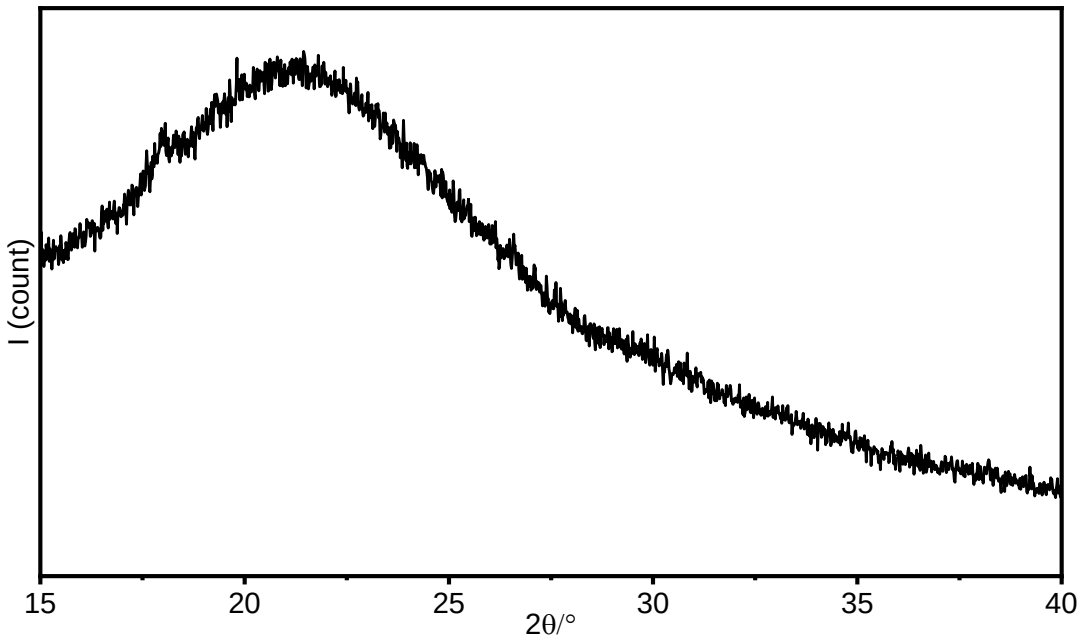

Figure 6.6 PXRD of AlI_3@CNT.

HRTEM has confirmed the microstructure of the confined Lewis acid, Figure 6.7 (a). As with many confined salts, the structure adopted is usually a narrow section of the bulk structure.[40, 41] Some expansion or contraction of the unit cell is usually seen as the material tries to accommodate itself within the nanotube cavity.[40] In this material, the crystal has aligned itself along the 112 (hkl) direction (within a 1.31 nm diameter SWCNT) but has been compressed compared to the bulk material.

Bulk aluminium iodide forms dimers when solid, in a monoclinic crystal system.[42] The dimers have two distinct aluminium iodine bond lengths, with the bridging iodine atoms having a slightly longer bond length of 2.670 Å than the terminal bonds, which are2.456 Å long. Figure 6.6 shows the crystal structure of aluminium iodide.

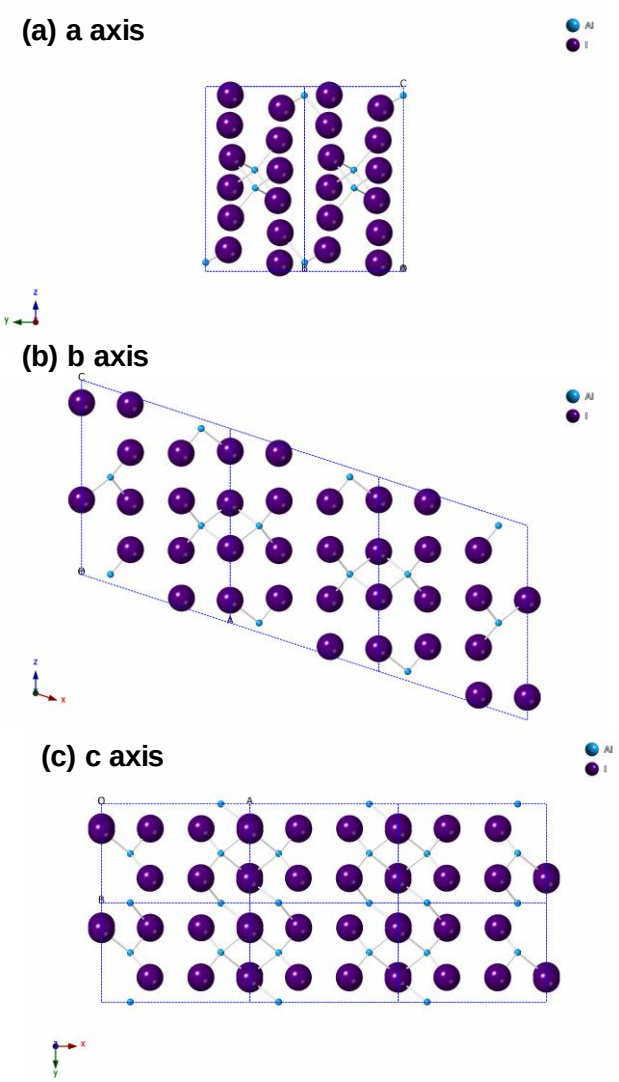

Figure 6.7 (a) Crystal structure of aluminium iodide looking at the a axis, (b) b axis and (c) c axis.

Zoomed sections of the micrograph and simulation highlight how much the crystal structure has been altered in order to accommodate itself within the cavity. It looks as if the rows of atoms have shifted to form perfect hexagonal units as highlighted in Figure 6.7 (d) compared to the bulk material which has a distorted hexagonal pattern in this projection, Figure 6.7 (e).

Few examples could be seen of the filling material. Bundling of the tubes, even after dispersing in NMP, contributed mostly to this problem but impurities (both from the filling procedure, and from remaining amorphous carbon that had survived the purification process) also posed an issue.

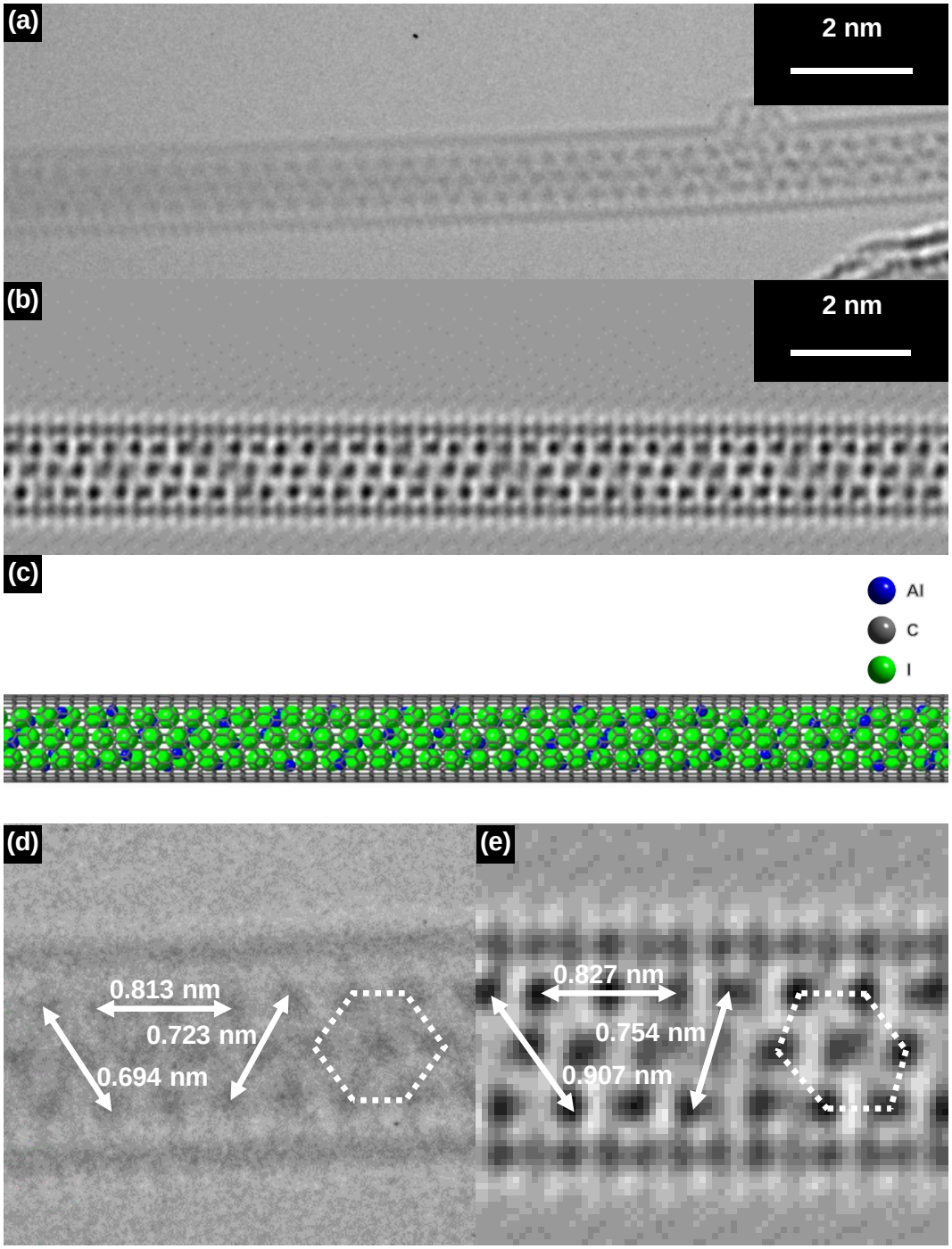

Figure 6.8 (a) HRTEM micrograph of a SWCNT filled with aluminium iodide. (b) HRTEM simulation of (a) using the bulk crystal structure of AlI_3 as the filling material. (c) Atomic model used to create (b). (d) Zoom of a section of (a) with distances highlighted. (e) Zoom of a section of (b) with distances highlighted. Compression of the confined material compared to the bulk can clearly be observed.

The aim of filling these nanotubes with a Lewis acid is to make them more susceptible to functionalisation. Charge transfer from the SWCNT to the Lewis acid will hope to attract nucleophiles at the side-wall and allow functionalisation to occur. As discussed in the previous chapters, Raman spectroscopy is a good way to determine if charge transfer

has occurred. The G-band will show blue or red shifts depending on the direction of the charge transfer. In this case, Raman mapping, in Figure 6.8, has been conducted on both filled SWCNTs and their empty SWCNT starting material to give a wider representation of the charge transfer effects across the sample. The spectra obtained were focussed on the G-band position in order to do this.

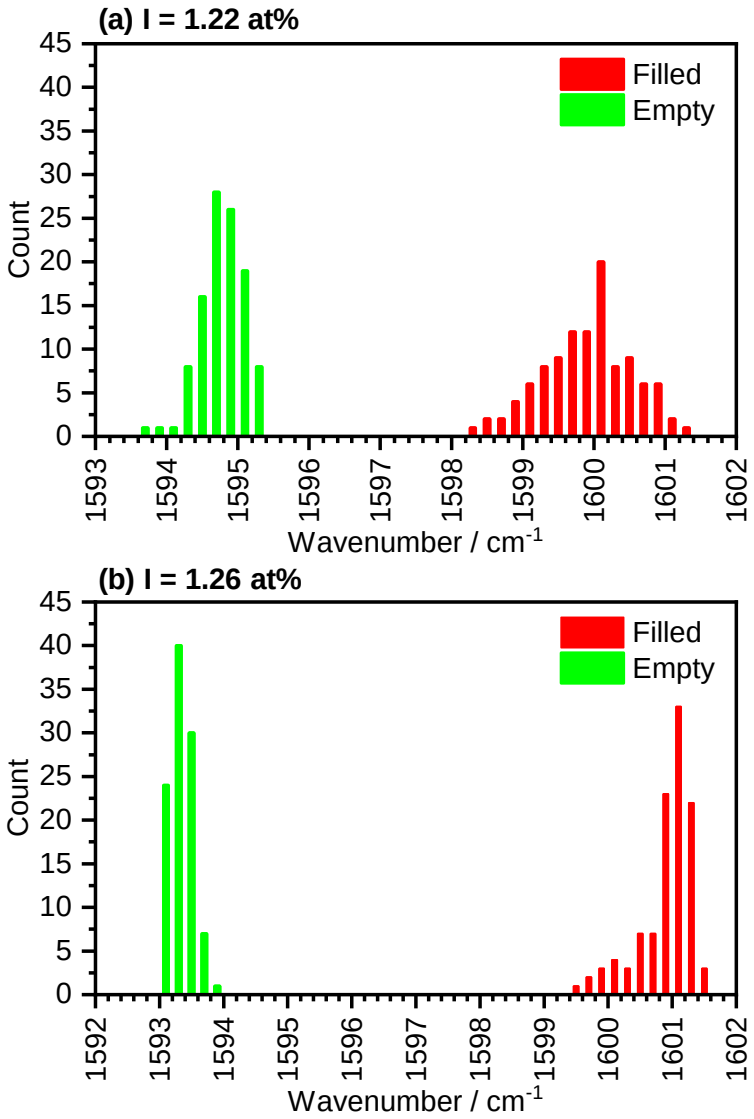

Figure 6.9 Histograms of G-band positions for two filled samples and their empty counterparts determined by Raman mapping spectroscopy.

It is clear to see that the G-band has shifted quite dramatically between the empty and filled samples. The blue shift also indicates that the charge transfer has gone from the SWCNT to the filling material as hoped. The first sample has shown a shift of ~5 cm^{-1} and the second has shown a shift of ~7.5 cm^{-1}. What is interesting is that none of the filled sample showed any empty SWCNTs. It would be expected that occasionally an empty nanotube would be excited and would have a non-shifted G-band. The shift in the G-

bands are not consistent either despite both samples having very similar filling yields. Heterogeneity in the samples may account for this as the mapped regions are still fairly small relative to the bulk sample. It is also known that SWCNTs within a bundle have a lot of influence on one another. This can be both a structural, such as a distortion of the cylindrical cross-section,[43] or electronic influence, such as changing from metallic to semi-conducting behaviour and vice versa.[44] It is therefore plausible that the presence of one filled nanotube could influence the electronic characteristics of other empty nanotubes within the same bundle, hence why all the G-bands appeared shifted in the filled samples.

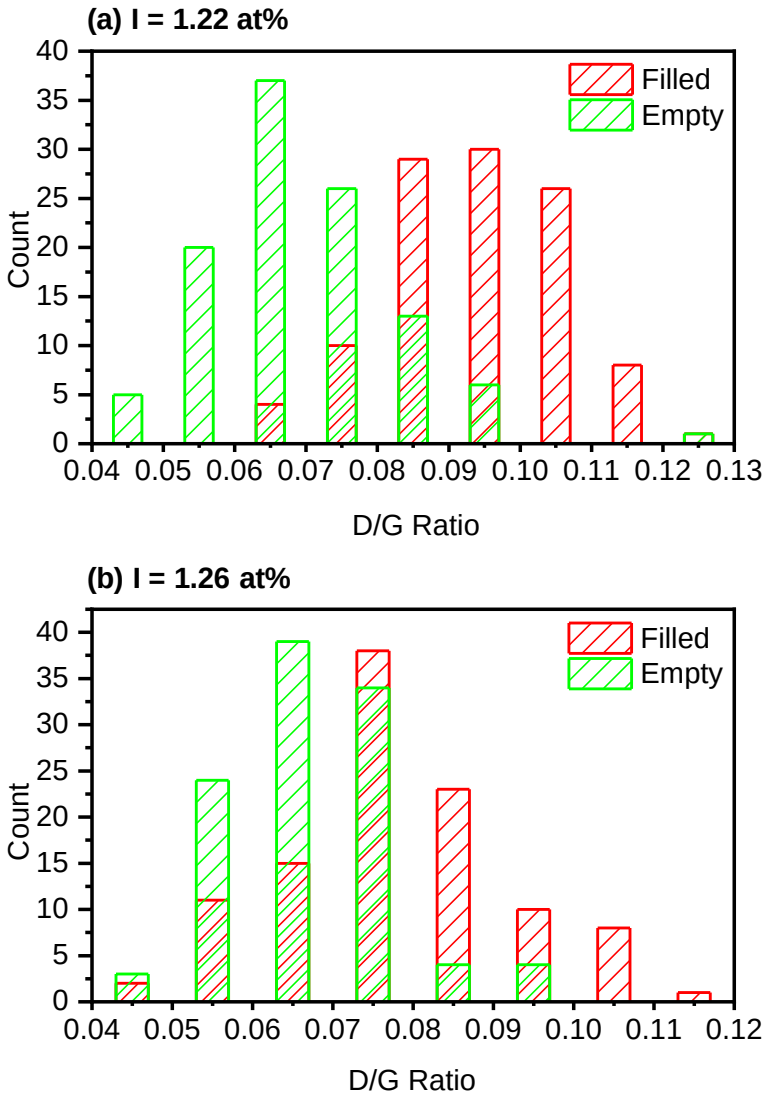

Figure 6.10 Histograms of D/G ratios for two filled samples and their empty counterparts determined by Raman mapping spectroscopy.

D/G ratios, Figure 6.9, of the samples shows that very minimal damage is done to the SWCNTs during the filling process. The very mild conditions of the filling procedure

account for this as the SWCNTs are heated twice under vacuum to no more than 250°C and are refluxed in dilute HCl, which is non-oxidising.

6.3.3 Functionalisation

Raman spectroscopy has proven that charge transfer has occurred in the filled samples. Attempts can now be made at determining if the filling material has made the nanotubes more prone to functionalisation. A simple Grignard reaction has been used to bond a functional group to the SWCNT wall. The Grignard reagent is nucleophilic so should be preferentially attracted to the filled samples as the charge transfer from the nanotube to the Lewis acid should create a net positive charge on the nanotube wall. 2-thienyl magnesium bromide has been chosen as the reagent as the sulfur heteroatom should be easy to detect using XPS.

Figure 6.11 Grignard functionalisation reaction between a SWCNT and the Grignard reagent 2-thienyl magnesium bromide.

Figure 6.12 (a) shows the sulfur content as a function of the iodine content of the sample before functionalisation. It is predicted that the better filled samples should have higher sulfur content as the charge transfer should be better. Raman spectroscopy has already seemingly confirmed that this is not necessarily the case, and the small margin of difference between the amount of filling observed between the samples may not have a noticeable effect with regards to the amount of sulfur detected. Unfortunately, it was also apparent that the filling material leaked out during the functionalisation reaction (Figure 6.12 (b)). The iodine content for the samples after the reaction show a noticeable drop.

The initial experiments combined the Grignard reagent and SWCNTs in THF and sonicated for two hours based on a procedure developed by Boul *et al.*[16] It was first noticed after these reactions that the filling material was leaking out. The prolonged sonication was either breaking the SWCNTs apart, dislodging the C_{60} caps or potentially displacing and impurities that had blocked the open ends of the filled nanotubes. As the filing material leaked out, it would reduce any charge transfer effects that may increase the effectiveness of the reaction. If the result showed a significant increase in sulfur content, then the leakage could be overlooked, as although it would have been interesting to see if the functionalisation occurred next to filled areas of the tube, the

main goal was to improve upon the empty nanotubes. However, this is not the case and it seems the leakage is having a direct effect in the lack of functionalisation seen.

A gentler approach involved combining the materials and stirring them for two hours, again in THF. A similar result was found though, with the filling material leaking out and no improvement over the empty nanotube samples. Leakage is also occurring when the reaction is only stirred for 15 minutes, and again no real improvement is seen in the sulfur content.

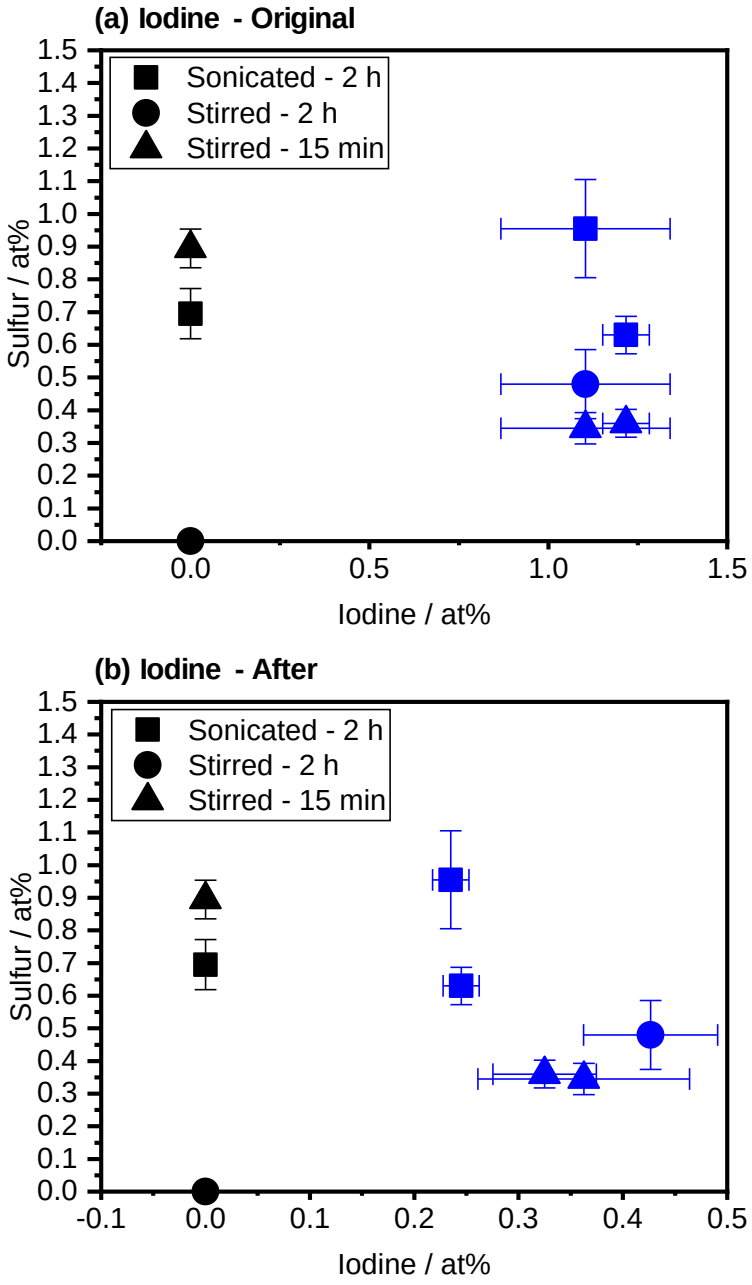

Figure 6.12 Sulfur content as a function of iodine content. (a) Iodine content of sample before reaction. (b) Iodine content of sample after reaction. Black indicates empty SWCNTs, blue indicates filled SWCNTs.

C_{60} is not particularly soluble in THF so it seems odd that the material is so sensitive to this solvent. Aluminium iodide will react with this solvent and will form long chain polymeric molecules from the ring opening of the THF molecule. This would have left behind a viscous product which was not observed during these experiments. Oddly, there was no correlation between the technique used and the extent of leakage as Figure 6.11 shows. The amount of iodine present was similar regardless of the reaction condition, with only the sonication experiment showing significantly less iodine. An alternative idea is that the Grignard reagent is reacting with the C_{60} causing them to "uncork" from the SWCNTs and allowing the filling material to escape. More work will have to be carried out though to confirm this though.

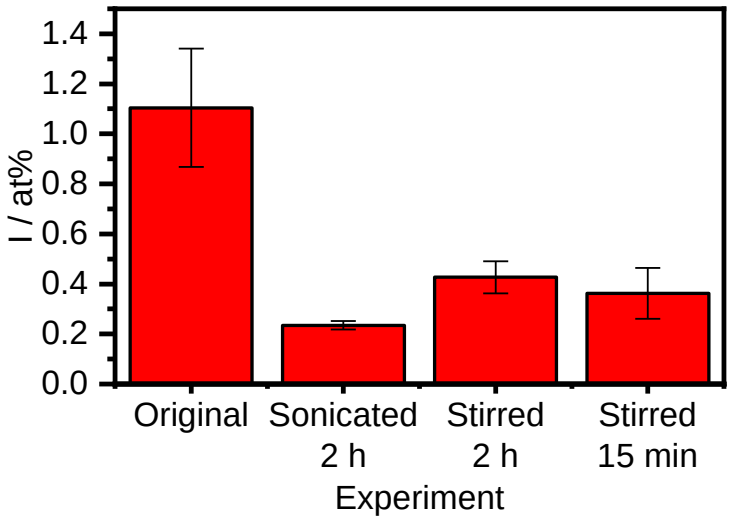

Figure 6.13 Comparison of iodine presence in a sample before and after functionalisation experiments.

6.4 Conclusion

SWCNTs were filled with aluminium iodide to create a composite material that would hopefully show improved functionalisation properties. A consistent procedure was developed which involved capping the sample with C_{60} in cyclohexane and then refluxing the sample in HCl to remove any impurities. The results were shown to be consistent, but the filling yield was still low when compared to the predicted value. HRTEM revealed that the Lewis acid has aligned itself along the 112 axes within a 1.31 nm nanotube but showed some compression when compared to the bulk material. It must be said that it may adopt other structures in differently sized SWCNTs. Few instances could be found when imaging the sample which could be put down to bundling and the presence of impurities in the sample.

Charge transfer was detected by Raman spectroscopy. Consistent blue shifts of the G-band showed that charge transfer from the SWCNT to the filling material was happening as hoped and compared well with the literature.[27] However, due to leakage of the filling material, no significant improvement in the functionalisation of the filled nanotubes was detected. Displacement of the capping agent and other impurities may have allowed leakage to occur, despite the relative insolubility of C_{60} in THF. Reactions between the THF and aluminium iodide may also have occurred which would also reduce its effectiveness. It would be worth investigating these reactions but within different solvent systems, although the narrow range of solvents that C_{60} is insoluble in and would not react with the Lewis acid is narrow.

Charge transfer is an often-touted reason for filling SWCNTs as there is great potential for being able to fine tune the band gap of a nanotube by filling it with a suitable material. However, there is still little work in which takes this to the next level and shows the enhanced properties filled nanotubes have over their empty counterparts. Furthering this work would provide real impetus to the field and prove that filling SWCNTs has real potential.

6.5 References

1. Singh, P.; Campidelli, S.; Giordani, S.; Bonifazi, D.; Bianco, A.; Prato, M., Organic functionalisation and characterisation of single-walled carbon nanotubes. *Chem. Soc. Rev.* **2009,** *38* (8), 2214-2230.
2. Srivastava, D.; Brenner, D. W.; Schall, J. D.; Ausman, K. D.; Yu, M. F.; Ruoff, R. S., Predictions of enhanced chemical reactivity at regions of local conformational strain on carbon nanotubes: Kinky chemistry. *J. Phys. Chem. B* **1999,** *103* (21), 4330-4337.
3. Basiuk, E. V.; Monroy-Pelaez, M.; Puente-Lee, I.; Basiuk, V. A., Direct solvent-free amination of closed-cap carbon nanotubes: A link to fullerene chemistry. *Nano Let.* **2004,** *4* (5), 863-866.
4. Clarke, C. J.; Tu, W. C.; Levers, O.; Brohl, A.; Hallett, J. P., Green and Sustainable Solvents in Chemical Processes. *Chem. Rev.* **2018,** *118* (2), 747-800.
5. Balasubramanian, K.; Burghard, M., Chemically functionalized carbon nanotubes. *Small* **2005,** *1* (2), 180-192.
6. Tobias, G.; Shao, L. D.; Salzmann, C. G.; Huh, Y.; Green, M. L. H., Purification and opening of carbon nanotubes using steam. *J. Phys. Chem. B* **2006,** *110* (45), 22318-22322.
7. Smith, M. R.; Hedges, S. W.; LaCount, R.; Kern, D.; Shah, N.; Huffman, G. P.; Bockrath, B., Selective oxidation of single-walled carbon nanotubes using carbon dioxide. *Carbon* **2003,** *41* (6), 1221-1230.
8. Miyata, Y.; Kawai, T.; Miyamoto, Y.; Yanagi, K.; Maniwa, Y.; Kataura, H., Chirality-dependent combustion of single-walled carbon nanotubes. *J. Phys. Chem. C* **2007,** *111* (27), 9671-9677.
9. Liu, J.; Rinzler, A. G.; Dai, H. J.; Hafner, J. H.; Bradley, R. K.; Boul, P. J.; Lu, A.; Iverson, T.; Shelimov, K.; Huffman, C. B.; Rodriguez-Macias, F.; Shon, Y. S.; Lee, T. R.;

Colbert, D. T.; Smalley, R. E., Fullerene pipes. *Science* **1998,** *280* (5367), 1253-1256.
10. Tasis, D.; Tagmatarchis, N.; Bianco, A.; Prato, M., Chemistry of carbon nanotubes. *Chem. Rev.* **2006,** *106* (3), 1105-1136.
11. Dyke, C. A.; Tour, J. M., Covalent functionalization of single-walled carbon nanotubes for materials applications. *J. Phys. Chem. A* **2004,** *108* (51), 11151-11159.
12. Hodge, S. A.; Bayazit, M. K.; Coleman, K. S.; Shaffer, M. S. P., Unweaving the rainbow: a review of the relationship between single-walled carbon nanotube molecular structures and their chemical reactivity. *Chem. Soc. Rev.* **2012,** *41* (12), 4409-4429.
13. Salzmann, C. G.; Llewellyn, S. A.; Tobias, G.; Ward, M. A. H.; Huh, Y.; Green, M. L. H., The role of carboxylated carbonaceous fragments in the functionalization and spectroscopy of a single-walled carbon-nanotube material. *Adv. Mat.* **2007,** *19* (6), 883-+.
14. Shao, L.; Tobias, G.; Salzmann, C. G.; Ballesteros, B.; Hong, S. Y.; Crossley, A.; Davis, B. G.; Green, M. L. H., Removal of amorphous carbon for the efficient sidewall functionalisation of single-walled carbon nanotubes. *Chem. Comm.* **2007,** (47), 5090-5092.
15. Mickelson, E. T.; Huffman, C. B.; Rinzler, A. G.; Smalley, R. E.; Hauge, R. H.; Margrave, J. L., Fluorination of single-wall carbon nanotubes. *Chem. Phys. Let.* **1998,** *296* (1-2), 188-194.
16. Boul, P. J.; Liu, J.; Mickelson, E. T.; Huffman, C. B.; Ericson, L. M.; Chiang, I. W.; Smith, K. A.; Colbert, D. T.; Hauge, R. H.; Margrave, J. L.; Smalley, R. E., Reversible sidewall functionalization of buckytubes. *Chem. Phys. Let.* **1999,** *310* (3-4), 367-372.
17. Nakamura, T.; Ishihara, M.; Ohana, T.; Tanaka, A.; Koga, Y., Sidewall modification of single-walled carbon nanotubes using photolysis of perfluoroazooctane. *Chem. Comm.* **2004,** (11), 1336-1337.
18. Peng, H. Q.; Alemany, L. B.; Margrave, J. L.; Khabashesku, V. N., Sidewall carboxylic acid functionalization of single-walled carbon nanotubes. *J Am. Chem. Soc.* **2003,** *125* (49), 15174-15182.
19. Wei, L.; Zhang, Y., Covalent sidewall functionalization of single-walled carbon nanotubes via one-electron reduction of benzophenone by potassium. *Chem. Phys. Let.* **2007,** *446* (1-3), 142-144.
20. Wei, L.; Zhang, Y., Covalent sidewall functionalization of single-walled carbon nanotubes: a photoreduction approach. *Nanotechnology* **2007,** *18* (49).
21. Chen, J.; Hamon, M. A.; Hu, H.; Chen, Y. S.; Rao, A. M.; Eklund, P. C.; Haddon, R. C., Solution properties of single-walled carbon nanotubes. *Science* **1998,** *282* (5386), 95-98.
22. Clancy, A. J.; Melbourne, J.; Shaffer, M. S. P., A one-step route to solubilised, purified or functionalised single-walled carbon nanotubes. *J. Mater. Chem. A* **2015,** *3* (32), 16708-16715.
23. Clancy, A. J.; Serginson, J. M.; Greenfield, J. L.; Shaffer, M. S. P., Systematic comparison of single-walled carbon nanotube/poly(vinyl acetate) graft-to reactions. *Polymer* **2017,** *133*, 263-271.
24. Wang, H.; Xu, J., Theoretical evidence for a two-step mechanism in the functionalization single-walled carbon nanotube by aryl diazonium salts: Comparing effect of different substituent group. *Chem. Phys. Let.* **2009,** *477* (1-3), 176-178.
25. Wunderlich, D.; Hauke, F.; Hirsch, A., Preferred functionalization of metallic and small-diameter single walled carbon nanotubes via reductive alkylation. *J. Mater. Chem.* **2008,** *18* (13), 1493-1497.

26. Miyata, Y.; Maniwa, Y.; Kataura, H., Selective oxidation of semiconducting single-wall carbon nanotubes by hydrogen peroxide. *J. Phys. Chem. B* **2006,** *110* (1), 25-29.
27. Kharlamova, M. V.; Volykhov, A. A.; Yashina, L. V.; Egorov, A. V.; Lukashin, A. V., Experimental and theoretical studies on the electronic properties of praseodymium chloride-filled single-walled carbon nanotubes. *J. Mat. Sci.* **2015,** *50* (16), 5419-5430.
28. Kharlamova, M. V.; Niu, J. J., Comparison of metallic silver and copper doping effects on single-walled carbon nanotubes. *App. Phys. a-Mat. Sci. Proc.* **2012,** *109* (1), 25-29.
29. Cambre, S.; Wenseleers, W., Separation and Diameter-Sorting of Empty (End-Capped) and Water-Filled (Open) Carbon Nanotubes by Density Gradient Ultracentrifugation. *Angew. Chem. Int. Ed.* **2011,** *50* (12), 2764-2768.
30. Kharlamova, M. V.; Kramberger, C.; Yanagi, K.; Sauer, M.; Saito, T.; Pichler, T., Separation of Nickelocene-Filled Single-Walled Carbon Nanotubes by Conductivity Type and Diameter. *Phys. Stat. Sol. B-Bas. Sol. State Phys.* **2017,** *254* (11), 5.
31. Khlobystov, A. N.; Scipioni, R.; Nguyen-Manh, D.; Britz, D. A.; Pettifor, D. G.; Briggs, G. A. D.; Lyapin, S. G.; Ardavan, A.; Nicholas, R. J., Controlled orientation of ellipsoidal fullerene C-70 in carbon nanotubes. *App. Phys. Let.* **2004,** *84* (5), 792-794.
32. Kharlamova, M. V., Advances in tailoring the electronic properties of single-walled carbon nanotubes. *Prog. Mat. Sci.* **2016,** *77*, 125-211.
33. Yashina, L. V.; Eliseev, A. A.; Kharlamova, M. V.; Volykhov, A. A.; Egorov, A. V.; Savilov, S. V.; Lukashin, A. V.; Puettner, R.; Belogorokhov, A. I., Growth and Characterization of One-Dimensional SnTe Crystals within the Single-Walled Carbon Nanotube Channels. *J. Phys. Chem. C* **2011,** *115* (9), 3578-3586.
34. Kharlamova, M. V.; Yashina, L. V.; Lukashin, A. V., Comparison of modification of electronic properties of single-walled carbon nanotubes filled with metal halogenide, chalcogenide, and pure metal. *App. Phys. a-Mat. Sci. Proc.* **2013,** *112* (2), 297-304.
35. Kharlamova, M. V.; Yashina, L. V.; Lukashin, A. V., Charge transfer in single-walled carbon nanotubes filled with cadmium halogenides. *J. Mat. Sci.* **2013,** *48* (24), 8412-8419.
36. Pichler, T.; Kramberger, C.; Ayala, P.; Shiozawa, H.; Knupfer, M.; Ruemmeli, M. H.; Batchelor, D.; Kitaura, R.; Imazu, N.; Kobayashi, K.; Shinohara, H., Bonding environment and electronic structure of Gd metallofullerene and Gd nanowire filled single-wall carbon nanotubes. *Phys. Stat. Sol. B-Bas. Sol. State Phys.* **2008,** *245* (10), 2038-2041.
37. Ayala, P.; Miyata, Y.; De Blauwe, K.; Shiozawa, H.; Feng, Y.; Yanagi, K.; Kramberger, C.; Silva, S. R. P.; Follath, R.; Kataura, H.; Pichler, T., Disentanglement of the electronic properties of metallicity-selected single-walled carbon nanotubes. *Phys. Rev. B* **2009,** *80* (20).
38. Eliseev, A. A.; Yashina, L. V.; Verbitskiy, N. I.; Brzhezinskaya, M. M.; Kharlamova, M. V.; Chernysheva, M. V.; Lukashin, A. V.; Kiselev, N. A.; Kumskov, A. S.; Freitag, B.; Generalov, A. V.; Vinogradov, A. S.; Zubavichus, Y. V.; Kleimenov, E.; Nachtegaal, M., Interaction between single walled carbon nanotube and 1D crystal in CuX@SWCNT (X = Cl, Br, I) nanostructures. *Carbon* **2012,** *50* (11), 4021-4039.
39. Perry, D. L., *Handbook of Inorganic Compounds*. CRC Press: 2016.
40. Sloan, J.; Friedrichs, S.; Meyer, R. R.; Kirkland, A. I.; Hutchison, J. L.; Green, M. L. H., Structural changes induced in nanocrystals of binary compounds confined within single walled carbon nanotubes: a brief review. *Inorg. Chim. Acta* **2002,** *330*, 1-12.

41. Sloan, J.; Friedrichs, S.; Flahaut, E.; Brown, G.; Bailey, S. R.; Coleman, K. S.; Xu, C.; Green, M. L. H.; Hutchison, J. L.; Kirkland, A. I.; Meyer, R. R., The characterisation of sub-nanometer scale structures within single walled carbon nanotubes. *Elec. Prop. Mol. Nanostruc.*, Kuzmany, H.; Fink, J.; Mehring, M.; Roth, S., Eds. 2001; Vol. 591, pp 277-282.
42. Troyanov, S. I.; Krahl, T.; Kemnitz, E., Crystal structures of GaX3 (X = Cl, Br, I) and AlI3. *Zeit. Kristal.* **2004,** *219* (2), 88-92.
43. Liu, J. Z.; Zheng, Q. S.; Wang, L. F.; Jiang, Q., Mechanical properties of single-walled carbon nanotube bundles as bulk materials. *J. Mech. Phys. Sol.* **2005,** *53* (1), 123-142.
44. Lammert, P. E.; Zhang, P. H.; Crespi, V. H., Gapping by squashing: Metal-insulator and insulator-metal transitions in collapsed carbon nanotubes. *Phys. Rev. Let.* **2000,** *84* (11), 2453-2456.

7 Final Conclusions and Outlook

The main aim of this work was to successfully fill SWCNTs with a range of new species to create new composite materials that had not been prepared before. These new materials have been fully characterised using simple and routine techniques and have been shown to have a purity far higher than what has been achieved elsewhere.[1]

Tetrahedral phosphorus molecules have been stabilised by their encapsulation within SWCNTs in higher proportions than by other methods.[2] Their encapsulation can be produced by either melt-phase, *m*-P@CNT, or vapour-phase, *v*-P@CNT, experiments. The *v*-P@CNT samples, in particular, had remarkably high filling yields, with 75% of all nanotubes exhibiting filling. Subtleties in the resulting structures has been identified. Melt-phase preparations result in a higher proportion of P_4 molecules whereas vapour-phase preparations show more polymerised structures. These new allotropes, the zigzag ladder and the single zigzag chain, are shown to be sensitive to the diameter of nanotube in which they are found and can be formed when provided with enough energy, either from a furnace or an electron beam. The relative abundancies of the structures have also shown good agreement with DFT calculations. The thermal properties of the materials show that melt-phase prepared samples have a delayed exothermic release when heated, caused by the leakage of the contained P_4 molecules and resulting oxidation. It is thought that this material could potentially be used as a delayed energy release material that can be used for when a large amount of energy is needed in a controlled manner. The *v*-P@CNT samples do not show such a result and is another effect of the more polymerised nature of the filling material which shows a much longer delayed leakage as the phosphorus structures have to re-form into tetrahedra before escaping the nanotube.

Arsenic has also been encapsulated and has shown similar results to the *v*-P@CNT samples in terms of the abundancies of each structure observed.[3] As_4 molecules have been imaged for the very first time and have been shown to form similar structures to confined phosphorus when the polymerise. This result underpins the chemical similarity arsenic shares with phosphorus.[4] DFT calculations have also shown good agreement with experimental observation. Similar thermal properties to the *v*-P@CNT samples were detected, with the delayed release of the arsenic material. This result seems to indicate the importance of the preparation method, as the *v*-P@CNT and As@CNT samples show structural and thermal similarities. It would be incredibly interesting if a

melt-phase synthesis could be prepared using yellow arsenic to show if the same similarities can be identified with the *m*-P@CNT samples.

The confinement of antimony was attempted, but only very low filling yields could be obtained. Some images were obtained though and seemed to show that the confined material adopts the zigzag ladder structure. Submerging the SWCNTs completely within the antimony material could provide better filling yield results and would be the next steps in these experiments.

Electronic density of states calculations have shown a wide variety of band gaps for the confined materials. Unfortunately, neither Raman nor XPS studies have been able to detect any consistent charge transfer or patterns. It is thought that the oxide presence, the uncontrollable polymerisations and the different behaviours of semi-conducting and metallic SWCNTs have made it difficult to fully understand these properties.[5] An idea to fill insulating boron nitride nanotubes may help to record the electronic properties of the confined phosphorus and arsenic.

In general, the DFT work has proved an invaluable resource in trying to understand the structures observed through experimental methods. Without these calculations there would still be speculation as to the true structure behind the double lined features seen in the pnictogen filled SWCNTs or if the single strand often observed running through the middle of filled tubes is from a straight or zigzag structure. Additionally, the energies calculated for each structure and the nudged elastic band calculations have also provided robust evidence as to how dynamic these composites are, which has been hard to capture using HRTEM techniques alone. The small activation energies calculated between the butterfly and tetrahedra structures has helped explain perhaps why the butterfly structure was never observed by HRTEM. Some of the results calculated, such as the band gaps, have been beyond the reach of this research to prove but they give us new avenues to explore to help improve our understanding of these novel structures.

There are some limitations to these techniques though. A major drawback is that these calculations have omitted the electron dosage under which the observed structures have been exposed to. This source of energy would likely impact the types and the proportions of the structures observed in this work but would have been quite complicated to have implemented for this study. It has also been proposed that the filling method may have also had an impact on the structures observed. There is computational work in the literature exploring the mechanisms for filling SWCNTs but given the time constraints and focus of this work, would have been impractical to attempt.

Aluminium iodide was also successfully contained within SWCNTs. Although the filling yields were low, the samples were pure and underwent the expected charge transfer behaviour with the SWCNTs. It was hoped that this would increase the effectiveness of a simple Grignard reaction, but unfortunately this could not be achieved. Finding the correct solvent system that suits both the C_{60} capping agent and aluminium iodide is the priority for taking these experiments to the next stage.

Throughout this research, additional ideas were formed, and initial results were collected that, unfortunately, were never followed up. These would be the starting points for carrying on the research presented in this thesis. One example would be examining SWCNTs filled with other Lewis acids. Boron iodide showed better filling yields than aluminium iodide, but more experiments are needed to formulate a consistent filling and work up method. More time should be spent on investigating the capping of the AlI_3@CNT samples as the filling material appeared to leak out during the functionalisation process. Investigating if the Grignard reagent is reacting with the C_{60} corks may also be worthwhile to get a satisfactory explanation of the leakage observed.

In regards to the pnictogen work, more experiments should be attempted to successfully fill SWCNTs with antimony. An initial experiment would be to use an extremely large excess of antimony to try and completely submerge the SWCNTs within the antimony melt and hopefully increase the filling yield. it would also be interesting to try and fill insulating boron nitride nanotubes. This may help determine the electronic properties of the various allotropes formed. Alternatively, separating the filled nanotubes into similar diameters using centrifugation techniques *a la* Cambré's work may also help determine the charge transfer process.[6] Factions of similar sized SWCNTs would help reduce competing effects from the different electronic properties of the various chiralities in the bulk samples during Raman spectroscopy and hopefully confirm the DFT results.

The stability of the pnictogen filled nanotubes could also be determined more accurately. Although anecdotally, no deterioration was noticed in the phosphorus and arsenic filled nanotubes, a formal investigation taking XPS and TGA measurements at regular intervals would help establish the stability of these materials. There is also potential for further work regarding the quantification of the filled tubes. Establishing how much of an individual nanotube is filled may help determine the filling mechanism. It could also help reveal why some tubes fill and why some remain empty. This would require dispersing the nanotubes before imaging them in order to resolve the individual nanotubes more

clearly as the method used in this thesis leads to large bundles and tangles of tubes that make it hard to pick out individual nanotubes.

Although many new and interesting things have been discovered during this process, it is hoped that this work can help solidify some of the fundamentals that have been perhaps lacking within this field. Focussing on determining the filling yield accurately and trying to create samples with as minimal external material as possible are seen as high priority issues which will be hugely important in progressing this area of research. Carbon materials have shown a remarkable versatility and will be essential in creating high-performance technologies, and hopefully filled carbon nanotubes can play a part in this landscape.

7.1 References

1. Xu, J.; Guan, L., Toward understanding the active site for oxygen reduction reaction on phosphorus-encapsulated single-walled carbon nanotubes. *RSC Adv.* **2013,** *3* (16), 5577-5582.
2. Hart, M.; White, E. R.; Chen, J.; McGilvery, C. M.; Pickard, C. J.; Michaelides, A.; Sella, A.; Shaffer, M. S. P.; Salzmann, C. G., Encapsulation and Polymerization of White Phosphorus Inside Single-Wall Carbon Nanotubes. *Angew. Chem. Int. Ed.* **2017,** *56* (28), 8144-8148.
3. Hart, M.; Chen, J.; Michaelides, A.; Sella, A.; Shaffer, M. S. P.; Salzmann, C. G., One-Dimensional Arsenic Allotropes: Polymerization of Yellow Arsenic Inside Single-Wall Carbon Nanotubes. *Angew. Chem. Int. Ed.* **2018,** *57* (36), 11649-11653.
4. Liu, B.; Köpf, M.; Abbas, A. N.; Wang, X.; Guo, Q.; Jia, Y.; Xia, F.; Weihrich, R.; Bachhuber, F.; Pielnhofer, F.; Wang, H.; Dhall, R.; Cronin, S. B.; Ge, M.; Fang, X.; Nilges, T.; Zhou, C., Black Arsenic–Phosphorus: Layered Anisotropic Infrared Semiconductors with Highly Tunable Compositions and Properties. *Adv. Mat.* **2015,** *27* (30), 4423-4429.
5. Kharlamova, M. V., Advances in tailoring the electronic properties of single-walled carbon nanotubes. *Prog. Mat. Sci.* **2016,** *77*, 125-211.
6. Cambre, S.; Wenseleers, W., Separation and Diameter-Sorting of Empty (End-Capped) and Water-Filled (Open) Carbon Nanotubes by Density Gradient Ultracentrifugation. *Angew. Chem. Int. Ed.* **2011,** *50* (12), 2764-2768.

Appendix Chapter 3 Additional Figures

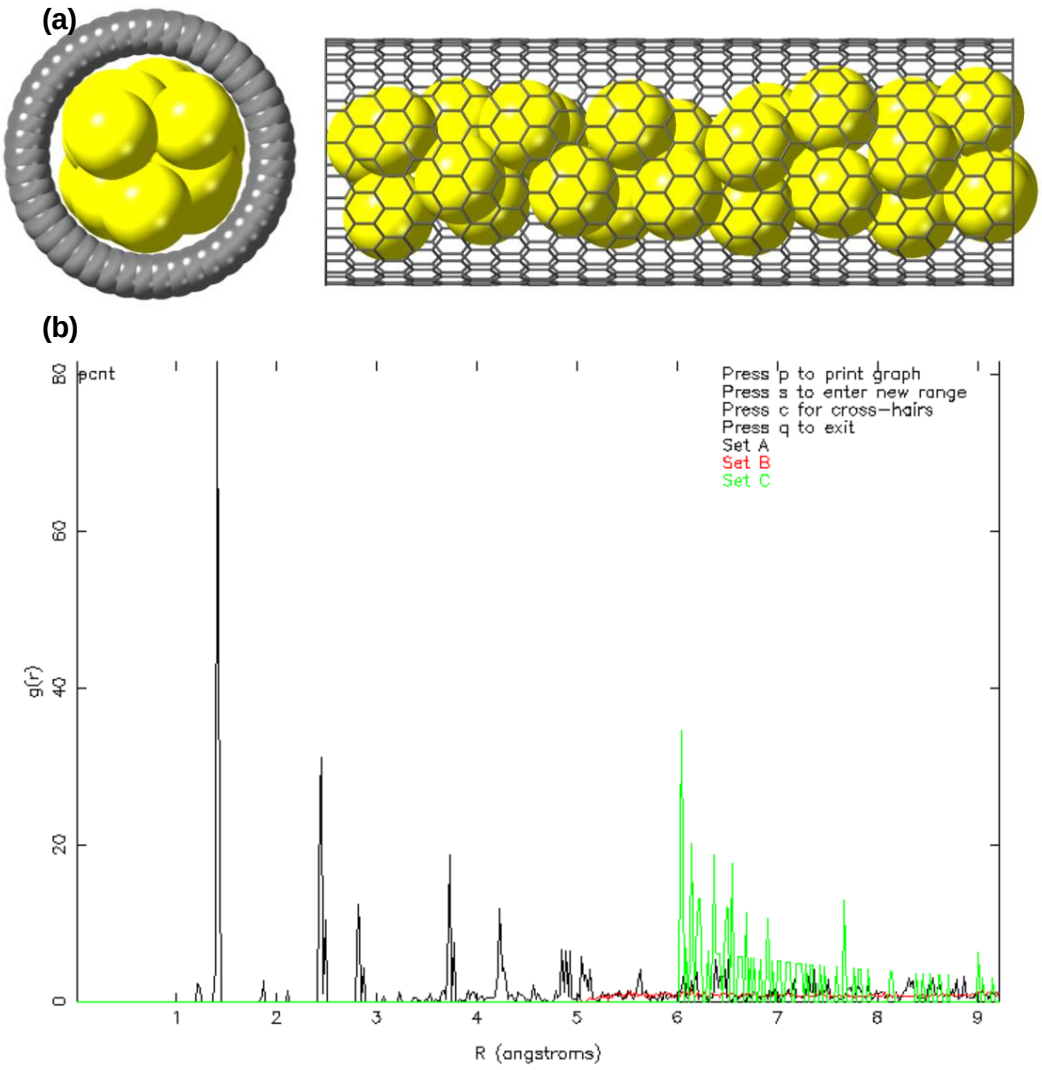

Figure A3.1 (a) Structure adopted by P_4 molecular spheres within a 1.8 nm diameter SWCNT. (b) Partial Distribution Functions for a $(25P_4)$@CNT composite.

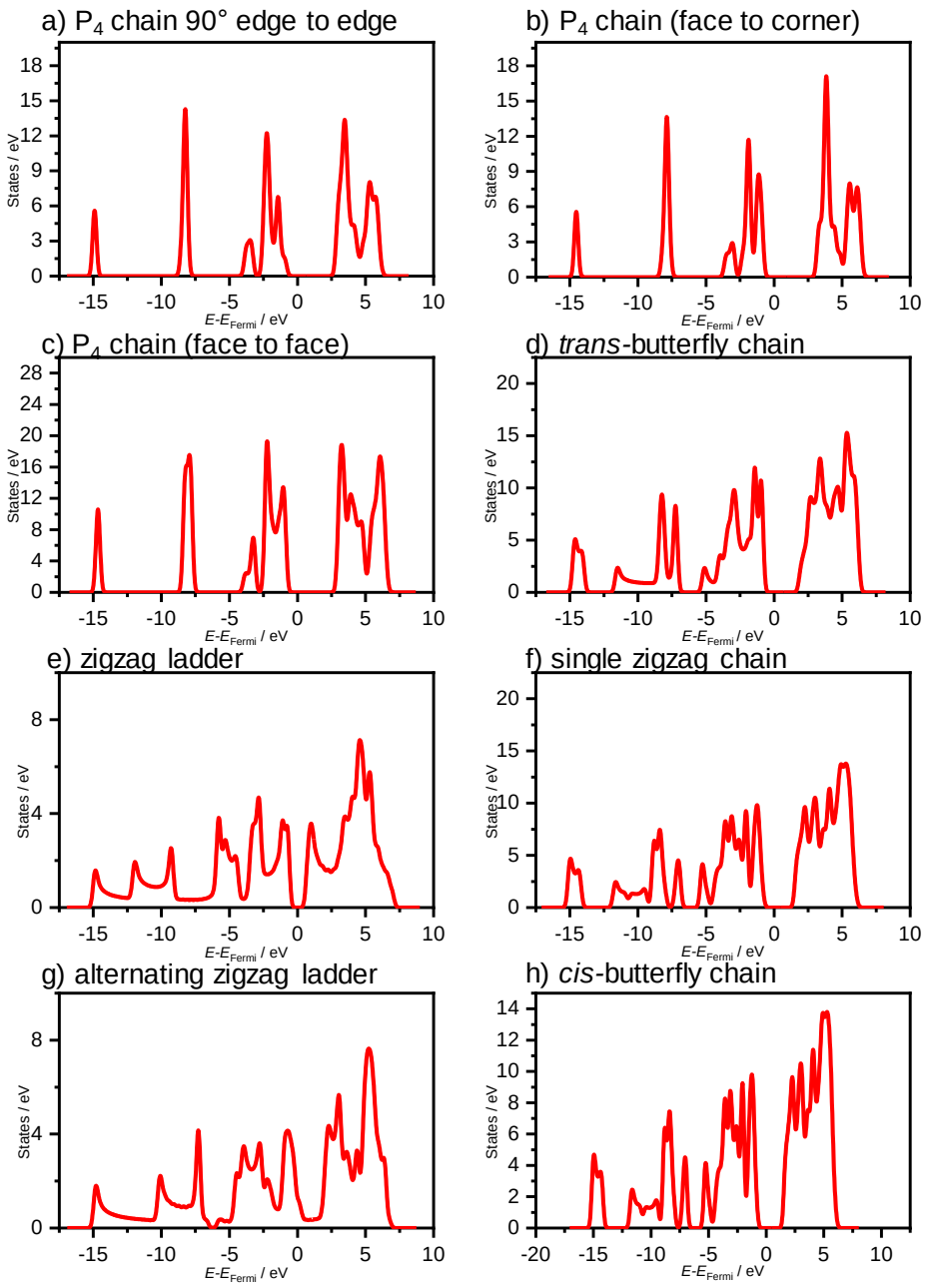

Figure A3.2 Electronic densities of states of the various free standing 1D phosphorus structures. Used to produce band gaps in Figure 3.28. Calculated by Ji Chen.

Appendix Chapter 4 Additional Figures

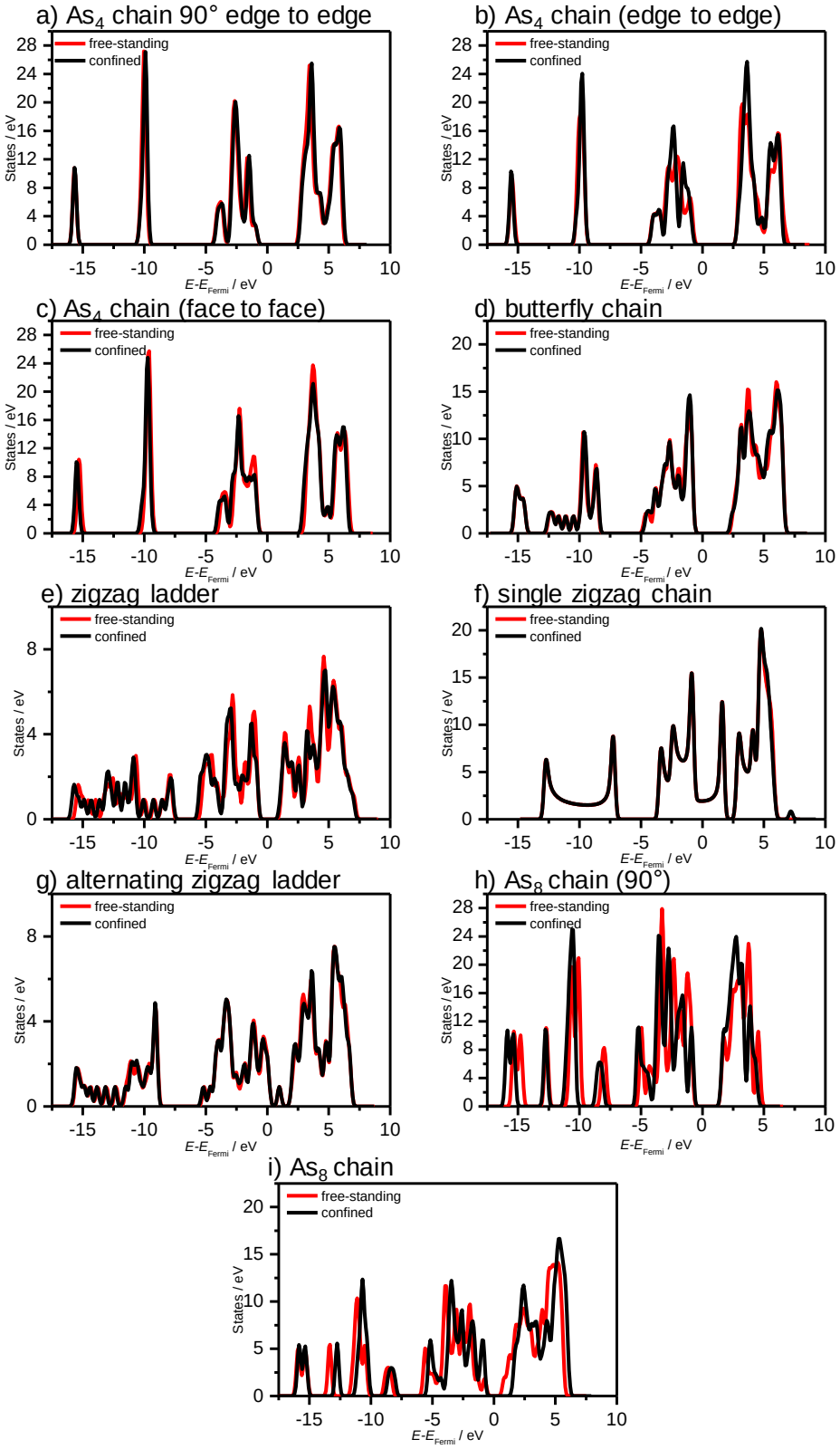

Figure A4.1 Electronic densities of states of the various 1D arsenic structures including confined (black) as well as free standing structures (red). Used to produce band gaps in Figure 4.19. Calculated by Ji Chen.

Appendix Chapter 5 Additional Figures

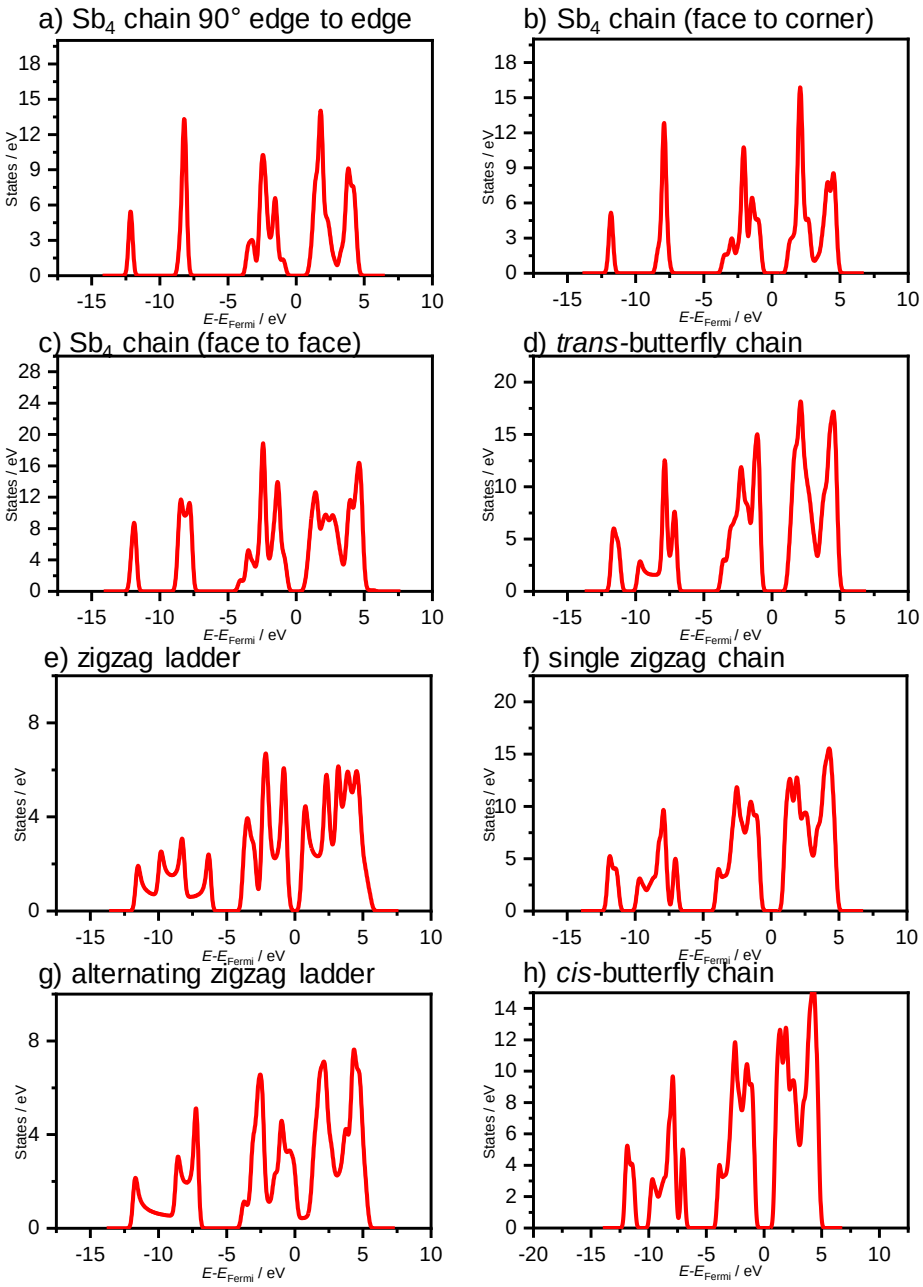

Figure A5.1 Electronic densities of states of the various freestanding 1D antimony structures. Calculated by Ji Chen.